EXPERIMENTAL STUDIES OF THE NOISE PRODUCED IN A SUPERSONIC NOZZLE BY UPSTREAM ACOUSTIC AND THERMAL DISTURBANCES

Thesis by

Jerome M. Auerbach

In Partial Fulfillment of the Requirements

For the Degree of

Doctor of Philosophy

California Institute of Technology

Pasadena, California

1975

(Submitted March 19, 1975)

To a Most Charming Lady

Called Betty

ACKNOWLEDGMENTS

As the experiment described in this thesis progressed from a seemingly insurmountable task into a working reality, the knowledge, skill, and help of several people proved to be indispensable. Their mention in the following paragraphs is only a small return for their contributions.

For his constant guidance, encouragement, and patience in times of crisis, the author expresses his deepest thanks to his advisor, Professor Edward E. Zukoski.

For their many suggestions in design of the experimental procedure and equipment, great appreciation is expressed to Professors W. D. Rannie, F. E. Marble, H. C. Martel, and Dr. Haskel Shapiro.

Sincere feelings of appreciation go to Mr. F. T. Linton for his skill in construction of the experimental apparatus, to Mr. Mark S. Bohn for his help in the computer aspects of the experiments, and to Mrs. R. Duffy for her excellent typing of the thesis.

Gratefully acknowledged is the financial support provided by the California Institute of Technology in the form of a Link-Pickering Fellowship and Graduate Research Assistantships, the Department of Transportation which funded the research, and the Veterans Administration which provided additional support through the G. I. Bill.

ABSTRACT

A novel noise source mechanism whereby sound is produced by time-dependent temperature nonuniformities in a flow with a mean velocity gradient is investigated experimentally. The research is part of a theoretical and experimental study of this noise source initiated by Professor F. E. Marble.

A steady accelerating flow was produced in a rectangular supersonic nozzle with an entrance Mach number of 0.2, an exit Mach number of 1.38, and a throat area of 1 $in.^2$. A rotary valve bleed flow system and an electrical wire resistance heater upstream of the nozzle introduced mass flow and temperature fluctuations into the nozzle flow at frequencies up to 500 Hz. Sound measurements were made at six positions along the nozzle and outside the nozzle assembly, which was enclosed in an anechoic chamber 10 ft. on a side.

All data acquisition and processing was done with a computer-controlled data acquisition system, making the experiment essentially "computerized." By interfacing the control circuitry of the bleed flow and heater systems to the data acquisition system, a digital signal-averaging technique was developed which enabled the sound produced by the bleed flow and temperature fluctuations to be detected and accurately measured in high-level backgrounds of turbulent flow noise.

By synchronization of the bleed flow and heater, a pure temperature disturbance without an associated pressure disturbance caused by heating was produced. This pure temperature disturbance was found to produce sound upon being convected through the nozzle. The novel noise source mechanism was thus verified.

Excellent agreement was found between the nozzle sound measurements and one-dimensional small disturbance theory applied to the flow occurring in the nozzle.

External field measurements yielded jet noise levels and spectra agreeing with other reported studies, spatial variation of the sound field due to a pure pressure fluctuation at the nozzle exit, and cross correlation data between the external sound field and the pressure fluctuations at the nozzle exit.

TABLE OF CONTENTS

LIST OF FIGURES

LIST OF SYMBOLS

a_*	speed of sound at nozzle throat
a_H	dimensionless heater performance parameter
a_k	Fourier cosine coefficient
A_l	heater wire surface area
A_n	amplitude of Fourier series component
A_o	amplitude of a periodic signal
A_T	total surface area of wire heater
$A_\xi(f)$	amplitude of spectral component of random variable ξ at frequency f
b_k	Fourier sine coefficient
C_p	specific heat at constant pressure
C_v	specific heat at constant volume
C_f	skin friction coefficient
C_k	complex Fourier coefficient
C_w	heat capacity of heater wire
$C_\xi(i\upsilon)$	characteristic function of the random variable ξ
CC_{12}	cross correlation coefficient
CF_{12}	cross correlation function
d	height of rectangular duct
D_e	hydraulic diameter of nozzle exit
D_k	complex Fourier coefficient
e_{ij}	rate of strain tensor
$\mathcal{E}$	empirical jet spreading constant
F	dimensionless heater wire ohmic dissipation
$G(\tau)$	Dirac comb function with argument τ

$\tilde{u}$	spectral component of fluctuating velocity
u_τ	shear velocity
$\overline{U}$	mean part of axial velocity
U	dimensionless mean velocity
u_i	Cartesian velocity components
x^*	distance from nozzle entrance to throat
$\overline{x}$	dimensionless nozzle coordinate
Z_1	dimensionless velocity fluctuation
Z_2	dimensionless pressure fluctuation
Z_3	dimensionless entropy fluctuation
α_1	duty cycle of heater voltage waveform
β	dimensionless angular frequency
β_1	dimensionless heater performance parameter
γ	isentropic index, c_p/c_v
δ^*	boundary layer displacement thickness
Δ_j	width of jet
$\Delta_{\frac{1}{2}}$	half width of jet
Δt_H	time for gas to pass through wire heater
$\Delta\Omega$	angular frequency resolution of a Fourier series
λ	wavelength
$\tilde{\pi}$	correction term to law of the wall velocity profile
ϕ_k	phase of Fourier series component
$\phi(f)$	phase distribution of Gaussian noise with frequency
Ψ	dimensionless source term
ρ	density
$\overline{\rho}$	mean part of density

p_-	upstream-running pressure wave (complex quantity)
p_{ref}	pressure at reference conditions
$p(\xi)$	probability density function of random variable ξ
q	dimensionless heat source term
$\dot{q}$	heat source
$\tilde{q}$	spectral component of heat source
r	distance from source or origin
R_l	heater wire resistance
R_N	signal noise ratio after N
Re_θ	Reynolds number based on momentum thickness
s	specific entropy
s'	fluctuating component of entropy
$\tilde{s}$	spectral component of fluctuating part of entropy
t	time
T_e	freestream temperature
T_o	heater voltage waveform period
T_t	stagnation temperature
$\overline{T}$	mean part of temperature field
T'	fluctuating component of temperature field
$\tilde{T}$	spectral component of temperature fluctuation
$\tilde{T}_g$	fluctuating component of gas
$\overline{T}_w$	average heater wire temperature
T_{aw}	adiabatic wall temperature
T_{ref}	reference temperature
u	axial velocity in one-dimensional nozzle
u'	fluctuating part of axial velocity

h	specific enthalpy
h_c	convection heat transfer coefficient
$h_o(x)$	nozzle contour separation at coordinate x for inviscid flow
$h_1(x)$	nozzle contour separation at coordinate x taking into account boundary layer corrections
H	compressible boundary layer shape factor
H_i	incompressible boundary layer shape factor
I	electrical current in heater wire
k_+	wave number of downstream-running pressure wave
k_-	wave number of upstream-running pressure wave
K	Kármán's constant
ℓ	half length of bleed flow region in rectangular duct
ℓ_c	length of supersonic jet potential core
ℓ_s	length of supersonic region of jet
L	length of wire heater in flow direction
L_c	length of jet potential core/jet diameter
L_s	length of jet supersonic region/jet diameter
$\dot{m}$	mass source
$\tilde{\dot{m}}$	spectral component of mass source
$\dot{m}_o$	mass flow rate of gas through heater
p	pressure
$\bar{p}$	mean component of pressure
p'	fluctuating component of pressure
$\tilde{p}$	spectral component of fluctuating pressure
p_t	stagnation pressure
p_+	downstream-running pressure wave (complex quantity)

ρ'	fluctuating part of density
ρ_e	freestream density
σ_1	r.m.s. noise level
τ_w	wall shear stress
τ_{ij}	viscous stress tensor
ξ	random variable
η	random variable
ζ	sum of a set of random variables
Θ	dimensionless heater wire temperature difference
ν	kinematic viscosity
ω	angular frequency
Ω_k	angular frequency of a Fourier series component with index k
υ	argument of characteristic function

I. THE JET NOISE PROBLEM

1.1 Introductory Remarks

The spread of the population of large cities into the once empty areas surrounding metropolitan airports has elevated noise emission from jet aircraft to a prime engine design consideration.

The significant progress to date in reduction of jet engine noise is illustrated by the following two facts. (i) The first takeoff of the McDonnell Douglas DC-10 at the Long Beach, California Airport (Spring, 1972) was witnessed by persons standing only tens of feet from the runway at the point of takeoff roll. No person suffered even the slightest discomfort from the engine noise. (ii) The supersonic transport, Concorde, with 4 Olympus engines (38,050 lbs. thrust per engine), creates no more noise during takeoff and landing than a Boeing 707 with 4 Pratt and Whitney JT3D-7 turbofan engines (19,000 lbs. thrust per engine). In spite of these advances, more improvement remains to be made to make frequent aircraft takeoffs, landings, and flyovers tolerable for the populace close to an airport.

This thesis is a small step towards this objective. In the next section, the noise associated with the different regimes of present-day jet engine operation will be described. The different noise sources will be enumerated, and emphasis will be placed on the one which will be the subject of this thesis. In the last sections of this chapter, the noise sources in jet engines will be presented on a formal basis with a brief summary of the major research efforts on them to date.

1.2 Noise Characteristics of Jet Engines

Jet engine noise can be classified into the following categories[1]: jet noise, rotor and fan noise, and combustion noise.

Jet noise arises from a number of sources within the engine and from the turbulent mixing layer which develops between engine exhaust jet and the ambient air. At full power operations, noise from the exhaust jet is the dominant type of noise in most present-day engines.

Rotor and fan noise, unlike jet noise, originates exclusively within the engine. During takeoffs and the throttle-back approaches and landings required at airports for noise abatement, this noise can immediately be recognized as a loud whine. In turbojets[2] (e. g. Pratt and Whitney, JT36-6), the compressor whine dominates the jet noise forward of the aircraft during throttle-back approaches. In the case of modern turbofans[2] (General Electric JT9D, CF6-50 for the DC-10, General Electric TF39 for the C5A, and Rolls Royce RB 211 for the Lockheed 1011), the fan noise dominates the jet noise during takeoff and landing operation.

During takeoff, the jet noise radiates towards the rear, but the fan noise radiates in all directions. During landings at low throttle settings, the fan noise is dominant over the hushed jet noise.

Fan and rotor noise originates from the interaction of the rotating fan and compressor rotor blades with the surrounding air. First, there are components of noise at multiples of the blade rotation frequency since the motion of the blades produces periodic pressure fluctuations as they pass a point in the fluid. Second, there is a com-

ponent of noise at the frequency of wake shedding from the blades. Wakes periodically incident on a blade result in periodic lift forces which in turn are transmitted to the surrounding fluid as periodic pressure fluctuations. The noise in the bypass duct is much greater when the duct flow is supersonic. Fan noise reduction is achieved by maintaining a subsonic blade tip speed, lining the bypass ducts with acoustic damping material, and mounting splitter plates with damping material in the engine nacelle.

Combustion noise is a product of nonuniform and nonsteady combustion in the engine. Although one would initially surmise that this noise is entirely due to the expansion and pressure rise of the fuel/air mixture upon combustion, there is another novel mechanism of combustion noise which is the subject of this thesis. The mechanism is based on the fact that when a fluid which contains a time-varying stagnation state (i.e., temperature or entropy fluctuations) is subjected to a mean velocity gradient, time-dependent pressure fluctuations (sound) are produced.

One can see the operation of this mechanism from the following description. Assume that a fluid contains small fluctuations in the temperature or, equivalently, the density and that it passes through a region which contains a mean velocity gradient which is essentially constant. As the density fluctuations pass that point in the flow, the "inertia force" of the fluid (density $\times$ velocity $\times$ velocity gradient) at that point varies in time due to the density fluctuations. This inertia force thus exerts time-varying pressures on neighboring regions of the fluid. These pressures act analogously to a moving

piston in a stationary gas and produce sound. Thus, the sound produced in a finite length of a fluid with a mean velocity gradient by density (or equivalently, entropy) fluctuations is that produced by a distribution of "inertia force pistons."

In a real jet engine, production of noise by this mechanism can take place in two locations; first, in the nozzles upstream of the turbine and in the turbine stators, and second, in the exit nozzle. In most present-day engines, the exit nozzle flow is accelerated to medium or high subsonic speeds; but in the engines for supersonic aircraft such as the Olympus 593 in the Concorde, the exhaust flow is accelerated to supersonic speeds by an adjustable convergent-divergent nozzle. At the throat of the nozzle, the convective acceleration is very strong and noise generation by the above-described mechanism would be most pronounced. Hence, it was decided to study the noise generation mechanism in a supersonic convergent-divergent nozzle. Once the experimental technique had been proven on this type of flow, the experimental apparatus and procedures could be adapted to measurements in a subsonic nozzle or in a geometry modeling the stator-rotor region of a turbine.

1.3 Production of Noise in a Region of General Fluid Motion

The mathematical description of noise production is derivable from the basic flow equations of continuity, momentum, energy, and state. These are written below in Cartesian tensor form as

Continuity

$$\frac{\partial \rho}{\partial t} + \frac{\partial (\rho u_i)}{\partial x_i} = \dot{m} \tag{1.1}$$

Momentum

$$\frac{\partial (\rho u_i)}{\partial t} + \frac{\partial}{\partial x_j}(\rho u_i u_j) = -\frac{\partial p}{\partial x_i} + \frac{\partial \tau_{ij}}{\partial x_j} + F_i + \dot{m} u_i \tag{1.2}$$

Thermodynamic Energy Equation

$$T \frac{Ds}{Dt} = \dot{q} + \frac{1}{\rho}(KT)_{,i} + \frac{1}{2\rho} \tau_{ij} e_{ij} \tag{1.3}$$

In the energy equation, Fourier's law of heat conduction is assumed to hold, and e_{ij}, the rate of strain tensor, is given by

$$e_{ij} = u_{i,j} + u_{j,i} \quad . \tag{1.4}$$

Equation of State

$$\rho = \rho(p, s) \quad . \tag{1.5}$$

This last equation will be used in differential form,

$$d\rho = \left(\frac{\partial \rho}{\partial p}\right)_s dp + \left(\frac{\partial \rho}{\partial s}\right)_p ds \quad . \tag{1.5a}$$

Since $(\partial p / \partial \rho)_s = a^2$, the speed of sound squared, (1.5a) becomes

$$d\rho = \frac{1}{a^2} dp + \left(\frac{\partial \rho}{\partial s}\right)_p ds \quad . \tag{1.6}$$

Eliminating ρu_i between (1.1) and (1.2) yields

$$\frac{\partial^2 \rho}{\partial t^2} = \frac{\partial^2 T_{ij}}{\partial x_i \partial x_j} + \frac{\partial^2 p \delta_{ij}}{\partial x_i \partial x_j} + \frac{\partial \dot{m}}{\partial t} - \frac{\partial F_i}{\partial x_i} - \frac{\partial (\dot{m} u_i)}{\partial x_i} \quad , \tag{1.7}$$

where $T_{ij} = \rho u_i u_j + \tau_{ij}$. From equation (1.5a) one gets the relationship

$$\frac{\partial^2 \rho}{\partial t^2} = \frac{1}{a^2} \frac{\partial^2 p}{\partial t^2} + \left(\frac{\partial \rho}{\partial s}\right)_p \frac{\partial^2 s}{\partial t^2} \quad . \tag{1.8}$$

Substituting (1.8) into (1.7) yields a wave equation for p :

$$\frac{1}{a^2} \frac{\partial^2 p}{\partial t^2} - \frac{\partial^2 p}{\partial x_i \partial x_i} = \left[\frac{\partial \dot{m}}{\partial t} - \left(\frac{\partial \rho}{\partial s}\right)_p \frac{\partial^2 s}{\partial t^2}\right] - \left[\frac{\partial F_i}{\partial x_i} - \frac{\partial (\dot{m} u_i)}{\partial x_i}\right] + \frac{\partial^2 T_{ij}}{\partial x_i \partial x_j} \quad . \tag{1.9}$$

From this last equation, one sees that sound production in a region of general fluid motion arises from sources of monopole, dipole, and quadrupole character:

monopole

Heat and Mass Addition: $\frac{\partial \dot{m}}{\partial t} - \left(\frac{\partial \rho}{\partial s}\right)_p \cdot \frac{\partial^2 s}{\partial t^2}$

dipole

Forces and Momentum Addition: $\frac{\partial F_i}{\partial x_i} - \frac{\partial (\dot{m} u_i)}{\partial x_i}$

quadrupole

Aerodynamic Stresses: $\frac{\partial^2 T_{ij}}{\partial x_i \partial x_j}$

The aerodynamic source term has been the most thoroughly investigated of the three. The first theoretical analyses of this source in terms of quadrupoles was done by Lighthill[3] and Proudman[4]. Subsequently, Ribner[5] showed that the aerodynamic source term could be described by fluid dilatations. Experiments to correlate the aerodynamic stresses in turbulent jets with the far field noise have been done by Chu[6], Lee[7], and Siddon and Rackl[8].

Since part of the experiments described in this thesis are an investigation of how the disturbances produced in the nozzle propagate outwards from the nozzle exit, it was necessary to review previous

work on investigation of noise from choked and supersonic jets. Powell[9-11] investigated the noise from both axisymmetric and two-dimensional choked jets and showed that at large levels of exit over-pressure, an interaction between the flow disturbances and the stationary cellular shock pattern results in an intense high-frequency noise (greater than 10 KHz). At low levels of overpressure, this noise would disappear. In this experiment, in which the jet will be kept as close to ideally expanded as possible, this mode of noise will not occur. The turbulence - shock interaction has been analyzed theoretically by Ribner[12, 13]. The method of analysis can be used to study the production of noise by the interaction of a thermal disturbance (entropy wave) with a shock.

More recent experimental observations of choked and supersonic jet noise have been done by Westley and Woolley[14]; Sheer and Horvay[15]; and Louis, Letty, and Patel[16]. All these investigators pointed out that the noise was produced by an extremely complex mechanism of shock turbulence interaction, oscillating shocks, jet boundary fluctuations, and Mach wave radiation. Thus, in considering the far field noise due to the pressure fluctuations produced in the nozzle, an extremely complex flow field must be taken into account. An excellent correlation of available noise data on supersonic jets has been completed by Howes[17]. His results will be enumerated in Chapter VI.

Since the dipole source (origin of fan and rotor noise) has no relevance to this experiment, a review will not be given. A summary of research in this area is given in reference 18.

The remaining source terms in equation (1.9) to be considered are the mass flow and entropy fluctuation terms. The effect of the mass flow fluctuations can be described by Ribner's theory[5] of aerodynamic noise by fluid dilatations. The noise due to entropy fluctuations passing through an accelerating flow is a novel source in which little previous work has been done. The first theoretical analysis of this mechanism was considered by Crocco[19] and Tsien[20]. The analysis was not directed towards jet noise but towards oscillations in rocket motors. They considered a nozzle with a constant convective acceleration, and for a given entropy fluctuation at the nozzle entrance, they calculated the pressure wave reflected back from the subsonic region of the nozzle into the combustion chamber. Marble and Candel[21] used this approach to calculate the pressure fluctuations produced at all points in a supersonic nozzle by a given entropy fluctuation at the nozzle entrance. The experimental verification of this analysis is one of the main objectives of this thesis.

Few other analyses of the "entropy fluctuation noise mechanism" seem to be recorded in the literature. Chang[22] considered the production of noise by the interaction of an entropy wave with normal and oblique shocks. Cuadra[23] calculated the second order solution for the production of sound waves by the interaction of an entropy wave with an infinitesimal area change in a one-dimensional flow.

No direct experimental analysis appears to have been done on the production of sound by entropy fluctuations in an accelerating flow. The closest type of research appears to be the work done at ONERA[24], which consists of attempts to correlate the far field noise of hot sub-

sonic jets with temperature fluctuations in the jet measured by cross beam techniques.

1.4 Research Goals

A novel noise source will be investigated for the first time experimentally. The experiments will yield detailed measurements showing how temperature or entropy fluctuations produce sound at each point in a given steady accelerating flow. The data will be compared with the theory of Marble and Candel[21]. The measurements will involve the solution of two complex problems. First, the sound produced by the temperature fluctuations must be sorted out of a resultant sound field produced by other sources in the experimental apparatus. Second, to show the existence of the novel noise source unambiguously, a pure entropy fluctuation must be produced. This will involve the exceedingly complex problem of cancelling the pressure disturbances caused by periodic heating of a gas.

All of the above objectives will be accomplished with the newest of the experimenter's tools -- the computer-controlled data acquisition system and solid-state integrated circuitry.

II. THEORETICAL MODEL FOR THE NOISE PRODUCED IN A ONE-DIMENSIONAL SUPERSONIC NOZZLE WITH UPSTREAM TEMPERATURE AND PRESSURE NONUNIFORMITIES

2.1 Governing Equations of the Flow

The one-dimensional flow of an ideal gas in a nozzle of cross-sectional area $A(x)$ is described by the equations of continuity, momentum, energy, and state:

$$\frac{\partial \rho}{\partial t} + \frac{1}{A}\frac{\partial}{\partial x}(\rho u A) = \dot{m} \tag{2.1}$$

$$\rho\left(\frac{\partial u}{\partial t} + u\frac{\partial u}{\partial x}\right) = -\frac{\partial p}{\partial x} \tag{2.2}$$

$$\frac{\partial s}{\partial t} + u\frac{\partial s}{\partial x} = \dot{q}/T \tag{2.3}$$

$$p/\rho = RT \tag{2.4}$$

The flow is assumed to consist of small time-dependent perturbations to the steady values of velocity, density, etc. Thus, the flow variables can be written

$$u = \overline{U}(x) + u'(x,t) \tag{2.5}$$

$$\rho = \overline{\rho}(x) + \rho'(x,t) \tag{2.6}$$

$$p = \overline{p}(x) + p'(x,t) \tag{2.7}$$

$$T = \overline{T}(x) + T'(x,t) \tag{2.8}$$

$$s = s'(x,t) \tag{2.9}$$

$\dot{m}$, the mass source term in equation (2.1), and $\dot{q}$, the heat source term, are considered to be small quantities.

Substituting equations (2.5) - (2.9) into equations (2.1) - (2.4) and neglecting products of the perturbation quantities yields the following zeroth and first order flow equations in the perturbation

quantities.

zeroth order:

continuity
$$\frac{1}{A}\frac{dA}{dx} + \frac{1}{\bar{\rho}}\frac{d\bar{\rho}}{dx} + \frac{1}{\bar{U}}\frac{d\bar{U}}{dx} = 0 \quad , \tag{2.10}$$

momentum
$$\bar{U}\frac{d\bar{U}}{dx} = -\frac{1}{\bar{\rho}}\frac{d\bar{p}}{dx} \quad . \tag{2.11}$$

Energy and the equation of state combine to give

$$\bar{p}\,\bar{\rho}^{-\gamma} = \text{const.} \tag{2.12}$$

first order:

continuity
$$\frac{\partial \rho'}{\partial t} + \bar{U}\frac{\partial \rho'}{\partial x} + u'\frac{d\bar{\rho}}{dx} + (\rho' U + u'\bar{\rho})\frac{1}{A}\frac{dA}{dx} + \rho'\frac{d\bar{U}}{dx} + \bar{\rho}\frac{\partial u'}{\partial x} = \dot{m} \, , \tag{2.13}$$

momentum
$$\frac{\partial u'}{\partial t} + u'\frac{d\bar{U}}{dx} + \bar{U}\frac{\partial u'}{\partial x} + \frac{\rho'}{\bar{\rho}}\bar{U}\frac{d\bar{U}}{dx} = -\frac{1}{\bar{\rho}}\frac{\partial p'}{\partial x} \, , \tag{2.14}$$

energy
$$\frac{\partial s'}{\partial t} + \bar{U}\frac{\partial s'}{\partial x} = \frac{\dot{q}}{\bar{T}} \quad , \tag{2.15}$$

state
$$\frac{p'}{\bar{p}} = \frac{\rho'}{\bar{\rho}} + \frac{T'}{\bar{T}} \quad . \tag{2.16}$$

The entropy perturbation s' can be expressed in terms of p' and ρ' as follows.

From the first law of thermodynamics,

$$Tds = dh - \frac{dp}{\rho} \quad . \tag{2.17}$$

For an ideal gas, the enthalpy can be expressed as a function of the temperature T,

$$dh = C_p dT.$$

Then, from (2.4) and (2.17),

$$ds = C_p\frac{dT}{T} - \frac{R dp}{p} \, . \tag{2.18}$$

Replacing the differentials by the perturbation quantities, one has

$$s' = C_p \frac{T'}{\overline{T}} - \frac{R\rho'}{\overline{p}} \quad . \tag{2.19}$$

Making use of (2.16) to eliminate the temperature term $T'/\overline{T}$ and using the ideal gas relations

$$C_p = C_v + R \ ,$$

$$\frac{C_p}{C_v} = \gamma$$

yields

$$\frac{s'}{C_v} = \frac{p'}{\overline{p}} - \gamma \frac{\rho'}{\overline{\rho}} \ . \tag{2.20}$$

2.2 Periodic Time Dependence

The time dependence of the perturbations can be described by a superposition of sinusoids. Since equations (2.13) - (2.15) are linear, it is only necessary to consider the behavior of one of these sinusoids and then derive a dispersion relation for an arbitrary frequency ω. This leads to the following representation for the perturbation quantities:

$$\begin{aligned}
u' &= \tilde{u}(x)\, e^{-i\omega t} \\
p' &= \tilde{p}(x)\, e^{-i\omega t} \\
\rho' &= \tilde{\rho}(x)\, e^{-i\omega t} \\
T' &= \tilde{T}(x)\, e^{-i\omega t} \\
s' &= \tilde{s}(x)\, e^{-i\omega t} \\
\dot{m} &= \tilde{m}(x)\, e^{-i\omega t} \\
\dot{q} &= \tilde{q}(x)\, e^{-i\omega t}
\end{aligned} \tag{2.21}$$

With the above time dependence, $\partial/\partial t \rightarrow -i\omega$ so that equations (2.13) to (2.15) become ordinary differential equations in x. The next step is non-dimensionalization of the flow equations, which will be explained below.

2.3 Non-Dimensionalization

The dimensionless form of the flow equations was made using the following dimensionless variables:

$$\bar{x} = x/x^* \qquad U = \bar{U}/a_* \qquad U' = dU/d\bar{x} \qquad M = \bar{U}/a$$

$$q = \tilde{q}/C_p\bar{T} \qquad \tilde{q} = \dot{q}x^*/a^* \qquad \Psi = q + \frac{\dot{m}x^*}{\bar{\rho}a^*} \tag{2.22}$$

$$\beta = \omega x^*/a_* \qquad Z_1 = \tilde{u}/\bar{U} \qquad Z_2 = \tilde{p}/\gamma\bar{p} \qquad Z_3 = \tilde{s}/C_p$$

First, the dimensionless form of the energy equation will be derived. Using the relations (2.21) and (2.22), the energy equation may be re-written to yield the following dimensionless ordinary differential equation:

$$\frac{dZ_3}{d\bar{x}} = \frac{i\beta Z_3}{U} + \frac{q}{U} . \tag{2.23}$$

Combining equations (2.10) and (2.13) and then dividing through by $\bar{\rho}$ yields:

$$\frac{1}{\bar{\rho}}\frac{\partial\rho'}{\partial t} + \bar{U}\left[\frac{1}{\bar{\rho}}\frac{\partial\rho'}{\partial x} - \rho'\frac{1}{\bar{\rho}^2}\frac{d\bar{\rho}}{dx}\right] + \left[\frac{\partial u'}{\partial x} - \frac{u'}{\bar{U}}\frac{d\bar{U}}{dx}\right] = \frac{\dot{m}}{\bar{\rho}} . \tag{2.24}$$

First and second terms in brackets are just

$$\bar{U}\frac{\partial}{\partial x}\left(\frac{\rho'}{\bar{\rho}}\right) \quad , \qquad\qquad \bar{U}\frac{\partial}{\partial x}\left(\frac{u'}{\bar{U}}\right) \quad ,$$

so (2.24) can be written:

$$\frac{\partial}{\partial t}\left(\frac{\rho'}{\bar{\rho}}\right) + \bar{U}\frac{\partial}{\partial x}\left(\frac{\rho'}{\bar{\rho}}\right) + \bar{U}\frac{\partial}{\partial x}\left(\frac{u'}{\bar{U}}\right) = \frac{\dot{m}}{\bar{\rho}} . \tag{2.25}$$

$\rho'/\bar{\rho}$ is eliminated from (2.25) in favor of p' and s' by using (2.20):

$$\frac{\partial}{\partial t}\left(\frac{p'}{\gamma\bar{p}} - \frac{s'}{C_p}\right) + \bar{U}\frac{\partial}{\partial x}\left(\frac{p'}{\gamma\bar{p}} - \frac{s'}{C_p}\right) + \bar{U}\frac{\partial}{\partial x}\left(\frac{u'}{\bar{U}}\right) = \frac{\dot{m}}{\bar{\rho}} \quad . \tag{2.26}$$

Using the relations (2.21) and (2.22), equation (2.26) is reduced to the following dimensionless form:

$$-i\beta(Z_2 - Z_3) + U\left(\frac{dZ_2}{d\bar{x}} - \frac{dZ_3}{d\bar{x}}\right) + U\frac{dZ_1}{dx} = \Psi - q \quad . \tag{2.27}$$

Equation (2.27) is the dimensionless continuity equation.

Lastly, the dimensionless form of the momentum equation will be derived. From equations (2.21),

$$\frac{\partial u'}{\partial t} = -i\omega u' .$$

Using this last relation in equation (2.13) in addition to (2.20) yields

$$-i\omega\frac{\tilde{u}}{\bar{U}} + \frac{\tilde{u}}{\bar{U}}\frac{d\bar{U}}{dx} + \frac{d}{dx}\bar{U}\left(\frac{\tilde{u}}{\bar{U}}\right) + \frac{d\bar{U}}{dx}\left(\frac{\tilde{p}}{\gamma\bar{p}} - \frac{\tilde{s}}{C_p}\right) = -\frac{1}{\rho\bar{U}}\frac{d\tilde{p}}{dx} \quad . \tag{2.28}$$

Now

$$\frac{d(\tilde{p}/\bar{p})}{dx} = \frac{1}{\bar{p}}\frac{d\tilde{p}}{dx} - \frac{\tilde{p}}{\bar{p}^2}\frac{d\bar{p}}{dx} \quad ,$$

and with equation (2.11), (2.28) is further modified to:

$$-i\omega\frac{\tilde{u}}{\bar{U}} + \frac{\tilde{u}}{\bar{U}}\frac{d\bar{U}}{dx} + \frac{d}{dx}\left(\bar{U}\frac{\tilde{u}}{\bar{U}}\right) + \frac{d\bar{U}}{dx}\left(\frac{\tilde{p}}{\gamma\bar{p}} - \frac{\tilde{s}}{C_p}\right) = \frac{-\gamma\bar{p}}{\rho\bar{U}}\frac{d(\tilde{p}/\gamma\bar{p})}{dx} + \gamma\left(\frac{\tilde{p}}{\gamma\bar{p}}\right)\frac{d\bar{U}}{dx} . \tag{2.29}$$

For an ideal gas, $\gamma\bar{p}/\bar{\rho} = a^2$, the speed of sound squared, so

$$\frac{\gamma\bar{p}}{\rho\bar{U}} = \frac{a^2}{\bar{U}} = \bar{U}\left(\frac{a^2}{\bar{U}^2}\right) = \frac{\bar{U}}{M^2} \ .$$

Therefore, using the relations in (2.22), (2.29) can be written as

$$-i\omega Z_1 + \frac{d\bar{U}}{dx}\left[2Z_1+Z_2(1-\gamma)-Z_3\right] + \bar{U}\,\frac{dZ_1}{dx} + \frac{\bar{U}}{M^2}\,\frac{dZ_2}{dx} = 0 \ . \qquad (2.30)$$

Multiplying this last equation by x^*/a^* gives the desired dimensionless form,

$$i\beta Z_1 + \frac{dU}{d\bar{x}}\left[2Z_1+Z_2(1-\gamma)Z_3\right] + U\,\frac{dZ_1}{d\bar{x}} + \frac{U}{M^2}\,\frac{dZ_2}{dx} = 0 \ . \qquad (2.31)$$

Combining equations (2.23) and (2.27) eliminates Z_3 between the two:

$$Z_2' = \frac{\Psi + i\beta Z_2}{U} - Z_1' \quad , \qquad (2.32)$$

where the $(\ )'$ denotes differentiation with respect to $\bar{x}$.

Combining equations (2.31) and (2.32) results in an equation for Z_1' in terms of Z_1, Z_2, and Z_3,

$$Z_1' = \frac{-i\beta(M^2Z_1-Z_2)+U'M^2\left[2Z_1-(\gamma-1)Z_2-Z_3\right]+\Psi}{U(1-M^2)} \ . \qquad (2.33)$$

Finally, combining equations (2.32) and (2.33) yields an equation for Z_2' in terms of Z_1, Z_2, and Z_3:

$$Z_2' = \frac{\Psi+i\beta Z_2}{U} + \frac{i\beta(M^2Z_1-Z_2)+U'M^2\left[Z_3+(\gamma-1)Z_2-2Z_1-\Psi\right]}{U(1-M^2)} \ . \qquad (2.34)$$

Equations (2.23), (2.33), and (2.34) form the set of three coupled first-order linear differential equations for Z_1, Z_2, and Z_3.

2.4 Method of Solution

For purposes of integrating (2.23), (2.33), and (2.34), a co-

ordinate system for $\bar{x}$ is chosen with the origin at the throat. As will be shown, this is convenient, since (2.33) and (2.34) have singularities at the throat making it necessary to start the integration of the equations there. Let $\bar{x}_1$ be the coordinate at the nozzle entrance ($\bar{x}_1 < 0$) and let $\bar{x}_2$ be the coordinate at the nozzle exit ($\bar{x}_2 > 0$).

At the throat there are no mass or heat sources ($\Psi \equiv 0$, $q \equiv 0$). Thus, in equation (2.33), if Z_1' is to be finite at $\bar{x} = 0$, and if the solution is to be physically meaningful there, we must have that

$$\bar{x} = 0 : \qquad -i\beta(Z_1 - Z_2) + U'[2Z_1 - (\gamma - 1)Z_2 - Z_3] = 0 \quad . \tag{2.35}$$

This condition also guarantees that Z_2' is finite at $\bar{x} = 0$, since

$$Z_2' = \frac{\Psi + i\beta Z_2}{U} - Z_1' \quad . \tag{2.32}$$

The solutions for Z_1 and Z_2 will now be analyzed in their particular and homogeneous parts. Let $Z_1^{(1)}$ and $Z_2^{(1)}$ denote the particular solutions of Z_1 and Z_2 . Equation (2.35) allows an infinite combination of values for $Z_1^{(1)}(0)$ and $Z_2^{(1)}(0)$; we take as values

$$\begin{aligned} Z_1^{(1)}(0) &= (U'Z_3(0))/(2U' - i\beta) \ , \\ Z_2^{(1)}(0) &= 0 \ . \end{aligned} \tag{2.36}$$

To start the integration process, $Z_1^{(1)}(0)$ must be known. This value is found from (2.33) using L'Hopitâl's rule.

The derivative of the denominator of the r.h.s. of (2.33) at $\bar{x} = 0$ is:

$$-(M^2)'U + U'(1 - M^2) = -M^2 U' \ , \tag{2.37}$$

and the derivative of the numerator is

$$-i\beta[M^{2'}Z_1^{(1)}+2Z_1^{(1)'}]+[M^{2'}U'+U'']\,[2Z_1^{(1)}-Z_3]+U'[2Z_1^{(1)'}+(\gamma-1)Z_1^{(1)'}-Z_3'].$$

(2.38)

Solving for $Z_1^{(1)'}$ yields the relation

$$Z_1^{(1)'}\left[1+\frac{U'(\gamma+1)-2i\beta}{M^{2'}U}\right] = \frac{-i\beta M^{2'}Z_1^{(1)}+(M^{2'}U'+U'')(2Z_1^{(1)}-Z_3)-Z_3'U'}{-M^{2'}U}\,.$$

(2.39)

$M^{2'}$ is evaluated from the one-dimensional isentropic flow relationships[25]:

$$M^2 = \frac{\bar{U}^2}{a^2} = \frac{\bar{U}^2}{a_*^2}\cdot\left(\frac{a_*^2}{a^2}\right) = U^2\left(\frac{a_*^2}{a^2}\right)$$

$$\frac{a_*^2}{a^2} = \frac{T_*}{T} = \frac{1+\frac{\gamma-1}{2}M^2}{1+\frac{\gamma-1}{2}M_*^2} = \frac{1+\frac{\gamma-1}{2}M^2}{\frac{\gamma+1}{2}}$$

so

$$\frac{M^2}{1+\frac{\gamma-1}{2}M^2} = \frac{2U^2}{\gamma+1}\,.$$

Differentiating this last expression and using the fact that M = 1 at the throat yields

$$M^{2'} = (\gamma+1)U'\,.$$

(2.39) can thus be written:

$$2Z_1'[U_*'(\gamma+1)-i\beta] = i\beta(\gamma+1)U_*'Z_1^{(1)}-[(\gamma+1)U_*'^2+U_*'']\,[2Z_1^{(1)}-Z_3]+Z_3'U'\,.$$

Let $A_1 = U_*'$, $A_2 = U'' + (\gamma+1)U_*'^2$. Then $Z_1^{(1)'}$ at $\underline{x} = 0$ can be written

$$Z_1^{(1)'} = \frac{1}{2}\,\frac{(i\beta(\gamma+1)A_1-2A_2)Z_1^{(1)}(0)+A_2Z_3(0)+A_1Z_3'(0)}{(\gamma+1)A_1-i\beta}\,, \qquad (2.40)$$

and from (2.32), $Z_2^{(1)'}$ at $\underline{x} = 0$ is given by

$$Z_2^{(1)'} = -Z_1^{(1)'}\,, \qquad (2.41)$$

since $U(0) = a_*/a_* = 1$, $Z_2^{(1)}(0) = 0$, and $\Psi = 0$.

Now consider the homogeneous equations. Let $Z_1^{(2)}$ and $Z_2^{(2)}$ be the homogeneous solutions which satisfy the differential equations:

$$Z_1^{(2)'} = \frac{\left\{-i\beta(M^2 Z_1^{(2)} - Z_2^{(2)}) + M^2 U'[2Z_1^{(2)} - (\gamma-1)Z_2^{(2)}\right\}}{(1-M^2)U} , \qquad (2.42)$$

$$Z_2^{(2)'} = -Z_1^{(2)'} + i\beta Z_2^{(2)}/U . \qquad (2.43)$$

For $Z_1^{(2)'}$ to be finite at the throat, require

$$\bar{x} = 0 : \qquad -i\beta(Z_1^{(2)} - Z_2^{(2)}) + U'[2Z_1^{(2)} - (\gamma-1)Z_2^{(2)}] = 0 . \qquad (2.44)$$

Since (2.44) allows an infinite combination $Z_1^{(2)}(0)$ and $Z_2^{(2)}(0)$, the following values are taken:

$$\begin{aligned} Z_1^{(2)}(0) &= \frac{(\gamma-1)U' - i\beta}{2U' - i\beta} , \\ Z_2^{(2)}(0) &= 1 . \end{aligned} \qquad (2.45)$$

The value of $Z_1^{(2)'}$ at $\bar{x} = 0$ must now also be found. The procedure is exactly similar to the calculation for $Z_1^{(1)'}$. The result is

$$Z_1^{(2)'}(0) = \frac{Z_1^{(2)}[i\beta(\gamma+1)A_1 - 2A_2] + \beta^2 + (\gamma-1)A_2 + i\beta(\gamma-1)A_1}{2[(\gamma+1)A_1 - i\beta]} \qquad (2.46)$$

where $A_1 = U_*'$,

$$A_2 = M^{2'} U_*' + U_*'' = (\gamma+1)U_*'^2 + U_*'' .$$

$Z_2^{(2)'}(0)$ is obtained from (2.43) and (2.46).

Having found the particular and homogeneous solutions, the complete solutions Z_1 and Z_2 are given by

$$Z_1 = Z_1^{(1)} + CZ_1^{(2)} \qquad (2.47)$$

$$Z_2 = Z_2^{(1)} + CZ_2^{(2)} \qquad (2.48)$$

where C is a constant of integration to be evaluated from the boundary conditions described below.

2.5 Boundary Conditions

For comparison of the theory with the experimental measurements, the following scheme was formulated.

Temperature and pressure measurements in the entrance section would be made for the steady and fluctuating components. From these measurements, spectral analysis would yield the values $\tilde{T}$, $\tilde{p}$ at the valve or heater driving frequency: then Z_2 and Z_3 follow from the formulas

$$Z_2 = \tilde{p}/\gamma\bar{p} \tag{2.49}$$

$$\tilde{s} = C_p \frac{\tilde{T}}{\bar{T}} - R\frac{\tilde{p}}{\bar{p}}$$

$$Z_3 = \frac{\tilde{s}}{C_p} = \frac{\tilde{T}}{\bar{T}} - \frac{\gamma-1}{\gamma}\frac{\tilde{p}}{\bar{p}} \tag{2.50}$$

The experimental value of Z_3 will be used to generate $Z_2^{(1)}(\bar{x})$, and then an experimental value of Z_2 measured at, say, $\bar{x}=\bar{x}_1$ can be used to evaluate C by:

$$C = \frac{Z_2(\bar{x}_1) - Z_2^{(1)}(\bar{x}_1)}{Z^{(2)}(\bar{x}_1)} \quad . \tag{2.51}$$

For most of the experimental data, the constant C was evaluated in terms of the "downstream running pressure wave" in the entrance section. A definition of this quantity as well as its special significance to the experiment will be given below.

Consider the flow in a one-dimensional nozzle with heat

sources upstream of the entrance. At any given instant of time, the pressure fluctuation at the nozzle entrance is the sum of (i) the pressure disturbances produced at the heat source, which propagate downstream at the sum of the speed of sound and the flow velocity; (ii) that portion of the pressure disturbance produced by the entropy (density) fluctuation passing through the nozzle, which is reflected upstream towards the nozzle entrance.

The first disturbance is intimately connected with one of the objectives of this thesis: to produce a pure temperature fluctuation in a flow (no associated pressure disturbances) and to demonstrate as theory predicts that this produces sound in a region of mean velocity gradient. In order to make this demonstration completely unambiguous, a device was constructed which produces entropy (temperature) fluctuations without the pressure disturbances associated with heating of the gas. The general scheme is to cancel the sound produced at the heater during formation of the entropy fluctuation. This cancellation process is more subtle than just reducing the magnitude of the pressure fluctuation at the heater to zero. At the heater, the pressure fluctuation is the sum of the pressure fluctuation due to periodic operation of the heater, the pressure fluctuation reflected back from the nozzle, and any pressure fluctuation originating from the flow region upstream of the heater. The quantity which must be cancelled is the total pressure disturbance which propagates downstream from the heater towards the nozzle. This disturbance will henceforth be called "the downstream running pressure wave."

The downstream running pressure wave is evaluated as follows. In the constant-area entrance section, the differential equation governing the pressure fluctuation p' is the familiar one-dimensional wave equation for a constant mean flow U . From reference 26, this equation is

$$\left[\frac{\partial}{\partial t} + U \frac{\partial}{\partial x} \right]^2 p' = a^2 \frac{\partial^2 p'}{\partial x^2} \quad . \tag{2.52}$$

The solution of this equation can be written

$$p' = p_+ e^{i\left[\frac{\omega x}{U+a} - \omega t \right]} + p_- e^{i\left[\frac{\omega x}{U-a} - \omega t \right]} \quad . \tag{2.53}$$

The first term on the right hand side of equation (2.53) represents a plane wave propagating in the flow direction with propagation speed U+a ; this is the downstream running wave. The second term on the right hand side represents a disturbance propagating upstream at U-a. This is the upstream running wave.

Recalling that $p' = \tilde{p} e^{-i\omega t}$, equation (2.53) can be simplified to

$$\tilde{p} = p_+ e^{ik_+ x} + p_- e^{ik_- x} \tag{2.54}$$

where k_+ and k_- are wave numbers given by

$$k_+ = \frac{\omega}{U+a} \quad , \qquad k_- = \frac{\omega}{U-a} \quad .$$

From the experimental data processing scheme, explained in Chapter 4, pressure fluctuation measurements will yield an amplitude and phase for $\tilde{p}$, i.e., $\tilde{p} = |\tilde{p}| e^{i\phi}$. Then from two such measurements in the entrance section, say, at x_a and x_b , p_+ and p_- are easily found by solving the equations

$$\tilde{p}(x_a) = p_+ e^{ik_+ x_a} + p_- e^{ik_- x_a} \quad ,$$
$$\tilde{p}(x_b) = p_+ e^{ik_+ x_b} + p_- e^{ik_- x_b} \quad . \tag{2.55}$$

Equations (2.55) are the basis for a cancellation process. Experiments for adjustment of a system to cancel out the heater pressure disturbance are as follows.

1. Set the system for assumed correct operation.
2. Run the experiment and measure the pressure fluctuation at two points in the entrance section.
3. Evaluate p_+ using equations (2.55).
4. If p_+ is too large, readjust the system and return to step 1.

It is desirable to also run experiments in which there is no or only partial cancellation of the downstream running pressure wave. The experimental data can then be used to verify that the theory predicts the correct interaction between the sound produced in the nozzle by the entropy fluctuations and a pure acoustic disturbance incident on the nozzle entrance, i.e., the downstream running pressure wave. For this situation, the constant of integration C in equation (2.48) is best evaluated in terms of p_+. This is done as follows. Once having evaluated p_+ and p_- from experimental measurements, one can write

$$Z_2(\bar{x}) = \frac{p_+}{\gamma \bar{p}} \exp\left[\frac{i\beta\bar{x}\sqrt{1+\frac{\gamma-1}{2}M^2}}{M+1\sqrt{\frac{\gamma+1}{2}}}\right] + \frac{p_-}{\gamma \bar{p}} \exp\left[\frac{i\beta\bar{x}\sqrt{1+\frac{\gamma-1}{2}M^2}}{M-1\sqrt{\frac{\gamma+1}{2}}}\right] \tag{2.56}$$

Using this form of $Z_2(\overline{x})$ in (2.51), C is readily evaluated in terms of p_+ and p_-, and thus the theoretical solution is fixed by use of the experimental values for the downstream running pressure wave.

This process will be described again in Chapter 6.

III. DESIGN OF THE EXPERIMENT

3.1 Objectives

Design and construction of the experimental apparatus was centered around the following pieces of equipment:

(a) an anechoic chamber to provide an essentially free space environment for external field sound measurements and to keep noise levels in the laboratory at a tolerable level;

(b) a blowdown wind tunnel which would provide a choked flow through a 1 in^2 throat at steady pressure and temperature for times up to 30 seconds;

(c) a heater which would produce an entropy wave of specified frequency and measurable amplitude;

(d) a pressure compensation system which would cancel the pressure fluctuations created at the heater and thus allow a pure entropy wave to propagate down the nozzle;

(e) instrumentation which would extract the low level signals produced by the entropy waves from a high background level of flow noise.

3.2 Anechoic Chamber

An anechoic chamber having a cubic working volume 10 feet on a side and a design cutoff frequency of 300 Hz was constructed for use in the experiment. The chamber was built for a small fraction of the cost of commercial models and met or exceeded the standards guaranteed by the commercial manufacturers. Details of construction and calibration are given in Appendix A, but a summary of the

performance is given here.

The quality of an anechoic chamber is given in terms of "deviation from the inverse distance law", which is defined as follows. If a point source of sound radiates in free space, the sound pressure level along a radial from the source varies inversely with distance. In an anechoic chamber which does not exactly simulate free space, the variation of sound pressure level produced by a point source at a fixed location in the chamber may not conform to the inverse distance law. The ratio between the sound level at a point in the chamber and the value it would have in free space expressed in units of decibels is the criterion for anechoic chamber performance. Commercial chambers specify a maximum deviation of ± 2 db for all frequencies above the cutoff frequency. Figures 3.1 to 3.7 show the performance of the chamber at frequencies of 200, 250, 300, 400, 1000, and 3000 Hz. The reference sound level is taken to be the level measured at a position one foot from the test speaker that is used to simulate the point source. Figures 3.1 and 3.2 show how sound pressure levels conform to the inverse distance law on a log-log plot, while figs. 3.3-3.7 show the actual deviation in decibels at various points in the chamber and at various frequencies. Note that close to the wedge tips or near the jet exhaust, deviations are the largest. However, at a foot away from the wedge tips deviations are far below the ±2 db deviation for frequencies greater than 300 Hz. Figure 3.2 displays the only sets of measurements taken in a vertical plane. The measurements show that the chamber walkway grating has no adverse effect on the performance of the chamber.

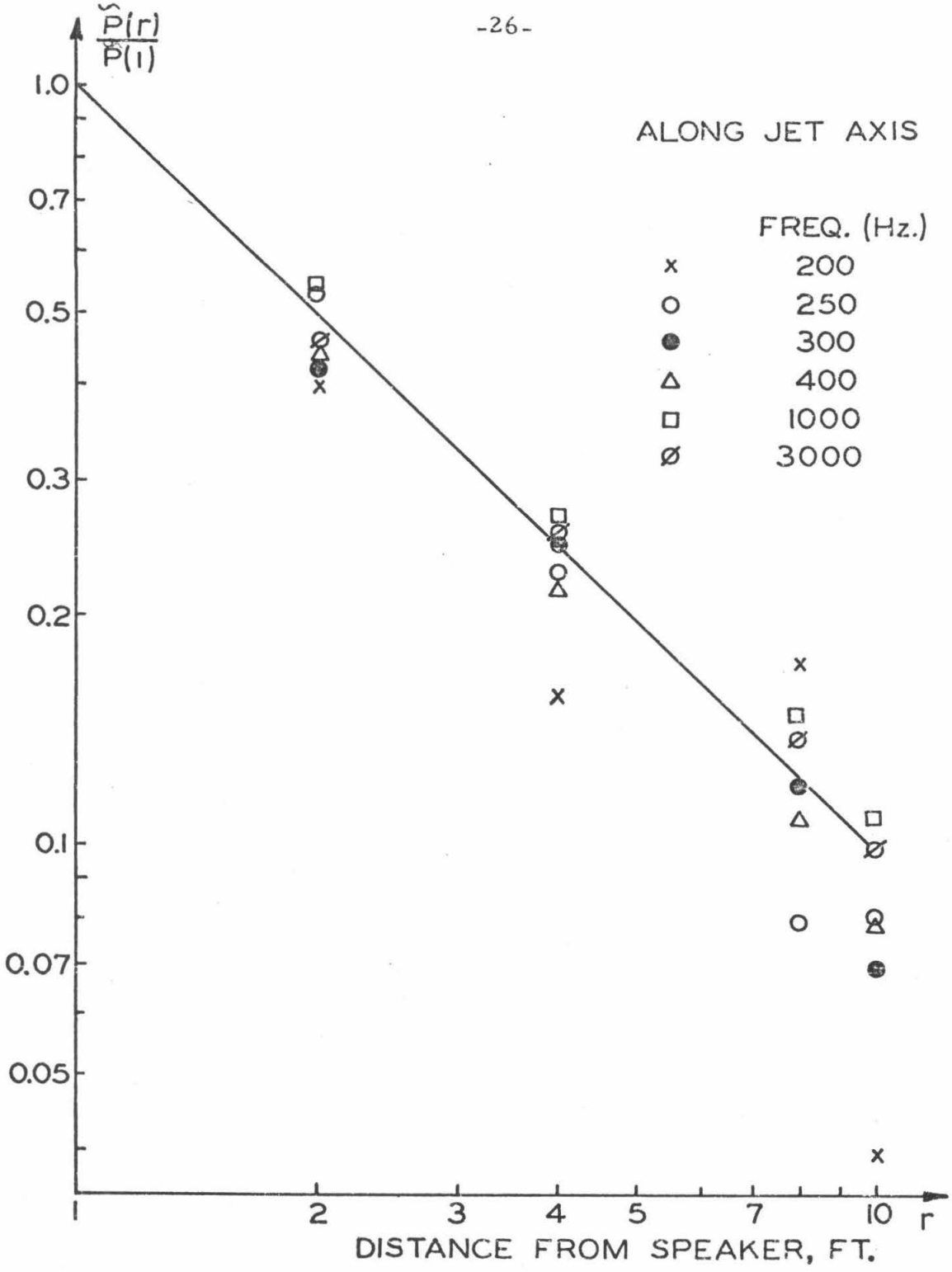

Fig. 3.1 Anechoic Chamber Performance Curve Along the Jet Axis.

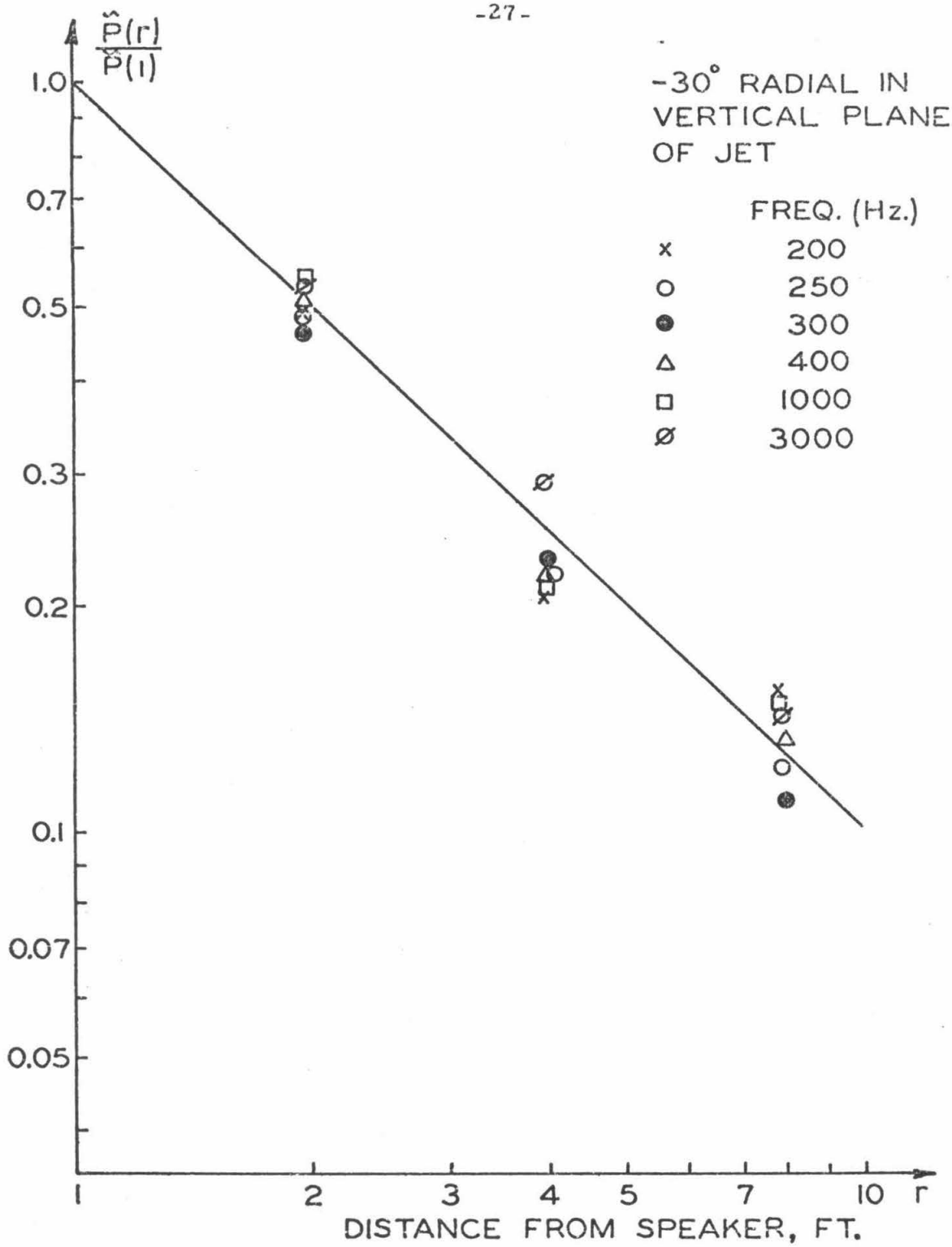

Fig. 3.2 Anechoic Chamber Performance Curve Along the -30°Radial in the Vertical Plane

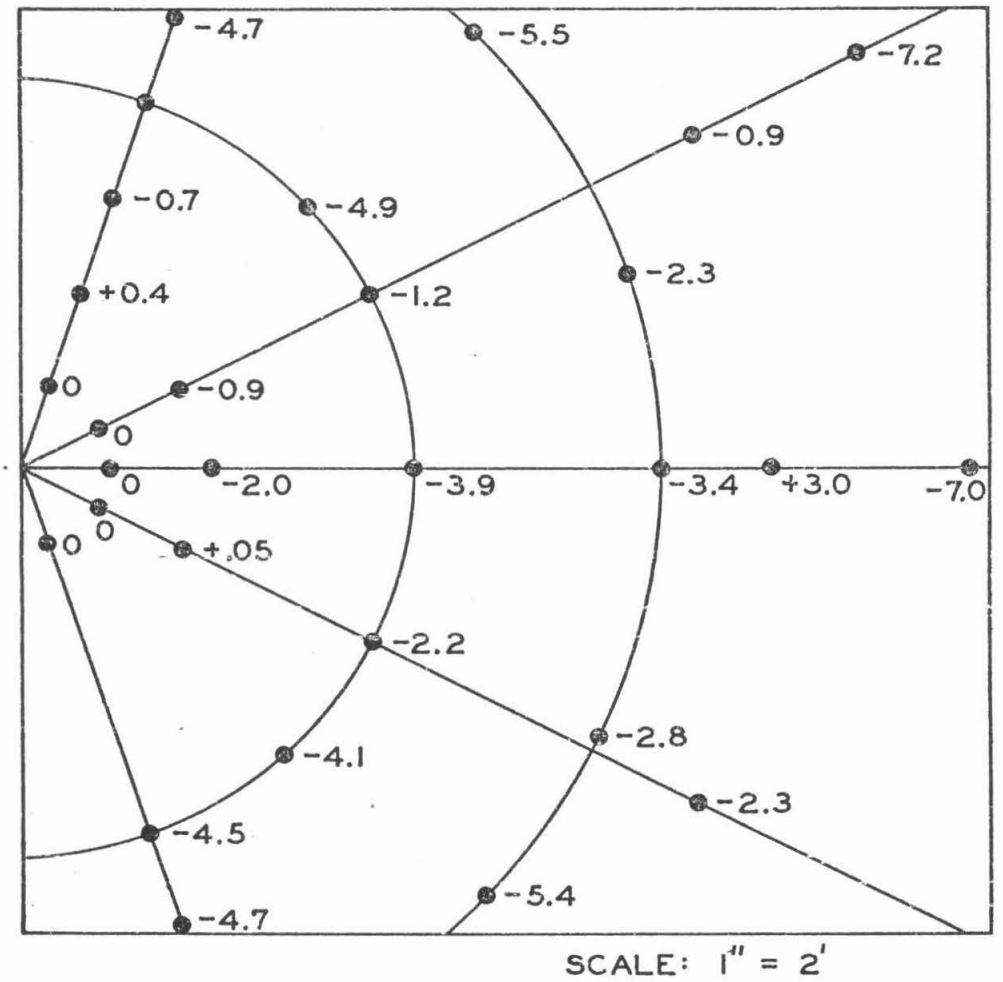

Fig. 3.3 Anechoic Chamber Performance Curve
Speaker Frequency 200 HZ
Horizontal Plane of Jet

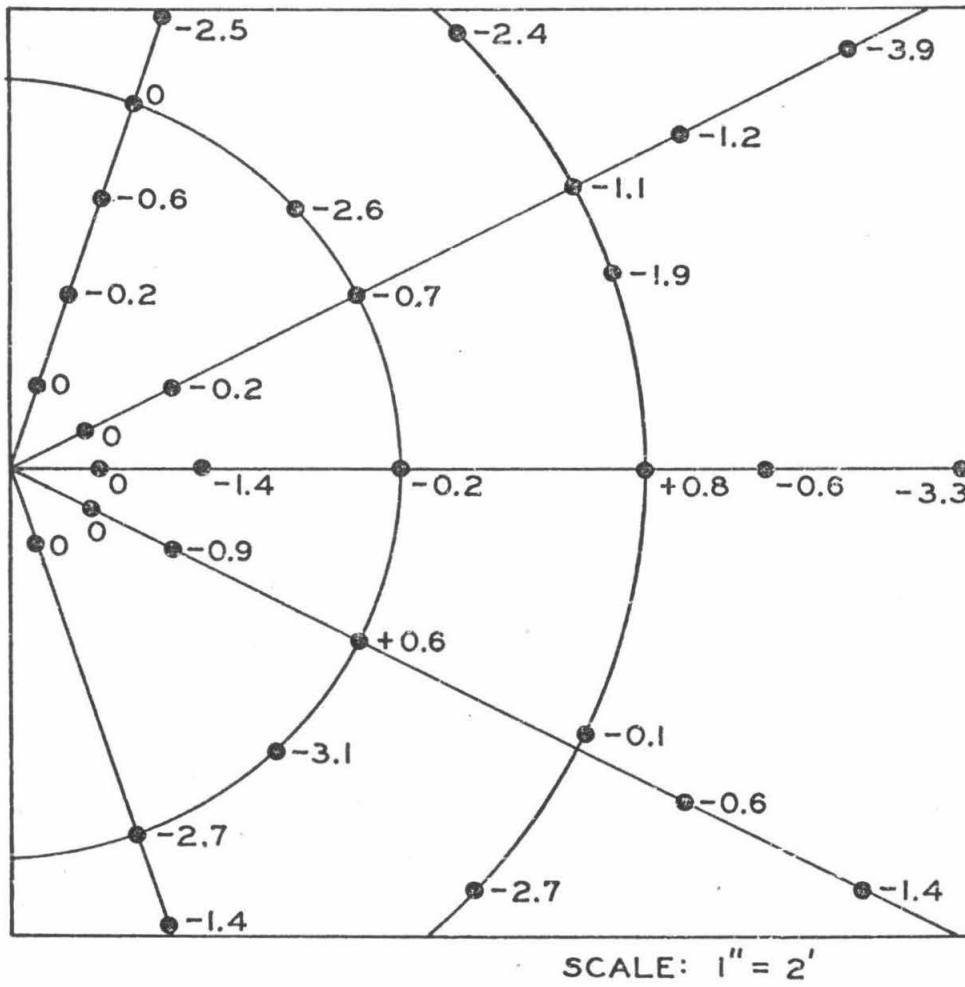

Fig. 3.4 Anechoic Chamber Performance Curve
Speaker Frequency 300 HZ
Horizontal Plane of Jet

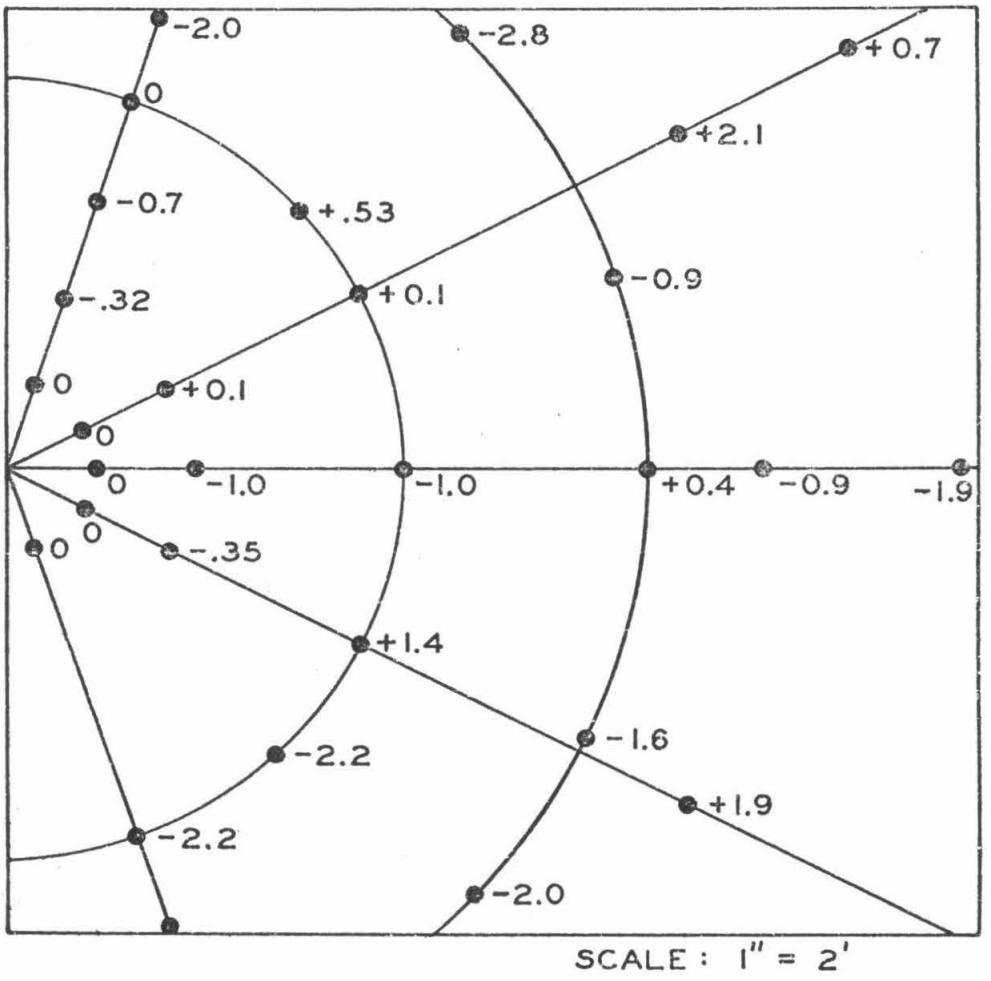

Fig. 3.5 Anechoic Chamber Performance Curve
Speaker Frequency 400 HZ
Horizontal Plane of Jet

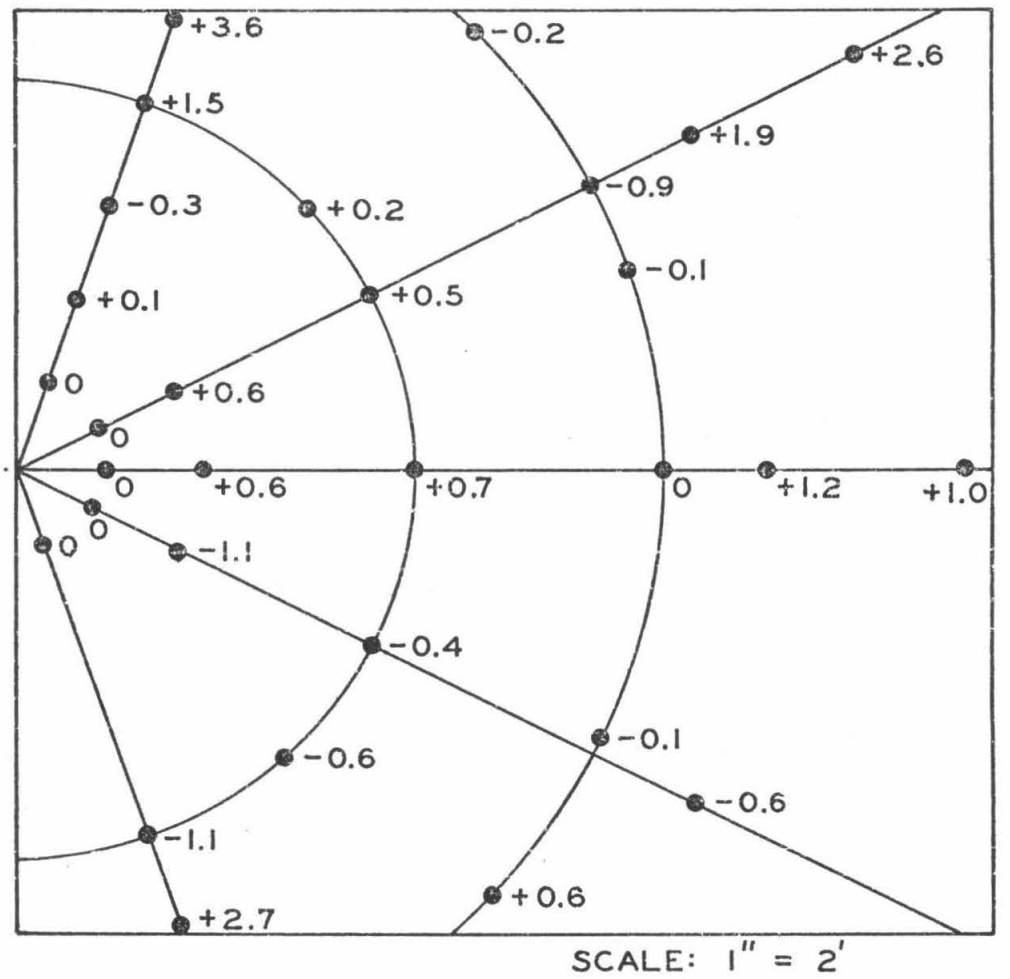

Fig. 3.6 Anechoic Chamber Performance Curve
Speaker Frequency 1000 HZ
Horizontal Plane of Jet

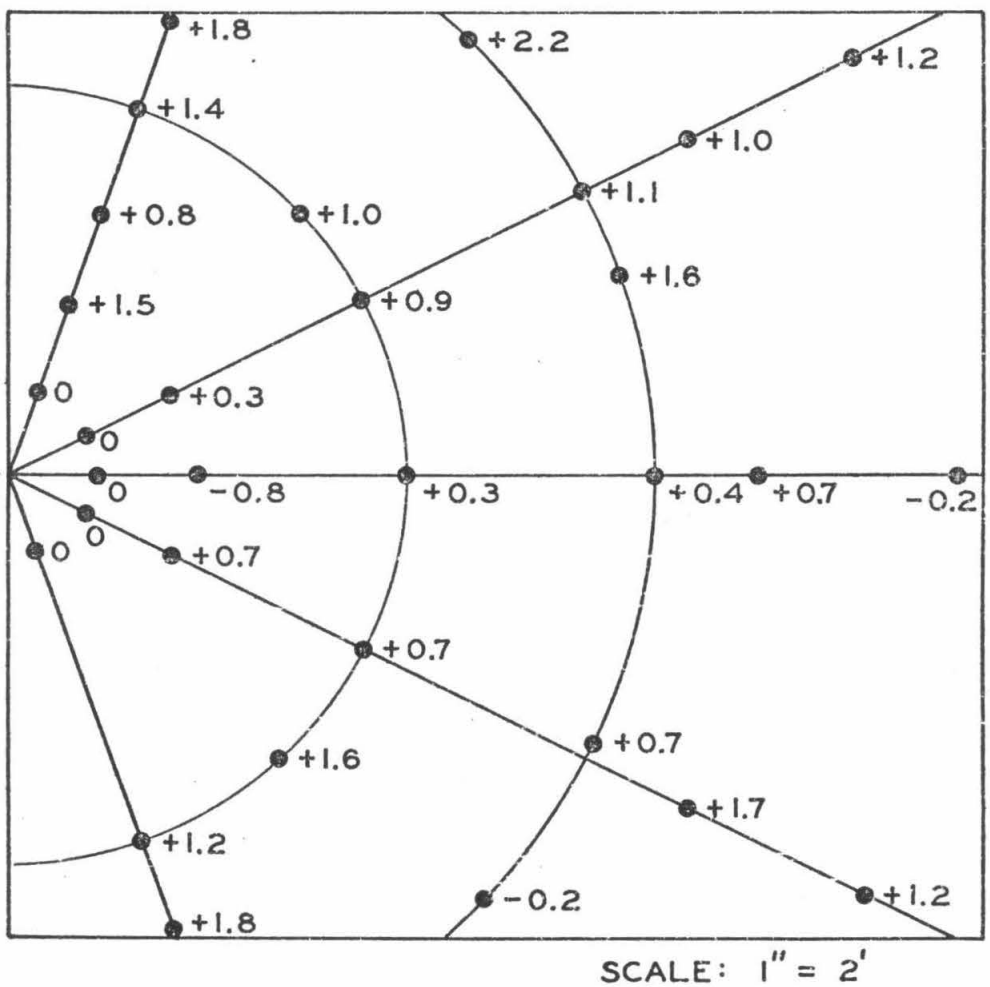

Fig. 3.7 Anechoic Chamber Performance Curve
Speaker Frequency 3000 HZ
Horizontal Plane of Jet

3.3 Blowdown Wind Tunnel System

3.3.1 Blowdown tunnel upstream equipment. A schematic of the blowdown tunnel complex is given in fig. 3.8. The tunnel uses as a working fluid standard purity gaseous nitrogen which is stored in 20 gas cylinders for a total of 6000 standard cubic feet. The gas is conveyed from the cylinders to the pressure regulators via a 50 ft length of $1\frac{1}{2}$" diameter extra-heavy walled steel pipe. A heavy steel gauge filter is placed just upstream of the regulators to prevent particulate matter from fouling the orifices of the regulators.

The regulators are chosen to provide the required tunnel pressure conditions down to a cylinder pressure of 600 psig. The function of the first regulator is to provide an essentially constant input pressure of 400 psig to the second regulator, which in turn controls the tunnel pressure. The regulators are dome type, and each is controlled by its own dome loader.

From the regulators, the nitrogen passes to an acoustically-treated, turbulence-reducing plenum chamber, a diagram of which is shown in fig. 3.9. The first part of the chamber consists of a 2 ft long 6-inch diameter steel tube holding a 2-inch diameter phenolic tube through which the gas flows to the turbulence reducing section. Surrounding this tube is packed $\frac{1}{2}$ lb/ft^3 fiberglas to eliminate sound wave reflections. Upon leaving the phenolic tube, the gas successively passes through a cone of perforated metal[33], a honeycomb of 0.1-inch diameter, 6-inch long plastic straws for flow straightening, and six successive screens of 44 mesh and .005-inch diameter wire. The blockage of the screens is less than 50 per cent, and therefore

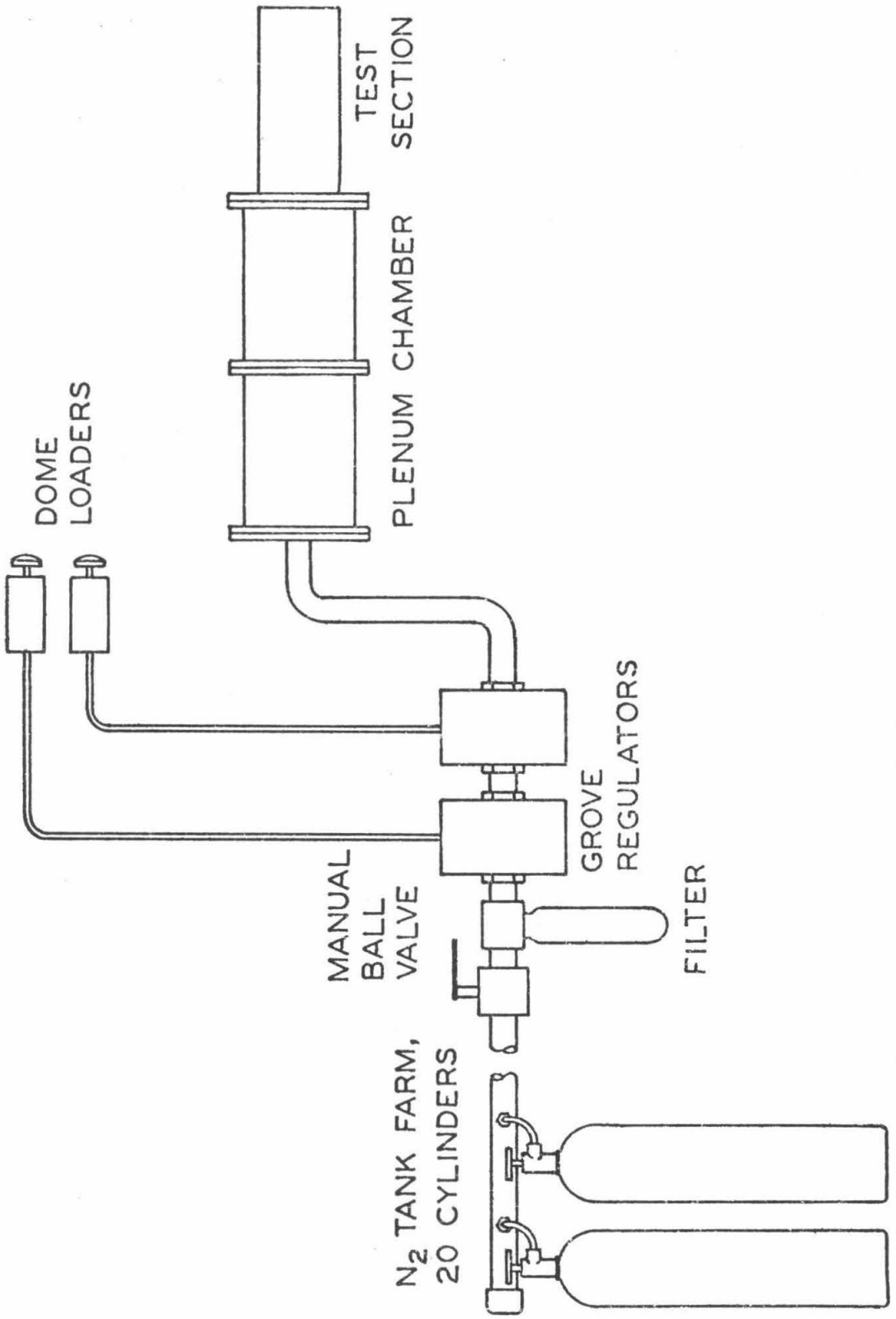

Fig. 3.8 Schematic of Blowdown Wind Tunnel System

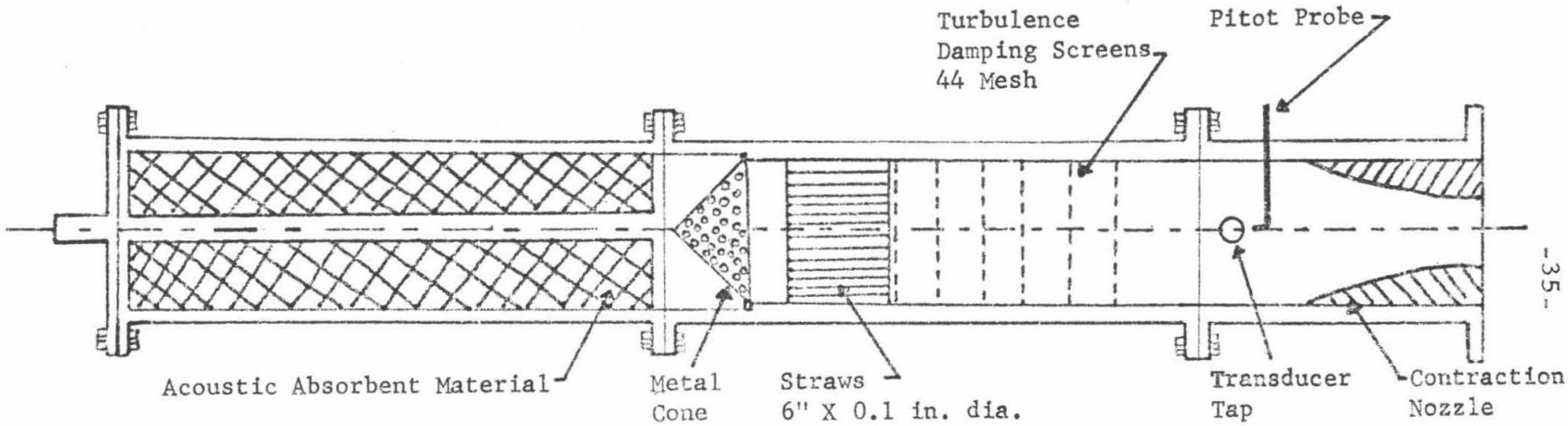

Fig. 3.9 Plenum Chamber Section of Blowdown Wind Tunnel

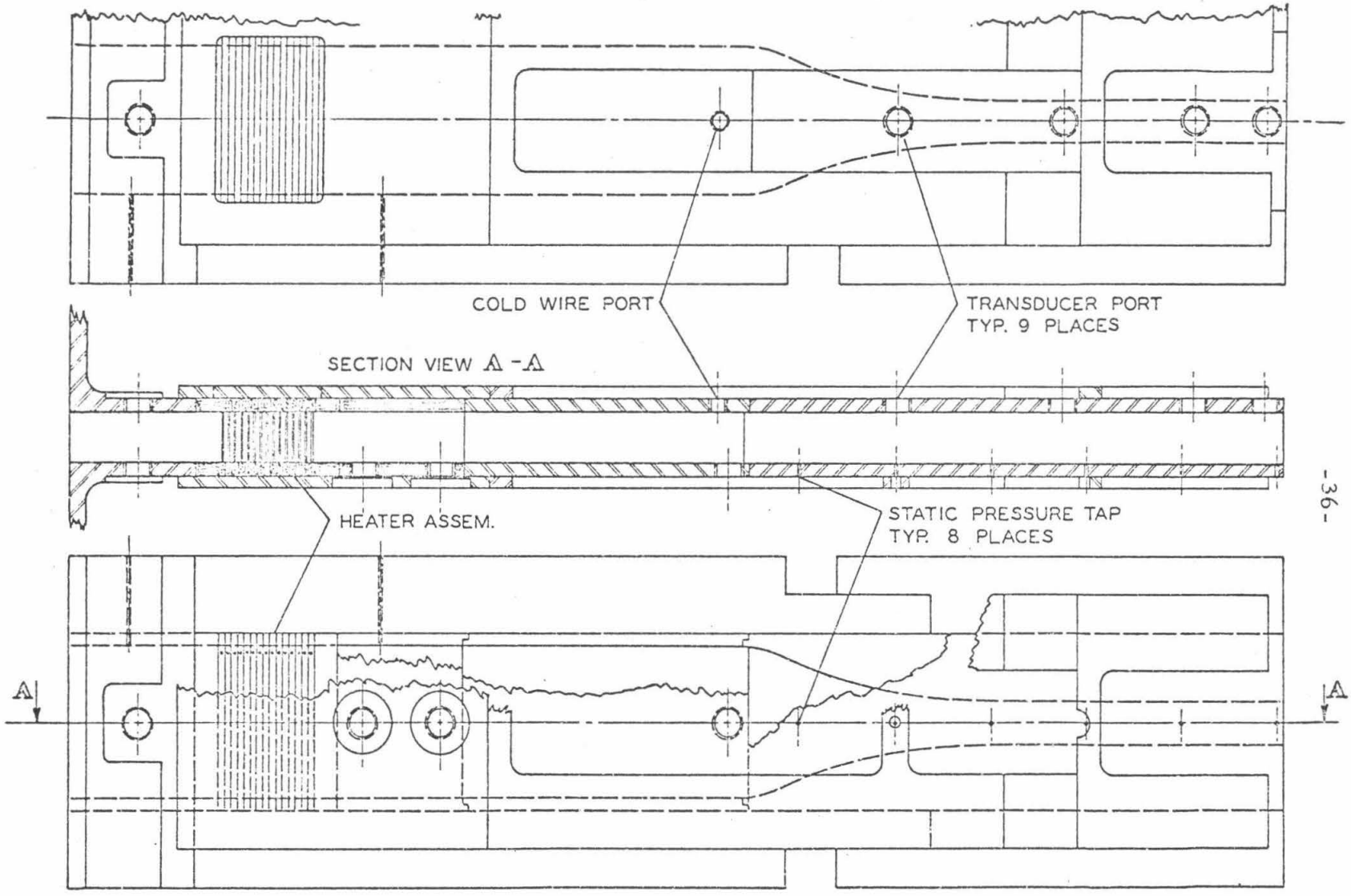

Fig. 3.10 Entrance Section and Nozzle

normal turbulence damping characteristics can be expected[34]. The last phase of the plenum chamber is a contraction nozzle to bring the flow to conform to the dimensions of the entrance section of the nozzle, a 1-inch by 3-inch rectangular cross section. The contraction nozzle has a cross section which changes gradually from a 6-inch diameter circle to a 1-inch by 3-inch rectangle at a point 9 inches downstream of the initial cross section. Immediately upstream of the nozzle is a tap for mounting a piezoelectric transducer to measure chamber noise levels and a mount for a pitot probe.

3.3.2 Entrance section. The test section of the blowdown tunnel consists of the entrance section and nozzle. The entrance section has three functions:

(a) to contain the thermal pulse heater (section 3.4) which produces the entropy wave;

(b) to support the rotary bleed valve system (section 3.5) which can produce either a pressure disturbance independently or in conjunction with the pulse heater to cancel pressure fluctuations caused by heater action in order to produce a pure entropy wave; and

(c) to contain mounts for all instrumentation necessary to determine entrance conditions for the nozzle.

A drawing of the test section of the blowdown tunnel is presented in fig. 3.10. All transducer taps shown will have positions specified with respect to the beginning of the nozzle (upstream negative, downstream positive).

The entrance section is 15 inches long, containing piezoelectric transducer ports at -14.5 in., -8.0 in., -6.5 in., and -0.5 in.;

static pressure taps at -12.75 in. and -7.5 in. for measuring the pressure drop across the heater; and a port for a cold-wire resistance thermometer probe at -0.9 in. The thermal pulse heater fits into the entrance section between positions -11 in. and -8.8 in. The right sideplate of the entrance section (looking downstream) contains the electrical connections for transferring current to the heater. The left sideplate of the entrance section is used for mounting the bleed valve system.

3.3.3 Supersonic nozzle. The nozzle is convergent-divergent with a 1 in^2 throat and a length of 11 inches. The width is 1 inch at all points along the nozzle. The design Mach number distribution locates the throat at 7.47 inches from the entrance.

The nozzle contour was specified to give a constant gradient Mach number distribution, except at the entrance where the condition of zero Mach number gradient was imposed. The entrance Mach number was chosen to be 0.2 and the exit Mach number 1.38. The Mach number distribution used to design the nozzle was thus

$$M(x) = .164 + .108x + .036\, e^{-3x} \qquad (3.1)$$

where x is in inches and measured from the nozzle entrance.

The nozzle contour was corrected for the presence of a boundary layer. Details of this analysis are presented in Appendix B, but a summary of the analysis and results is given here.

The boundary layer analysis is based on the assumption that each side of the nozzle contour is reduced in effective flow width by the boundary layer displacement thickness, $\delta^*(x)$. It is assumed that the boundary layers have identical shapes on the nozzle sidewall

and contours.

Let $h_o(x)$ be the uncorrected distance between opposite nozzle contours and $h_1(x)$ be the corrected distance, i.e., the distance that the contours must be separated so that the free stream flow area is the same as for an inviscid flow with a contour separation of $h_o(x)$. See Appendix B for $h_o(x)$ as a function of M. From the above requirements, it follows that $h_o(x)$, $h_1(x)$, and $\delta^*(x)$ satisfy the following equation:

$$[h_1(x)-2\delta^*(x)][1-2\delta^*(x)] = h_o(x)\cdot 1 \tag{3.2}$$

where the 1 indicates the 1-inch width of the nozzle.

$$h_1(x) = \frac{h_o(x) + 2\delta^*(x)}{[1-2\delta^*(x)]} + O(\delta^{*2}) \tag{3.3}$$

$\delta^*(x)$ was computed for the free stream flow given by equation (3.1) using the Karman-Polhausen integral method[35]. The boundary layer was taken to be a logarithmic velocity profile with corrections for a negative pressure gradient in the mean flow. The solution for δ^* first involved solving the following first-order differential equation for θ, the boundary layer momentum thickness:

$$\frac{d\theta}{dx} = -\left[3.147 - \frac{0.2M^2}{1+.2M^2}\right]\frac{1}{M}\frac{dM}{dx}\theta + \frac{.000443(1+.2M^2)^{.604}\,\theta^{-.268}}{(1+.144M^2)^{.799}\,M^{.268}}. \tag{3.4}$$

Equation (3.4) is derived in detail in Appendix B. The first term on the right hand side of equation (3.4) contains terms derived from the logarithmic velocity profile. The second term is a special form of the Ludweig-Tillman skin friction coefficient[36] for compressible

flows. In Appendix B, an expression for the compressible shape factor $H = \delta^*/\theta$ is derived,

$$H = 1.147(1+.2M^2)+.2M^2 \quad . \tag{3.5}$$

Thus, having found $\theta(x)$ by integration of (3.4), $\delta^*(x)$ is given by $H(x)\theta(x)$.

The problem in integrating equation (3.4) lies in the choice of a suitable initial value of θ. In the entrance section of the wind tunnel, the pulse heater creates a complex wake formation, so at best only an estimate of θ can be made. A value of .02 inches was assumed. Equation (3.4) was integrated using a fourth order Runge-Kutta method with a 0.1 in. step. The result is shown in fig. 3.11. One fact is immediately evident from the curves. For small Mach numbers, the negative pressure gradient which tends to decrease θ and δ^* dominates any increase in θ and δ^* by the viscous stresses represented by the second term on the right hand side of equation (3.4).

The values of $\delta^*(x)$ computed by equations (3.4) and (3.5) were applied to equation (3.3). The nozzle was machined to the contour $h_1(x)$.

The performance of the nozzle was measured by making a pitot-static measurement in the entrance section to determine entrance Mach number, and then static pressure measurements at x = 0 in., 1 in., 3 in., 5 in., 7 in., 9 in., and 11 in., along with a pressure difference measurement between pitot tubes in the entrance section and at x = 10 in. to get the Mach number distribution along the nozzle.

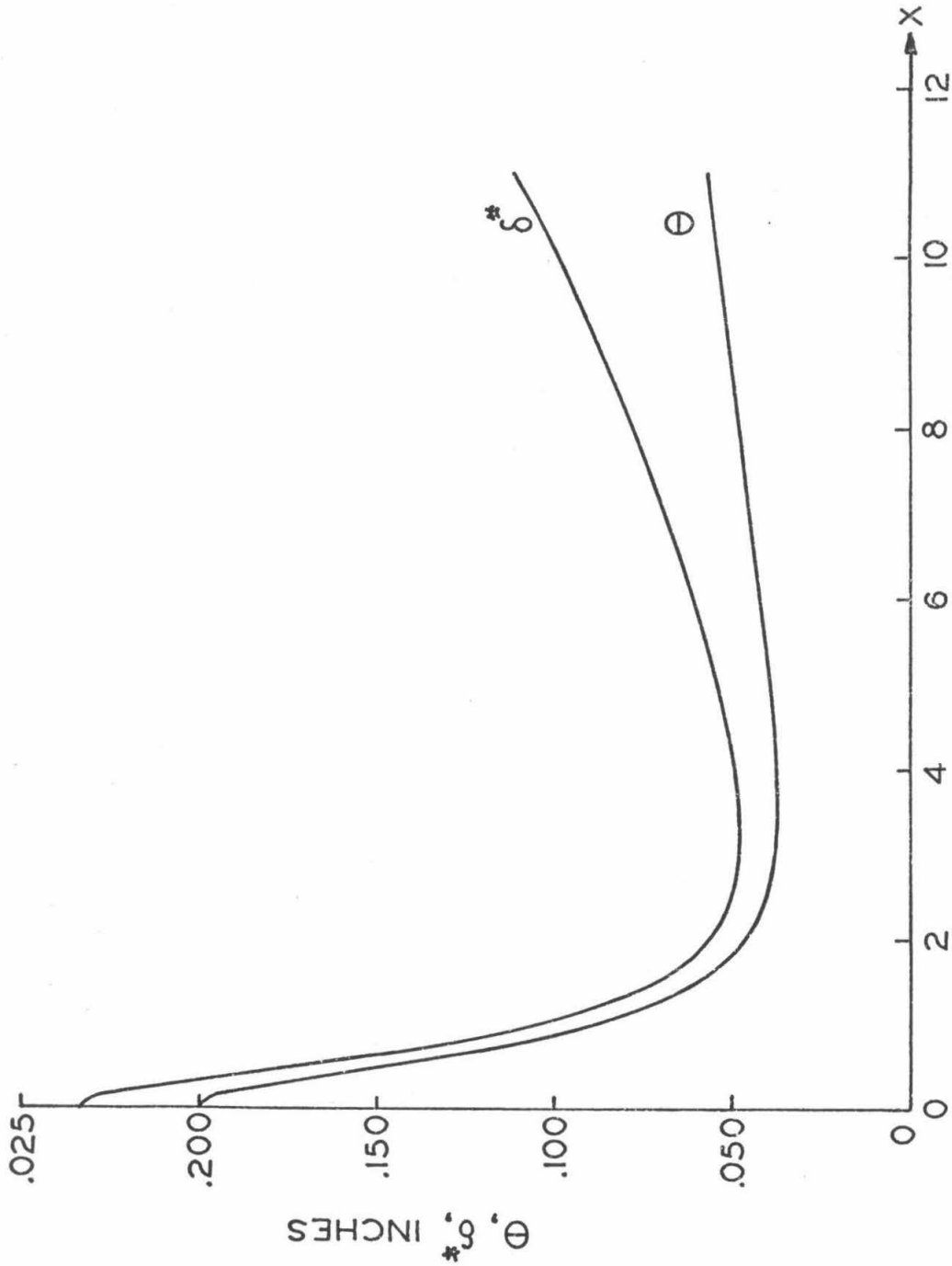

Fig. 3.11 Nozzle Boundary Layer Momentum and Displacement Thicknesses

From the pitot and static measurements in the entrance section, the Mach number was calculated from the relation

$$\frac{p}{p_t} = \left(1 + \frac{\gamma - 1}{2} M^2\right)^{-\gamma/\gamma - 1} \tag{3.6}$$

where $\gamma = 1.4$.

From the pitot measurement in the entrance section and the pressures at x = 1 in., 3 in., 5 in., 7 in., 9 in., and 11 in., six values of Mach number along the nozzle were computed using equation (3.6). The results are shown in fig. 3.12.

The third measurement was based on the fact that the loss in stagnation pressure across a normal shock is a function of the Mach number. One pitot tube was placed in the entrance section, and one at x = 10 in. The stagnation pressure at the upstream pitot tube was measured along with the pressure difference between the two pitot tubes. Using the ratio between the downstream and upstream stagnation pressures as data, the normal shock relations gave the Mach number at x = 10 in. The result is shown as a triangular point on fig. 3.12. Note that it is entirely consistent with the other data points.

It is interesting to consider the value of the boundary layer corrections to the nozzle contour. From fig. 3.11 one sees that at the throat (7.47 in.) the displacement thickness is .008 in. If there were no boundary layer correction to the contour, the free stream throat area would be .97 $in.^2$ instead of 1.00 $in.^2$. At the nozzle exit, the displacement thickness is .011 in. For no boundary layer correction, the free stream exit area would be 1.06 $in.^2$ instead of

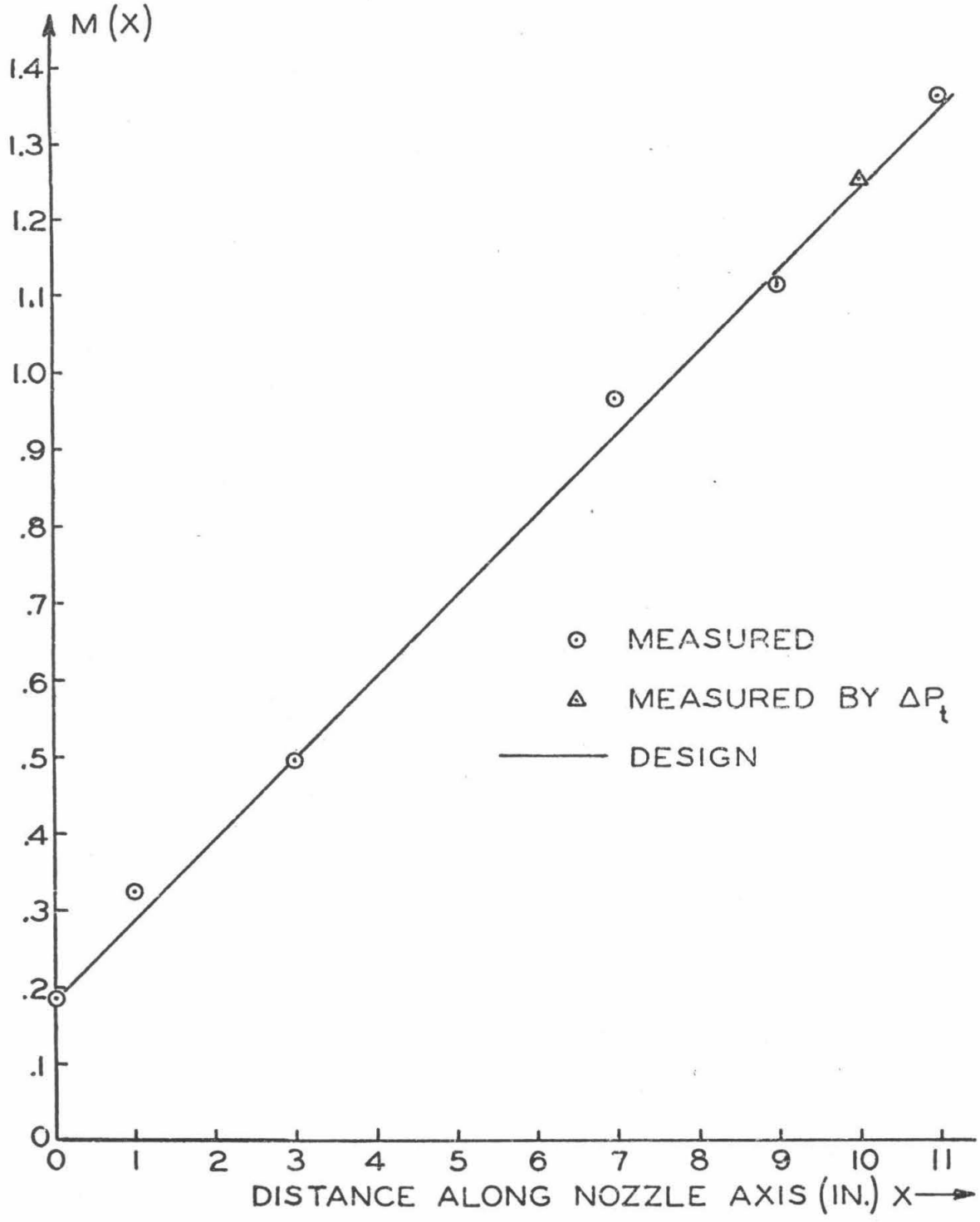

Fig. 3.12 Supersonic Nozzle Performance

1.10 $in.^2$. In both cases the exit area/throat area ratios are almost the same (1.093 and 1.10).

3.4 Thermal Pulse Heater

3.4.1 The alternatives. The most critical point in the evolution of the experiment was the development of a device which would produce temperature fluctuations in the gas flow at a specified frequency and a detectable amplitude. This device also had to meet the requirement that it would not produce noise or auxiliary signals that would interfere with the correct operation of the instrumentation. Also, it must not be excessively costly or hazardous, and should be such that it could be coupled with a gas bleed or expansion device that would cancel the pressure caused by the heating action, thus resulting in the production of a pure entropy wave.

The following schemes were considered: (i) spark gap heater, (ii) resistance wire heater, (iii) chemical heater, (iv) laser device. Scheme (iv) was completely out of the question since the laser output needed would be of the order of a megawatt because of poor energy transfer characteristics from the laser light to the gas. Moreover, the laser would be prohibitively costly.

Scheme (iii) was unfeasible because a controlled high-frequency combustion process was judged to be unattainable. Scheme (i) had two drawbacks, the first being that it would require a huge bank of high-voltage capacitors (making it economically unfeasible); the second and prime prohibitive factor, however, would be that the electrical noise and gas ionization produced would most probably

nullify proper operation of instrumentation such as hot wire anemometers, cold wire resistance thermometers, and piezoelectric transducers.

The electrical resistance heater appeared to be the most promising alternative, and it was selected for development. It would not be prohibitively costly to build, it would not produce electrical noise that would saturate electronic instrumentation, nor would it need hazardous power sources such as kilovolt power supplies. However, the one drawback of the resistance heater is its gross inefficiency,which will be explained below.

3.4.2 Heater design and performance. The heater was modelled by an array of current-carrying wires immersed in a gas flow. To produce a temperature fluctuation in the wires, a periodic rectangular voltage waveform was impressed upon the wires. A rectangular voltage waveform was selected because of the relatively simple design required for the high power pulse generator needed to produce this voltage.

The differential equation governing the wire temperature is:

$$C_w \frac{dT_w}{dt} = I^2(t)R_l - h_c A_l (T_w - T_\infty) \qquad (3.7)$$

where T_w = wire temperature

T_∞ = gas free stream temperature

$I(t)$ = wire current

R_l = wire resistance

A_l = wire surface area

C_w = heat capacity of wire

h_c = heat transfer coefficient of wire, evaluated at mean film temperature

This equation is considered in detail in Appendix C and is solved for the case of a rectangular power wave of period T_o and duty cycle $\alpha_1 T_o$. It is then found that the maximum wire temperature fluctuation for a given power input occurs for $\alpha_1 = \frac{1}{2}$. Then an array of parallel wires is considered with total heat transfer area A_T in a gas mass flow of $\dot{m}_o$. The end result of the calculation is that the ratio of the temperature fluctuation in the gas, $\tilde{T}_g$, and the average wire temperature rise, $\overline{T}_w - T_\infty$, is given as a function of the square wave period, T_o:

$$\frac{\tilde{T}}{\overline{T}_w - T_\infty} = \frac{2}{\beta_1}\left\{\frac{1 + e^{a_H} - 2e^{a_H/2}}{e^{a_H} - 1}\right\} \tag{3.8}$$

where

$$\beta_1 = \frac{\dot{m}_o c_p}{h_c A_T}$$

c_p = specific heat at constant pressure

$$a_H = \frac{T_o}{C_w / h_c A_1}$$

To illustrate the behavior of equation (3.8), numerical values for the actual heater in the experiment will be used. The heater design is a compromise between size, electrical power requirements, and durability.

A diagram showing the construction of the thermal pulse heater is given in fig. 3.13. The heater consists of 15 banks of 25 parallel strands of .004-inch diameter 80-20 nichrome wire. The strands

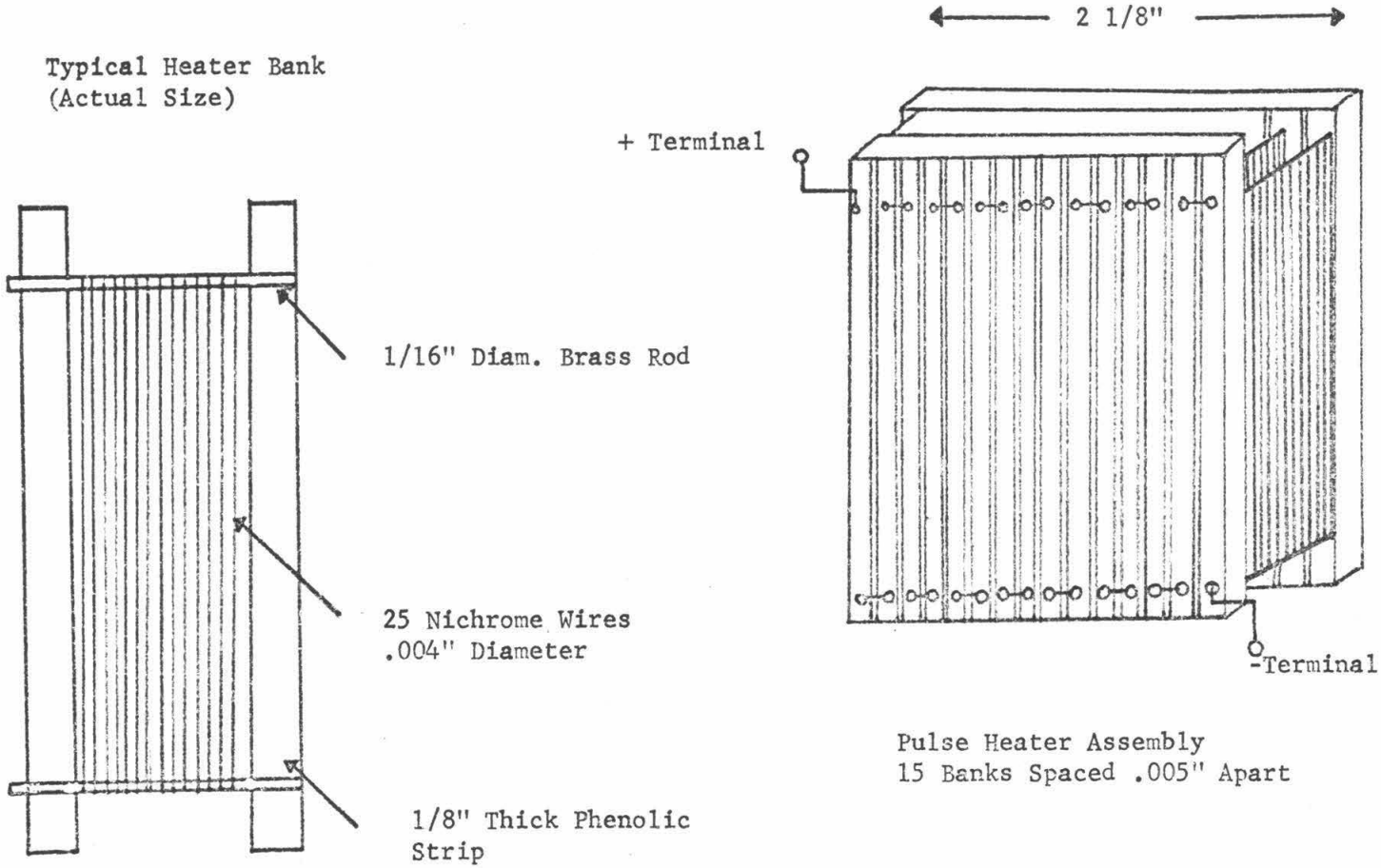

Fig. 3.13 Thermal Pulse Heater Construction

are soldered at each end to a 1/16-inch diameter brass rod. The rods are spaced 2 3/4 inches apart and mounted on 1/8-inch thick phenolic strips. The strips are spaced .005 in. apart using brass shim spacers. The small gaps formed by the shims are used for the bleed compensation system, to be described later. The banks are connected electrically in series.

Numerical values for use in equation (3.8) are based on .004 in. wire diameter, 2.75 in. wire length, a gas flow of 1.04 lbm/sec at M = 0.2 with flow properties evaluated at 64°F and 3 atm pressure. Two iterations were made to determine mean film temperature and wire temperature. The results of the calculations are shown in figs. 3.14, 3.15, and 3.16.

Figure 3.14 shows $(\overline{T}_w - T_\infty)/\widetilde{T}_g$ as a function of square wave frequency. This graph immediately reveals the gross inefficiency of the heater: for frequencies at and above 400 Hz, the wire temperature must be hundreds of degrees centigrade just to produce a 1°C temperature fluctuation in the gas. Figure 3.15 presents this concept in a more quantitative display. Note that as a gas temperature fluctuation of 5°C is required, the nichrome is pushed towards its melting temperature. Another point to be considered is the electrical power requirement. The combined wire resistance of the heater is 5 ohms. If V is the square wave voltage, the average wire temperature $\overline{T}_w$ is related to V by:

$$hA(\overline{T}_w - T_\infty) = \frac{V^2}{2R} \quad . \tag{3.9}$$

A plot of this relationship for the heater designed for the experiment is given in fig. 3.16. Note that 275 volts produces a $\overline{T}_w$ of 280°F.

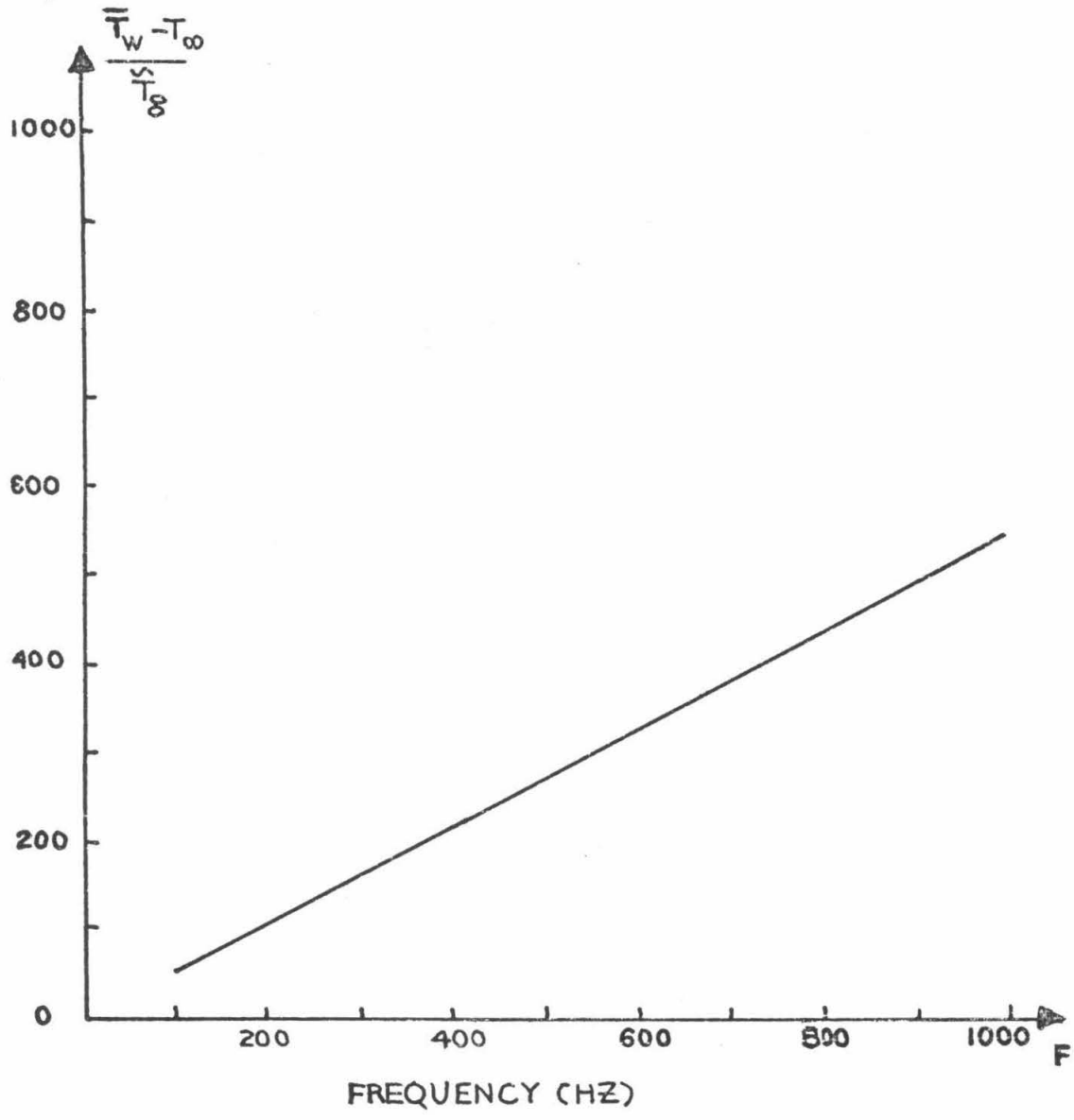

Fig. 3.14 Wire Heater Temperature-Frequency Response Function

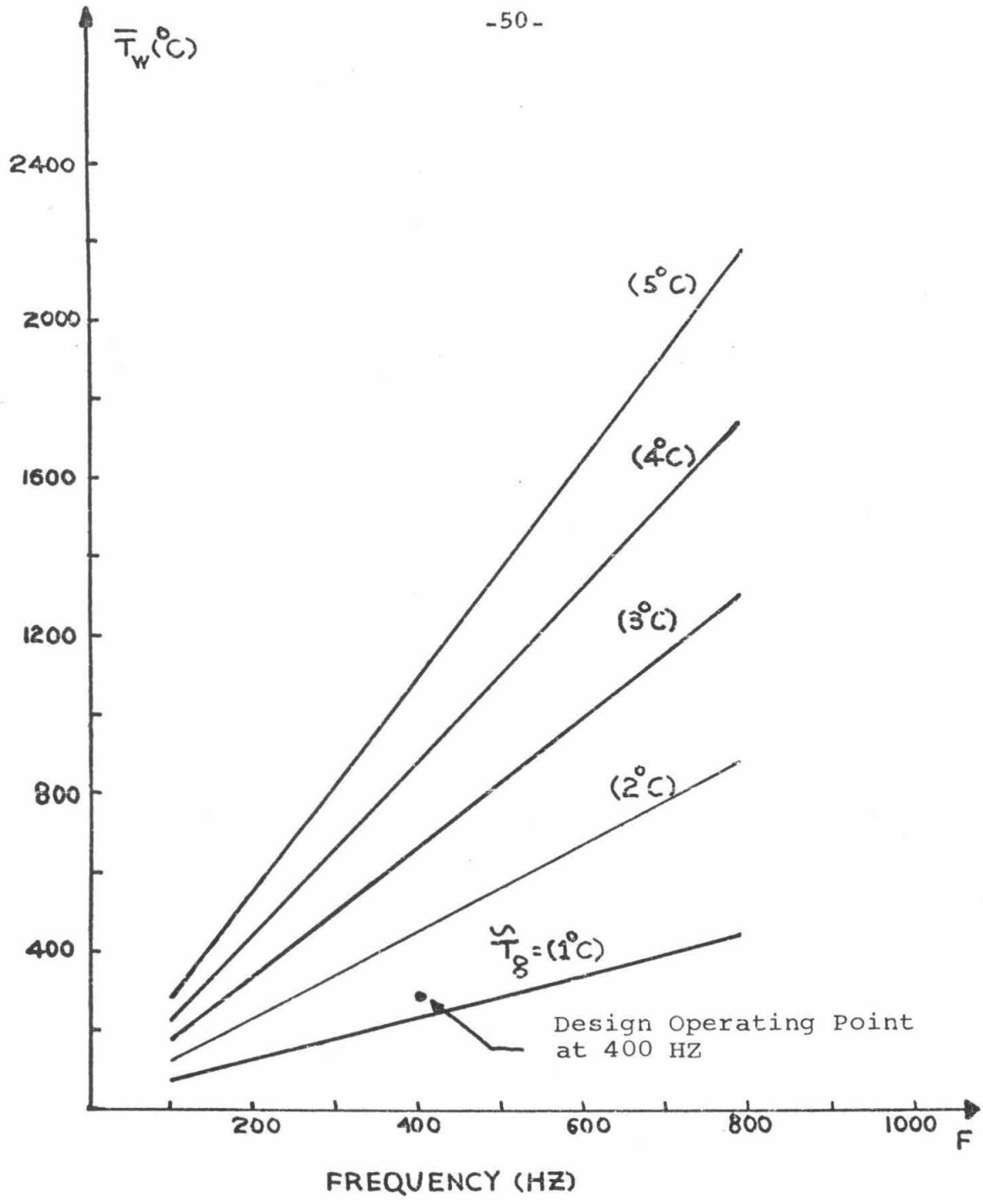

Fig. 3.15 Heater Wire Average Temperatures Required to Produce Gas Temperature Fluctuations of Various Amplitudes and Frequencies

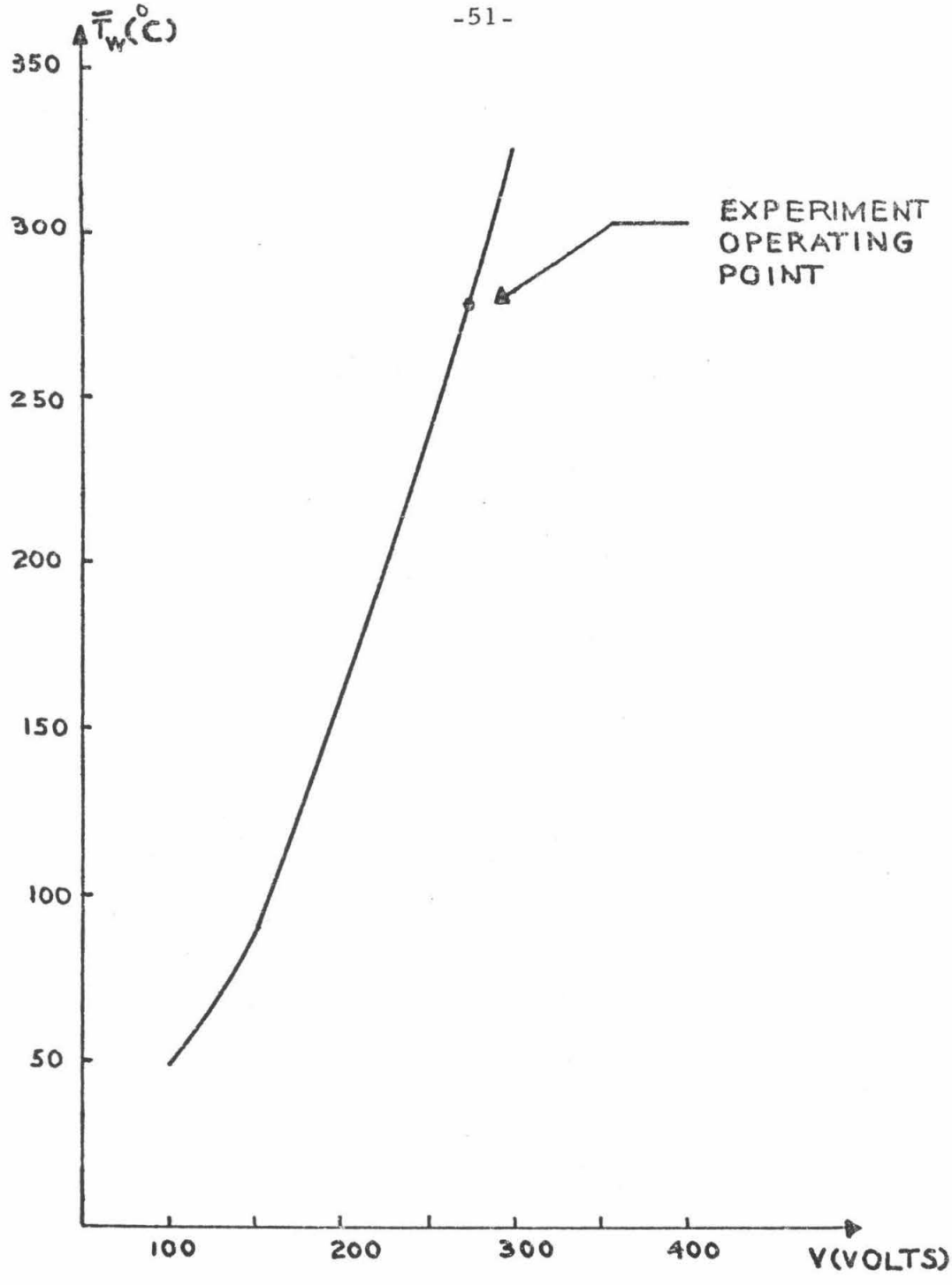

Fig. 3.16 Average Heater Wire Temperature as a Function of Applied Voltage

At 400 Hz, fig. 3.8 indicates that a gas temperature fluctuation of only a little more than a degree centigrade is attainable at this value of applied heater voltage. Therefore, for a $1^{\circ}C$ gas temperature fluctuation, one is confronted with the design of a pulse generator capable of switching 60 amperes at 300 volts! This is further discussed in Section 3.7, Electrical and Electronic Equipment.

One other point in the performance of the heater must be considered: the fact that it is of finite length, and therefore the temperature waveform imparted to the gas is reduced because of a smearing effect. The effect of this "smearing" on the fluctuation amplitude is considered in detail in Appendix B. The result is that the amplitude is reduced by the factor

$$\left(1 - \frac{\Delta t_H}{2T}\right), \tag{3.10}$$

where Δt_H is the travel time of the gas through the heater, and T is the square wave period.

$$\Delta t_H = \frac{L}{U} = \frac{\text{heater length}}{\text{gas velocity}}$$

For a voltage frequency of 400 Hz, L = 2 inches and U = 200 ft/sec.

$$1 - \frac{\Delta t_H}{2T} = .83$$

so at 400 Hz, a 300-volt, 60-ampere square wave produces at best a $.9^{\circ}C$ gas temperature fluctuation. This is still a high estimate since the effect of wakes behind the wires and conduction effects from the wires to supports have not been taken into account.

3.5 Bleed Valve System

3.5.1 Functions. The bleed valve system has two functions: (i) to produce pressure fluctuations at various frequencies in the entrance section for studies of the propagation of pure pressure disturbances in the nozzle; (ii) to cancel out the pressure disturbance produced by the heater so a pure entropy or heat wave will be produced.

3.5.2 Construction and operation. A diagram of the bleed valve is presented in fig. 3.17. The working part of the valve is a 0.5-in. diameter ground steel shaft which is rotated at angular speeds up to 250 Hz by a precision hysteresis synchronous motor. Shaft support during operation is provided by two air bearings. As shown in fig. 3.17, gas is bled from the entrance section through slits in the pulse heater frame, then through the hole in the shaft, and then to the atmosphere through an orifice plate which controls the rate of bleed.

A second hole is drilled in the shaft at ninety degrees to the large hole. This hole passes light from a source to a phototransistor detector circuit twice per shaft revolution. The output from the phototransistor is fed through a delay circuit, and after some signal conditioning is used to fire the pulse heater. Thus, the pulse heater can be fired at any position of the valve shaft. This is the principle of the compensation system: by adjusting the amplitude and phase of the bleed flow relative to the time of heater firing, the pressure fluctuation due to heater action can be cancelled. The phototransistor circuit also serves as the basic element of the "signal averaging process." This will be described in detail in the next chapter.

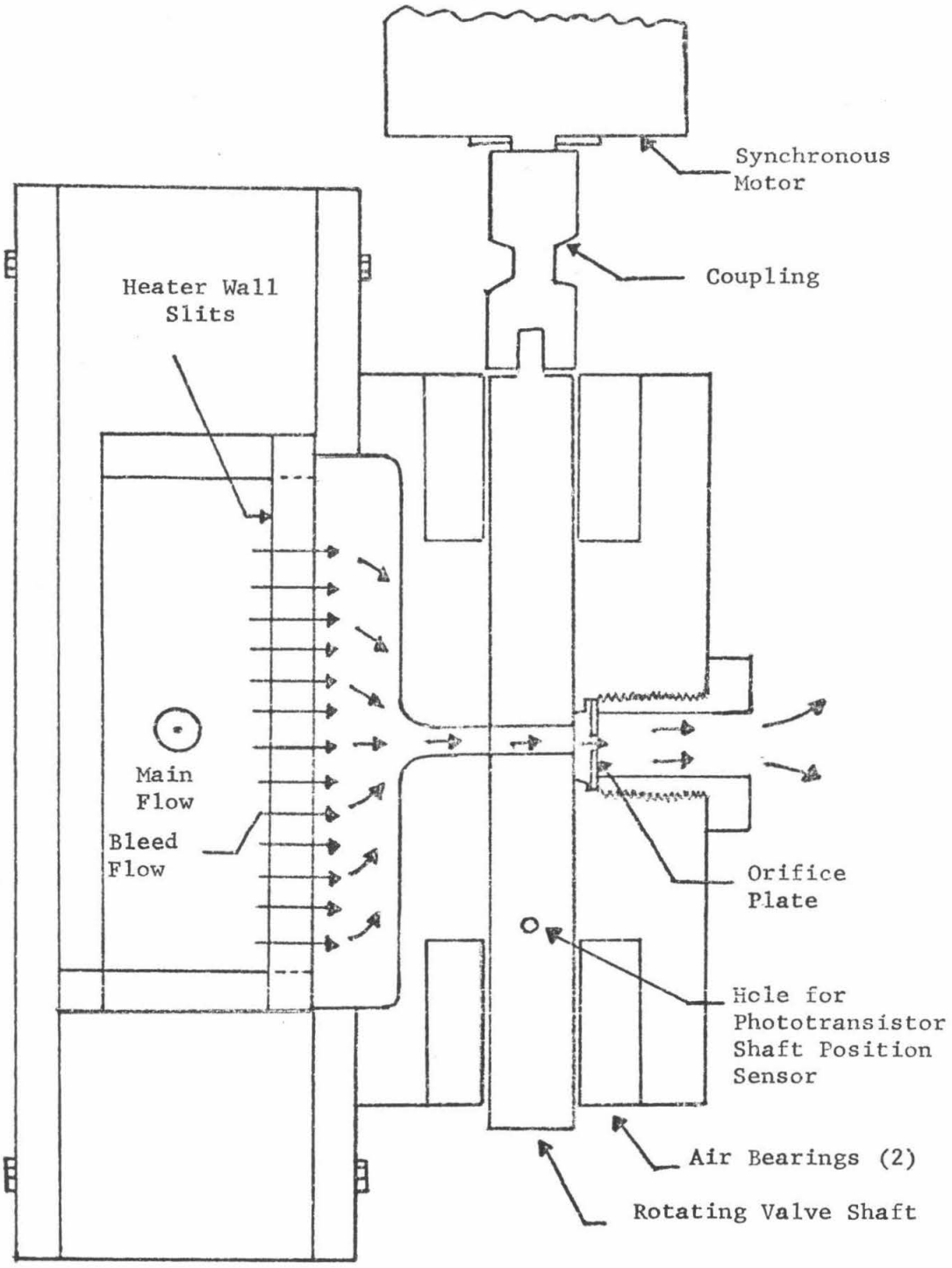

Fig. 3.17 Bleed Valve System

3.6 Electrical and Electronic Circuitry

3.6.1 Heater circuitry. The required supporting equipment for the pulse heater and bleed valve system necessitated the construction of a large amount of electrical and electronic circuitry. This section will describe, from a functional viewpoint, the role of the circuitry in the experiment. Detailed diagrams and descriptions of operation of this circuitry are given in Appendix D.

Figure 3.18 presents a functional block diagram of the control circuitry. The pulse train that controls the heater voltage waveform is produced in either the self-running pulse generator or by the heater/valve synchronization circuitry. The self-running pulse generator is used to operate the pulse heater independently of the bleed valve system. After amplification its control pulses can produce various rectangular voltage waveforms across the heater.

Recall from the last subsection that the bleed valve shaft contains a small hole which passes light to a phototransistor for a short interval of time at twice the valve rotation frequency. The phototransistor forms the basic element of the valve position detector circuit. Every time the output of this circuit goes high, the shaft is at one of two specific positions, and at these two positions, the bleed flow is the same because of the symmetry of the shaft. Hence, the valve position detector circuit defines a fixed magnitude and phase of the bleed flow when its output is high.

The output of the valve position detector circuit goes to the heater/valve synchronization circuitry where the output can be delayed a specified time with respect to the valve position detector cir-

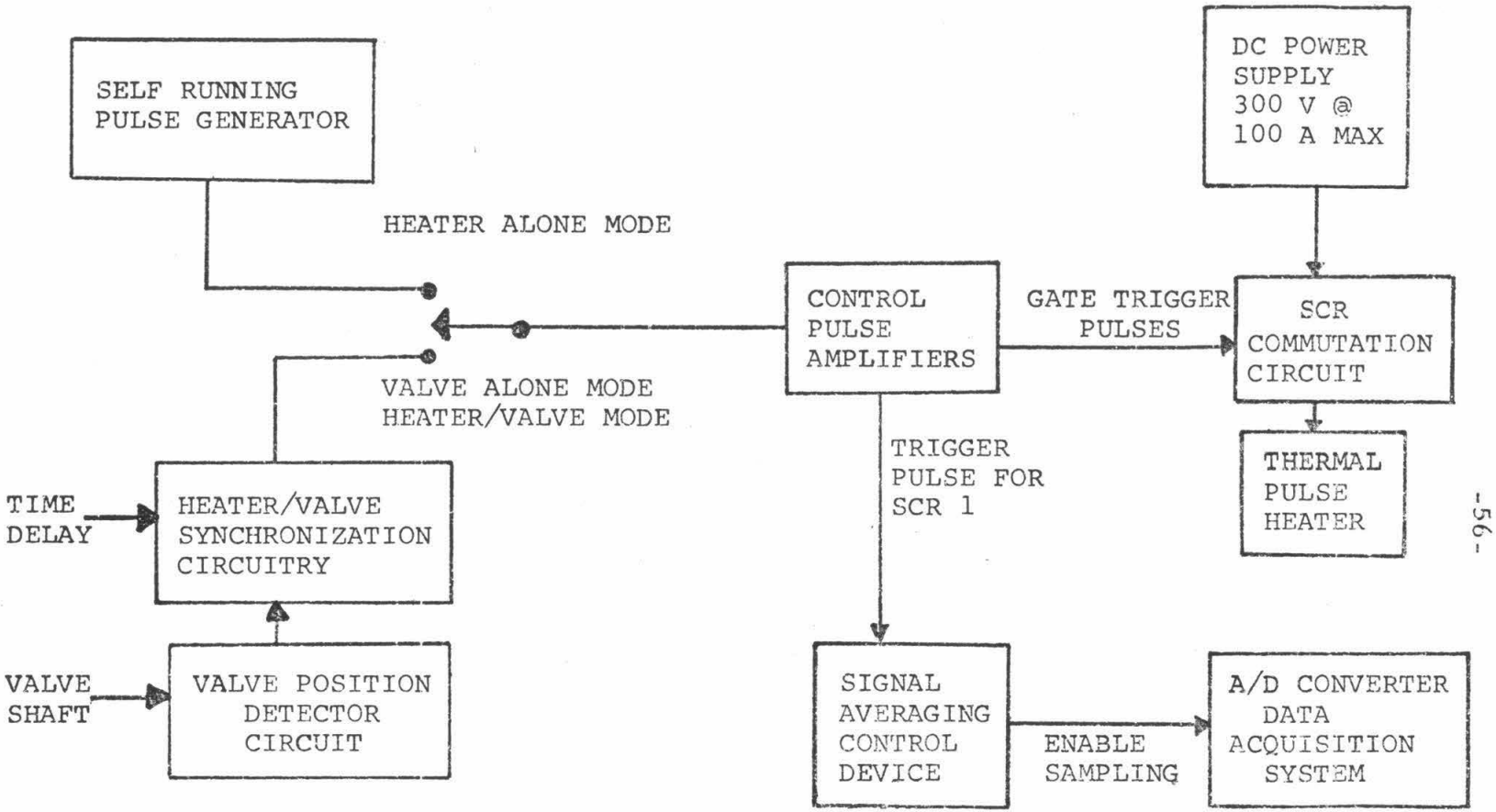

Fig. 3.18 Control Circuitry Function Diagram

cuit output pulse. The output pulses of the synchronization circuitry are amplified before being used to control the operation of the thermal pulse heater. The synchronization circuitry is the basic element in the process of producing a pure entropy wave. Changing the time delay in the circuit allows one to fire the heater at various phases of the bleed process. One of these phases has flow characteristics which will cancel out the pressure fluctuations caused by heater pulsing and hence produce the condition of a pure entropy wave propagating downstream into the nozzle.

The outputs of the above described control circuitry are of extremely low power and must be amplified before being used to produce the pulse heater waveform at levels of hundreds of volts and tens of amperes. The necessary amplification is provided by the control pulse amplifier circuits.

The high-voltage high current square wave voltage waveform across the thermal pulse heater is produced by a double silicon controlled rectifier[39] (SCR) commutation circuit energized by a D. C. power supply which can maintain 300 volts at currents up to 100 amperes. The SCR's are switched on and off by the outputs of the control pulse amplifiers. Details are in Appendix D.

3.6.2 Signal averaging control device. As stated in Section 3.1, one of the objectives of the experiment's design was to develop devices which would extract the low level signals produced by the heater and bleed valve from a high noise level background of flow noise. This objective was achieved by linking the A/D converter of the data acquisition system used in the experiment with the control

circuitry by means of the signal averaging control device, indicated on fig. 3.18. An analysis of the signal averaging process will be given in Chapter IV, but for now a brief summary of the signal averaging process is necessary to describe the operation of the device.

Consider a signal imbedded in a background level of random noise. Suppose a set of N records of the signal and noise were taken such that the records always started at the same phase of the signal. It will be shown in Chapter IV that if these N records are added, the signal/noise ratio increases by the factor $\sqrt{N}$. The signal averaging control device takes as an input the pulse train used to trigger the SCR controlling the pulse heater and produces an output pulse which always starts the A/D converter at the time the heater is fired. Thus, every data record in the data acquisition system starts at the same phase of the heater signal, so signal averaging can be performed. Note from fig. 3.18 that the valve can be run independently of the heater by disconnecting the control pulse amplifiers from the heater circuit. The output of the control pulse amplifiers can then be used for signal averaging of pressure signals produced by the bleed valve.

3.7 Instrumentation and Data Acquisition System

3.7.1 Instrumentation. Instrumentation was provided to measure the following quantities: (1) static pressures in the entrance section and nozzle, (2) static temperature in the entrance section, (3) gas temperature fluctuations produced by the pulse heater, (4) pressure fluctuations in the entrance section and nozzle, and (5) sound field external to the entrance section and nozzle.

Static pressure was measured at any of nine stations in the entrance section and nozzle by a system of pressure taps connected through a nine-position manifold to a Columbia Research Labs PDP-50A diaphragm-type transducer (range 0 - 50 psia).

Static temperature in the entrance section was measured with a Chromel-Alumel thermocouple with an associated amplifier circuit.

Measurement of the gas temperature fluctuation produced by the heater was accomplished using a very small diameter cold-wire resistance thermometer and a hot wire anemometer set modified for cold wire measurements. The wire resistance thermometer used was a DISA 55F05 temperature probe which consisted of a 1 μm diameter platinum wire held on two stainless steel prongs. The probe current was limited to 0.2 ma to ensure gas velocity fluctuations would not alter the resistance readings.

Voltage fluctuations across the wire were detected and amplified using a Shapiro-Edwards Model 50 constant-current anemometer set. The amplifier provided a gain of approximately 50,000 necessary to bring the microvolt variations across the cold wire up to a value usable by the data acquisition system.

Pressure fluctuations in the entrance section and nozzle were measured with three Columbia Research Laboratories Model 100-P piezoelectric transducers and Model 4102 charge amplifiers. The three transducers were alternated between the nine available transducer ports. The transducer/amplifier systems operated at a sensitivity of .02 psi/volt.

External sound field measurements were made by a Bruel &

Kjaer type 4136 1/4-inch microphone with a type 2618 preamplifier. The output of the 2618 preamplifier was further amplified by a Bruel and Kjaer type 2607 precision amplifier before the output signals were sent to the data acquisition system. The microphone was mounted on a stand constructed of aluminum tubing. All parts of the stand close to the microphone were covered with fiberglas sheet.

3.7.2 Data acquisition system. All data acquisition and processing operations were accomplished with a Hewlett Packard 2100 Data Acquisition System. The central unit of the system is a Hewlett Packard 2100 computer[43] with a 16K memory. Peripheral units include an analog digital converter, a magnetic tape unit, a moving head disc system with a storage capacity of over a million words, a paper tape reader unit, and a digital plotter.

A functional diagram of the data acquisition system and instrumentation is given in fig. 3.19. The low pass filter shown between the A/D converter and instruments which measure fluctuating signals is needed to prevent "aliasing errors" that would otherwise occur in the calculation of the spectra of the fluctuating signals. A detailed discussion of aliasing errors is given in Section 4.4. The low pass filter is a seven-pole Butterworth type. The filter was especially constructed for the experiment. Details of construction are given in Section D.7 of Appendix D.

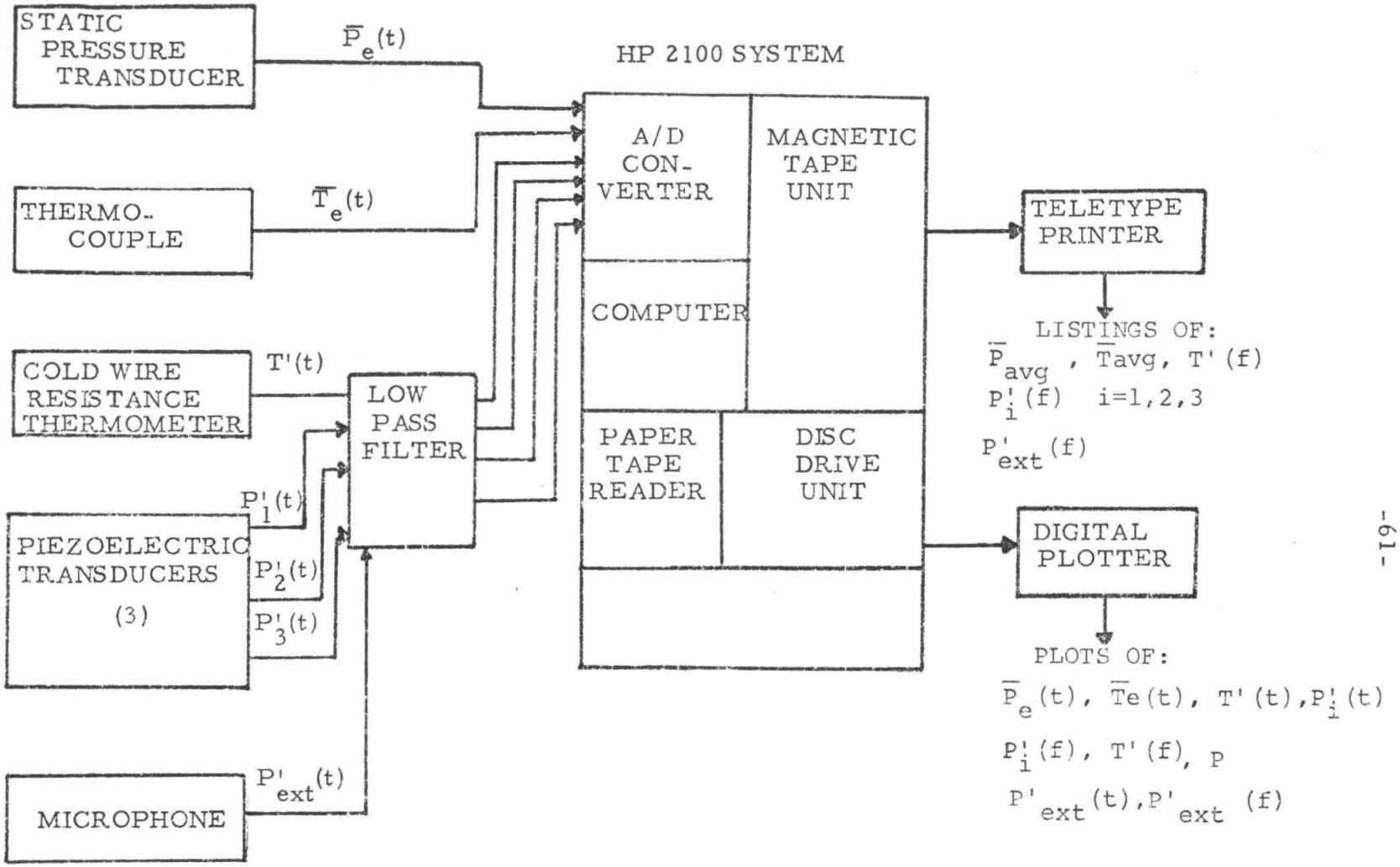

Fig. 3.19 Instrumentation and Data Acquisition System

IV. DATA ACQUISITION AND PROCESSING

4.1 Scope

Chapter III concluded with a description of the data acquisition system that would record and process the outputs of the several units of instrumentation. This chapter will continue with the topic of the data acquisition system, but instead of equipment will describe the mathematical and numerical techniques used to process the data.

The following major numerical operations were necessary for data reduction: (1) signal averaging of digital records of data, (2) Fast Fourier Transform of non-periodic data in digital records, (3) evaluation of Fourier coefficients of periodic data in digital records, (4) cross correlation of data in digital form.

4.2 The Signal Averaging Process

4.2.1 Summing signal and noise records. The signal averaging process is a numerical scheme to increase the signal/noise ratio of a periodic signal buried in a strong background of white Gaussian noise. If a number N of digital records of only the periodic signal are added such that corresponding elements of the records have an identical phase of the signal or the same phase ± an integral multiple of 2π, then the resultant amplitude will be N times the amplitude of the signal.

Now consider adding records of random noise of zero mean value. Because of the random phases of the noise one would expect additions of corresponding elements to increase at a smaller rate than the additions of the in-phase signal records. The result of these

additions is best expressed by the root mean square level of the noise, after N sums. Let σ_1 be the r.m.s. value of the noise of one record and A_o the periodic signal amplitude. The signal-to-noise ratio is defined by

$$R = A_o/\sigma_1 \quad . \tag{4.1}$$

After N sums, R will have the form

$$R = \frac{NA_o}{f(N)\sigma_1} \quad . \tag{4.2}$$

The problem is thus to find f(N).

4.2.2 Properties of white Gaussian noise. White Gaussian noise is defined by the following properties[44]. Let ξ be a Gaussian random variable: then its probability density distribution is given by:

$$p(\xi) = \frac{1}{\sqrt{2\pi}\ \sigma_1} \exp\left[-\xi^2/2\sigma_1^2 \right] \tag{4.3}$$

where σ_1 is the r.m.s. value of ξ given by

$$\sigma_1 = \left[\int_{-\infty}^{\infty} \xi^2 p(\xi)\, d\xi \right]^{\frac{1}{2}} \quad . \tag{4.4}$$

Let $\tilde{\xi}(f)$ be the spectrum of ξ; then for white Gaussian noise,

$$\tilde{\xi} = A_{\xi}(f)\, e^{i\phi(f)} \tag{4.5}$$

where $A_{\xi}(f)$ = const.,

$\phi(f)$ is a random variable between the limits

$$-\pi \leq \phi(f) \leq \pi \quad . \tag{4.6}$$

Experimental results to be given in Chapter V indicated that the flow noise in the entrance section and nozzle conformed at least roughly to the equations (4.5) and (4.6).

Let ξ_1 be a set of continuous Gaussian random variables at

time t_1 , where

$$-\infty < \xi_1 < \infty \ ;$$

ξ_2 be a set of continuous Gaussian random variables at time t_2 , where

$$-\infty < \xi_2 < \infty \ ;$$

$$\vdots$$

ξ_N be a set of continuous Gaussian random variables at time t_N .

The joint probability density function $\xi_1, \xi_2, \xi_3, \ldots, \xi_N$ is denoted by $p(\xi_1, \xi_2, \xi_3, \ldots, \xi_N)$.

Assuming the variables $\xi_1, \xi_2, \ldots, \xi_N$ are statistically independent, the joint probability density function can be expressed in terms of the density functions of each of the variables ξ_i :

$$p(\xi_1, \xi_2, \xi_3, \ldots, \xi_N) = p(\xi_1)\, p(\xi_2) \ldots p(\xi_N) \quad . \tag{4.7}$$

The next step in the analysis leading to the determination of the function f(N) in equation (4.2) is to calculate the probability density function for the sum of the ξ_i :

$$\zeta = \xi_1 + \xi_2 + \ldots \xi_N = \sum_{i=1}^{N} \xi_i \quad . \tag{4.8}$$

First, it is necessary to introduce the Fourier transform of the probability density function known as the <u>characteristic function</u>.[45]

$$C_{\xi}(i\upsilon) = \int_{-\infty}^{\infty} e^{i\upsilon\xi}\ p(\xi)d\xi \tag{4.9}$$

Then introducing the characteristic functions for the variables ξ_1, $\xi_2, \ldots, \xi_N$,

$$
\begin{aligned}
C_{\xi_1}(i\upsilon) &= \int_{-\infty}^{\infty} e^{i\upsilon\xi_1} p_1(\xi_1)d\xi_1 \\
C_{\xi_2}(i\upsilon) &= \int_{-\infty}^{\infty} e^{i\upsilon\xi_2} p_2(\xi_2)d\xi_2 \\
&\vdots \\
C_{\xi_N}(i\upsilon) &= \int_{-\infty}^{\infty} e^{i\upsilon\xi_N} p_N(\xi_N)d\xi_N
\end{aligned}
\tag{4.10}
$$

The characteristic function of ζ, which is a function of $\xi_1, \xi_2, \ldots, \xi_N$, is defined by

$$
C_\zeta(i\upsilon) = \int_{-\infty}^{\infty} \cdots \int_{-\infty}^{\infty} e^{i\upsilon\zeta} p(\zeta)d\xi_1 d\xi_2 \cdots d\xi_N \quad . \tag{4.11}
$$

Since the value of ζ is determined by the values of ξ_i, it follows that $p(\zeta)$ is given by the density function of equation (4.7)

$$
p(\zeta) = p(\xi_1, \xi_2, \ldots, \xi_N)
$$

Combining equations (4.7) and (4.11) yields

$$
C_\zeta(i\upsilon) = \int_{-\infty}^{\infty} e^{i\upsilon\xi_1} p_1(\xi_1)d\xi_1 \int_{-\infty}^{\infty} e^{i\upsilon\xi_2} p_2(\xi_2)d\xi_2 \cdots \int_{-\infty}^{\infty} e^{i\upsilon\xi_N} p_N(\xi_N)d\xi_N \tag{4.12}
$$

and then using the relation (4.10) yields

$$
C_\zeta(i\upsilon) = C_{\xi_1}(i\upsilon) \cdot C_{\xi_2}(i\upsilon) \cdots C_{\xi_N}(i\upsilon) \quad . \tag{4.13}
$$

Thus, the characteristic function of ζ is the product of the characteristic functions of each of the variables ξ_i

$$
C_\zeta(i\upsilon) = \prod_{i=1}^{N} C_{\xi_i}(i\upsilon) \quad . \tag{4.14}
$$

$p(\zeta)$ is found by taking the inverse Fourier transform of (4.14)

$$p(\zeta) = \frac{1}{2\pi} \int_{-\infty}^{\infty} C_{\zeta}(i\upsilon) e^{-i\upsilon\zeta} d\upsilon \quad . \tag{4.15}$$

Using the definition of ζ in (4.8) and the relationship (4.14) allows (4.15) to be written in the form

$$p(\zeta) = \frac{1}{2\pi} \int_{-\infty}^{\infty} C_{\xi_1}(i\upsilon)\, e^{-i\upsilon\xi_1} \cdots C_{\xi_N}(i\upsilon) e^{-i\upsilon\xi_N} d\upsilon \quad . \tag{4.16}$$

Assuming as before that each ξ_i is white Gaussian noise with zero mean value and has the same root mean square value σ_1, the probability density function of ξ_i is given by

$$p_i(\xi_i) = p(\xi_i) = \frac{1}{\sqrt{2\pi}\,\sigma_1} \exp\left[-\xi_i^2/2\sigma_1^2\right] \quad . \tag{4.17}$$

The next step is to evaluate the characteristic function of ξ_i. Substituting (4.17) into (4.9) yields

$$C_{\xi_i}(i\upsilon) = \frac{1}{\sqrt{2\pi}\,\sigma_1} \exp\left[-\frac{\sigma_1^2\upsilon^2}{2}\right] \int_{-\infty}^{\infty} \exp\left[-\frac{(\xi_i - i\sigma_1^2\upsilon)^2}{2\sigma_1^2}\right] d\xi_i \quad . \tag{4.18}$$

Let $z = \xi_i + iy$ and let z define a complex plane; then along the line $z = \xi_i - i\sigma^2\upsilon$, $dz = d\xi_i$, so (4.17) is a line integral in the complex plane along a line contour parallel to the real axis and at a distance $\sigma^2\upsilon$ below it.

To evaluate the integral, Cauchy's theorem[46] will be used for the contour shown in fig. 4.1.

The integral to be evaluated, written in terms of z, is:

$$\frac{1}{\sqrt{2\pi}\,\sigma_1} e^{-\sigma_1^2\upsilon^2/2} \int_{-\infty - i\sigma_1^2\upsilon}^{\infty - i\sigma_1^2\upsilon} e^{-z^2} dz \quad . \tag{4.19}$$

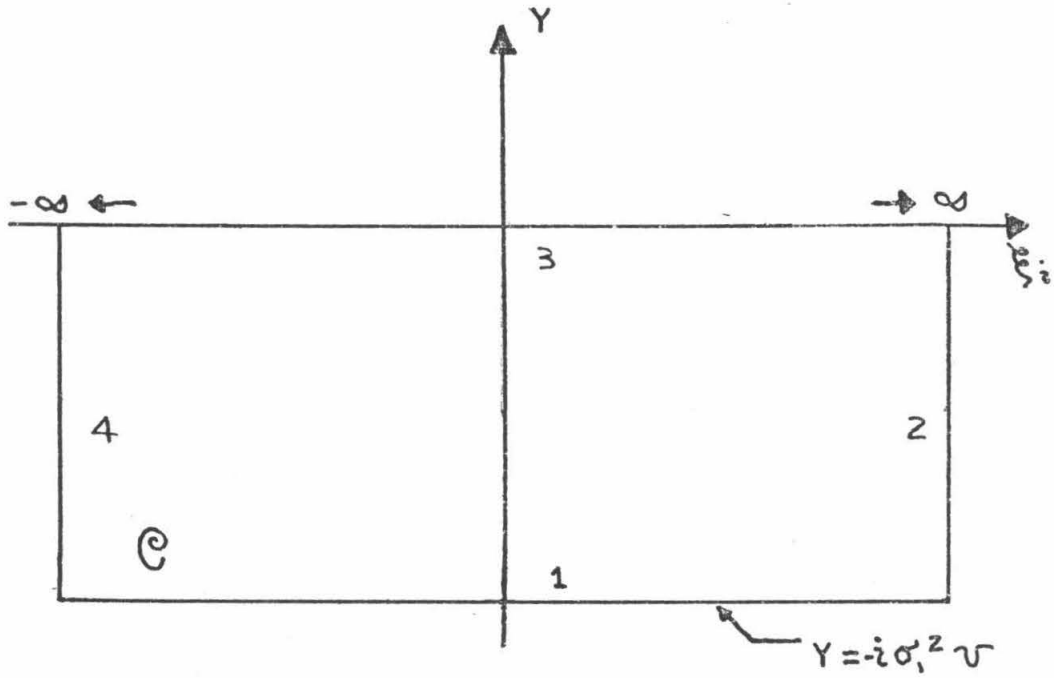

Fig. 4.1 Integration Contour for Inversion
of Characterisitic Function

Since

$$f(z) = \frac{1}{\sqrt{2\pi}\,\sigma_1} e^{-\sigma_1^2 \upsilon^2/2} e^{-z^2}$$

is analytic in the z plane, one has, by Cauchy's theorem:

$$\int_{\mathcal{C}} f(z)\, dz = 0 \ .$$

Now

$$\int_2 f(z)dz = \int_4 f(z)dz = 0 \ ,$$

since $f(z) \to 0$ as $|z| \to \infty$. Thus,

$$\int_1 f(z)dz = -\int_3 f(z)dz \ ,$$

but

$$-\int_3 f(z)dz = \left\{ -\int_{-\infty}^{\infty} e^{-\xi_i^2/2\sigma_1^2} d\xi_i \right\} e^{-\sigma_1^2 \upsilon^2/2} \frac{1}{\sqrt{2\pi}\,\sigma_1}$$

which can be readily simplified to

$$-\int_3 f(z)dz = e^{-\sigma_1^2 \upsilon^2/2} \ . \tag{4.20}$$

Thus, the characteristic function of ξ_i is simply

$$C_{\xi_i}(i\upsilon) = e^{-\sigma_1^2 \upsilon^2/2} \qquad i = 1, \ldots, N \ . \tag{4.21}$$

Substituting equations (4.21) into (4.15) yields

$$p(\zeta) = \frac{1}{2\pi} \int_{-\infty}^{\infty} e^{-N\sigma_1^2 \upsilon^2/2} e^{-i\upsilon\zeta}\, d\upsilon \ . \tag{4.22}$$

This integral is readily evaluated by completing the square in the argument of the exponential. The result is

$$p(\zeta) = \frac{1}{\sqrt{2\pi N}\,\sigma_1} e^{-\zeta^2/2N\sigma_1^2} \ . \tag{4.23}$$

Evaluating the r.m.s. value of ζ by the formula

$$(\overline{\zeta}^2)^{\frac{1}{2}} = \int_{-\infty}^{\infty} \zeta^2 \, p(\zeta) d\zeta$$

gives the result

$$(\overline{\zeta}^2)^{\frac{1}{2}} = \sqrt{N}\,\sigma_1 \quad . \tag{4.24}$$

Equation (4.24) gives the form of f(N) in equation (4.2)

$$f(N) = \sqrt{N}$$

so the signal/noise ratio after N signal averaging operations is:

$$R_N = \sqrt{N}\,R_o \quad . \tag{4.25}$$

Hence, for example, the signal-to-noise ratio of a periodic signal embedded in noise can be increased a factor of 10 by adding 100 records of the signal and noise.

4.2.3 Signal averaging process for the data acquisition system. The signal averaging process is accomplished on the data acquisition system using the A/D converter, computer, and disc drive. A typical acquisition cycle is as follows. The A/D converter is started exactly at the time the heater is fired or the valve shaft is at a given position by means of the signal-averaging control device (Section 3.6). The computer then stores 6144 words of data from six A/D channels during the "sample pause" of the cycle. During the "pause" portion of the cycle, the data are transferred from the computer core to one track of the magnetic disc. Storage capability of one track is 6144 words. After this cycle is repeated N times, N tracks of the disc will contain data records starting at the same phase of the heater or valve signal. The computer then selects data words corresponding to the same phase relative to heater firing or

valve position from each of the N tracks of the disc, adds them, divides by N , and then stores the result on a new disc track. The end result is 6144 numbers of signal-averaged data.

Use of the disc was mandatory because of the small size core (16K) of the computer. With a 32K core computer capability, the acquisition and averaging processes could have been completely performed in the computer and would have resulted in the reduction of the long "pause time" cycle necessary for core-to-disc data transfer.

The size of the disc also limited N, the number of signal-averaging operations. Since the operating system software for the computer was stored on the disc as well as programs in absolute binary form, only 120 to 140 tracks were available for data storage. With signal averaging done entirely within the computer, this limitation is eliminated; N is then limited by the time constant conditions that can be maintained in the blowdown tunnel.

4.3 Spectral Analysis

4.3.1 Spectrum of flow noise by the Fast Fourier Transform.

To obtain a spectrum of the flow noise in the entrance section and nozzle as well as a spectrum of the jet noise, the Fast Fourier Transform method was used. This method, known as the Cooley-Tukey algorithm, is described in refs. 47 and 48. A FORTRAN IV program of this algorithm developed by Hewlett Packard[49] was modified for specific use by the data acquisition system for this experiment. The algorithm requires that the number of data samples be an integer power of 2 . In the experiment, each record of fluctuating data contains 1024

words of data. The frequency resolution of the transform is the reciprocal of the total sampling time. With the record size given above, a sampling rate of 10 KHz/channel gives a resolution of 10 Hz, a sampling rate of 20 KHz/channel gives a resolution of 20 Hz, etc. The maximum frequency of the spectrum for which the transform is meaningful is half the sampling frequency usually called the Nyquist frequency. The Nyquist frequency is based on the criterion that if a transform is to be meaningful at a given frequency, at least two data points per cycle must be given.

4.3.2 Spectral analysis of signal-averaged data records. The signal-averaged records of fluctuating data were periodic at either the valve or the heater frequency and higher harmonics. The Fast Fourier Transform cannot be applied to a period record of data unless the record contains exactly an integral number of cycles at all frequencies in the waveform. Thus, in order to get a correct spectrum, it was necessary to develop an alternate form of spectrum computation. It was decided to use the ordinary integral method of evaluating the Fourier coefficient. The method will be derived in detail below.

4.3.3 Discrete Fourier series. Let $f(t)$ be a continuous function of time. Suppose $f(t)$ is sampled digitally at times 0, $\pm \Delta t$ $\pm 2\Delta T, \ldots, \pm n\Delta t, \ldots$. Then the discrete sampled form of $f(t)$ denoted by $f^*(t)$ can be expressed as

$$f^*(t) = \sum_{n=-\infty}^{\infty} f(t)\delta(t-n\Delta t)\Delta t \quad . \tag{4.26}$$

$\delta(t-n\Delta t)$ is the Kronecker delta defined by

$$\delta(t-n\Delta t)\Delta t = 1 \qquad t = n\Delta t \tag{4.27}$$

$$\delta(t-n\Delta t)\Delta t = 0 \qquad t \neq n\Delta t \tag{4.28}$$

Suppose $f^*(t)$ is periodic on the interval $-T/2 \leq t \leq T/2$, then $f^*(t)$ can be written as a Fourier series[50]

$$f^*(t) = \sum_{k=0}^{\infty} a_k \cos \frac{2\pi kt}{T} + b_k \sin \frac{2\pi kt}{T} \tag{4.29}$$

where

$$\begin{aligned} a_k &= \frac{2}{T} \int_{-T/2}^{T/2} f^*(t) \cos \frac{2\pi kt}{T}\, dt \quad , \\ b_k &= \frac{2}{T} \int_{-T/2}^{T/2} f^*(t) \sin \frac{2\pi kt}{T}\, dt \quad . \end{aligned} \tag{4.30}$$

Let T consist of 2N sampling intervals,

$$T = 2N\Delta t \quad . \tag{4.31}$$

Then there are 2N+1 discrete samples of f(t) in $f^*(t)$ in the interval $-T/2 \leq t \leq T/2$. Thus, one can write

$$f^*(t) = \sum_{n=-N}^{N} f(t)\delta(t-n\Delta t)\Delta t \quad . \tag{4.32}$$

Equations (4.30) - (4.32) can thus be combined to give

$$\begin{aligned} a_k &= \frac{2}{2N\Delta t} \int_{-T/2}^{T/2} \sum_{n=-N}^{N} f(t)\delta(t-n\Delta t)\Delta t \cos \frac{2\pi kt}{2N\Delta t}\, dt \quad , \\ b_k &= \frac{2}{2N\Delta t} \int_{-T/2}^{T/2} \sum_{n=-N}^{N} f(t)\delta(t-n\Delta t)\Delta t \sin \frac{2\pi kt}{2N\Delta t}\, dt \quad . \end{aligned} \tag{4.33}$$

Simplifying the above equations yields

$$a_k = \frac{1}{N} \sum_{n=-N}^{N} \int_{-T/2}^{T/2} f(t)\delta(t-n\Delta t) \cos \frac{\pi kt}{N\Delta t}\, dt \tag{4.34a}$$

$$b_k = \frac{1}{N} \sum_{n=-N}^{N} \int_{-T/2}^{T/2} f(t)\delta(t-n\Delta t) \sin \frac{\pi k t}{N\Delta t}\, dt \qquad (4.34b)$$

For a large number of samples as in the case of the experiment, Δt is small; then $\delta(\ )$ can be treated as a Dirac delta function such that

$$\int_{-\infty}^{\infty} f(p)\,\delta(p-a)\,dp = f(a) \ . \qquad (4.35)$$

Then with this relationship and the fact that for $f^*(t)$, t assumes only the values $n\Delta t$ $n = -N, \ldots, N$, the Fourier coefficients (4.34) become

$$a_k = \frac{1}{N} \sum_{n=-N}^{N} f(n\Delta t) \cos \frac{\pi k n}{n} \qquad (4.36a)$$

$$b_k = \frac{1}{N} \sum_{n=-N}^{N} f(n\Delta t) \sin \frac{\pi k n}{N} \qquad (4.36b)$$

Instead of using a_k and b_k to represent the spectral components of the fluctuation signals, the following amplitude and phase representation will be utilized:

$$\begin{aligned} &\text{amplitude:} && A_k = \sqrt{a_k^2 + b_k^2} \\ &\text{phase:} && \phi_k = \tan^{-1} \frac{b_k}{a_k} \end{aligned} \qquad (4.37)$$

Equations (4.36) are called discrete Fourier coefficients of a discrete sampled function. The properties of interest of the coefficients are: (1) frequency resolution, (2) largest value of k for which coefficients are meaningful, (3) relating k to the corresponding frequency.

Recall the form of the sine and cosine terms in equation (4.30)

$$\sin \frac{2\pi k}{T} \ , \qquad \cos \frac{2\pi k}{T} \ .$$

The argument $(2\pi kt)/T$ can be written as $\Omega_k t$ where

$$\Omega_k = k \frac{2\pi}{T} \ .$$

It immediately follows that the frequency increment or frequency resolution is

$$\Delta\Omega = \frac{2\pi}{T} \quad . \tag{4.38}$$

Thus, the coefficients of the index k are an average over a frequency range $\Omega_k - \Delta\Omega$ to $\Omega_k + \Delta\Omega$. The relationship between k and some frequency ω is

$$k = \text{integer value } \left(\frac{\omega}{\Delta\Omega} \right) ,$$

where ω lies in the range $k\Delta\Omega$ and $(k+1)\Delta\Omega$.

The upper limit of k corresponds to the Nyquist frequency explained in the last section. Recall that the Nyquist frequency is based on the criterion that there must be at least two data points per cycle for a meaningful value of the Fourier coefficient. The Nyquist frequency is $1/(2\Delta T)$, but $\Delta t = T/2N$; so

$$\Omega_{k_{Nyquist}} = \frac{2\pi N}{T} = N\Delta\Omega \ . \tag{4.39}$$

Hence, the maximum value of k is equal to N .

4.3.4 Computer spectrum calculations of signal-averaged data records. The objective of the spectral analysis of signal-averaged records was to find the amplitude and phase of pressure or temperature fluctuations at the heater or valve frequency. Thus, only a small set of Fourier coefficients was needed, and calculation of a whole spectrum was unnecessary. To calculate the amplitude and phase of the fluctuations at the driving frequency, the following data processing scheme was used.

Digital records of pressure and temperature fluctuations contained 1024 values. The reason for the number 1024 is based on the

fact that six channels of data were taken on each signal-averaging cycle and then stored on one track of the disc, which could hold a maximum of 6144 words (6 × 1024).

From the 1024 word data records the discrete Fourier coefficients were evaluated as follows. First, the data record was truncated so that the new record contained the maximum possible number of cycles corresponding to the bleed or heater frequency. The record length was then increased or decreased by one data point to give an even number 2N of sampling intervals Δt. At a sampling rate of 10 KHz and a bleed or heater frequency of 400 Hz, this results in only an error of 1 part in 2500 in computing a_k and b_k. The values of a_k and b_k are computed from the truncated record using equations (4.38). To indicate the sharpness of the signal-averaged spectrum about the heater or bleed frequency ω, the values of a_k and b_k were computed for the frequencies $\omega-2\Delta\Omega$, $\omega-\Delta\Omega$, ω, $\omega+\Delta\Omega$, and $\omega+2\Delta\Omega$. Chapter V will describe the sharpness of the signal-averaged spectra obtained in the the experiment.

4.4 Aliasing Errors

This section gives a brief description of aliasing errors and the measures taken in the experiment to prevent them.

4.4.1 Description of aliasing. Aliasing errors are exclusively a result of the digital sampling process; that is, aliasing errors arise when there is no continuous record of data, but only a set of data points at equally spaced intervals.

Aliasing errors are associated with alias frequencies. Alias

frequencies are two frequencies such that if sinusoidal waveforms of these two frequencies were sampled digitally, subsequent analysis could not discern which frequency was sampled. The situation is shown in fig. 4.2. The diagram reveals that the sampling cannot distinguish the sinusoid of frequency f_o from the sinusoid of frequency f_1. For this reason, f_o and f_1 are called alias frequencies. f_o is always lower than the sampling frequency f_s, while f_1 is always higher.

Thus, if a data sample contains frequency exponents above f_s, a spectral analysis for some frequency $f < f_s$ will be erroneous. For a correct spectrum, the transducer outputs must be sent through a low-pass filter which eliminates all frequency components above f_s. This was done in the experiment by using the low-pass Butterworth filter described in section 3.7.2. To complete this section on aliasing, a mathematical description will be given.

4.4.2 Mathematical description of aliasing errors. Let $V(\tau)$ be a periodic function defined in the interval $-T/2 \leq \tau \leq T/2$. Without loss of generality, $V(\tau)$ is taken to have zero mean value.

$V(\tau)$ can be expressed as a Fourier series

$$V(\tau) = \sum_{k=1}^{\infty} C_k e^{\frac{2\pi i k \tau}{T}} \tag{4.40}$$

where $C_k = a_k - ib_k$

$$a_k = \frac{2}{T} \int_{-T/2}^{T/2} V(\tau) \cos \frac{2\pi k \tau}{T} \, d\tau$$

$$b_k = \frac{2}{T} \int_{-T/2}^{T/2} V(\tau) \sin \frac{2\pi k \tau}{T} \, d\tau$$

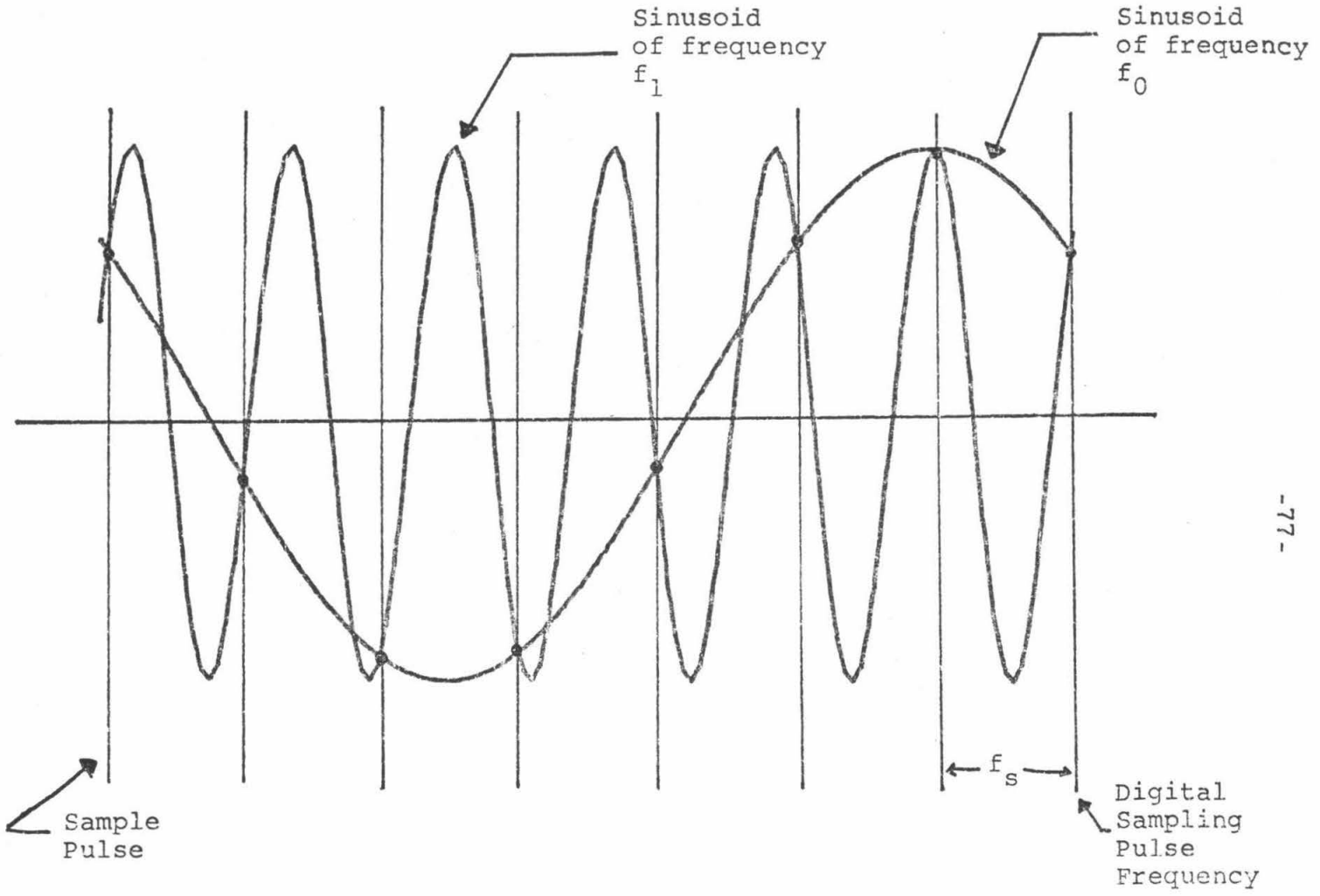

Fig. 4.2 Waveform Diagram Showing Relationship between Alias Frequencies and Digital Sampling Frequency

Let $\tilde{V}(\tau)$ be the discrete sampled form of $V(\tau)$ at times 0, $\pm \Delta t$, $\pm 2\Delta t$, ...; then $\tilde{V}(\tau)$ can be written

$$\tilde{V}(\tau) = \sum_{n=-\infty}^{\infty} \Delta t\, \delta(\tau - n\Delta t) V(\tau) \tag{4.41}$$

where the delta function has been defined in equations (4.29) and (4.30).

The interval T is assumed to contain an integral number of sampling intervals Δt:

$$T = M\Delta t \ . \tag{4.42}$$

Let D_k be a Fourier coefficient of $\tilde{V}(\tau)$. Then

$$D_k = \frac{2}{T} \int_{-T/2}^{T/2} \sum_{n=-\infty}^{\infty} \Delta t\, \delta(\tau - n\Delta t) V(\tau) e^{-\frac{2\pi i k \tau}{T}} d\tau \ . \tag{4.43}$$

The function

$$G(\tau) = \sum_{n=-\infty}^{\infty} \Delta t\, \delta(\tau - n\Delta t)$$

is a periodic even function of period Δt. It can hence be expanded as a Fourier cosine series[51]. Applying equations (4.29) and (4.30) with T replaced by Δt yields the series

$$G(\tau) = 1 + 2 \sum_{m=1}^{\infty} \cos \frac{2\pi m \tau}{\Delta t} \ . \tag{4.44}$$

Combining (4.43) and (4.44) yields

$$D_k = \frac{2}{T} \int_{-T/2}^{T/2} V(\tau) e^{-\frac{2\pi i k \tau}{T}} d\tau + \frac{1}{T} \sum_{m=1}^{\infty} \int_{-T/2}^{T/2} \cos \frac{2\pi m \tau}{\Delta t}\, e^{-\frac{2\pi i k \tau}{T}} V(\tau) d\tau \ . \tag{4.45}$$

The first term on the right hand side of (4.45) is c_k, the true Fourier coefficient; the second term represents erroneous contributions. This last term will now be evaluated. Using equations (4.40) and (4.42), the integral can be written:

$$\frac{1}{T}\sum_{m=1}^{\infty}\sum_{\ell=1}^{\infty}\int_{-T/2}^{T/2}\cos\frac{2\pi m\tau}{\Delta t}\cos\frac{2\pi k\tau}{M\Delta t}\left[a_\ell\cos\frac{2\pi\ell\tau}{M\Delta t}-ib_\ell\sin\frac{2\pi\ell\tau}{M\Delta t}\right]d\tau \quad (4.46)$$

Since the cosine and sine terms contain any integral number of periods in the interval T, any two form an orthogonal set. Now note the trigonometric identities:

$$\cos\frac{2\pi k\tau}{M\Delta t}\cos\frac{2\pi\ell\tau}{M\Delta t} = \cos\frac{2\pi(k-\ell)\tau}{M\Delta t}+\cos\frac{2\pi(k+\ell)\tau}{M\Delta t} \quad (4.47a)$$

$$\cos\frac{2\pi k\tau}{M\Delta t}\sin\frac{2\pi\ell\tau}{M\Delta t} = \sin\frac{2\pi(k-\ell)\tau}{M\Delta t}+\sin\frac{2\pi(k-\ell)\tau}{M\Delta t} \quad (4.47b)$$

Then because of the orthogonality condition, only the cosine pair (4.47a) will contribute to the integral for values

$$\begin{aligned}\ell &= Mm-k\\ \ell &= Mm+k\end{aligned} \quad (4.48)$$

Thus, the integral (4.46) reduces to

$$\frac{1}{2}\sum_{m=1}^{\infty} a_{Mm-k}+a_{Mm+k}\ , \quad (4.49)$$

so the Fourier coefficient D_k differs from the true Fourier coefficient C_k by

$$D_k = C_k+\frac{1}{2}\sum_{m=1}^{\infty}\{a_{mM-k}+a_{Mm+k}\}\ . \quad (4.50)$$

Consider a_{mM} for $m = 1$: a_M corresponds to the term

$$\frac{2\pi M\tau}{T} = \frac{2\pi M\tau}{M\Delta t} = \frac{2\pi\tau}{\Delta t}\ ;$$

but $1/\Delta t$ is the sampling frequency, so $k = M$ is the index at the sampling frequency f_s. Now let k correspond to a frequency f. Then (4.50) can be written equivalently as

$$D(f) = C(f)+\frac{1}{2}\sum_{m=1}^{\infty}\{a(mf_s-f)+a(mf_s+f)\}\ . \quad (4.51)$$

That is, the Fourier coefficient for a digitally-sampled waveform differs from the true Fourier coefficient by the sum of the cosine coefficients at frequencies $mf_s - f$ and $mf_s + f$. Hence, if the waveform is filtered so that there are zero amplitude components for frequencies greater than $f_s - f$, there will be no aliasing error; the digitally sampled waveform yields the true Fourier coefficient.

4.5 Cross Correlation Analysis

4.5.1 Usage. Cross correlation analysis was used for processing of the external field noise measurements to be described in Chapter VI. Cross correlation coefficients were calculated for signal-averaged pressure fluctuation records at the nozzle exit and signal-averaged sound pressure levels at various positions in the anechoic chamber.

4.5.2 The cross correlation function. Let $p_1'(t)$ be the pressure fluctuation with zero mean at the nozzle exit, and let $p_2'(t)$ be the sound pressure level with zero mean in the external field of the jet. Then the cross correlation function of p_1' and p_2' for a time lag τ is defined by

$$CF_{12}(\tau) = \lim_{T \to \infty} \frac{1}{T} \int_{-T/2}^{T/2} p_1'(t)\, p_2'(t+\tau)\, dt \,. \qquad (4.52)$$

Equation (4.52) is defined in the strict mathematical sense for an infinite sampling time with an infinite number of samples. To deal with the experimental data which consist of finite length groups of discrete sampled data, an approximate form of equation (4.50), explained in the next subsection, was used.

4.5.3 Computer calculation of the cross correlation function using discrete sampled data. Consider two digital records of data. Each record contains N data values separated by the sampling interval Δt.

The time t is given by

$$t = i\Delta t \qquad 0 \le i \le N-1 \ , \tag{4.53}$$

and the lag τ can be expressed by

$$\tau = m\Delta t \ . \tag{4.54}$$

The following change of notation occurs as one goes from the continuous variables to the discrete variables

$$\begin{aligned} p_1'(t) &\rightarrow p_1'(i\Delta t) \equiv f_i \\ p_2'(t+\tau) &\rightarrow p_2'((i+m)\Delta t) \equiv g_{i+m} \end{aligned} \tag{4.55}$$

The integral in (4.52) becomes a sum over the part of each set of N data values which are a time $m\Delta t$ apart. It is obvious that this part consists of only N-m values in each group. Thus, the cross correlation function for the discrete sets of data becomes:

$$CF_{12}(m) \approx \frac{1}{N-m} \sum_{i=1}^{N-m} f_i g_{i+m} \ . \tag{4.56}$$

The question now arises as to what values of m and N will make $CF_{12}(m)$ a good approximation of the true correlation function defined in equation (4.52). Phillips, James, and Nichols[52] have considered the case of the cross correlation of periodic functions. Fortunately, the signal-averaged pressure fluctuations in this experiment are also periodic, so that a direct application of their results can be made. Their results can be stated as follows. Consider two signals of angular

frequency ω. Then the cross correlation function will be within 2 per cent of its true value if, for a sampling interval Δt,

$$N \geq \frac{22\pi}{\omega \Delta t}$$
$$m \leq \frac{N}{4} \tag{4.57}$$

In the experiments to be described in Chapter VI, N corresponded to 40 cycles of the sinusoids; this is almost 4 times as great as the 11 cycles required by the first of equations (4.56). m was taken to be N/4.

Computer calculations of the cross correlation function were performed using equation (4.57). The records of the transducer and microphone outputs were modified so that the record had zero mean. Let $\hat{f}_i$ and $\hat{g}_i$ be the initial transducer outputs; the correction for zero mean was done by the operations

$$f_i = \hat{f}_i - \frac{1}{N} \sum_{i=1}^{N} \hat{f}_i$$
$$g_i = \hat{g}_i - \frac{1}{N} \sum_{i=1}^{N} \hat{g}_i \tag{4.58}$$

Spectral analyses of the cross correlation function at the valve and heater frequencies and their harmonics were made using equations (4.33). The result of these analyses gave the important result of the degree of cross correlation between the pressure fluctuations at the valve or heater frequency located at the nozzle exit and far field.

4.54 Cross correlation coefficient. The degree of correlation is usually expressed by the cross correlation coefficient, which is the cross correlation function divided by the product of the r.m.s.

value of each signal. In general, one has

$$CC_{12}(\tau) = \lim_{T\to\infty} \int_{-T/2}^{T/2} \frac{p_1'(t)\,p_2'(t+\tau)}{(\overline{p_1'^2})^{1/2}\,(\overline{p_2'^2})^{1/2}}\,dt \quad . \tag{4.59}$$

In the experiment, one is interested in the cross correlation coefficient for the components of the pressure fluctuations at the driving frequency.

Let $A^1(\omega_o)$ be the amplitude of the Fourier component of the first pressure fluctuation corresponding to the valve or heater frequency ω_o. Let $A^2(\omega_o)$ be the corresponding component for the second pressure fluctuation. If $CF_{12}(\omega_o, \tau) = A_{12}\exp[i(\omega_o\tau + \phi)]$ is the spectral component of the cross correlation function at ω_o, then the cross correlation coefficient takes the form

$$CC_{12}(\omega_o, \tau) = \frac{A_{12}\,e^{i(\omega_o\tau + \phi)}}{\frac{A^2(\omega_o)}{\sqrt{2}}\;\frac{A^1(\omega_o)}{\sqrt{2}}} \quad . \tag{4.60}$$

The quantity of interest is the amplitude of the right hand side of (4.60):

$$CC_{12}(\omega_o) = \frac{2A_{12}(\omega_o)}{A^1(\omega_o)A^2(\omega_o)} \quad . \tag{4.61}$$

This last quantity will be calculated for the data in Chapter VI.

V. EXPERIMENTAL RESULTS: THE NOZZLE SOUND FIELD

5.1 Scope

Having described the experimental and analytical techniques for the study of the nozzle sound field, this is an appropriate place to begin a discussion of the experimental results.

The study of the nozzle sound field was made in three stages. First, with the bleed valve system and thermal pulse heater deactivated, measurements of the background flow noise were made. This was done first,to check if the noise was of sufficiently random nature so that the signal-averaging process described in Chapter IV could be applied; second, to check if any abnormal background noise existed in the test section. For example, if the pressure regulators chattered, the resultant sound produced would show up in the flow noise study.

Next, the bleed valve system was operated alone to produce pure pressure disturbances in the nozzle. The result of these experiments showed the behavior of a pure pressure disturbance in the nozzle. The results are enlightening in the sense that they can be compared to the case of both pressure and entropy disturbances in the nozzle. This comparison immediately shows the existence of the "entropy" noise source mechanism.

The study also proved the effectiveness of the signal-averaging process; the bleed valve was used instead of the heater in order to eliminate the risk of destroying the latter during preliminary tests.

The third phase of the study involved measuring the sound field produced by operating the thermal pulse heater alone and then

with the bleed valve system so as to produce a pure entropy wave -- that is, a downstream-running entropy disturbance accompanied by a zero amplitude downstream-running pressure wave. The experiments verified the theory of Marble and Candel[21] in that it predicts correctly the production of sound by entropy waves and the interaction of this sound with pressure disturbances arising elsewhere. The most significant result was that shown by the bleed valve and heater combined operation -- that the propagation of time-dependent entropy fluctuation through a region of flow with a mean velocity gradient produces sound.

5.2 Flow Noise in the Entrance Section and Nozzle

The first set of experiments conducted in the entrance section and nozzle was for the purpose of determining the nature of the background flow noise. The flow noise in the entrance section and nozzle originated from two sources.

(i) In the upstream region of the plenum chamber (see Section 3.2 and fig. 3.9), nitrogen exits from the 2-in. phenolic tube into the 6-in. diameter open area between the acoustic absorbent material and metal cone. In this region, the shear layers, large eddys , and small jets originating in the pores of the metal cone produce significant aerodynamic noise.

(ii) The turbulent velocity field along the entire extent of the entrance section nozzle produces a strong sound field.

The resultant noise level at any point in the tunnel is a complex combination of the geometry, steady operating conditions (tunnel

pressure level) and the above two sources. Because the noise level in the tunnel is unique, it would be of no use to compare it to tunnel noise measurements by other authors. Comparison with boundary-layer noise measurements would also be difficult because reported noise spectra start at frequencies of 5 K Hz, which is above the frequency limit (4 K Hz) of observation of noise in this experiment.

The objective of the noise study in this experiment is qualitative rather than quantitative: to determine whether the noise is sufficiently random so that signal averaging can be applied. If the study revealed a non-random fluctuation such as occurs when using a compressor steady-flow tunnel rather than a blowdown tunnel, one would have to devise a more sophisticated signal extraction process than signal averaging.

Pressure fluctuation measurements were made at the six entrance section and nozzle transducer ports. On the graphs that follow, the transducer ports are indicated by a sequence number from 2 to 7. The relation between the sequence number and the location of the port relative to the nozzle entrance is as follows.

Transducer Port No.	Position*
2	-8.0 in.
3	-0.5 in.
4	+3.0 in.
5	+6.375 in.
6	+9.25 in.
7	+10.75 in.

* - upstream of nozzle entrance
\+ downstream of nozzle entrance

At a sampling rate of 10 KHz, 1024-word digital records of the pressure fluctuations were made at each transducer position. Using the results of Chapter 4, one can see that the frequency resolution of calculated noise spectra will be 10 Hz, and the Nyquist frequency 5 KHz. To prevent aliasing, the Butterworth low-pass filter (section 3.7) was connected between the transducers and A/D converter of the data acquisition system.

Table 5-1 shows the r.m.s. value of the noise level at each transducer position. The r.m.s. noise level appears to be constant throughout the tunnel. One would expect that as the static pressure drops, the noise level would drop also. However, an explanation for this constant value may lie in the fact that when turbulence is convected through a mean velocity gradient, it produces sound. This was noted in Chapter I. The theory of this turbulence - sound conversion was developed by Ribner[12, 13].

Spectral calculations were performed on each of the 1024-word data records using the Fast Fourier Transform. Since the Fourier transform is to be only used formally for an infinitely long data record, and since in the experiment the records were 0.1 seconds long, the problem of what window function to use in the spectral calculations arose. An excellent guide to the use of window functions in spectral calculations is given in ref. 51; use will be made of this reference in the following paragraphs.

The data records entering the computer are equivalent to the product of a function that exists for all time and a rectangular gate pulse of height unity and width equal to the duration of the sampling

T_s. The latter is called a rectangular window.

Let f(t) be the infinitely long function, w(t) be the window function, and $f_s(t)$ be the sampled function. Then

$$f_s(t) = f(t)\, W_s(t) \quad , \tag{5.1}$$

where

$$\begin{aligned} W_s(t) &= 1 && 0 \le t \le T_s \\ W_s(t) &= 0 \quad \Big\} && \begin{matrix} t < 0 \\ t > T_s \end{matrix} \end{aligned} \tag{5.2}$$

Amplitude and phase spectra for the flow noise measured at transducer positions 3, 5, and 7 are shown in figs. 5.1 to 5.9. These three positions give a complete picture of the noise all along the tunnel; in the entrance section (low subsonic flow), just upstream of the throat (high subsonic flow), and near the nozzle exit (low supersonic flow).

As can be seen from the graphs, the phase spectra are randomly distributed and the amplitude spectrum is almost constant except for a few discrete spikes. Thus, the flow noise is a relatively good approximation to white Gaussian noise except for the spikes, which can be attributed to the use of a rectangular window function. The use of this window function imposes abrupt end conditions on the sampled waveform. The Fast Fourier Transform interprets these abrupt changes as being made out of discrete frequency components and adds them to the spectrum of the true waveform.

This problem is solved by using a window function which has smooth ends. A commonly-used window function which has this characteristic plus minimal side lobes in the frequency domain is the Hanning window function[51], given by

$$W_s(t) = \frac{1}{2}\left(1 + \cos\frac{2\pi t}{T_s}\right) \qquad -T_s/2 \le t \le T_s/2$$

$$= 0 \qquad |t| > T_s/2 \tag{5.3}$$

This window function was applied to the data records from which the spactra of figs. 5.1 to 5.9 were computed. The results are shown in figs. 5.10 to 5.18. Note that in all the graphs of the amplitude spectra on a linear scale, the sharp discrete peaks have disappeared. The resulting spectra definitely display random phase distributions and amplitude distributions which contain components at all frequencies not differing by more than a factor of two. This leads one to conclude that the flow noise is a good approximation to white Gaussian noise and can be subjected effectively to a signal-averaging process. The degree of effectiveness will be considered in the next section.

Table 5-1. R.M.S. Values of Blowdown Tunnel Noise Flow

Transducer Position	Coordinate (in.)	R.M.S. Sound Power Level (psia)	R.M.S. Sound Power Level (dba)
2	-8.0	.008298	129.77
3	-0.5	.010619	131.27
4	3.0	.014852	134.19
5	6.375	.012964	133.01
6	9.25	.012547	132.72
7	10.75	.011223	131.75

Fig. 5.1 Amplitude Spectrum of the Flow Noise at Transducer Position 3. Spectrum computed with a Rectangular Window Function.

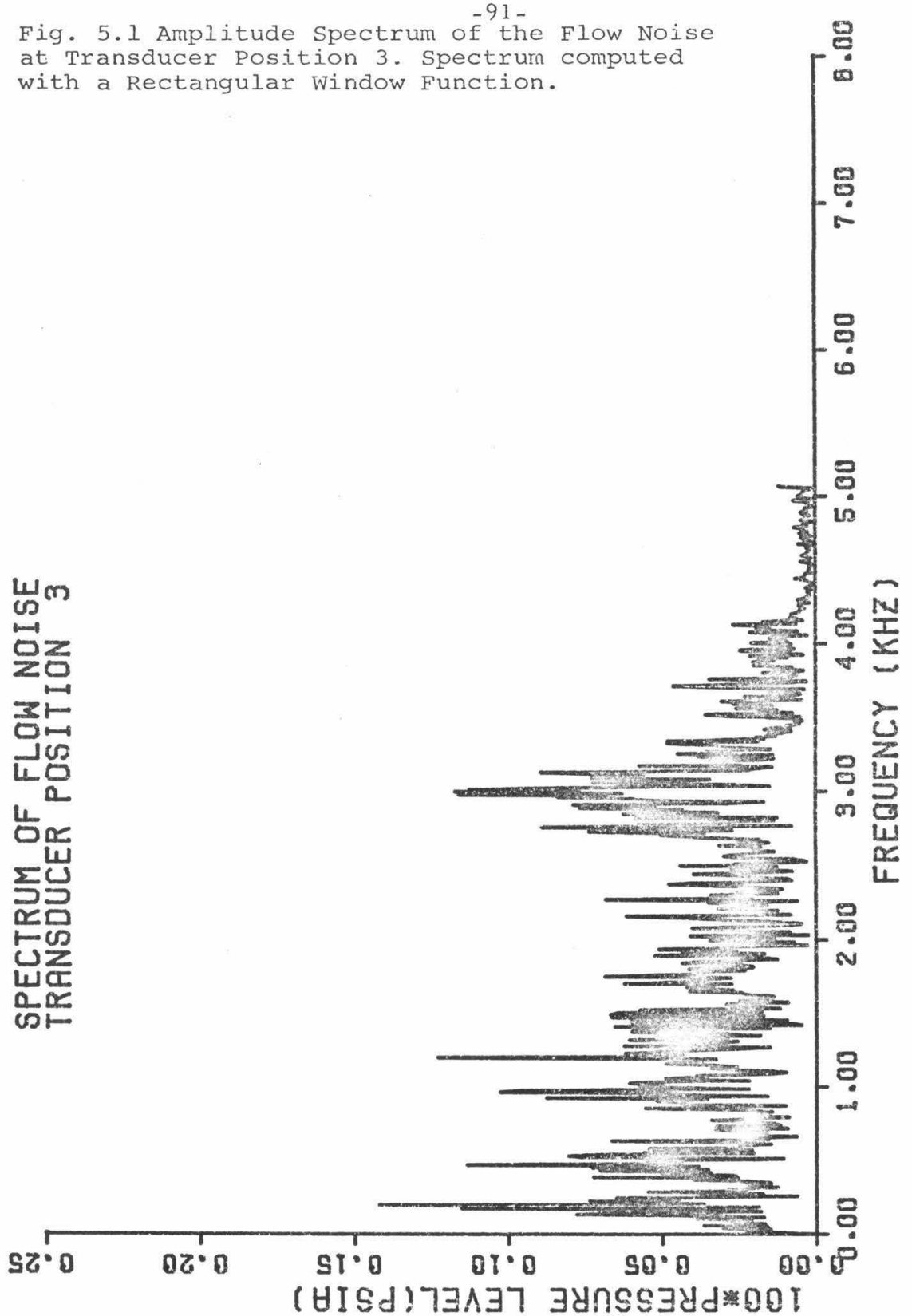

Fig. 5.2 Amplitude Spectrum on a Logarithmic Scale of the Flow Noise at Transducer Position 3. Spectrum computed with a Rectangular Window Function.

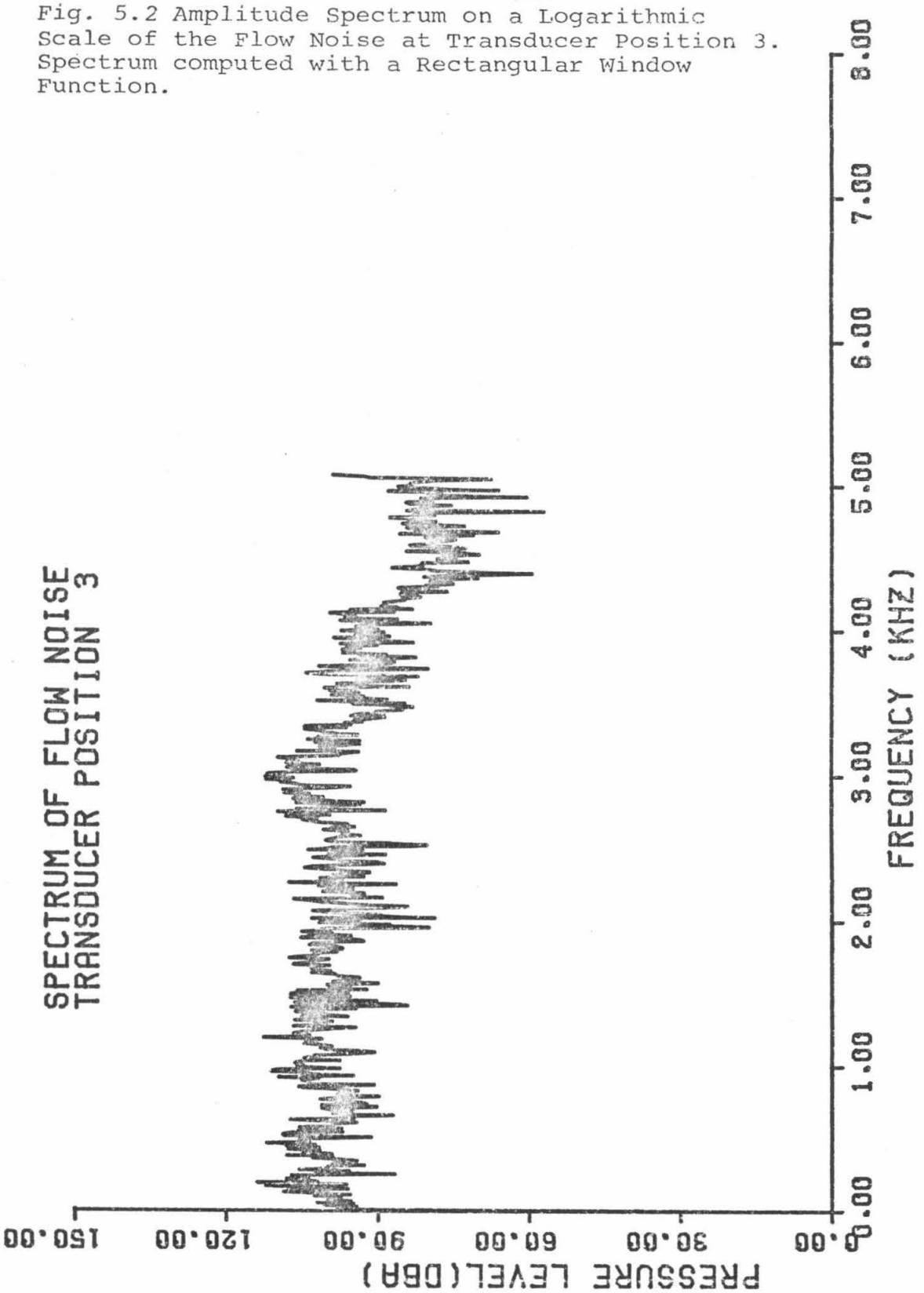

Fig. 5.3 Phase Spectrum of the Flow Noise at Transducer Position 3. Spectrum computed with a Rectangular Window Function.

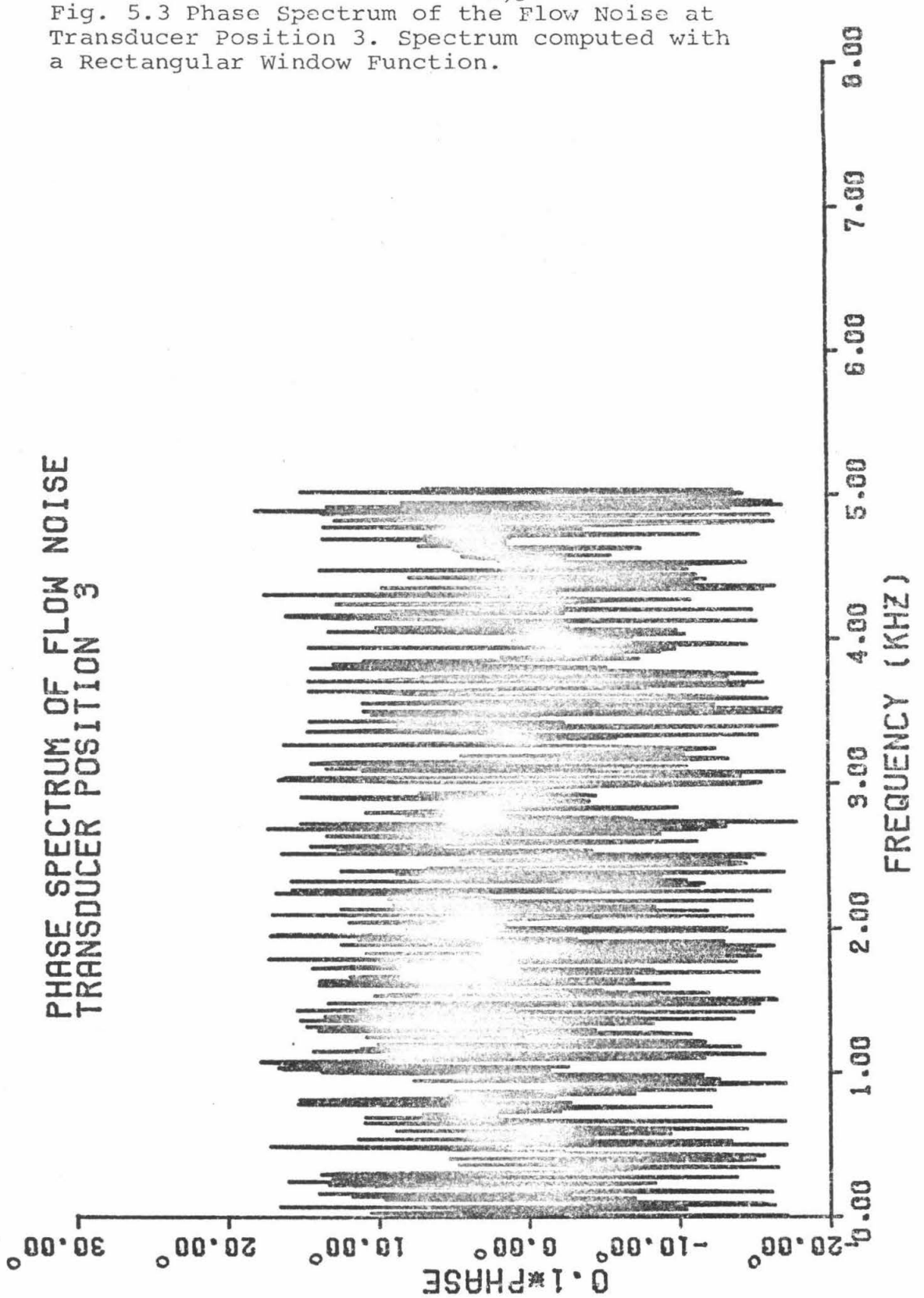

Fig. 5.4 Amplitude Spectrum of the Flow Noise at Transducer Position 5. Spectrum computed with a Rectangular Window Function.

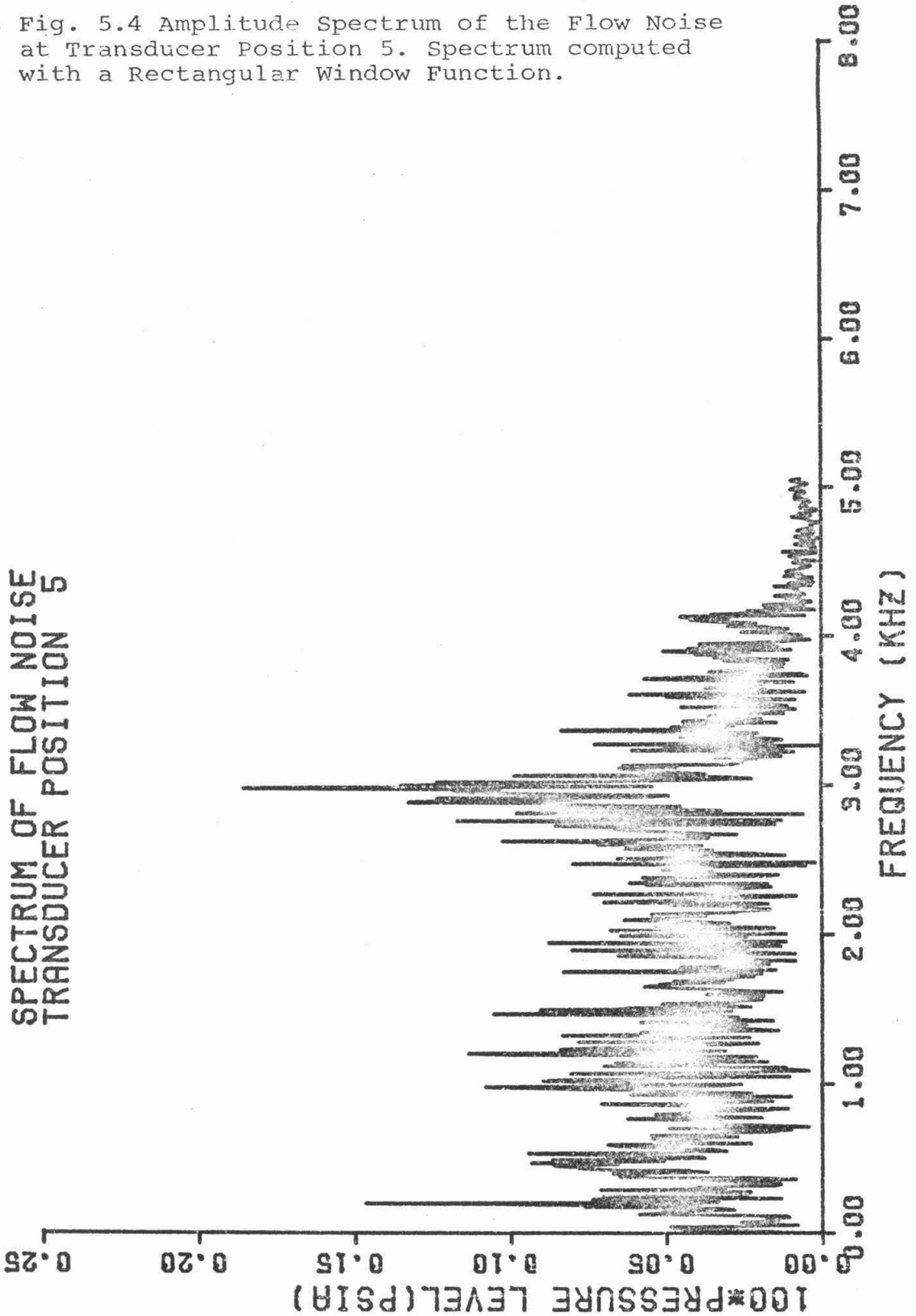

Fig. 5.5 Amplitude Spectrum on a Logarithmic Scale of the Flow Noise at Transducer Position 5. Spectrum computed with a Rectangular Window Function.

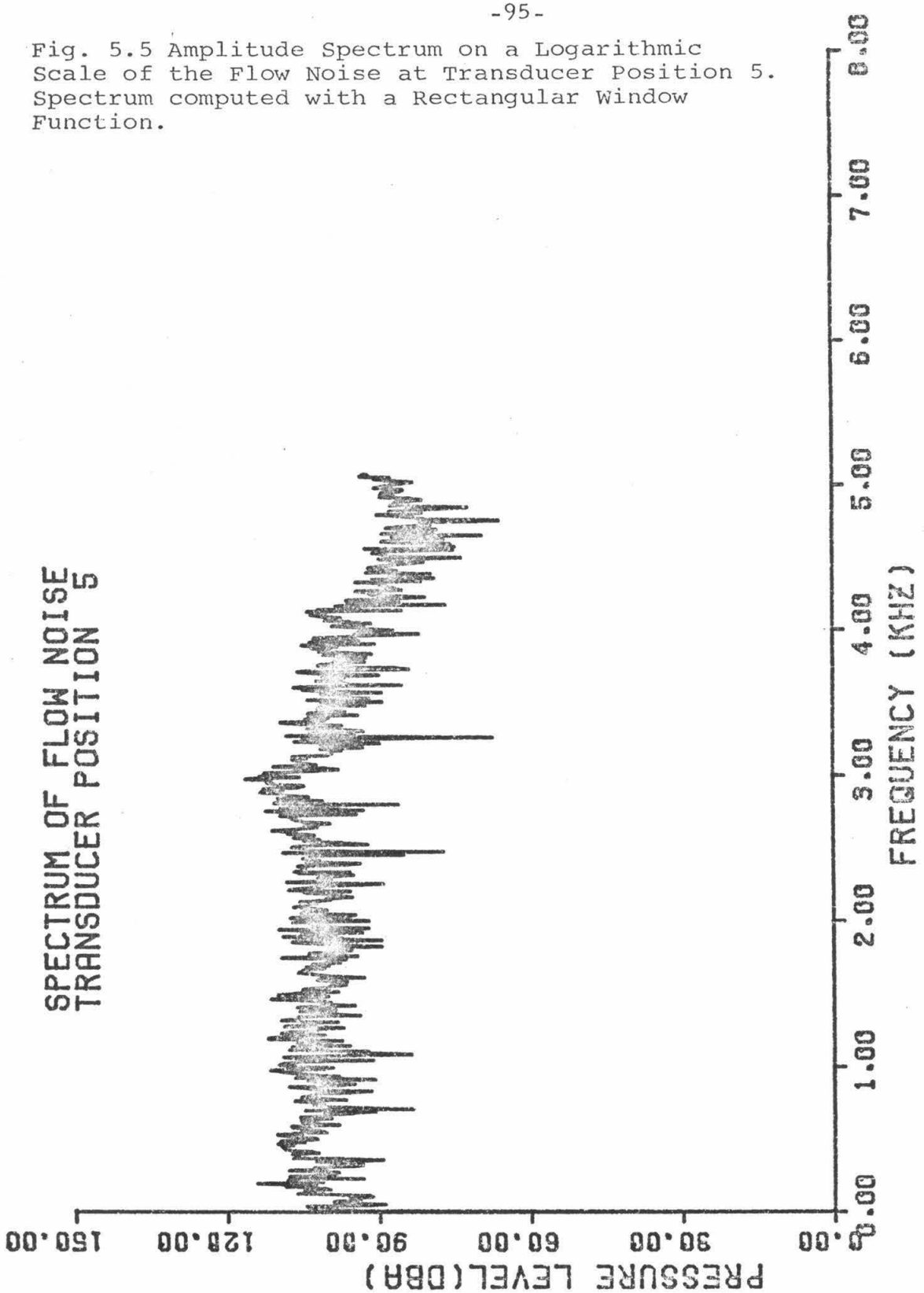

Fig. 5.6 Phase Spectrum of the Flow Noise at Transducer Position 5. Spectrum computed with a Rectangular Window Function.

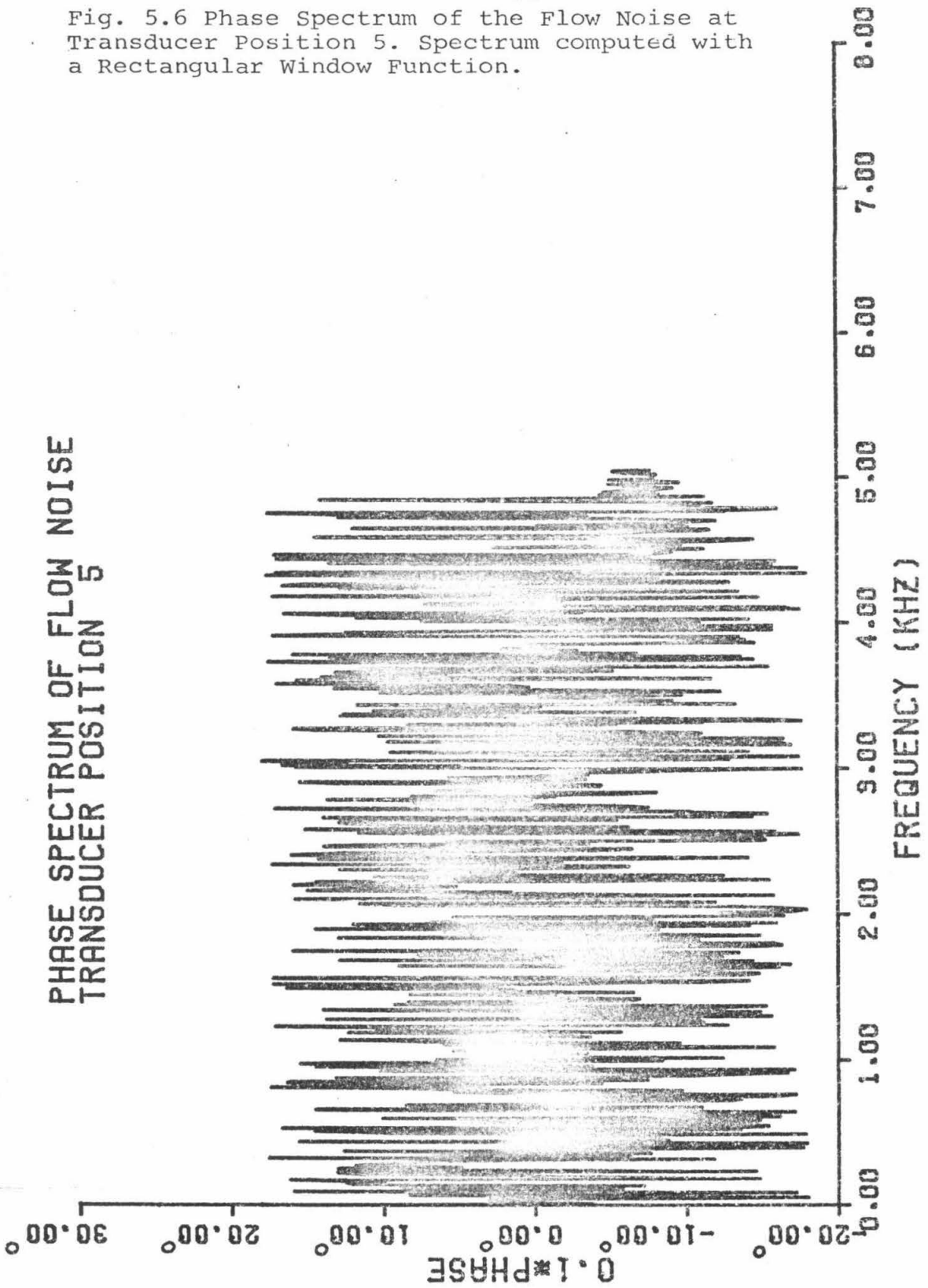

Fig. 5.7 Amplitude Spectrum of the Flow Noise at Transducer Position 7. Spectrum computed with a Rectangular Window Function.

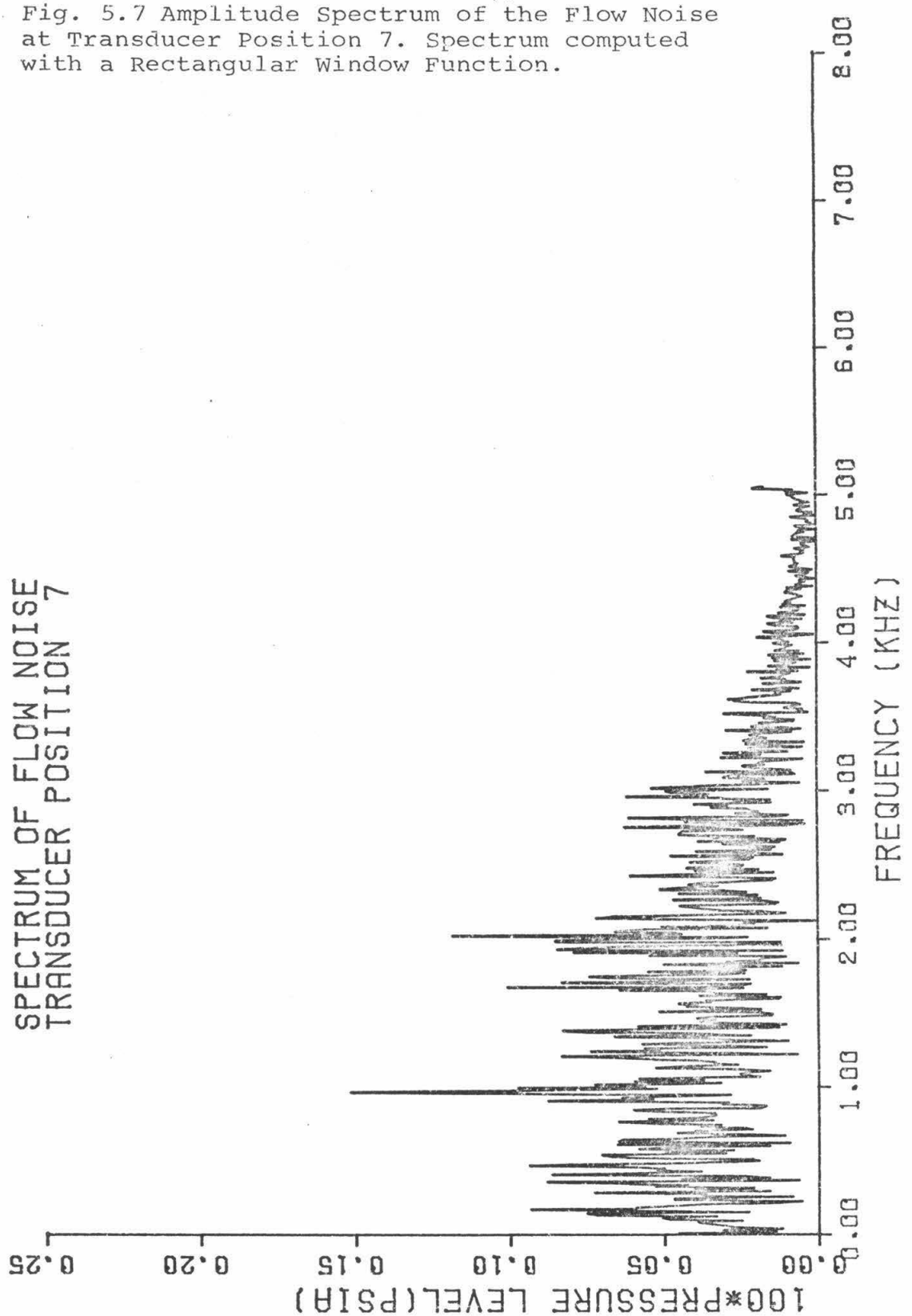

Fig. 5.8 Amplitude Spectrum on a Logarithmic Scale of the Flow Noise at Transducer Position 7. Spectrum computed with a Rectangular Window Function.

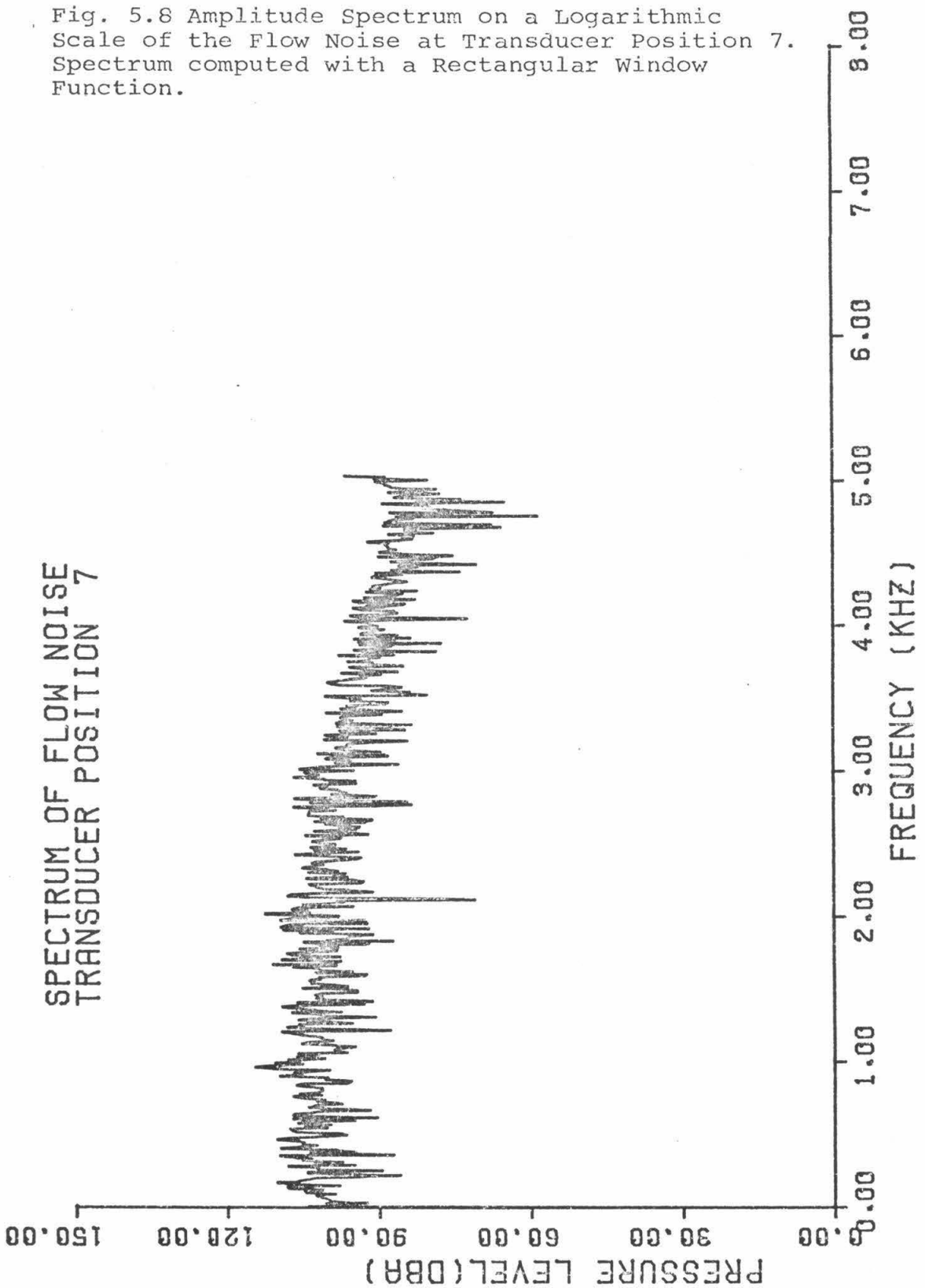

Fig. 5.9 Phase Spectrum of the Flow Noise at Transducer Position 7. Spectrum computed with a Rectangular Window Function.

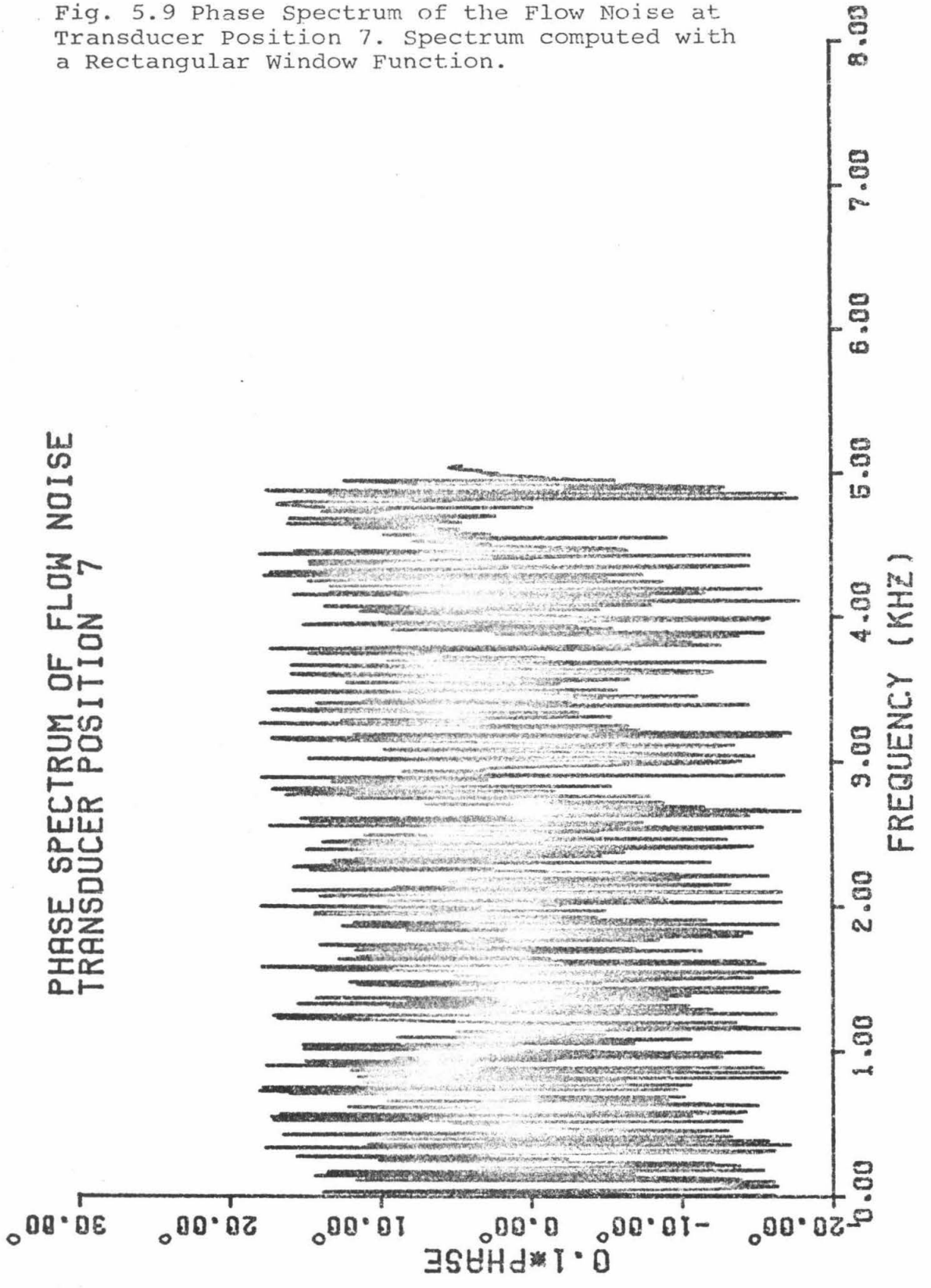

Fig. 5.10 Amplitude Spectrum of the Flow Noise at Transducer Position 3. Spectrum computed with a Hanning Window Function.

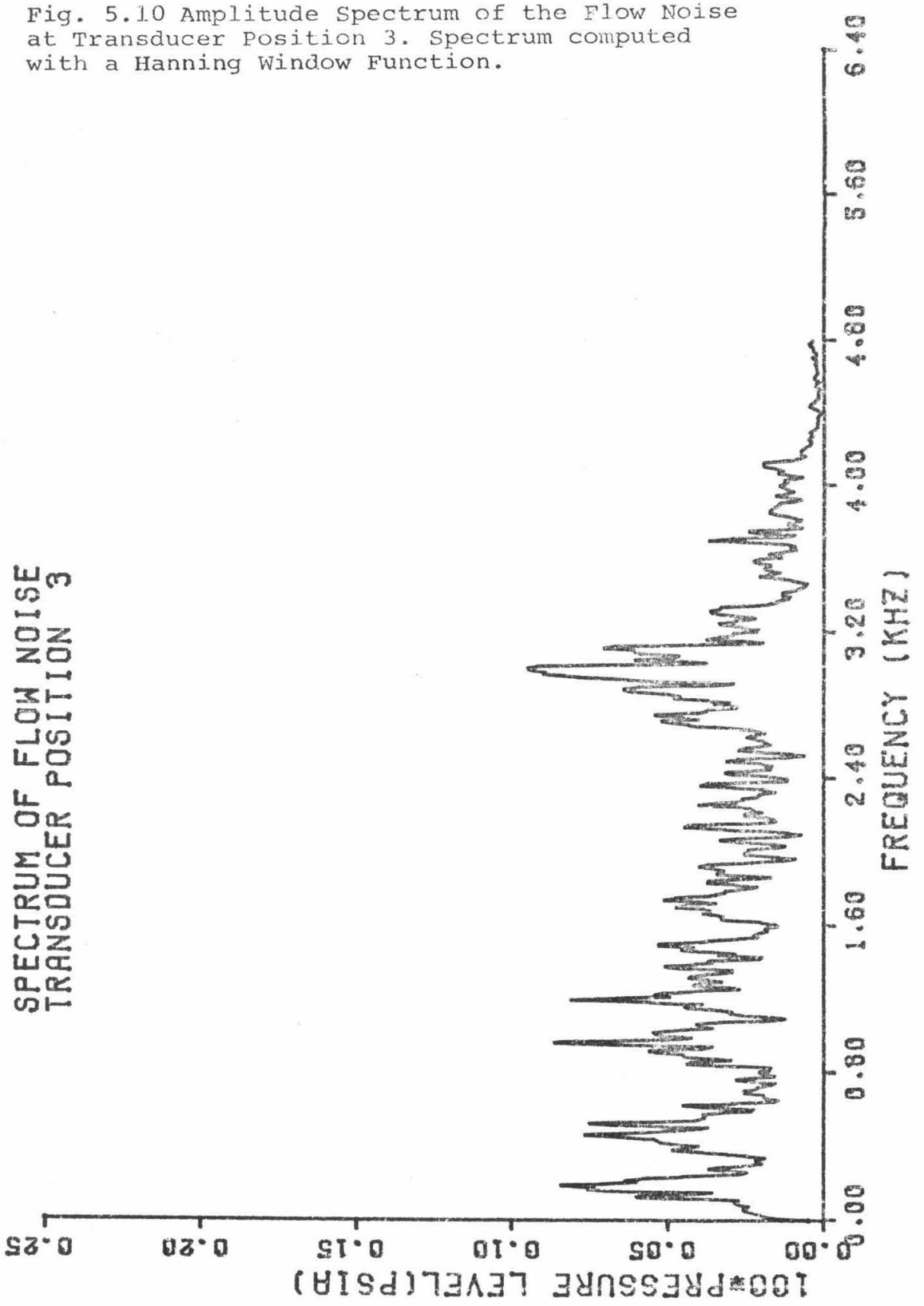

Fig. 5.11 Amplitude Spectrum on a Logarithmic Scale of the Flow Noise at Transducer Position 3. Spectrum computed with a Hanning Window Function.

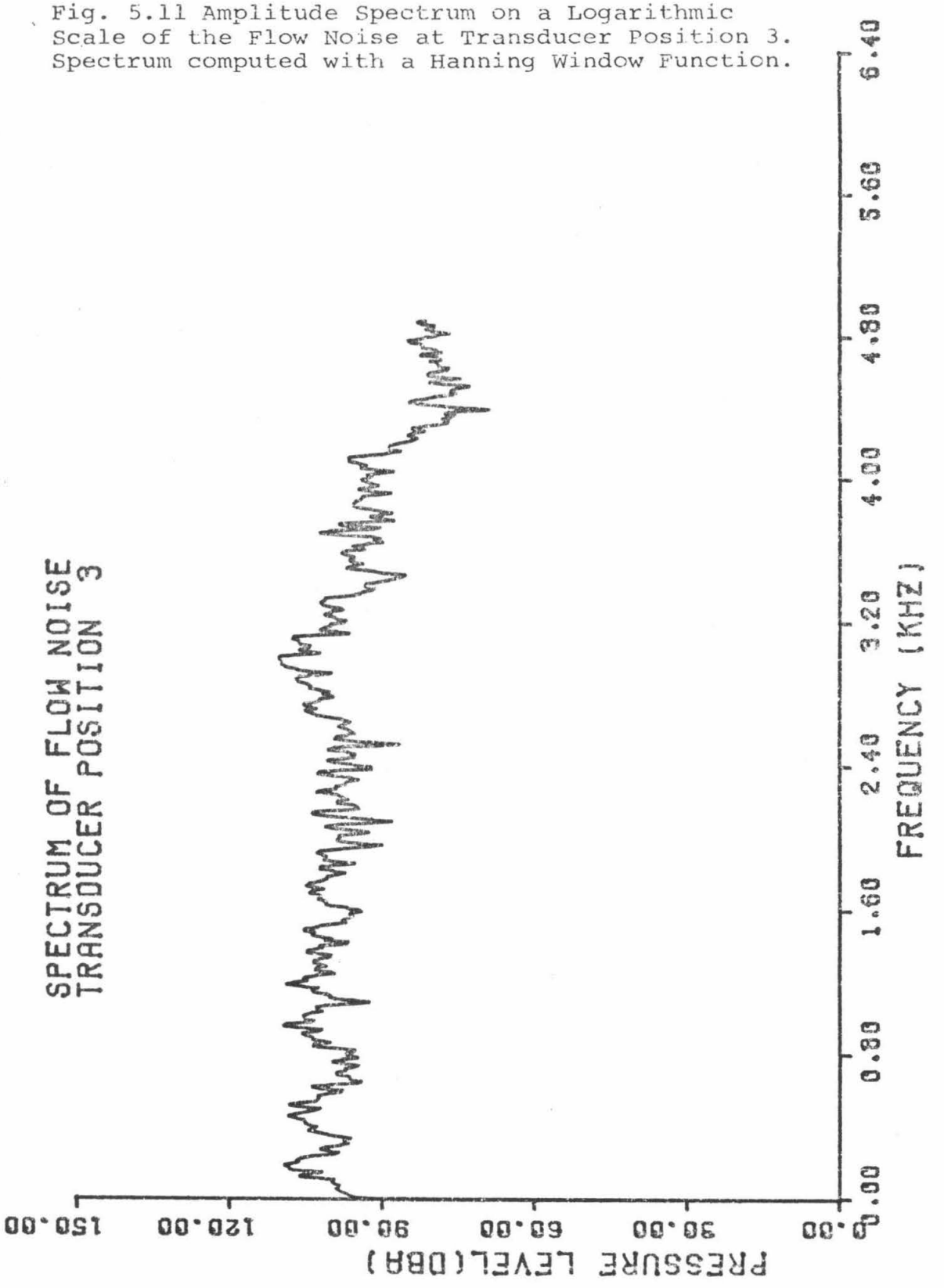

Fig. 5.12 Phase Spectrum of the Flow Noise at Transducer Position 3. Spectrum computed with a Hanning Window Function.

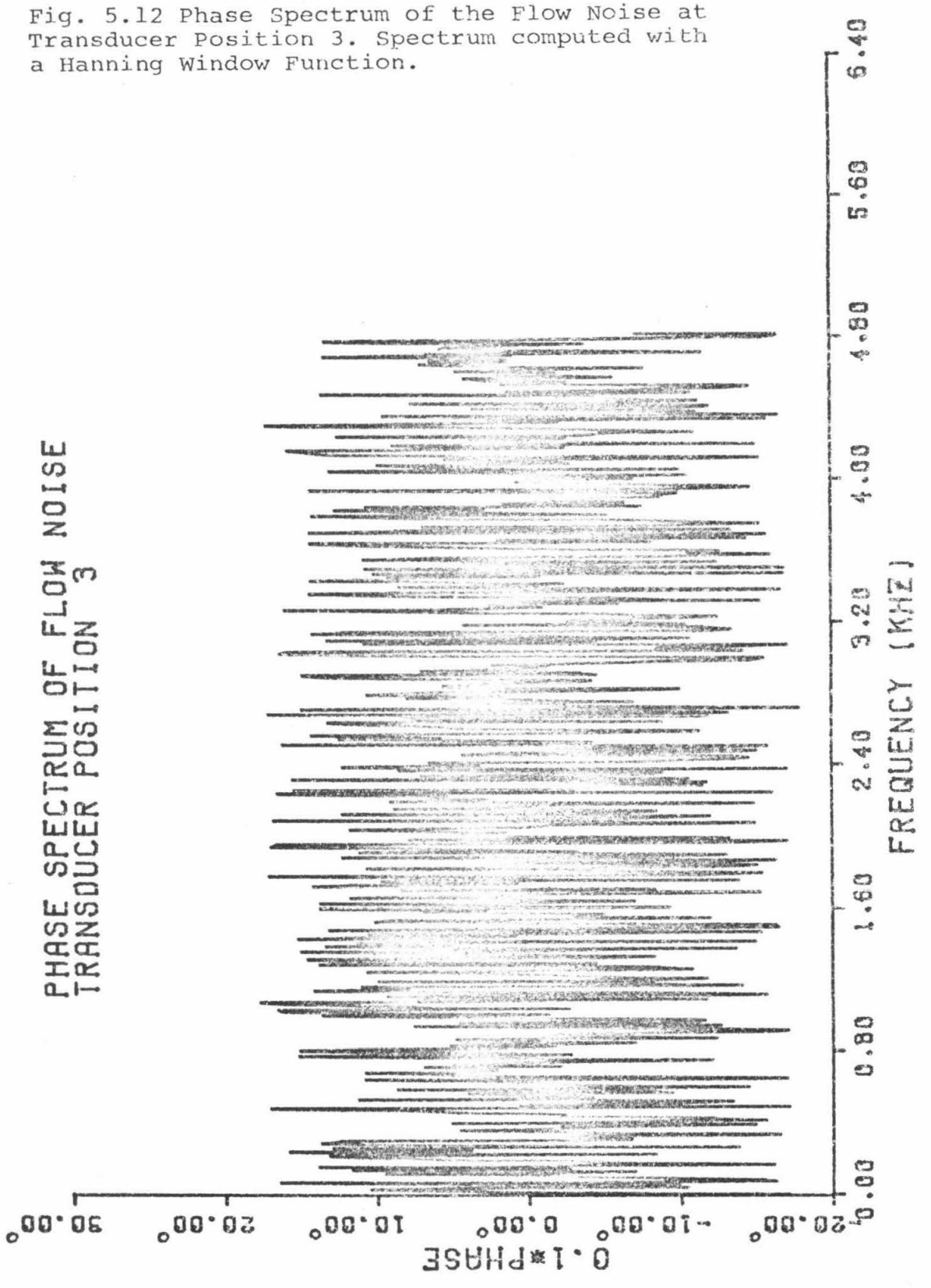

Fig. 5.13 Amplitude Spectrum of the Flow Noise at Transducer Position 5. Spectrum computed with a Hanning Window Function.

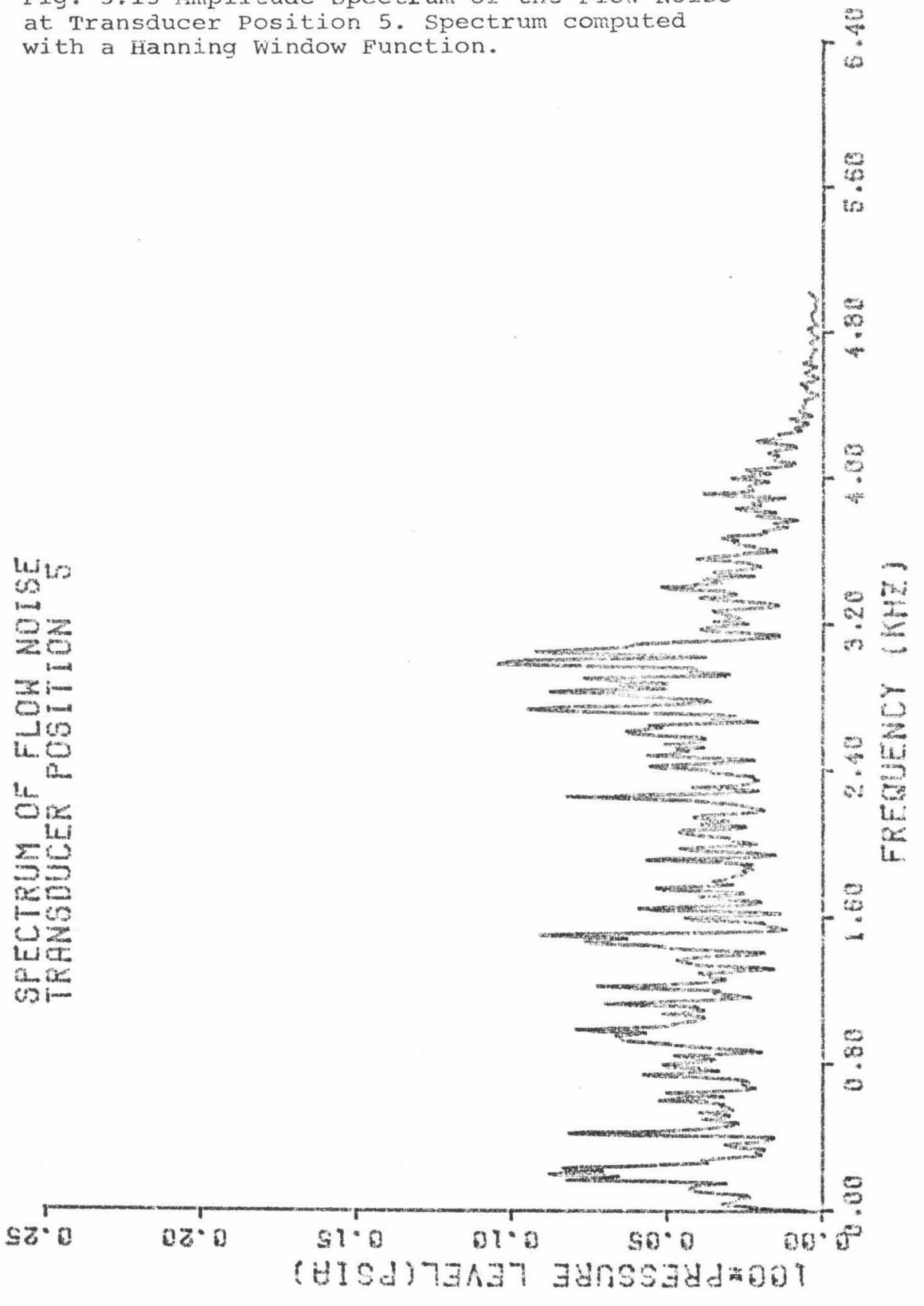

Fig. 5.14 Amplitude Spectrum on a Logarithmic Scale of the Flow Noise at Transducer Position 5. Spectrum computed with a Hanning Window Function.

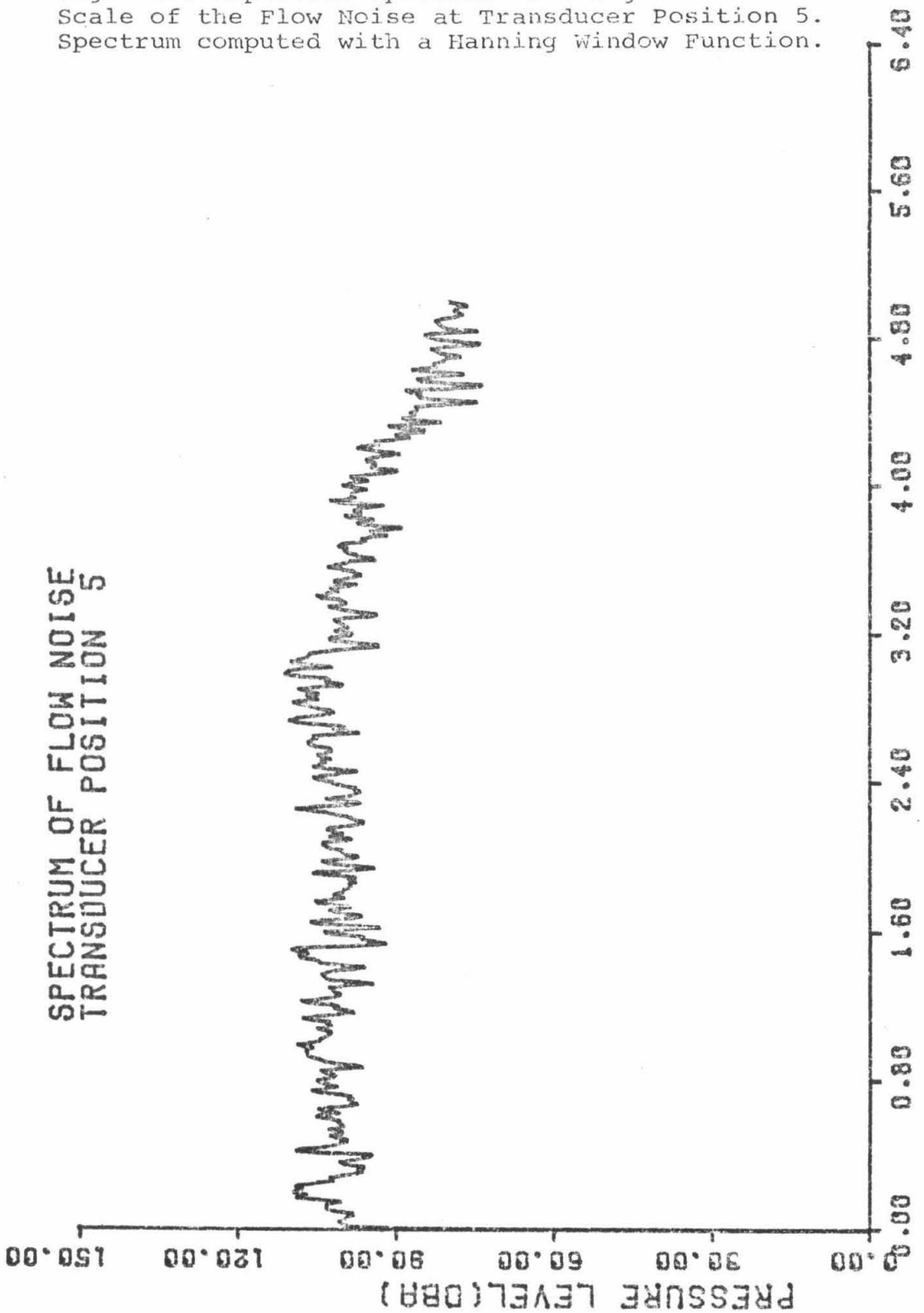

Fig. 5.15 Phase Spectrum of the Flow Noise at Transducer Position 5. Spectrum computed with a Hanning Window Function.

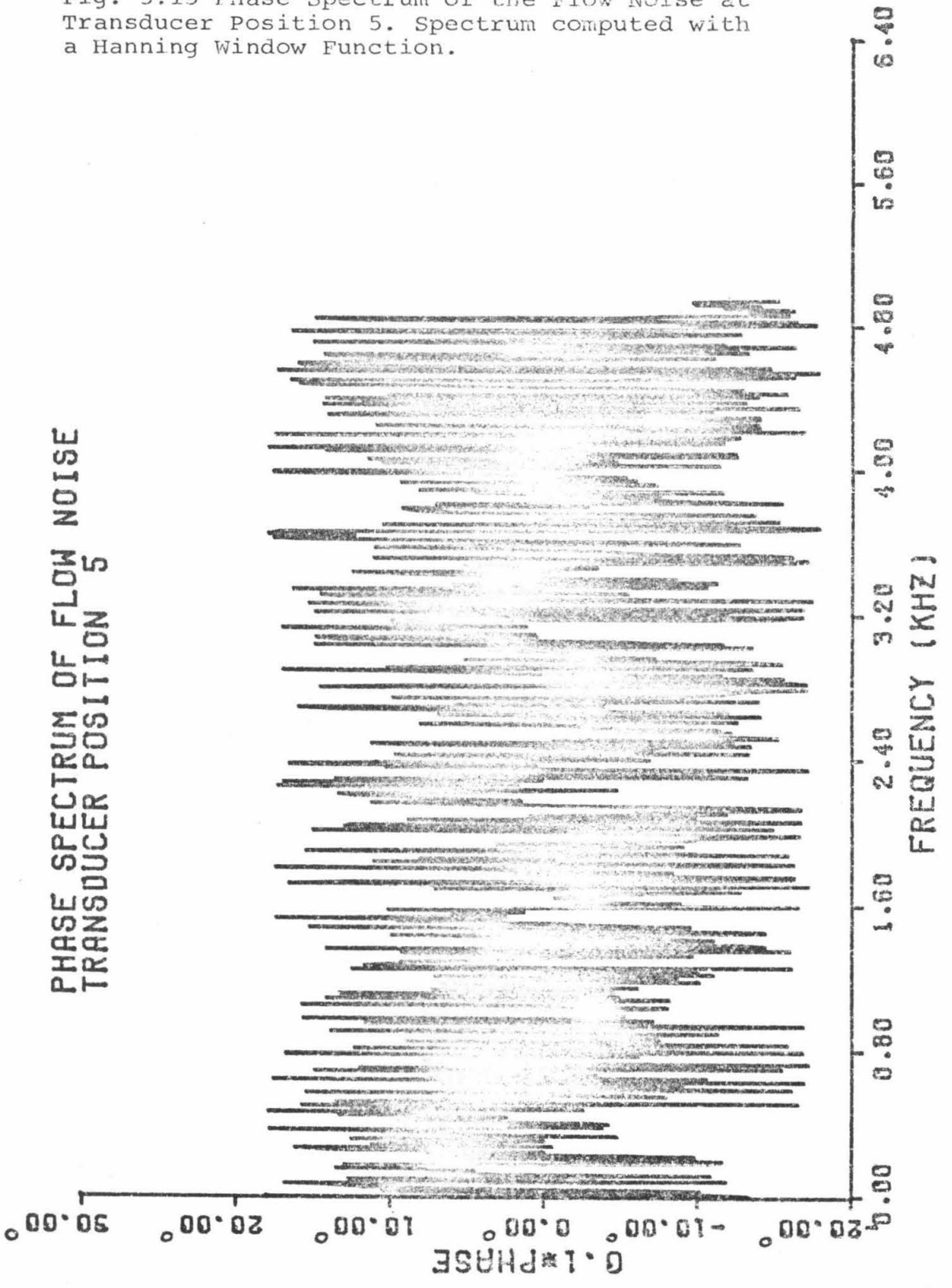

Fig. 5.16 Amplitude Spectrum of the Flow Noise at Transducer Position 7. Spectrum computed with a Hanning Window Function.

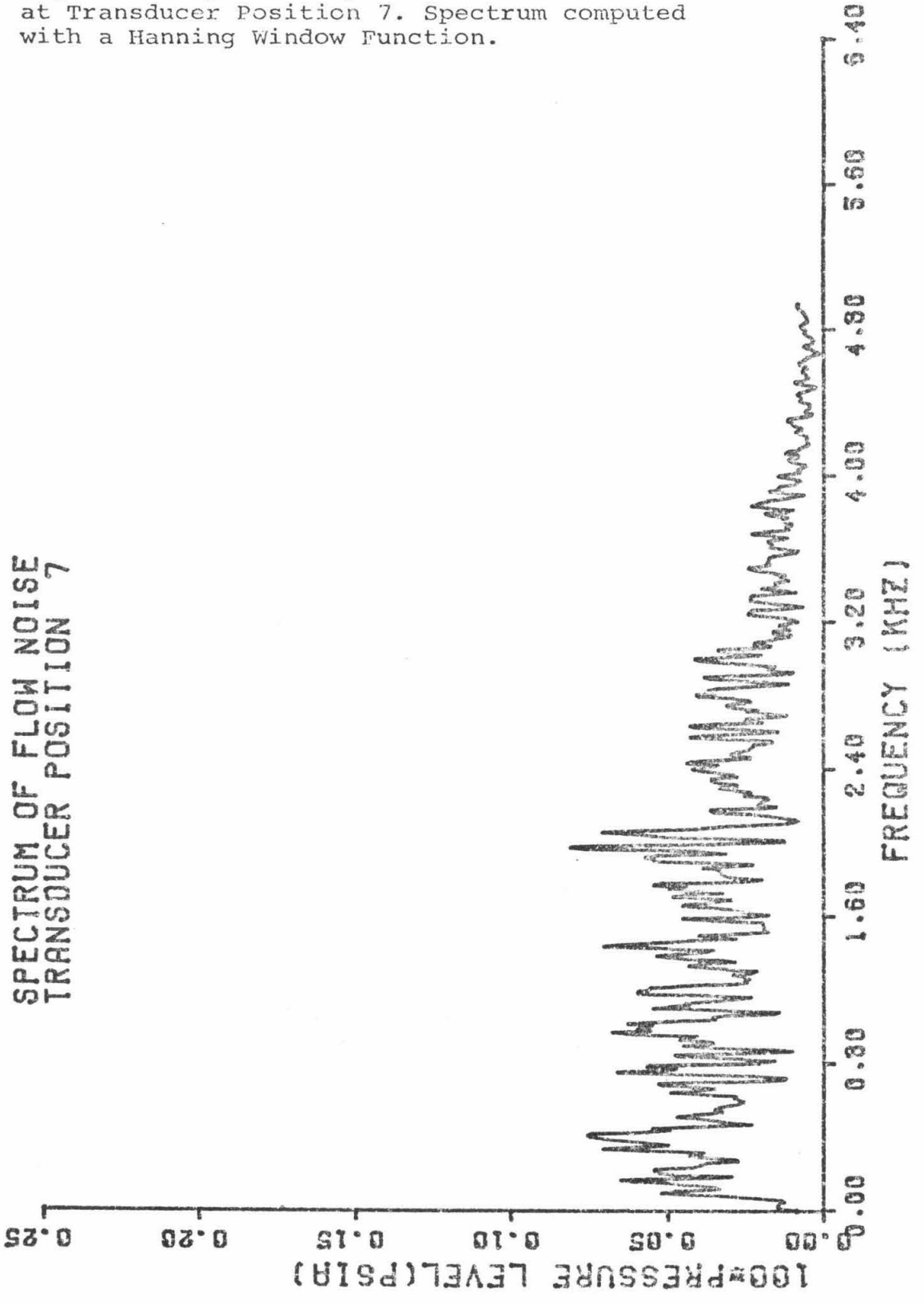

Fig. 5.17 Amplitude Spectrum on a Logarithmic Scale of the Flow Noise at Transducer Position 7. Spectrum computed with a Hanning Window Function.

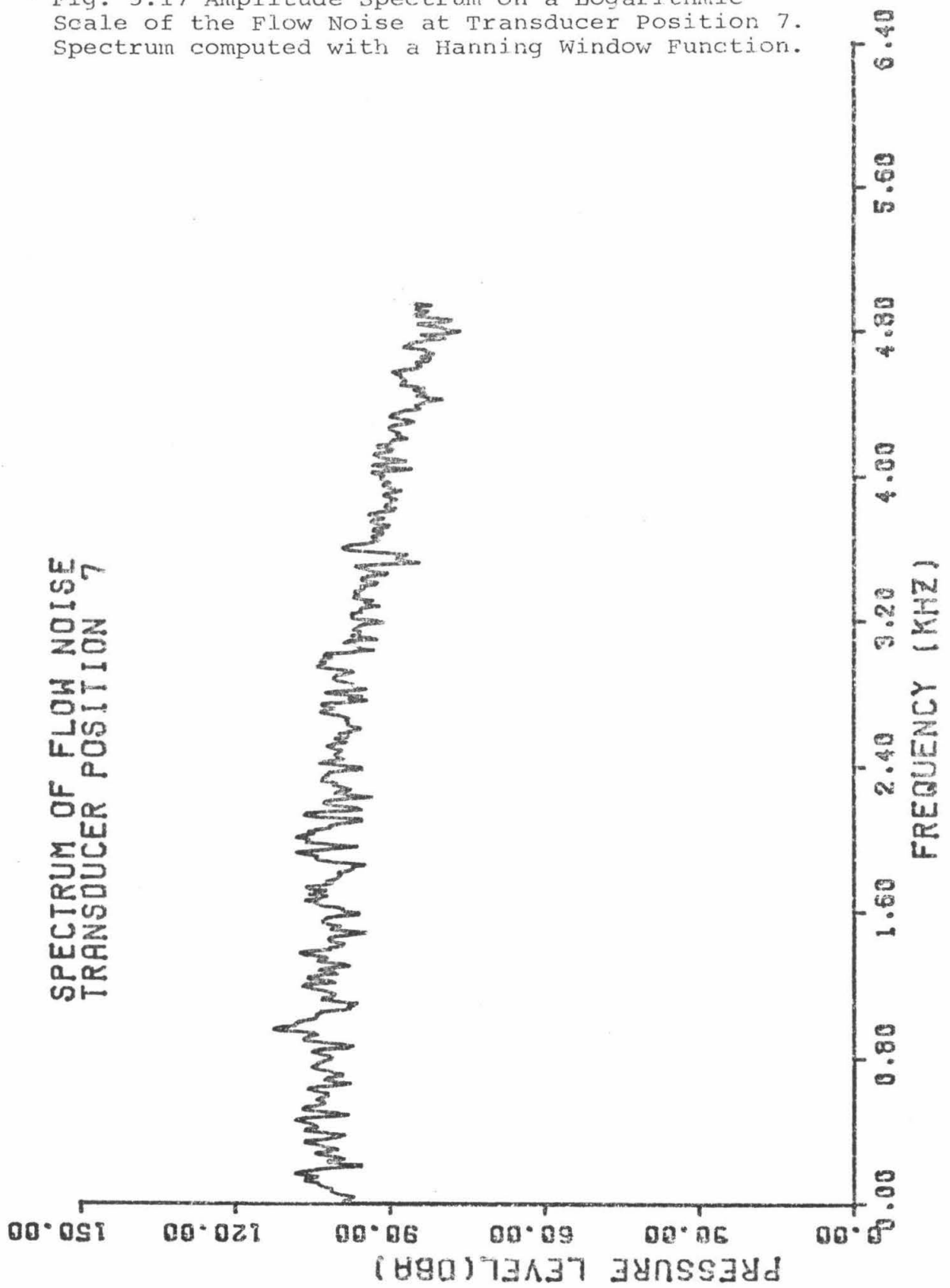

Fig. 5.18 Phase Spectrum of the Flow Noise at Transducer Position 7. Spectrum computed with a Hanning Window Function.

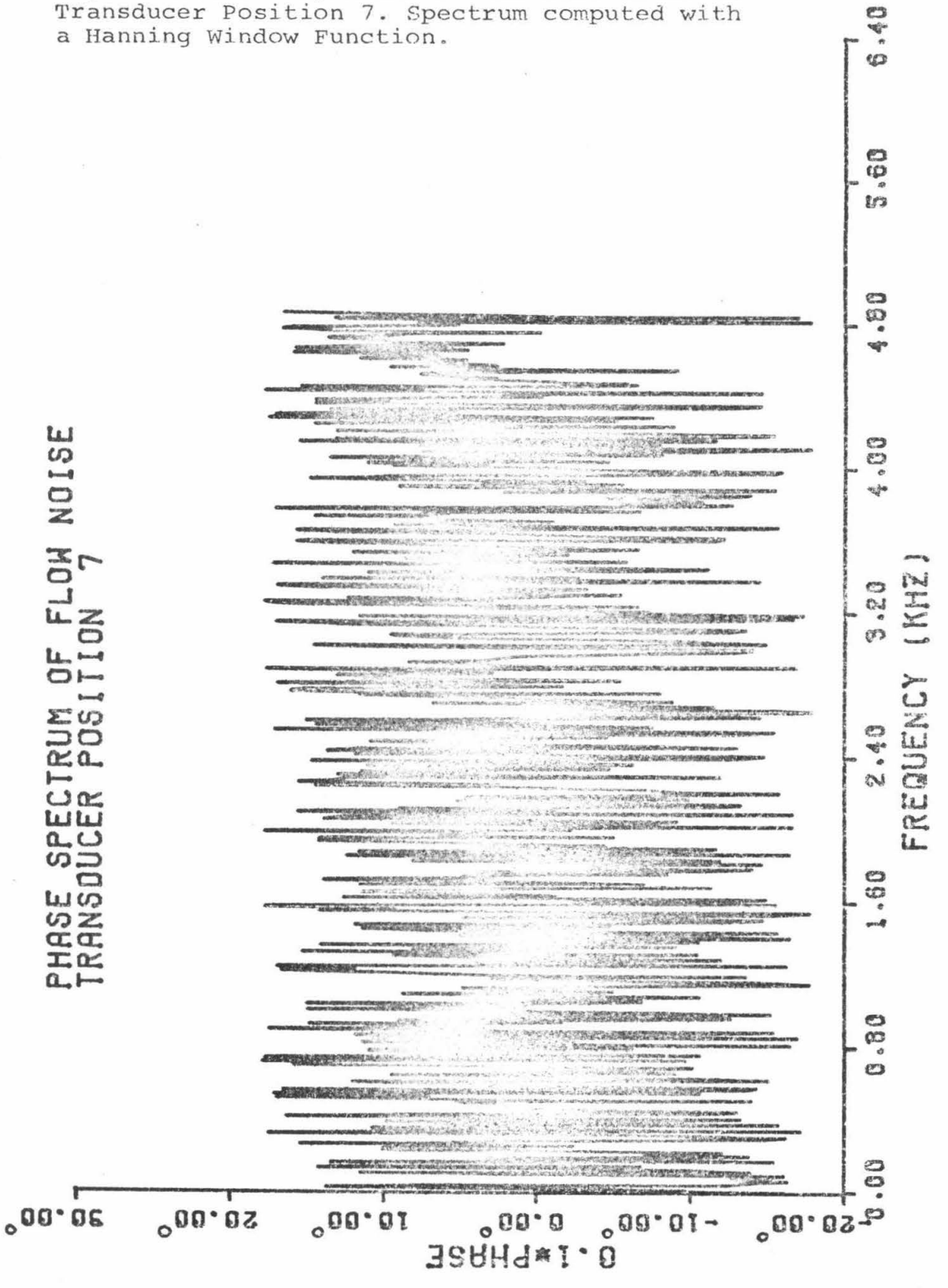

5.3 Effectiveness of the Signal-Averaging Process

5.3.1 R.M.S. Noise Level Reduction. Having ascertained the random nature of the flow noise, the next step was to determine how fast the average r.m.s. noise level decreased as digital records of noise were added. The question posed was specifically: would N additions of records give a new r.m.s. level greater than or less than the factor $1/\sqrt{N}$ predicted for ideal Gaussian white noise? To investigate this question, 100 records of 1024 digital words were taken of the flow noise at transducer position 3 and also of the external jet noise at 3 ft. from the nozzle exit. The A/D converter was started each time by the self-running pulse generator described in Chapter III. The heater and bleed valve were inactive, so the generator only provided a periodic "enable" signal for the A/D converter. Various groups of records were added, and then divided by the number of records in that group. The r.m.s. value of each resultant record was then calculated and then divided by the r.m.s. value of one record. The results are shown in fig. 5.19. The abscissa indicates the number of additions, N. The straight line drawn indicates the $1/\sqrt{N}$ relationship on a log-log plot. The digital averaging process shows excellent agreement with the random noise theory of Chapter IV. Conclusions at this point in the experiment were that the signal-averaging process was operational and well understood.

5.3.2 Signal-averaged waveforms. This section will show the increase of signal noise ratio for the pressure fluctuations produced by the bleed valve and pulse heater. The first sequence of waveforms (figs. 5.20 to 5.24) are for the pressure fluctuation at

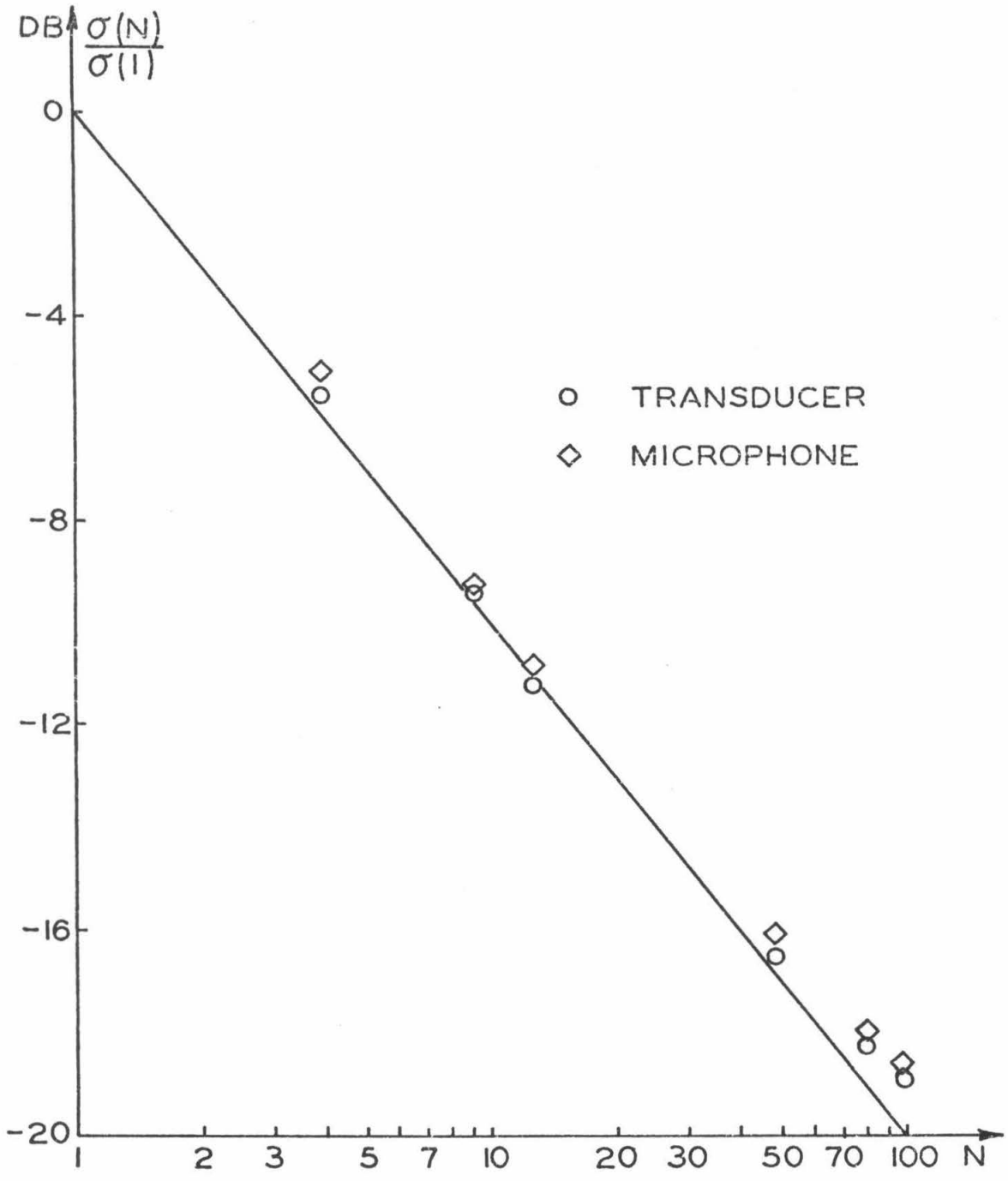

Fig. 5.19 Effectiveness of the Signal Averaging Process

transducer position 3 produced by the bleed valve run at 400 Hz and with a 7/64-in. diameter orifice setting the magnitude of the bleed flow. Figure 5.20 shows one half of the 1024 digital record for one data acquisition cycle. Sampling rate was 20 KHz. Without previous indications, the 400 Hz waveform is indistinguishable from the noise. A Fourier analysis on this waveform using the formulas (4.33) and (4.34) would result in large numerical errors. Taking a Fourier integral of several of these records juxtaposed to reduce the noise is also infeasible because adjacent records would have to be phase matched. This is impossible because the phase of the 400 Hz bleed valve signal cannot be discerned in the noise background. Figure 5.21 shows 25 records added. For each record, the A/D converter was started at the time the phototransistor circuit gave maximum output, so the records always start at the same phase of the bleed flow. Note that the 400 Hz bleed valve signal is now clearly distinguishable, but there is still some low-frequency noise modulation of the 400 Hz signal. In fig. 5.22, for 49 signal-averaging operations, there is still a small amount of low frequency noise. In figs. 5.23 and 5.24, the amplitude of the 400 Hz signal is constant for 64 and 100 signal-averaging operations, respectively. From these figures, it can also be seen that at 400 Hz the bleed wave does not produce a pure 400 Hz signal but there is some distortion due to the harmonics at 1600 Hz and 2000 Hz. Hence, the data show that the signal-averaging process used here does an excellent signal extraction operation. Thus, a digital acquisition system with a relatively inexpensive and compact interface (signal-averaging control device, section 3.6.2) can do the work of several

Fig. 5.20 Pressure Fluctuation Waveform at the Nozzle Entrance during Operation of the Bleed Valve at a frequency of 400 HZ. No signal averaging has been applied.

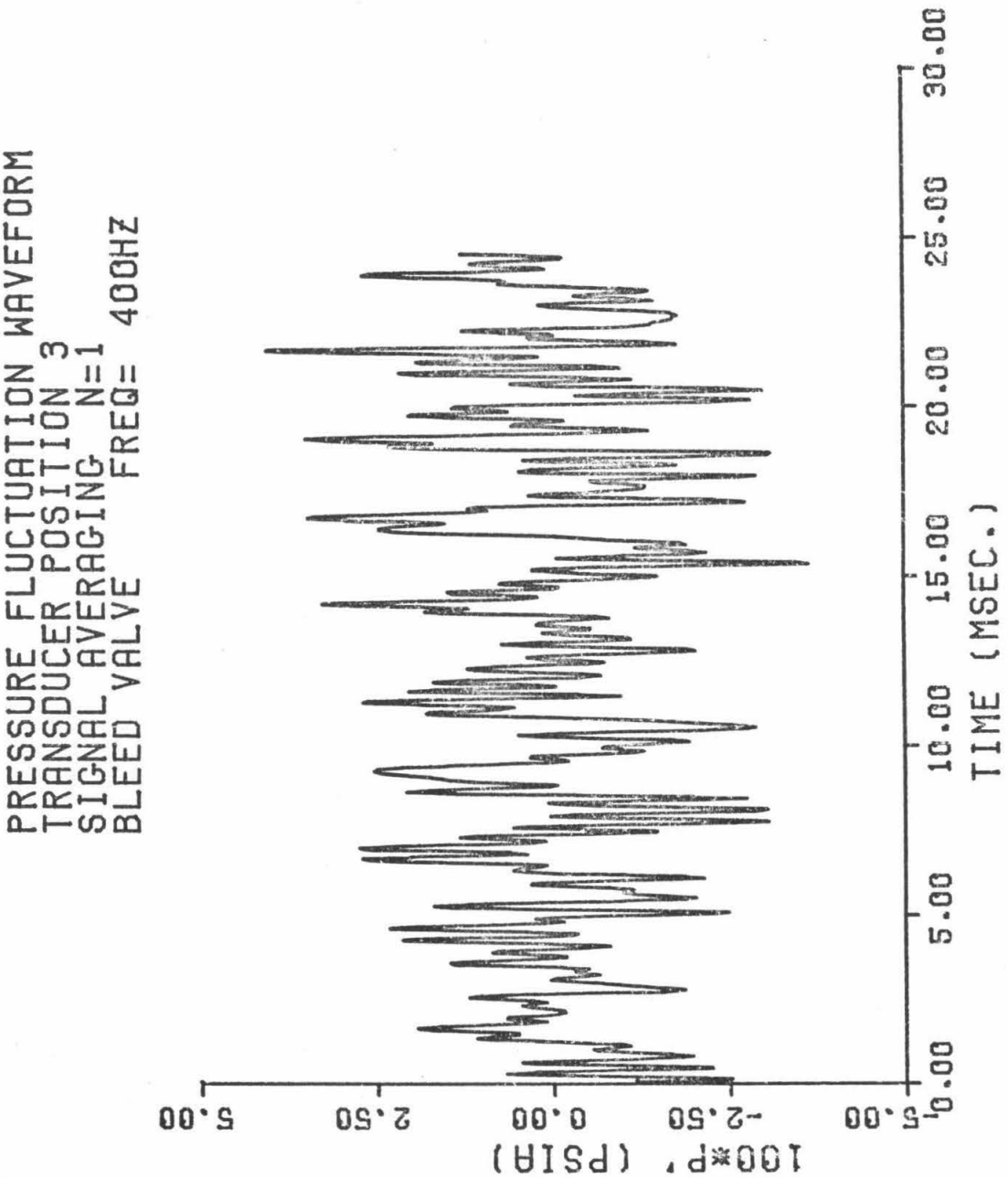

Fig. 5.21 Pressure Fluctuation Waveform obtained by addition of 25 digital records of the pressure fluctuation at the nozzle entrance during operation of the bleed valve at a frequency of 400 HZ.

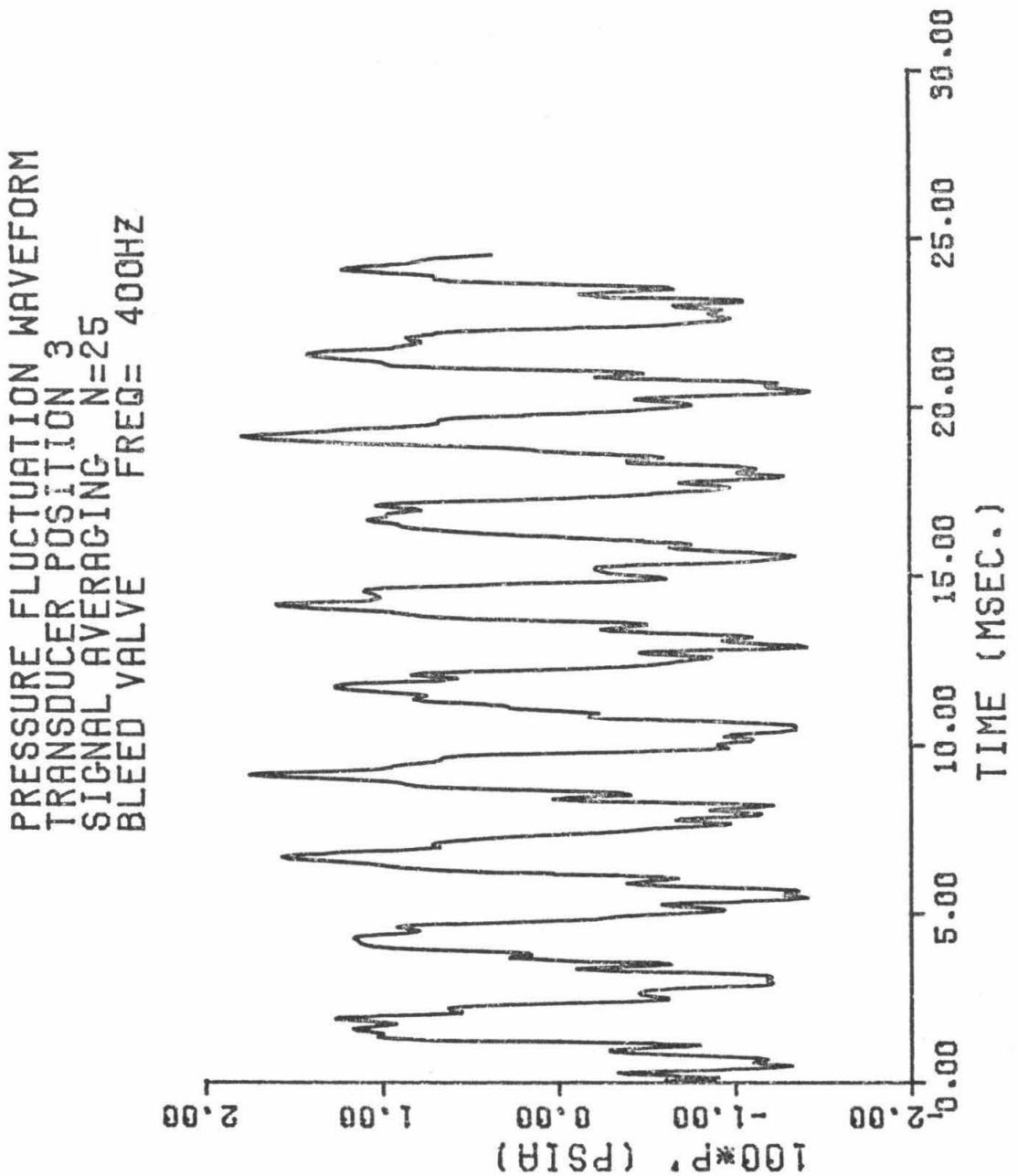

Fig. 5.22 Pressure Fluctuation Waveform obtained by addition of 49 digital records of the pressure fluctuation at the nozzle entrance during operation of the bleed valve at a frequency of 400 HZ.

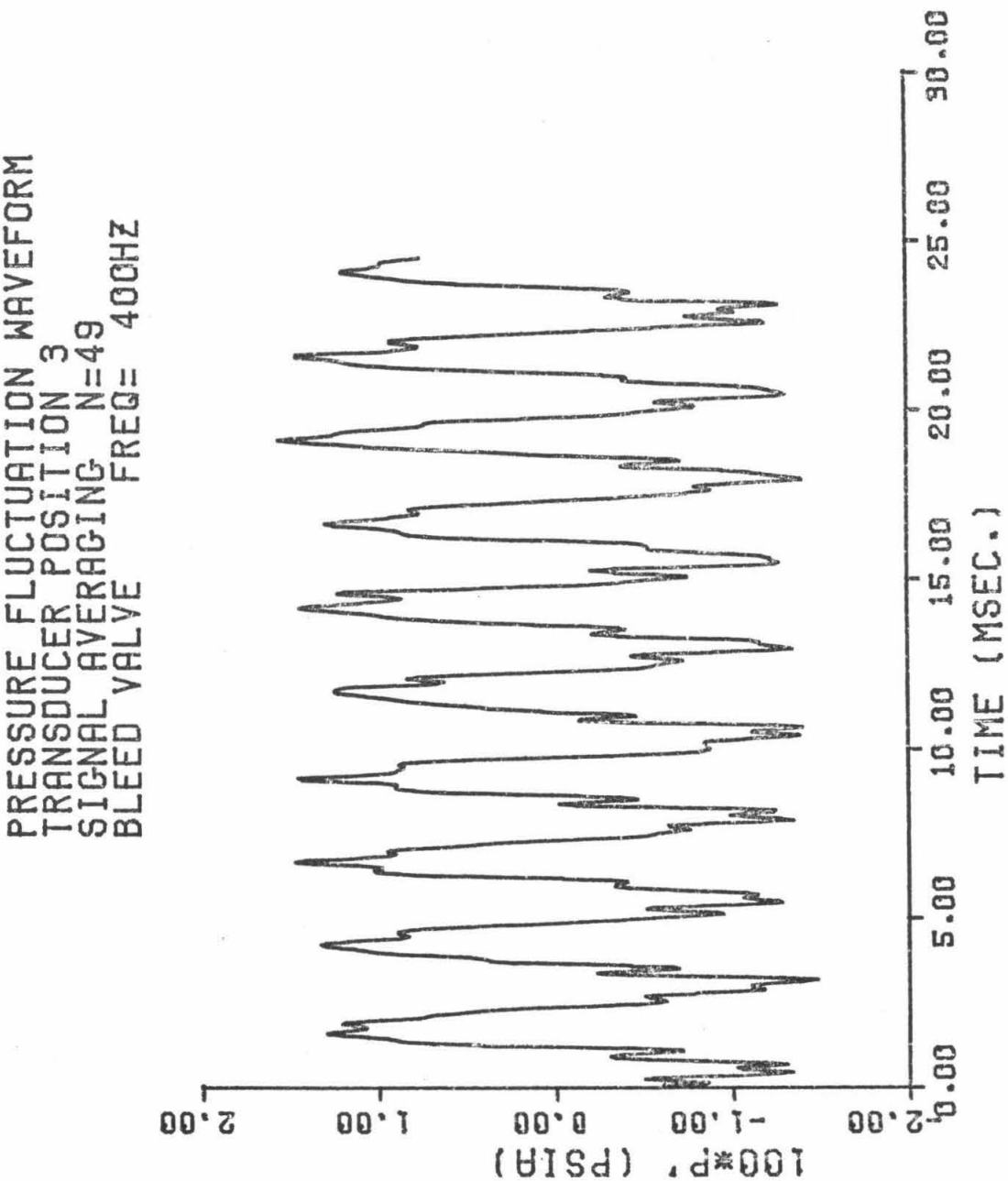

Fig. 5.23 Pressure Fluctuation Waveform obtained by addition of 64 digital records of the pressure fluctuation at the nozzle entrance during operation of the bleed valve at a frequency of 400 HZ.

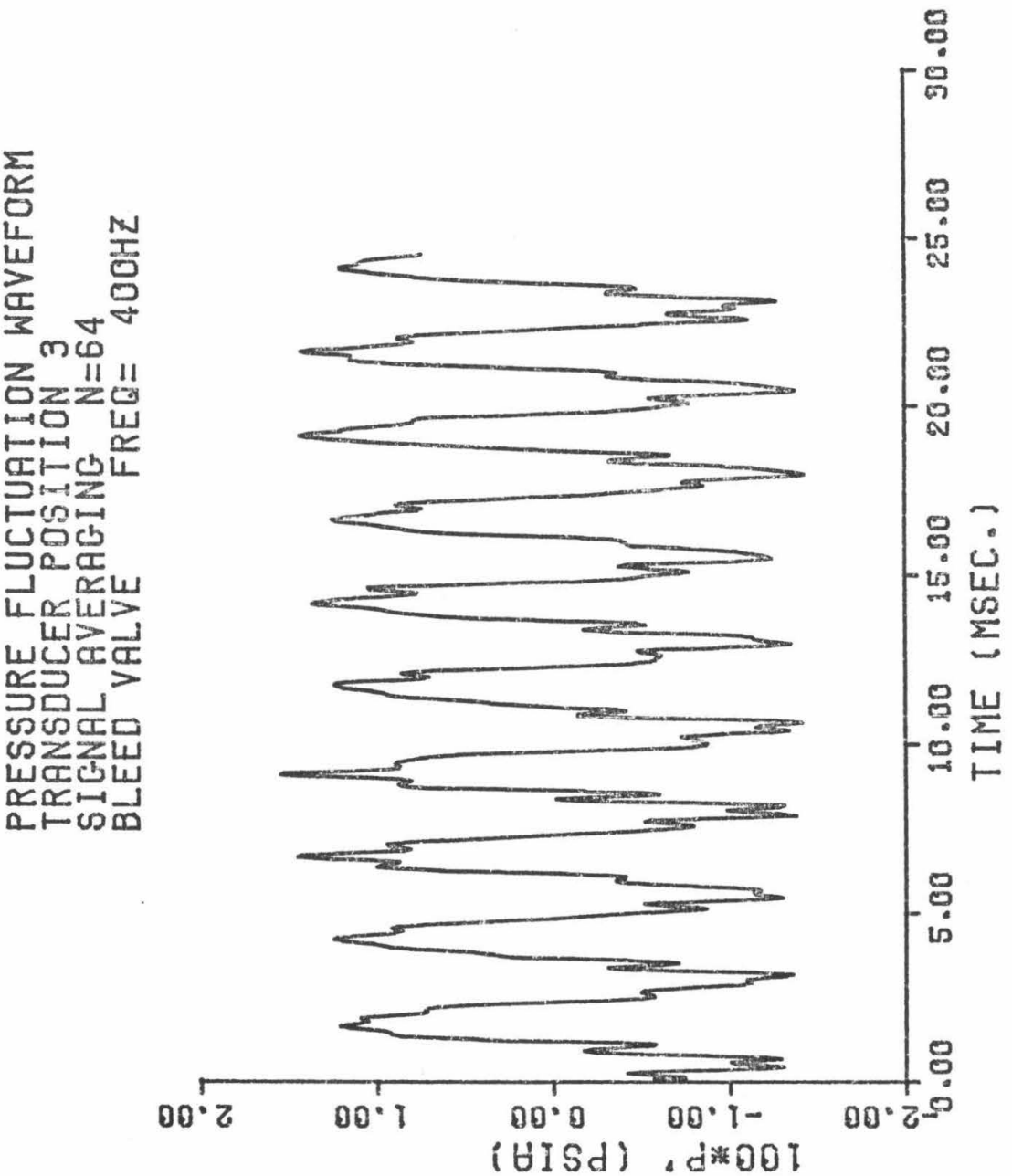

Fig. 5.24 Pressure Fluctuation Waveform obtained by addition of 100 digital records of the pressure fluctuation at the nozzle entrance during operation of the bleed valve at a frequency of 400 HZ.

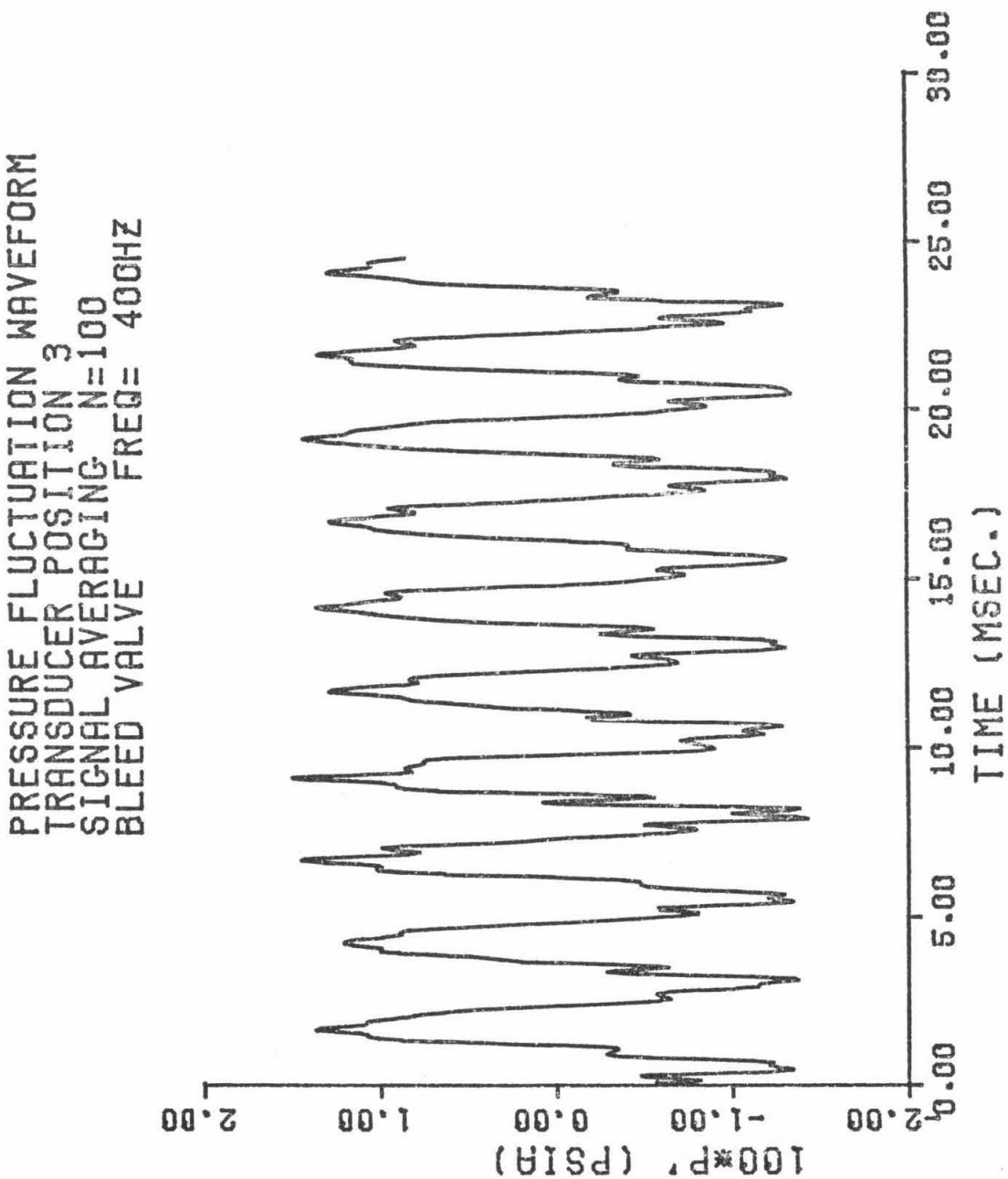

"lock-in amplifiers."

Figures 5.25 and 5.26 show the results of 100 signal-averaging operations on the pulse heater produced pressure fluctuations at the nozzle exit (transducer position 7) for frequencies of 250 Hz and 500 Hz, respectively. The waveform of fig. 5.25 still contains a small amount of high-frequency noise. This noise is reduced in effect when the Fourier integral is computed over the large numbers of cycles in the record. Figure 5.26 shows that pressure waveform at 500 Hz contains a large amount of noise, even though close examination of the waveform shows a strong 500 Hz component. A Fourier analysis of this waveform also indicated a large 500 Hz component, implying that the high-frequency noise cancelled in the computation of the Fourier coeffecient taken over a large number of cycles at 500 Hz. Still, the large amount of noise indicated that the heater was losing its effectiveness at 500 Hz and that the upper heater frequency for experiments should be set at 500 Hz.

Having noted the sharpness of the signal-averaged waveforms in the time domain, it is also of interest to look at their sharpness in the frequency domain. This is best accomplished by looking at a small portion of the spectrum of the waveform centered about the bleed valve or heater frequency. By "small" is meant one or two spectrum frequency increments on either side of the valve or heater frequency. Figures 5.27 and 5.28 are two examples of these local spectra. Each graph was developed as follows.

(i) Figure 5.27: The bleed valve was run at 400 Hz and a 1024-word data record was made at a sampling rate of 40 KHz.

Fig. 5.25 Pressure Fluctuation Waveform obtained by addition of 100 digital records of the pressure fluctuation at the nozzle exit during operation of the thermal pulse heater at a frequency of 250 HZ.

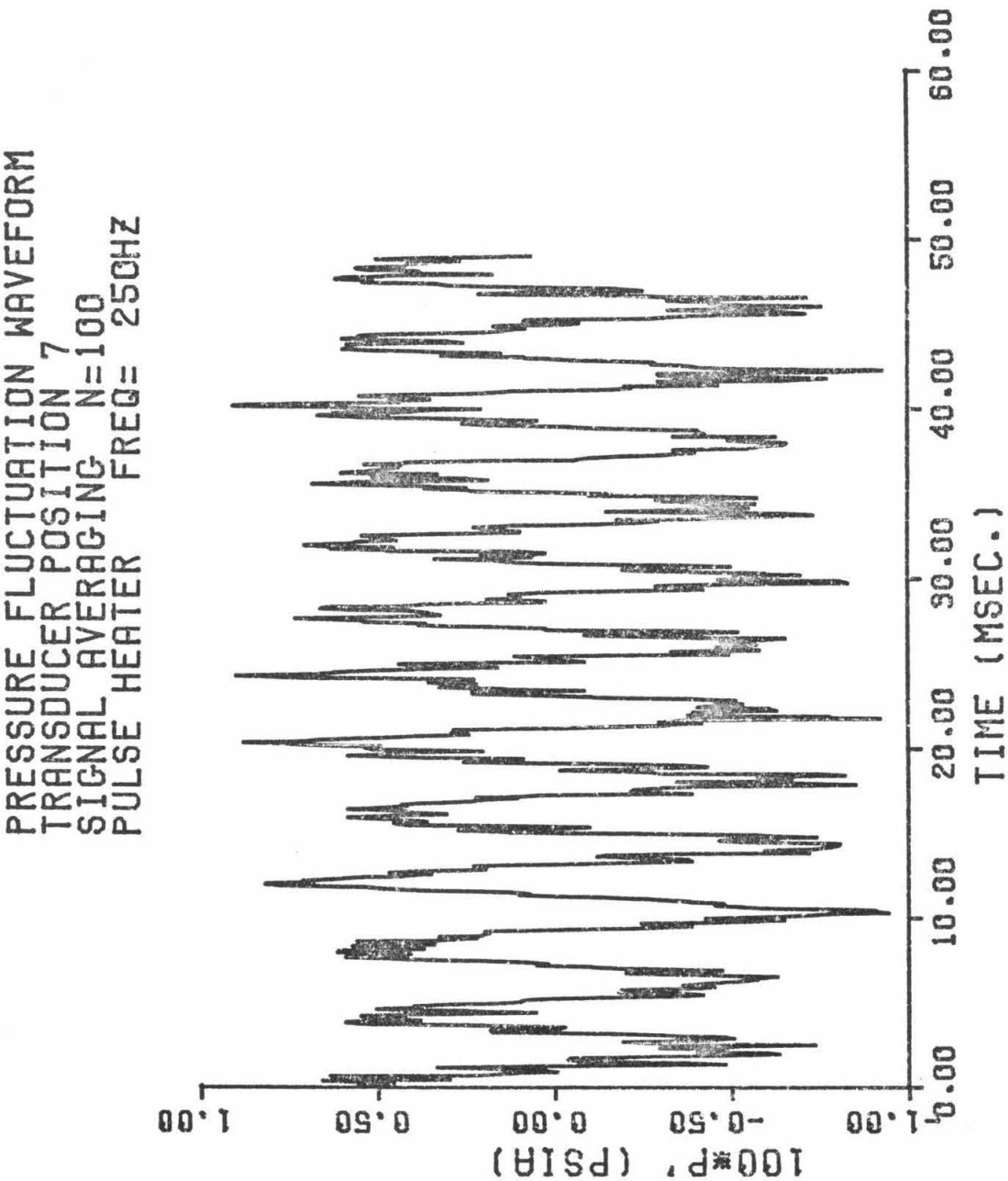

Fig. 5.26 Pressure Fluctuation Waveform obtained by addition of 100 digital records of the pressure fluctuation at the nozzle exit during operation of the thermal pulse heater at a frequency of 500 HZ.

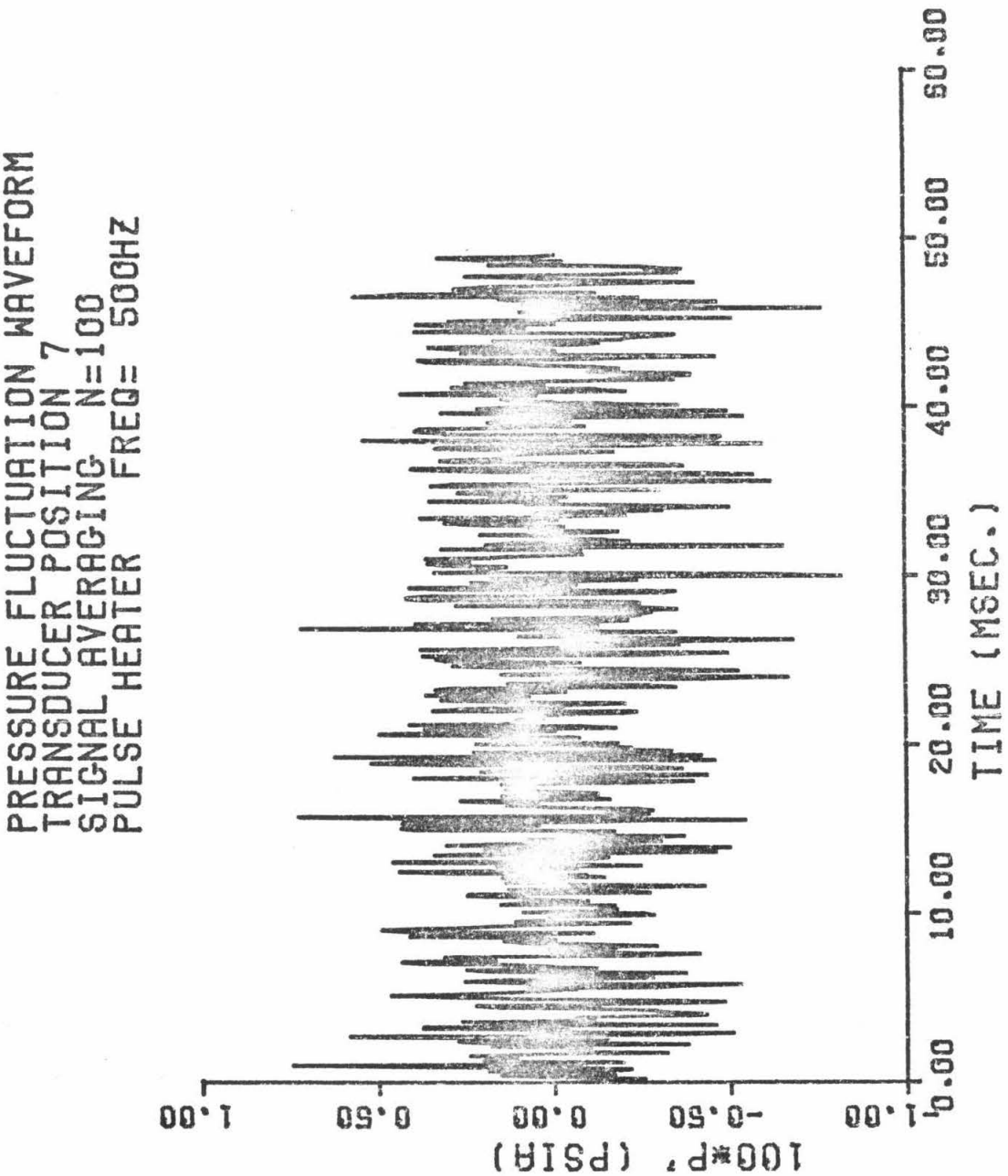

Fig. 5.27 Portion of the Spectrum for a Signal Averaged Pressure Fluctuation Waveform. The plot shows the sharpness of the spectrum about the bleed valve frequency.

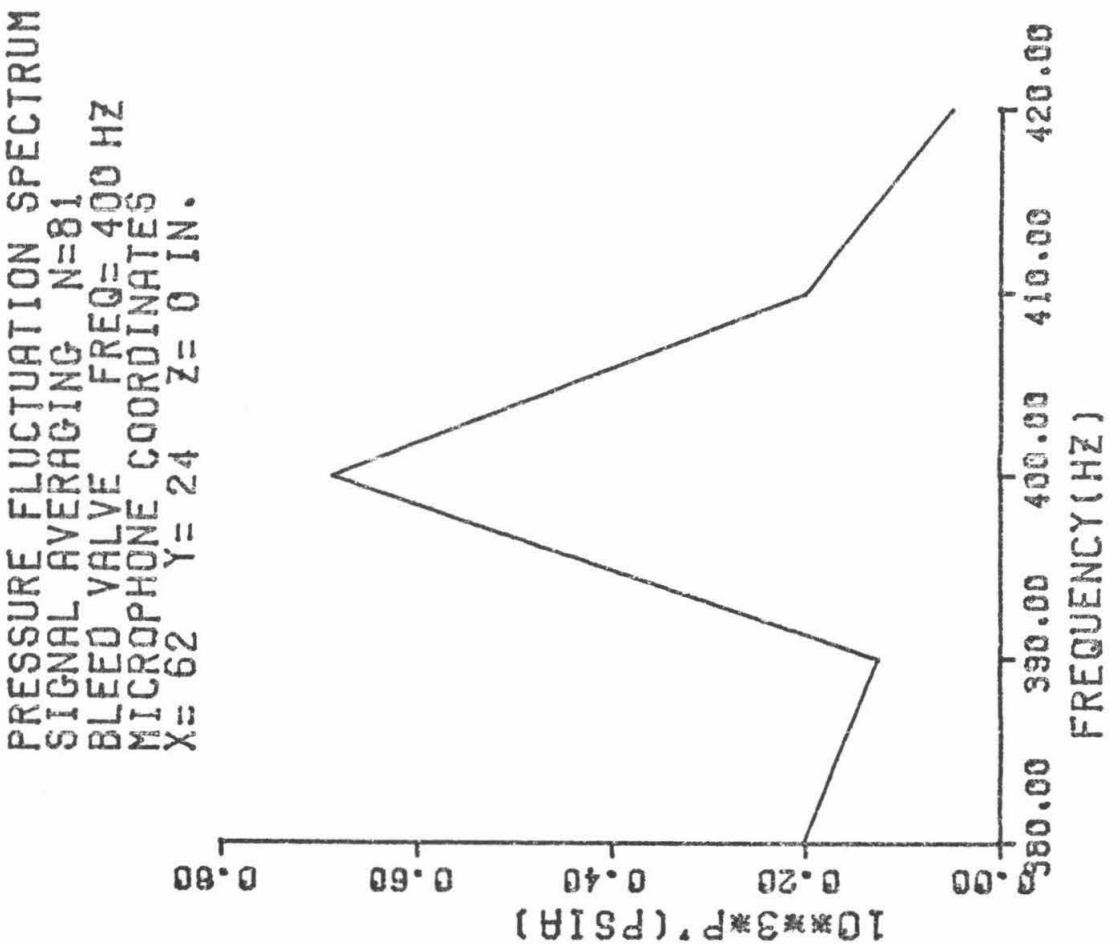

Fig. 5.28 Portion of the Spectrum for a Signal Averaged Pressure Fluctuation Waveform. The plot shows the sharpness of the spectrum about the pulse heater frequency.

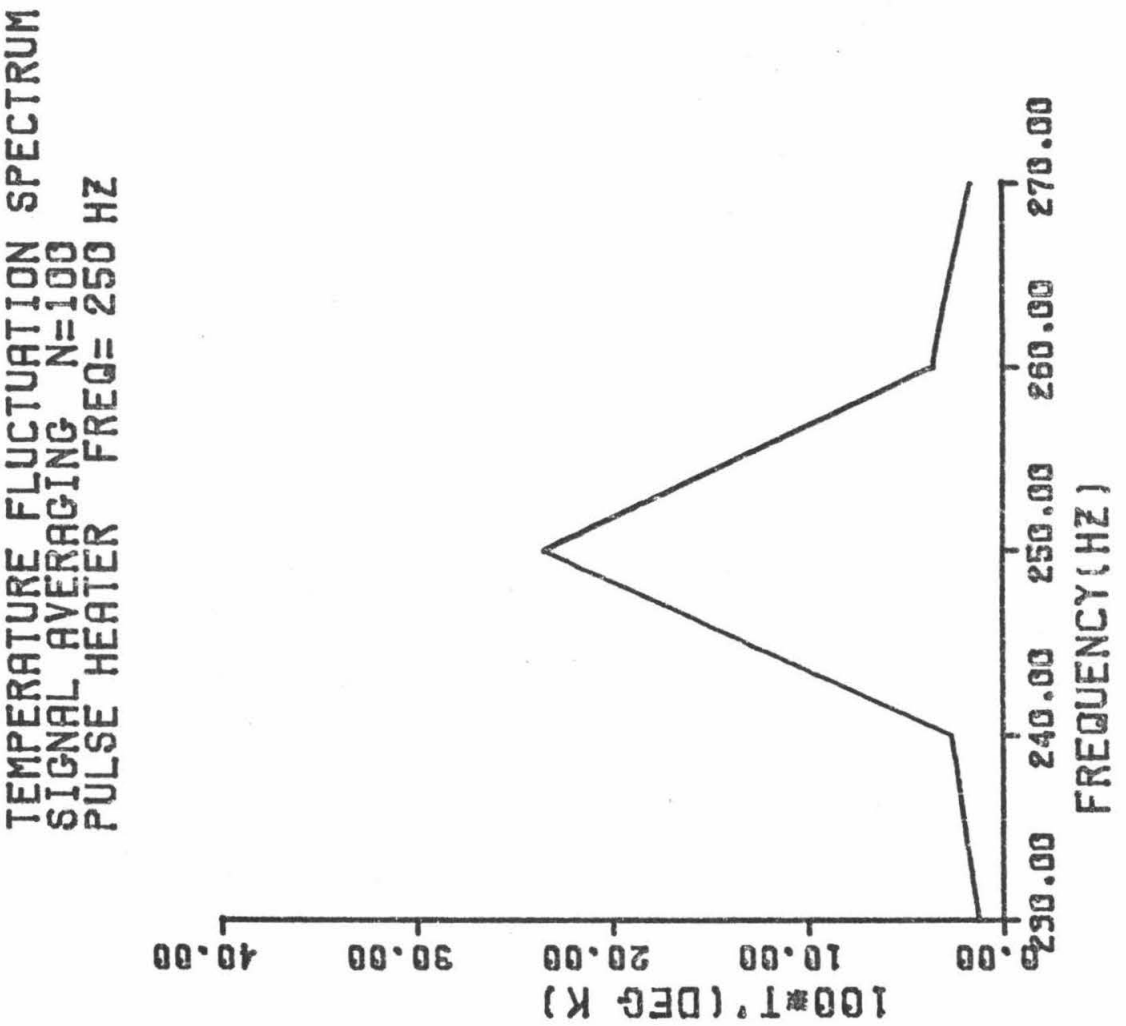

From this data record, Fourier sine and cosine coefficients were calculated at the bleed frequency, ± one spectrum frequency increment from the bleed frequency, ±two frequency increments from the bleed frequency. For a 1024-word record taken at a sampling rate of 40 K Hz, the frequency increment is 40 Hz (see Chapter IV). From the cosine and sine terms, an amplitude of the pressure fluctuation was calculated at the five frequencies and then plotted. The results show that the signal-averaged waveform is very sharp about the valve frequency, unlike the noise spectra in figs. 5.1 to 5.18.

(ii) Figure 5.28: The heater was run at 250 Hz and a 1024-word data record was made at a sampling rate of 10 K Hz. Spectrum calculations are the same as described above. The spectrum frequency increment, however, for a 10 K Hz sampling rate is 10 Hz.

5.4 Propagation of Pure Pressure Disturbances in the Nozzle

5.4.1 Scope. Since, in an actual jet engine, pressure fluctuations produced by temperature nonhomogeneities are accompanied by pressure fluctuations originating from pressure type sources such as turbulence and fan noise, it seemed appropriate to study the behavior of pressure disturbances in the nozzle that originated solely from pressure disturbances in the entrance section. These pressure disturbances would be produced by operation of the bleed valve system.

Such a study of pressure disturbances in a supersonic nozzle has not been reported in the literature. The results also provide a basis for checking numerical calculation schemes and showing the effect of the entropy wave for the case of the "uncompensated heater

operation," that is, the case for which the pulse heater was operated with no effort made to cancel the downstream running pressure disturbances caused by heater operation.

5.4.2 Analysis of the bleed valve flow in the entrance section. As indicated in fig. 3.16, the bleed valve flow is through only one side of the entrance section.

The aim of the system is to produce a one-dimensional pressure disturbance, but the one-sided flow will produce transverse mode which may not attenuate rapidly enough to make the theory of Chapter II valid in application here. To determine whether or not transverse modes existed in the entrance section, both analytical and experimental investigations were carried out.

The analytical investigation modelled the bleed system by the pressure fluctuations produced by a periodic normal velocity on a segment of one wall of an infinitely long rectangular duct. The underlying assumption of the analysis was that the transverse modes died out rapidly; hence, the entrance section, as far as these transverse modes were concerned, could be represented by an infinitely long duct. Details of the analysis are given in Appendix E, but the pertinent results are presented here.

The analysis had as the end result the calculation of the axial attenuation functions of the transverse modes. The functions were found as shown in Appendix E to be decaying exponentials with a decay constant given by

$$\sqrt{\frac{n^2\pi^2}{(1-M^2)d^2} - \frac{(t)^2}{a^2(1-M^2)^2}}$$

where

n = mode number n = 1, 2, 3, . . .

d = width of entrance section = 1 in.

M = Mach number in entrance section = 0.2

ω = angular frequency of bleed flow

Table 5-2 shows the decay constants for n = 1, 2, 3, 4 for frequencies of 250 Hz, 300 Hz, 400 Hz, and 500 Hz. It can be seen from the tabulated results that the lowest mode is reduced to 1/25 of its initial amplitude 1 inch from the end of the bleed slits; a greater attenuation occurs for the higher modes.

Table 5-2. Axial Attenuation Coefficients for Transverse Modes.

	attenuation coefficient (in.$^{-1}$)			
Mode	250 Hz	300 Hz	400 Hz	500 Hz
1	3.2181	3.2170	3.2143	3.2108
2	6.4398	5.4392	6.4379	6.4361
3	9.6607	9.6603	9.6594	9.6582
4	12.8814	12.8811	12.8804	12.8796

Hence, the analysis showed that in the entrance section, the transverse modes produced by the bleed valve are negligible only a fraction of an inch from the bleed valve slits. However, an experimental check on this result was felt necessary, so the following investigation was conducted.

Transducers were mounted in both vertical walls opposite each other at positions of -6.5 in., -4.5 in., -2.5 in., and -0.5 in. with respect to the nozzle entrance. If transverse modes existed,

pressure fluctuation magnitude and phase measurements would not be the same for each pair. For just plane waves in the entrance, pairs of measurements would be the same. The results of the measurements are shown in figs. 5.29 and 5.30. Each cluster of points is for a pair of transducers for several experiments. More than one set of measurements is given to show repeatibility. The large discrepancy at x = -6.5 in. was found to be due to the fact that one transducer was mounted on the valve block side plate and that this plate transmitted to the transducer mechanical vibrations arising from the rotating shaft hitting the air-bearing sleeves. No other transducer was so affected; this was checked by hitting the valve block impulsively and then monitoring all transducer outputs.

The results of the analysis of Appendix E and the measurements shown in figs. 5.27 and 5.28 definitely confirm that the bleed valve system produces a plane wave disturbance in the entrance section and nozzle.

5.4.3 Sound field produced by the bleed valve in the nozzle. Having discussed the fundamentals of operation of the bleed system, the results of the sound measurements and a comparison with theory will now be made. The results are shown in figs. 5.29 to 5.44. There are four sets of curves: each set comprising four figures corresponds to a different frequency and hence a different value of dimensionless frequency β as follows:

Frequency	β	Frequency	β
250 Hz	.96	300 Hz	1.16
400 Hz	1.54	500 Hz	1.93

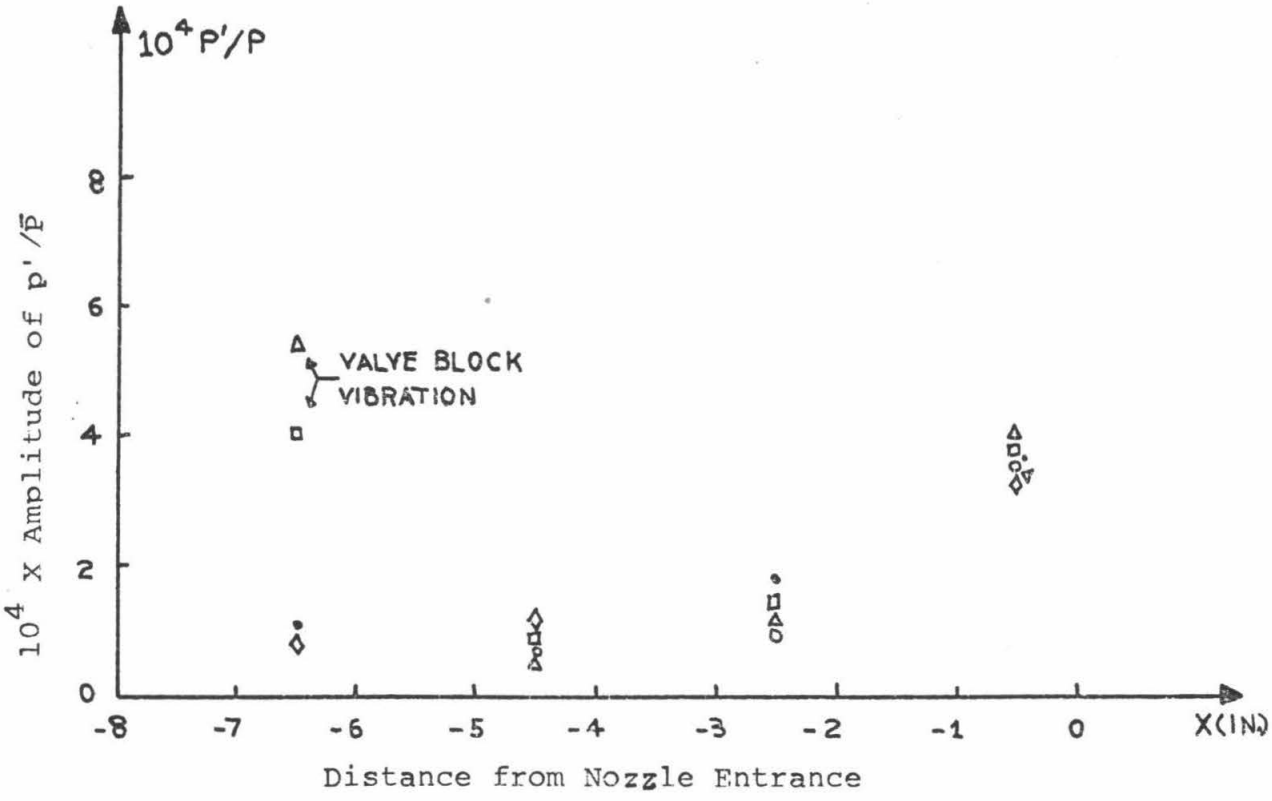

Fig. 5.29 Measurements of the Amplitude of the 400 HZ. Component of the Pressure Fluctuation Produced by the Bleed Valve in the Entrance Section. Measurements show absence of transverse modes.

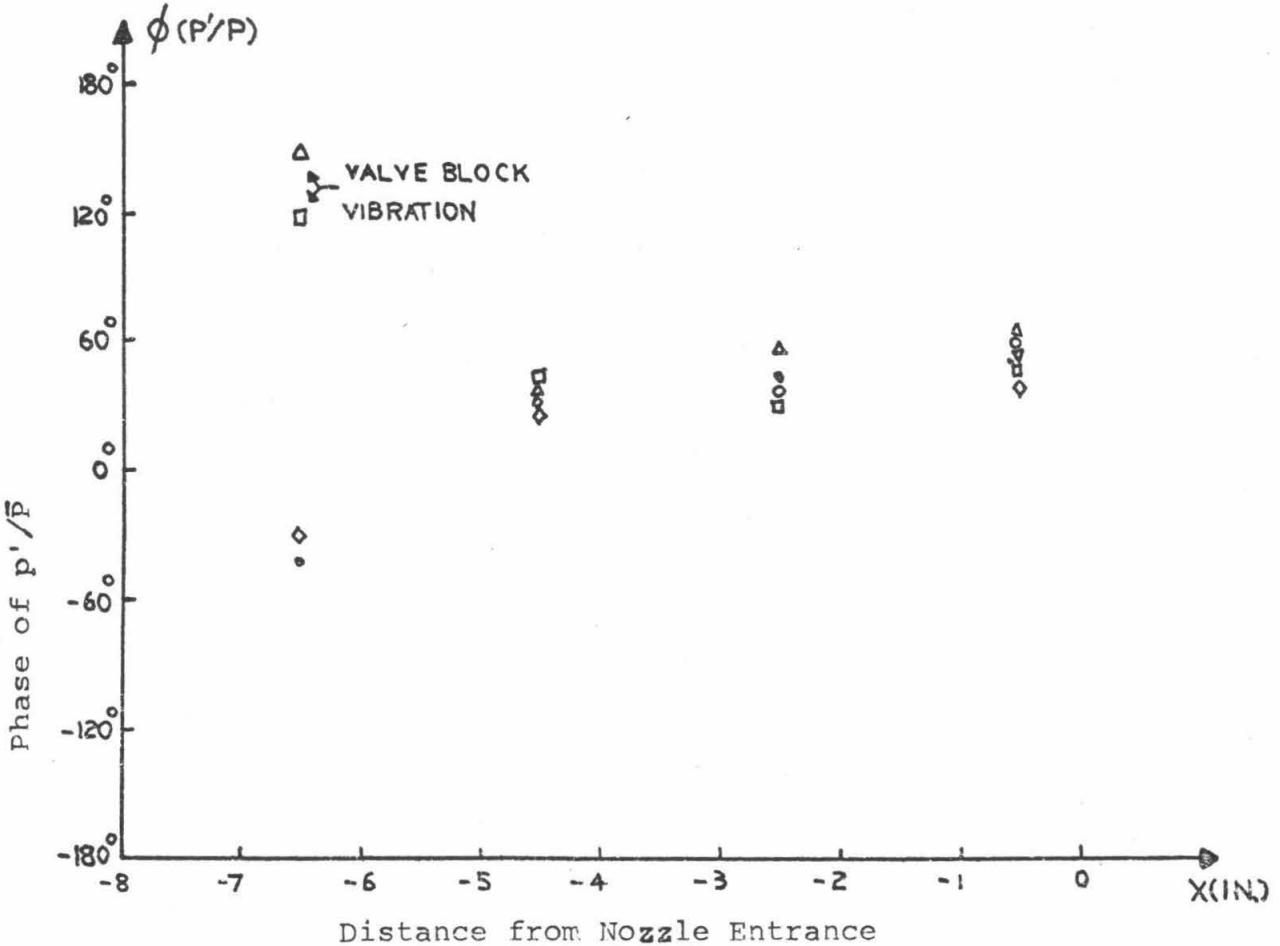

Fig. 5.30 Measurements of the Phase of the 400 HZ Component of the Pressure Fluctuation Produced by the Bleed Valve in the Entrance Section. Measurements show absence of transverse modes.

Recall $\beta = \omega \ell^* / a^*$ (Section 2.3).

The first two figures of each set show the magnitude and phase of the spectral component of $p'/\bar{p}$ at the bleed valve frequency and the theoretical solutions calculated with the measured magnitude and phase data at transducer position 3. The second two curves of the set show the experimental points and theoretical solutions in the case when the latter are calculated with the measured values of amplitude and phase of the spectral component of the downstream running pressure wave at the bleed flow frequency. This downstream-running pressure wave was evaluated from measurements of $p'/\bar{p}$ at -8.0 in. and -0.5 in. in the entrance section and use of equations (2.52).

Examination of the graphs shows good agreement in magnitude and excellent agreement in phase between theory and experiment. The curve all show the same characteristic behavior of the magnitude of $p'/\bar{p}$ within the nozzle: it is essentially constant. Candel[21] defined a transmission coefficient for pressure fluctuations as the ratio of the value of $p'/\bar{p}$ at the nozzle exit to the value of $p'/\bar{p}$ at the nozzle entrance as a function of the entrance and exit numbers and β. From figs. 5.31 - 5.46 one can see for these experiments that the transmission coefficients have values from about 1.0 to 1.2.

Candel[21] found that for a constant acceleration nozzle with an entrance Mach number of .022 and an exit Mach number of 1.52, the transmission coefficients assumed values between 1.0 and 1.2 for values of β between 0 and 2.0.

Fig. 5.31 Theoretical Solution and Experimental Data for the Amplitude of the Sound Field at 250 HZ Produced by Operation of the Bleed Valve. Theoretical solution is calculated with the value of $p'/\bar{P}$ measured at 0.5 in. upstream of the nozzle entrance. Error limits shown are typical.

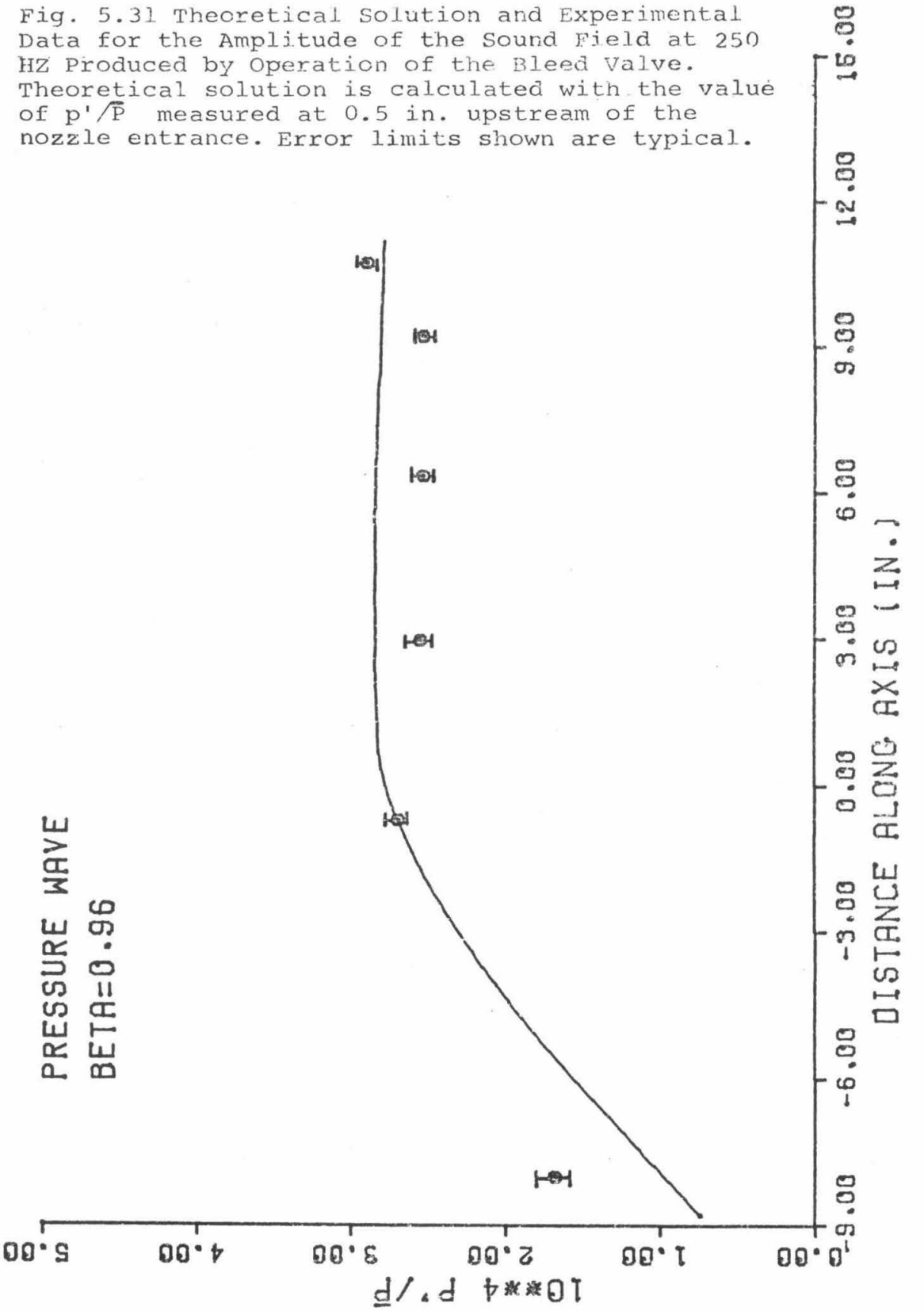

Fig. 5.32 Theoretical Solution and Experimental Data for the Phase of the Sound Field at 250 HZ Produced by Operation of the Bleed Valve. Theoretical Solution is calculated with the value of the phase of $p'/\bar{P}$ measured at 0.5 in. upstream of the nozzle entrance. Error limits shown are typical.

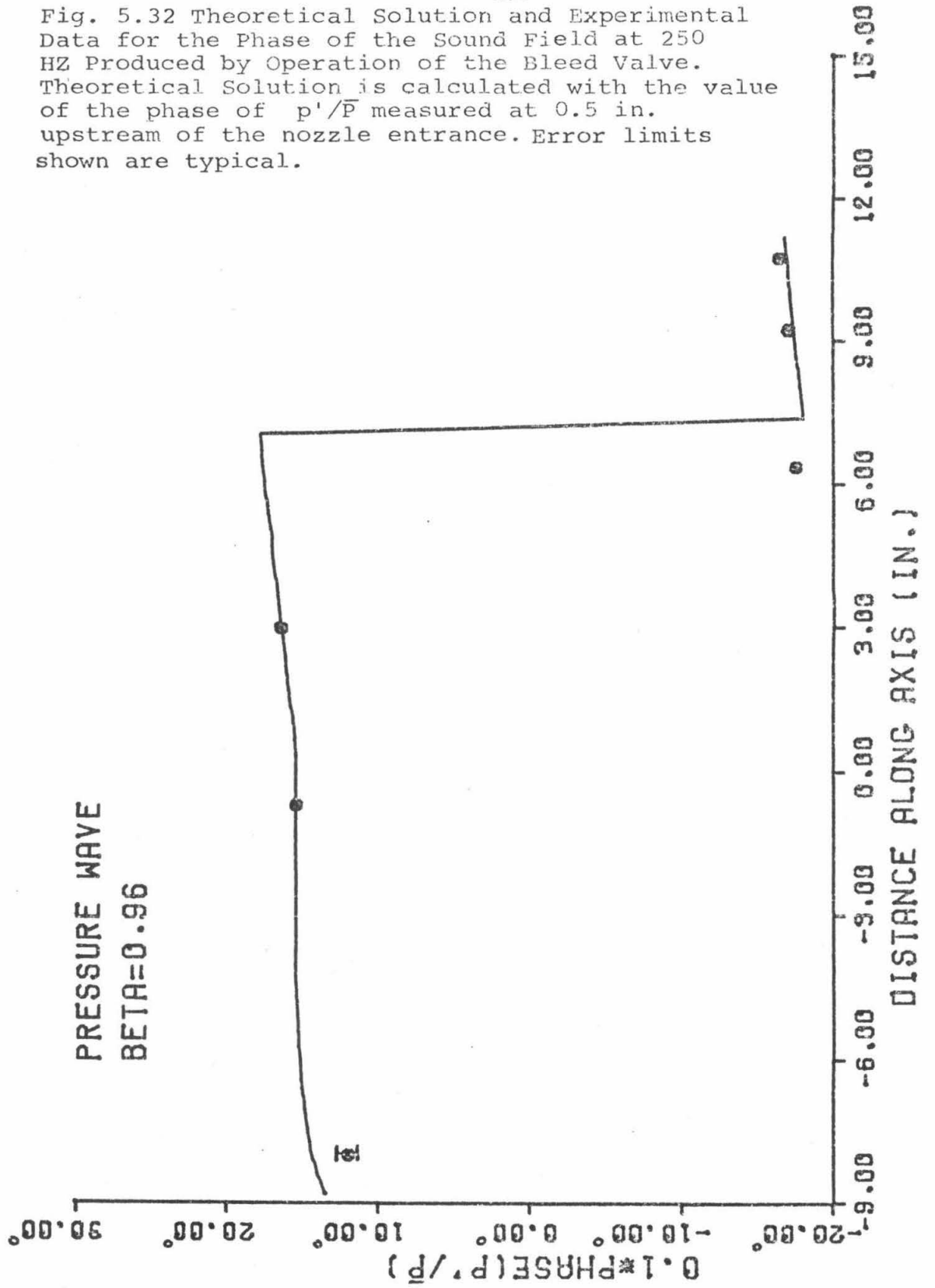

Fig. 5.33 Theoretical Solution and Experimental Data for the Amplitude of the Sound Field at 250 HZ Produced by Operation of the Bleed Valve. Theoretical solution is calculated with the value of the downstream running pressure wave computed from measurements of p' at two points in the entrance section.

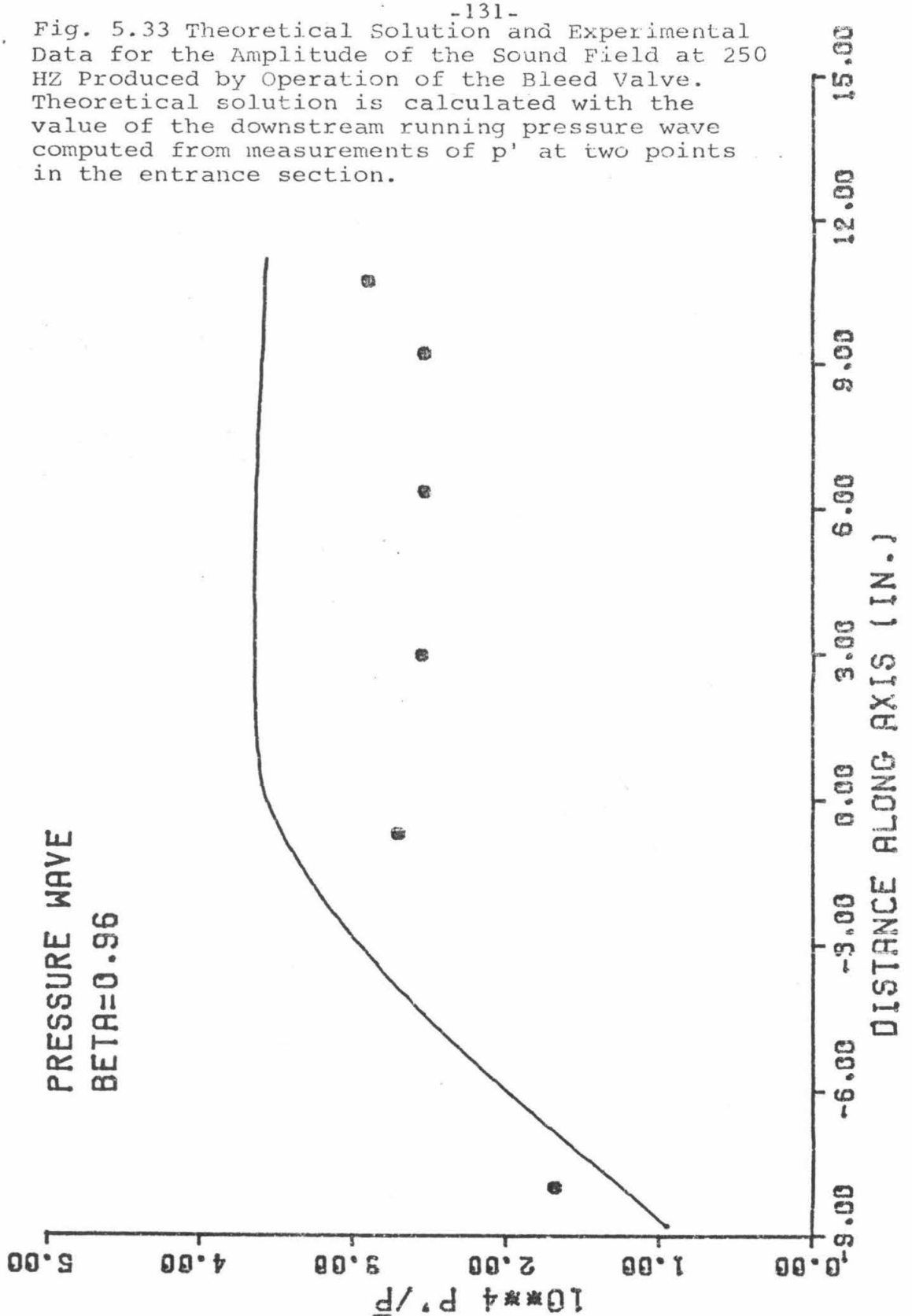

.Fig. 5.34 Theoretical Solution and Experimental Data for the Phase of the Sound Field at 250 HZ Produced by Operation of the Bleed Valve. Theoretical Solution is calculated with the value of the phase of the downstream running pressure wave computed from measurements of p' at two points in the entrance section.

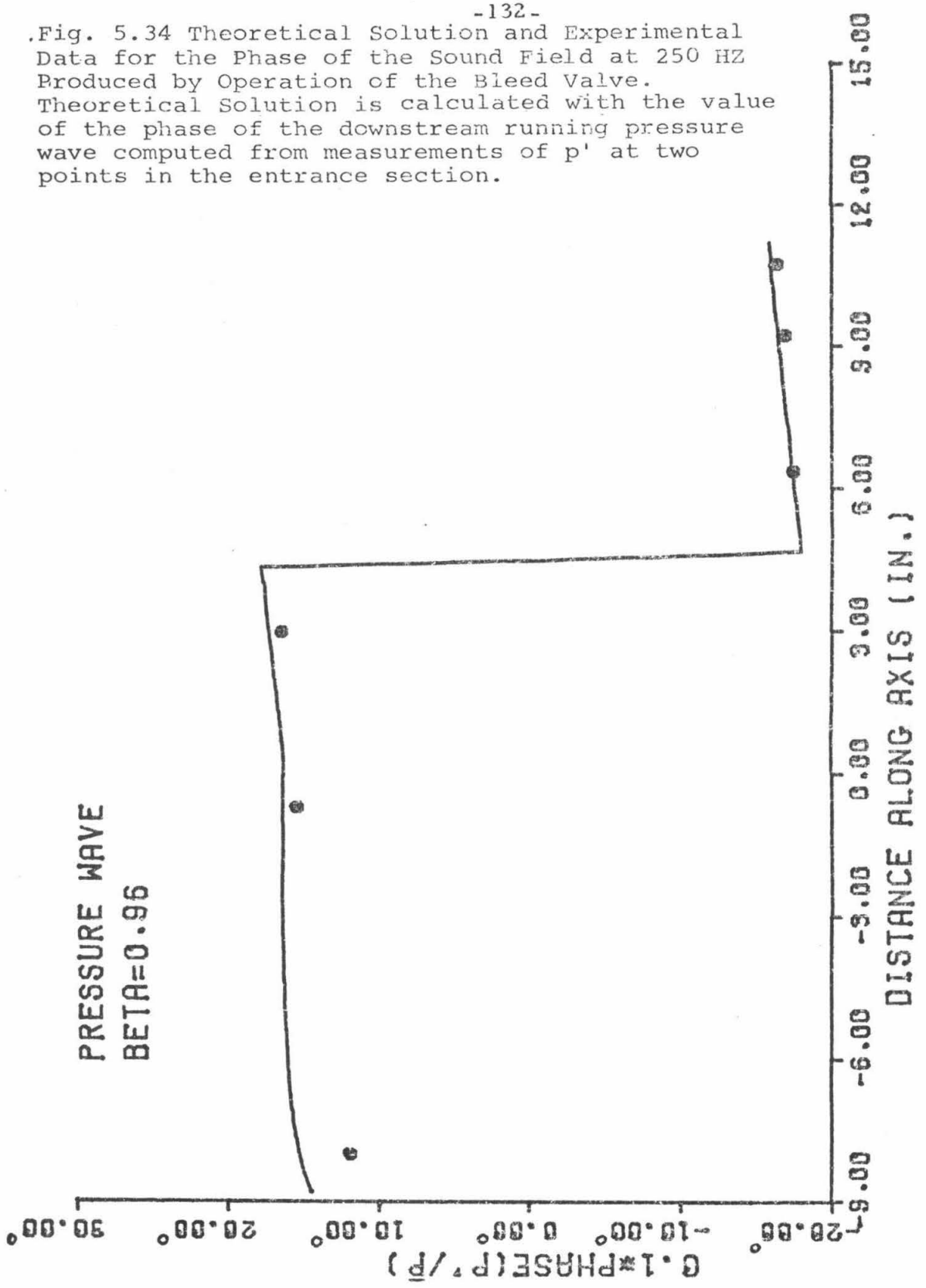

Fig. 5.35 Theoretical Solution and Experimental Data for the Amplitude of the Sound Field at 300 HZ Produced by Operation of the Bleed Valve. Theoretical solution is calculated with the value of $p'/\bar{P}$ measured at 0.5 in. upstream of the nozzle entrance.

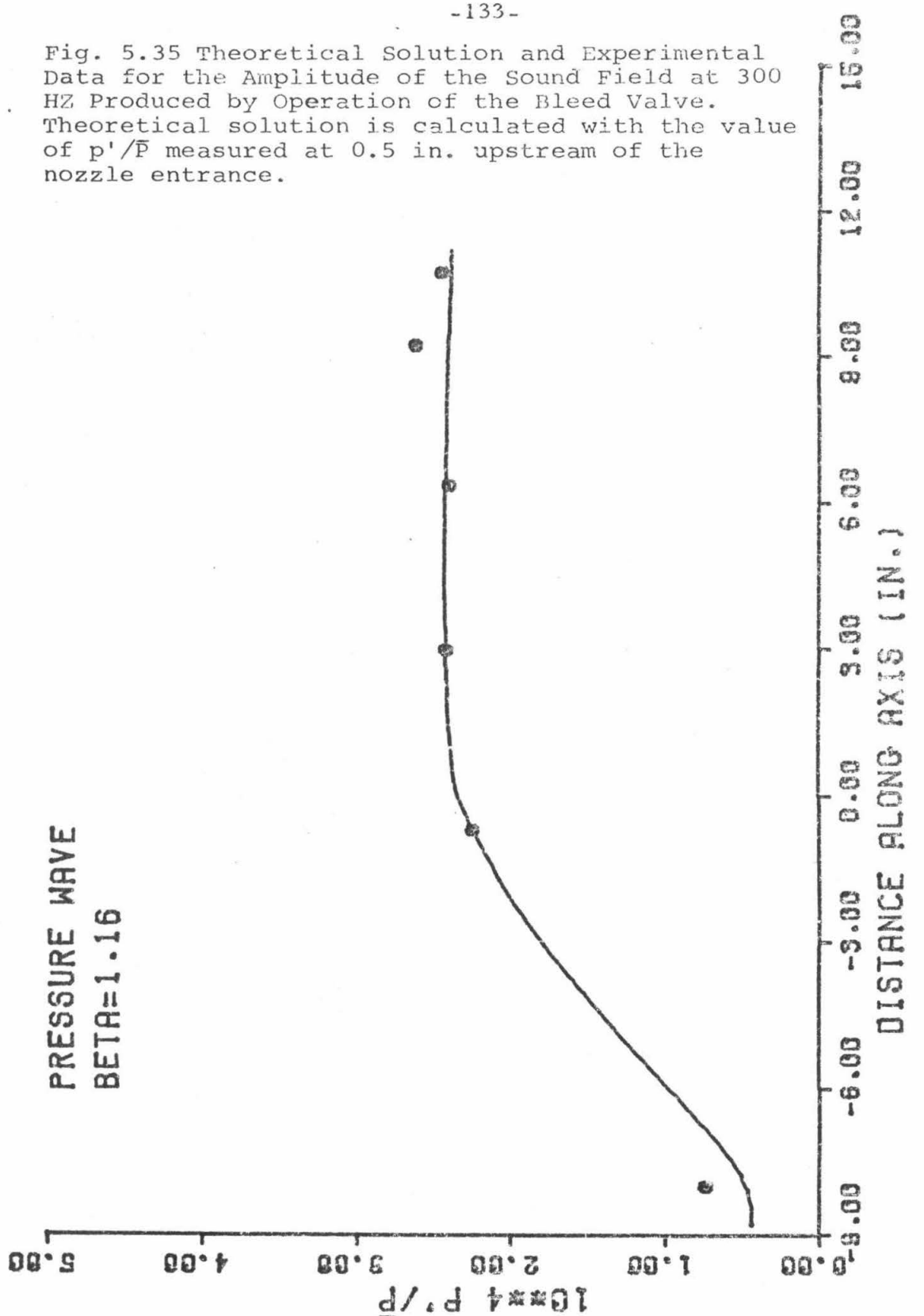

Fig. 5.36 Theoretical Solution and Experimental Data for the Phase of the Sound Field at 300 HZ Produced by Operation of the Bleed Valve. Theoretical solution is calculated with the value of the phase of $p'/\bar{P}$ measured at 0.5 in. upstream of the nozzle entrance.

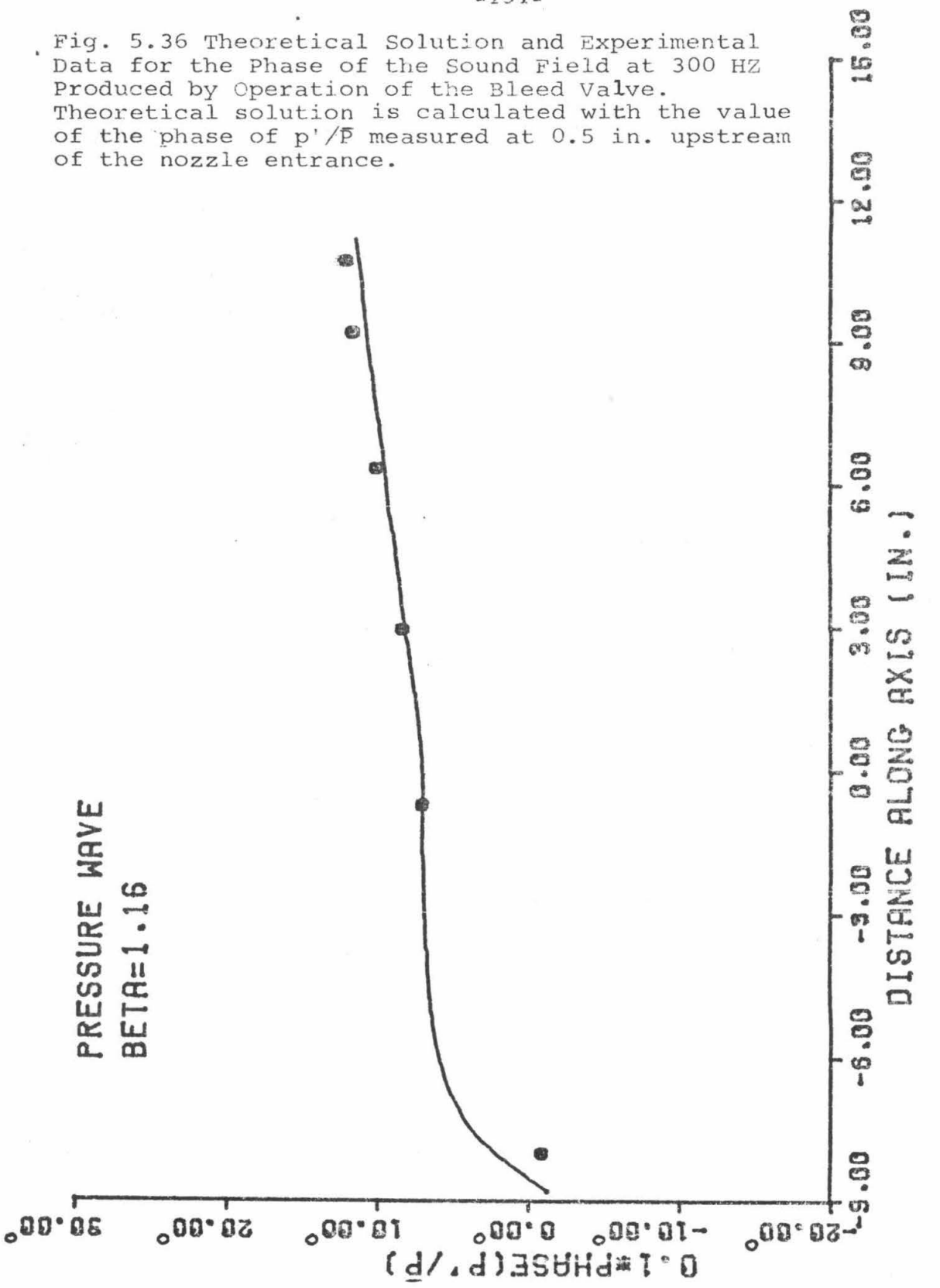

Fig. 5.37 Theoretical Solution and Experimental Data for the Amplitude of the Sound Field at 300 HZ Produced by Operation of the Bleed Valve. Theoretical solution is calculated with the value of the downstream running pressure wave computed from measurements of p' at two points in the entrance section.

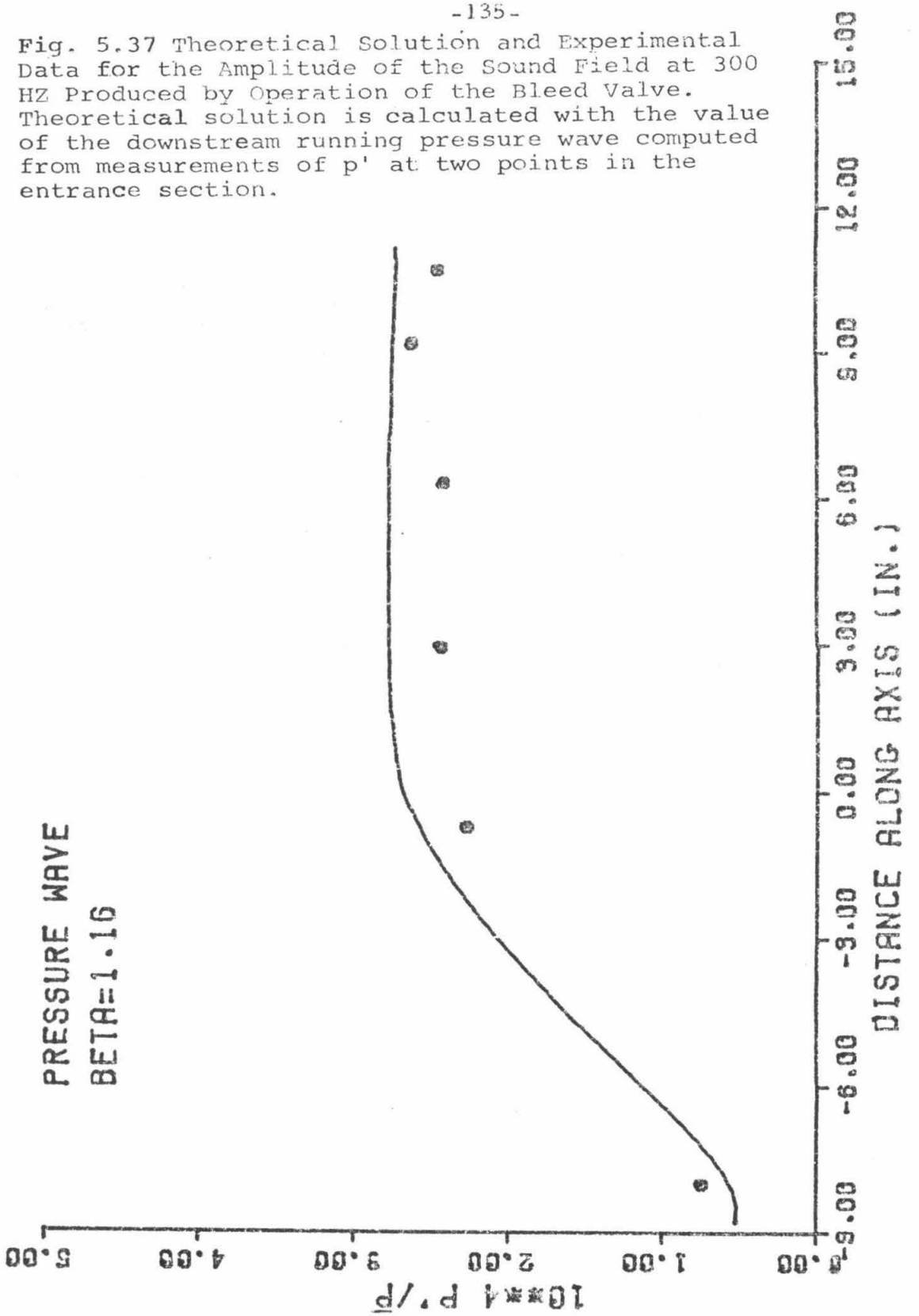

Fig. 5.38 Theoretical Solution and Experimental Data for the Phase of the Sound Field at 300 HZ Produced by Operation of the Bleed Valve. Theoretical Solution is calculated with the value of the phase of the downstream running pressure wave computed from measurements of p' at two points in the entrance section.

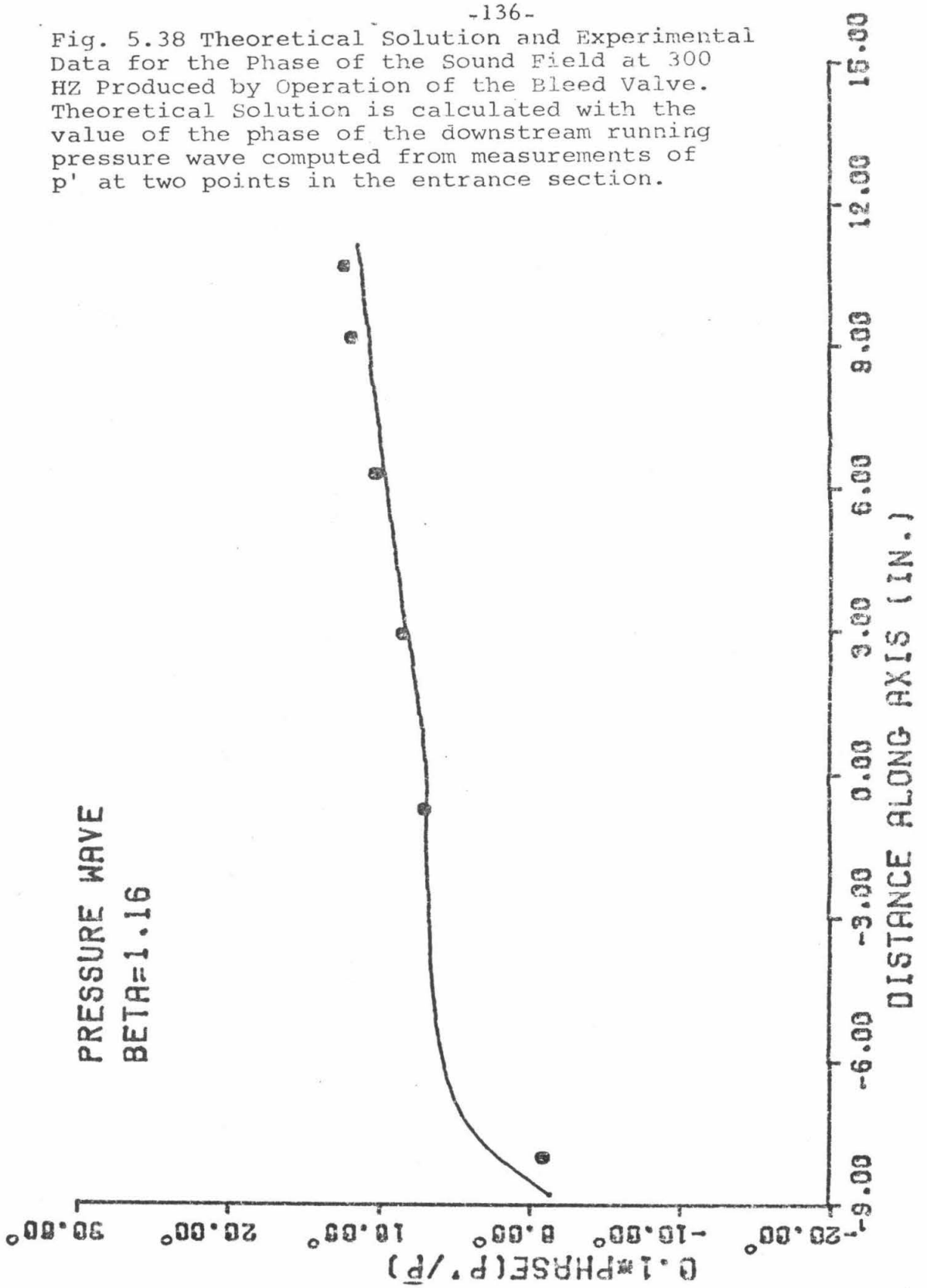

Fig. 5.39 Theoretical Solution and Experimental Data for the Amplitude of the Sound Field at 400 HZ Produced by Operation of the Bleed Valve. Theoretical solution is calculated with the value of $p'/\bar{P}$ measured at 0.5 in. upstream of the nozzle entrance.

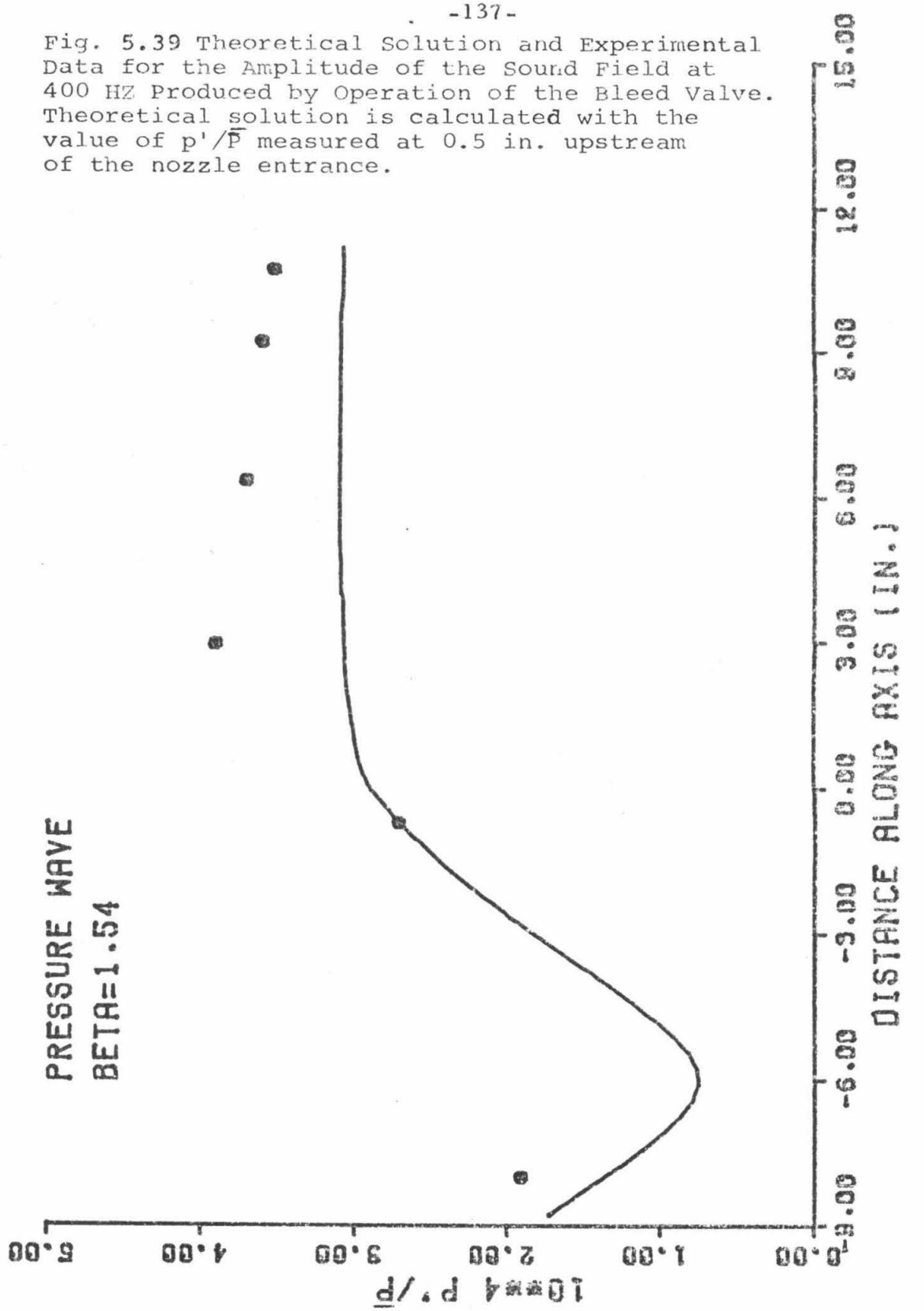

Fig. 5.40 Theoretical Solution and Experimental Data for the Phase of the Sound Field at 400 HZ Produced by Operation of the Bleed Valve. Theoretical solution is calculated with the value of the phase of $p'/\bar{P}$ measured at 0.5 in. upstream of the nozzle entrance.

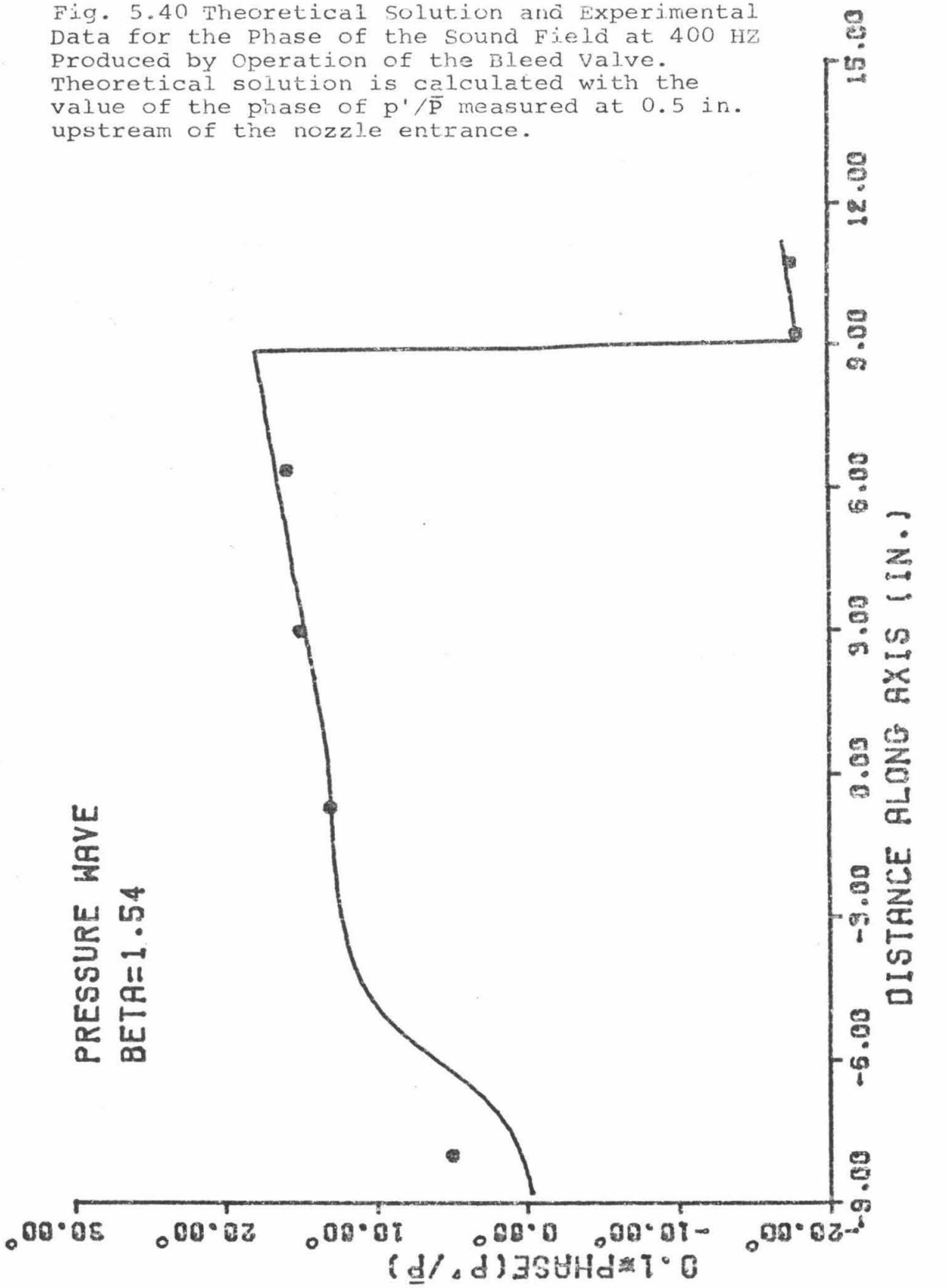

Fig. 5.41 Theoretical Solution and Experimental Data for the Amplitude of the Sound Field at 400 HZ Produced by Operation of the Bleed Valve. Theoretical solution is calculated with the value of the downstream running pressure wave computed from measurements of p' at two points in the entrance section.

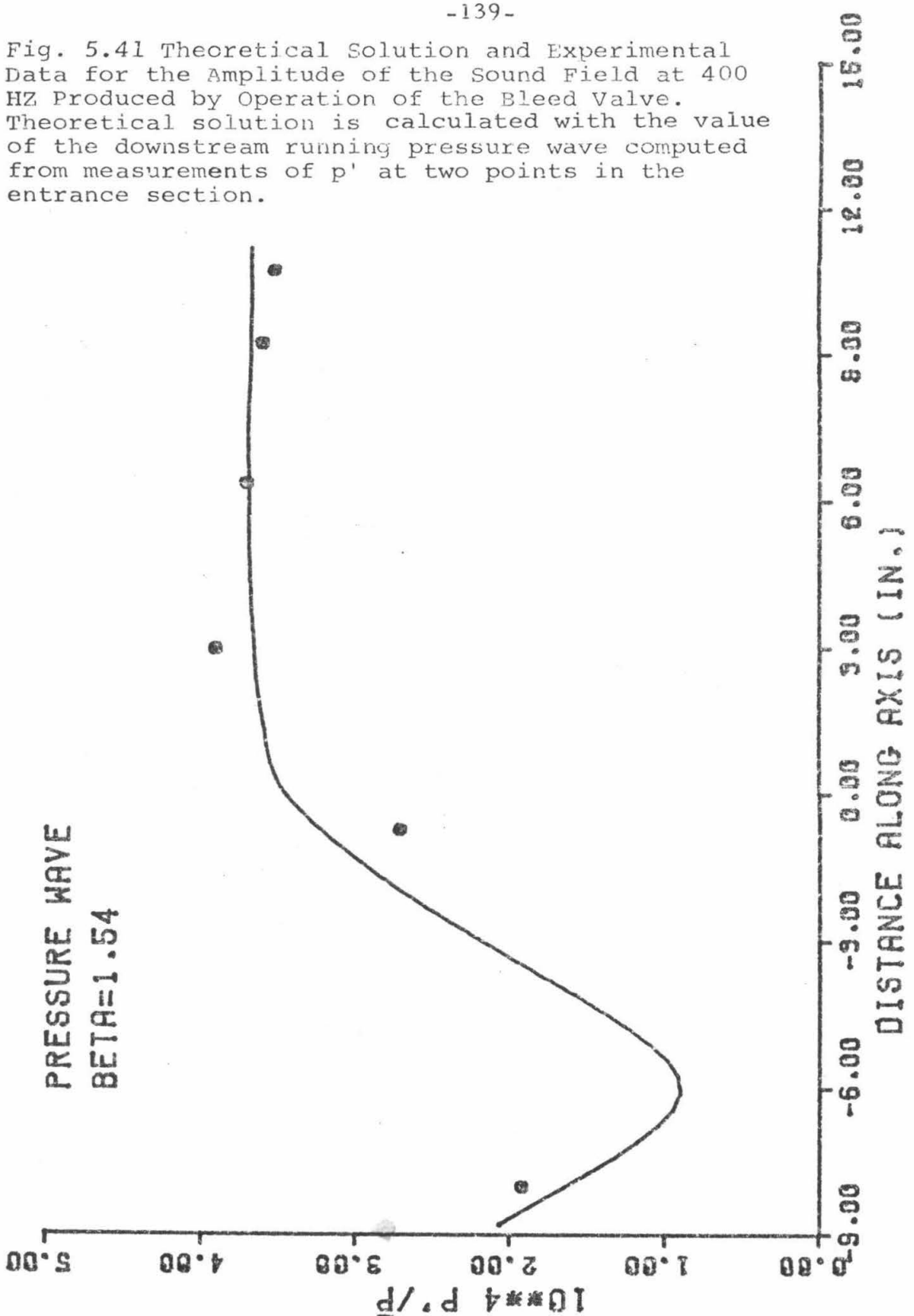

Fig. 5.42 Theoretical Solution and Experimental Data for the Phase of the Sound Field at 400 HZ Produced by Operation of the Bleed Valve. Theoretical solution is calculated with the value of the phase of the downstream running pressure wave computed from measurements of p' at two points in the entrance section.

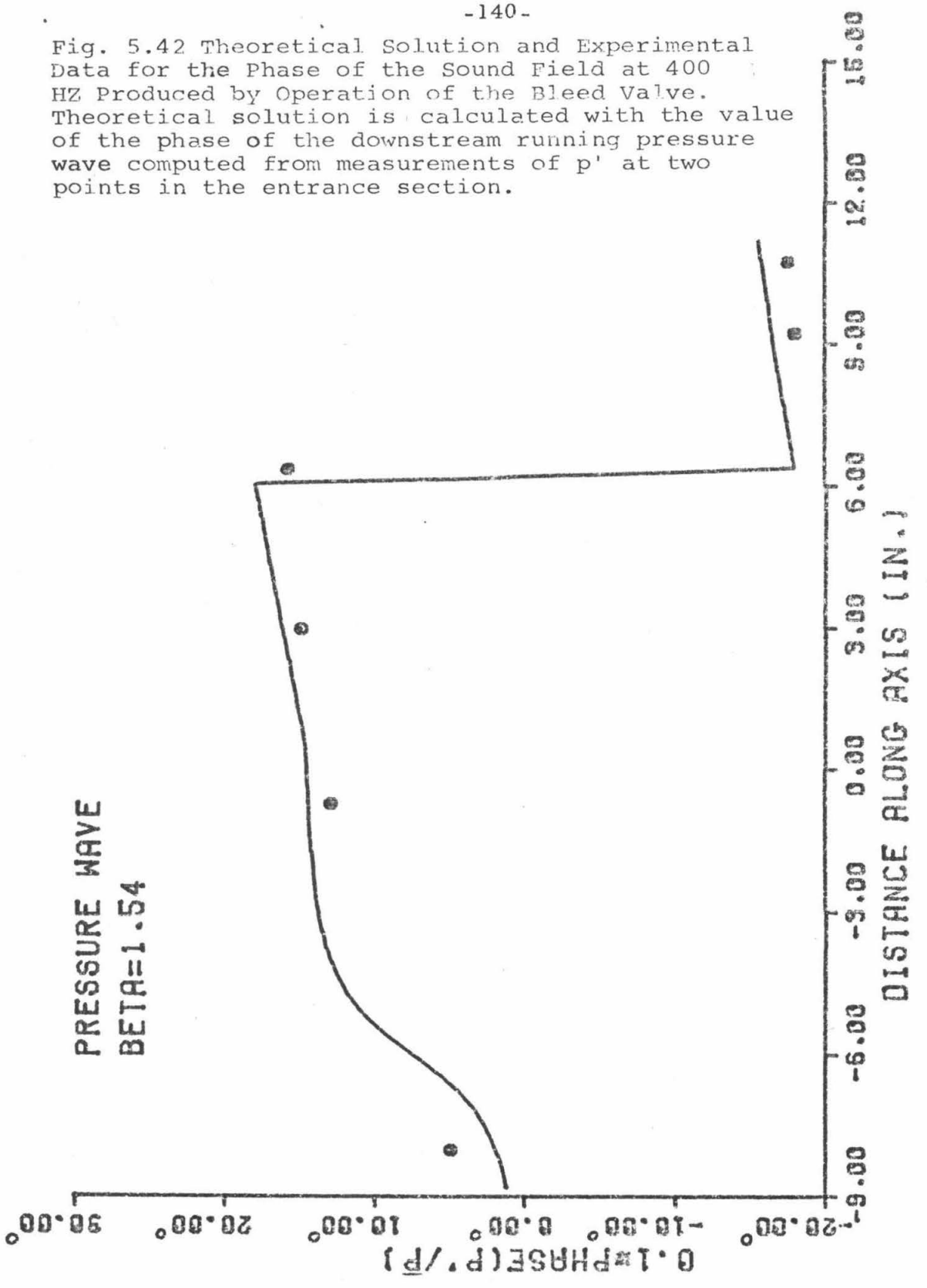

Fig. 5.43 Theoretical Solution and Experimental Data for the Amplitude of the Sound Field at 500 HZ Produced by Operation of the Bleed Valve. Theoretical solution is calculated with the value of $p'/\bar{P}$ measured at 0.5 in. upstream of the nozzle entrance. Error limits shown are attributed to high residual noise.

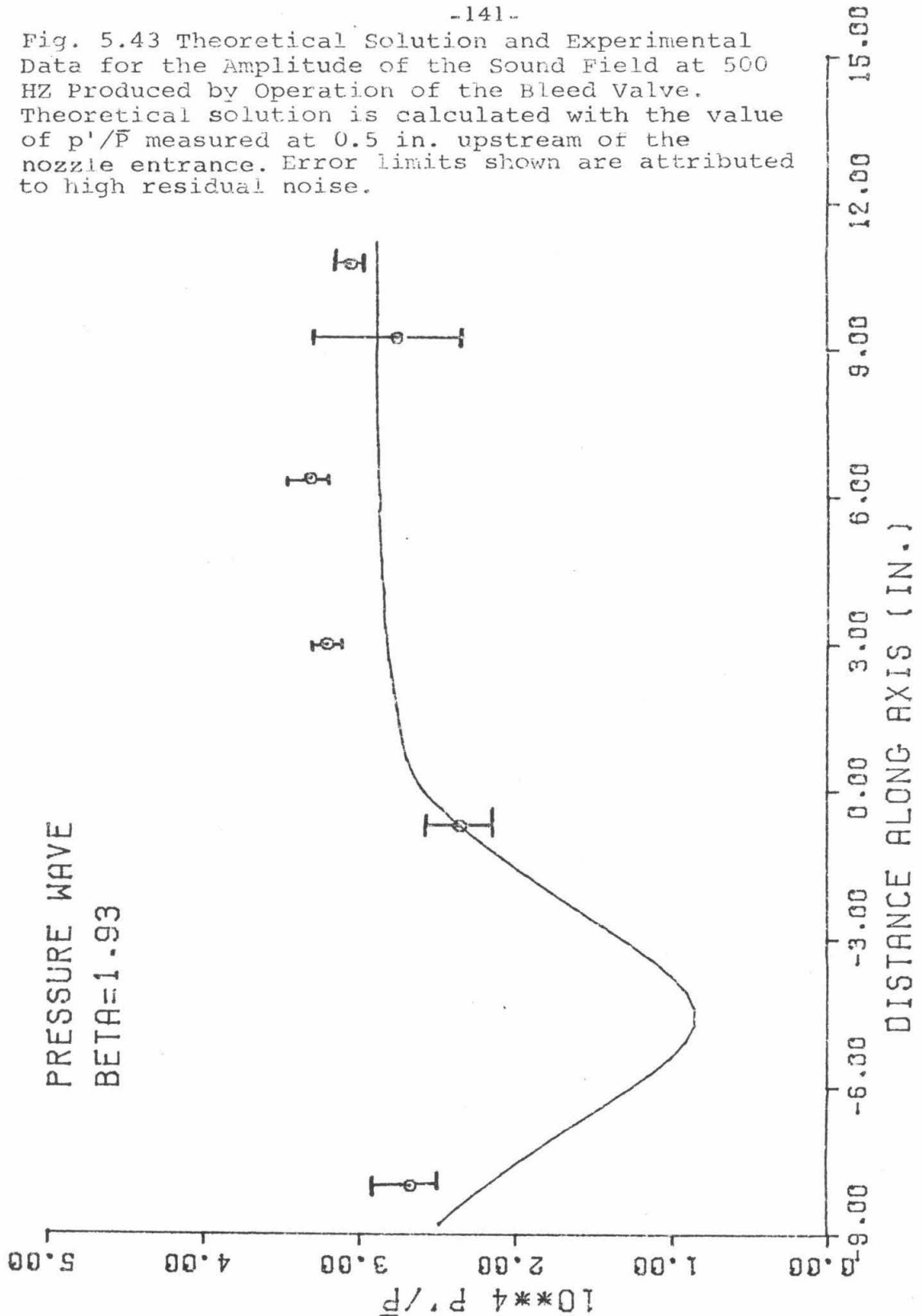

Fig. 5.44 Theoretical Solution and Experimental Data for the Phase of the Sound Field at 500 HZ Produced by Operation of the Bleed Valve. Theoretical solution is calculated with the value of the phase of $p'/\bar{P}$ measured at 0.5 in. upstream of the nozzle entrance. Note errors limits for phase are much smaller than corresponding errors in amplitude on page 141.

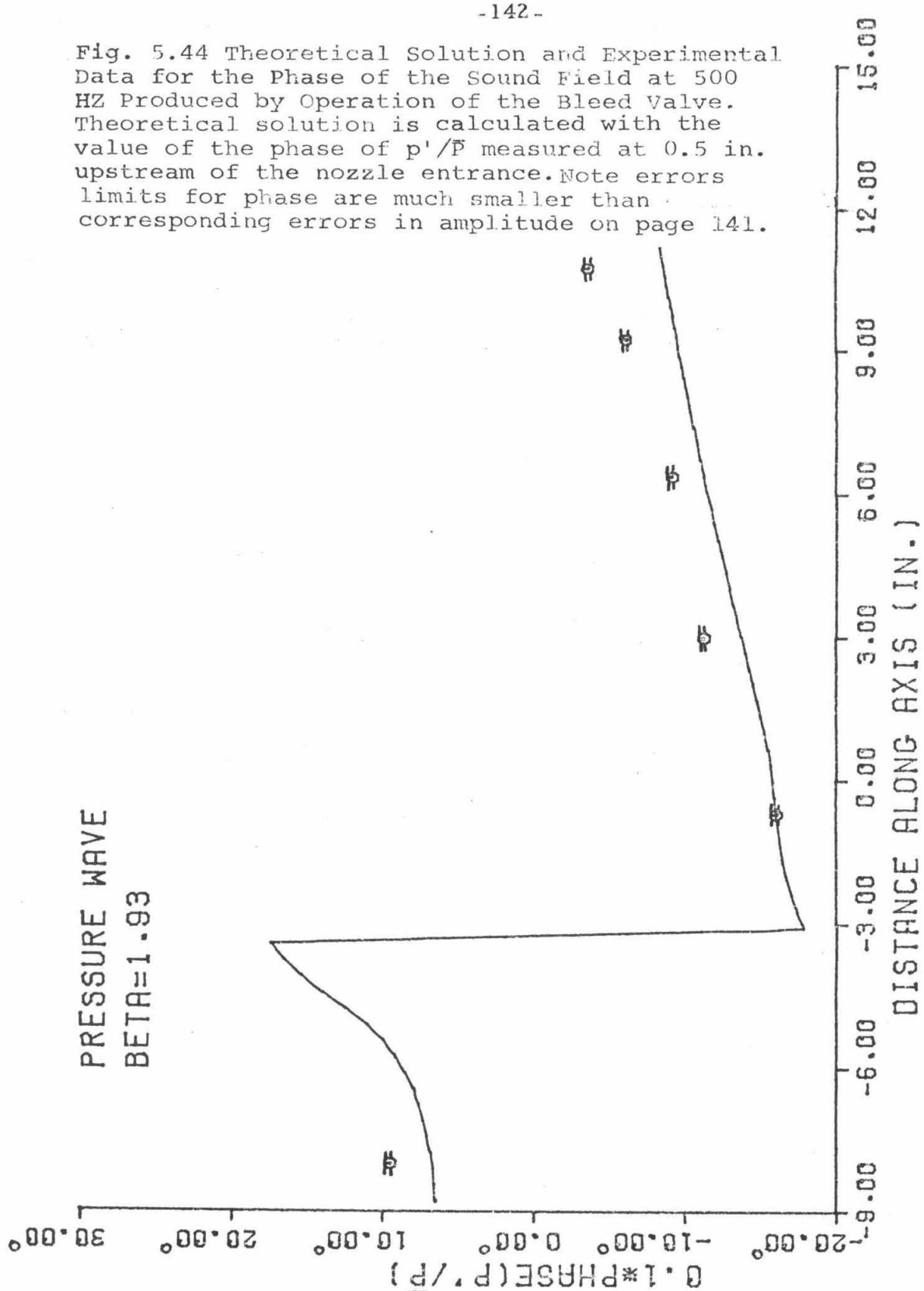

Fig. 5.45 Theoretical Solution and Experimental Data for the Amplitude of the Sound Field at 500 HZ Produced by Operation of the Bleed Valve. Theoretical solution is calculated with the value of the downstream running pressure wave computed from measurements of p' at two points in the entrance section.

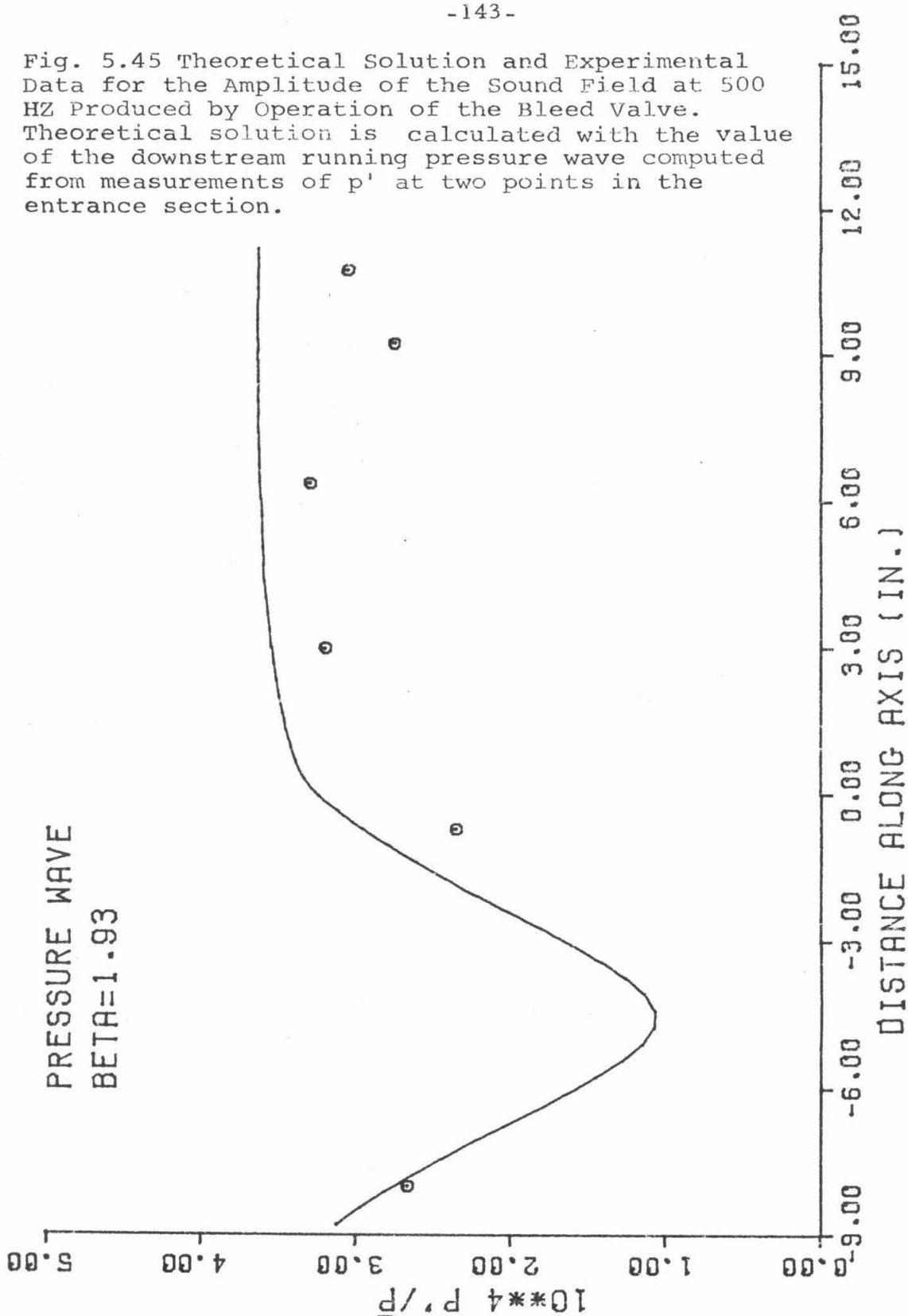

Fig. 5.46 Theoretical Solution and Experimental Data for the Phase of the Sound Field at 500 HZ Produced by Operation of the Bleed Valve. Theoretical solution is calculated with the value of the phase of the downstream running pressure wave computed from measurements of p' at two points in the entrance section.

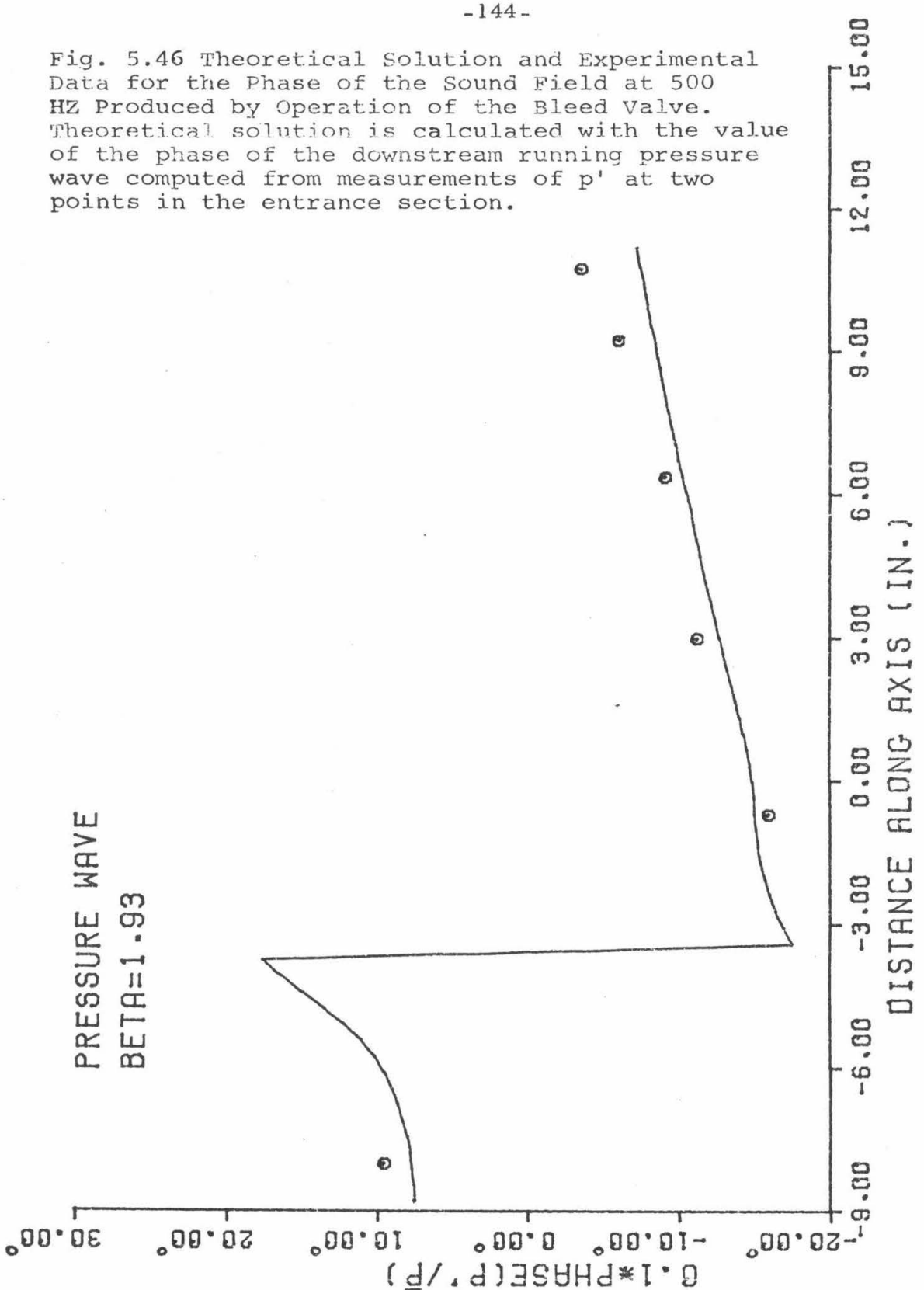

In contrast to the flat behavior of the amplitude of p'/p in the nozzle for the four values of β used in the experiment, the behavior of p'/p in the entrance section is quite different for increasing values of β. As β increases, a nodal pattern develops in the entrance section. This is to be expected since, as explained in Section 2.5, the form of the theoretical solution for sound waves in a constant-area duct is

$$p' = p_+ e^{i\left[\frac{\omega x}{U+a} - \omega t\right]} + p_- e^{i\left[\frac{\omega x}{U-a} - \omega t\right]} . \qquad (2.53)$$

For different values of p_+, p_- and ω, one expects to see different sinusoidal variations of p' in the entrance section. These variations for larger values of ω (equivalently β) will have more of a complete nodal pattern.

The existence of a nodal form for the distribution of p'/p brings up an important point in relation to the definition of the transmission coefficient defined by Candel. As the value of β increases, one would expect that eventually a node could occur at the entrance section station of the nozzle; then the transmission coefficient would be unreasonably large and essentially meaningless. In view of this, one might redefine the transmission coefficient as the ratio of the pressure fluctuation at the nozzle exit to the magnitude of the downstream running wave in the entrance section.

5.5 Investigation of Entropy and Pressure Disturbances in the Nozzle

5.5.1 Scope. The second phase of the experiments consisted of measuring the sound field produced by the pulse heater operating alone. The bleed valve system was not used to cancel the pressure

rises produced at the heater. In this mode of operation, both forward-running pressure waves and entropy waves were produced which could be used as inputs to the theory of Chapter II and thus check if it correctly described the interaction between pressure and entropy waves. The heater was run at frequencies of 250 Hz, 300 Hz, 400 Hz, and 500 Hz, corresponding to values of β = .96, 1.16, 1.54, 1.93, respectively.

5.5.2 Processing of temperature fluctuation data. As explained in Chapter III, the temperature fluctuation in the gas produced by the heater was measured by a 1 μm-diameter cold-wire resistance thermometer probe monitored in a constant-current hot-wire anemometer system. When the current in the heater was switched off by the SCR's, a large negative voltage spike was generated in the probe due to the sudden decrease in magnetic field (Faraday's law). The result of this electrical noise pickup by the probe is shown in fig. 5.47. The plot shows a periodic waveform consisting of a noisy sinusoidal wave and negative spikes occurring at 250 Hz. The former is the probe's response to the gas temperature fluctuation, while the latter is electrical pickup due to the switching off of the heater.

Since the temperature fluctuation data records were digital, a digital filter program could be written to eliminate the spikes and replace the value of the spike by a value equal to the amplitude of the sinusoid corresponding to the temperature fluctuation. The results of applying this digital filter to the record of fig. 5.47 is shown in fig. 5.48. It can be seen that the temperature fluctuation measurement contains a considerable amount of noise even after 100 signal-averaging

Fig. 5.47 Temperature Fluctuation Waveform
Without Noise Spike Filtering

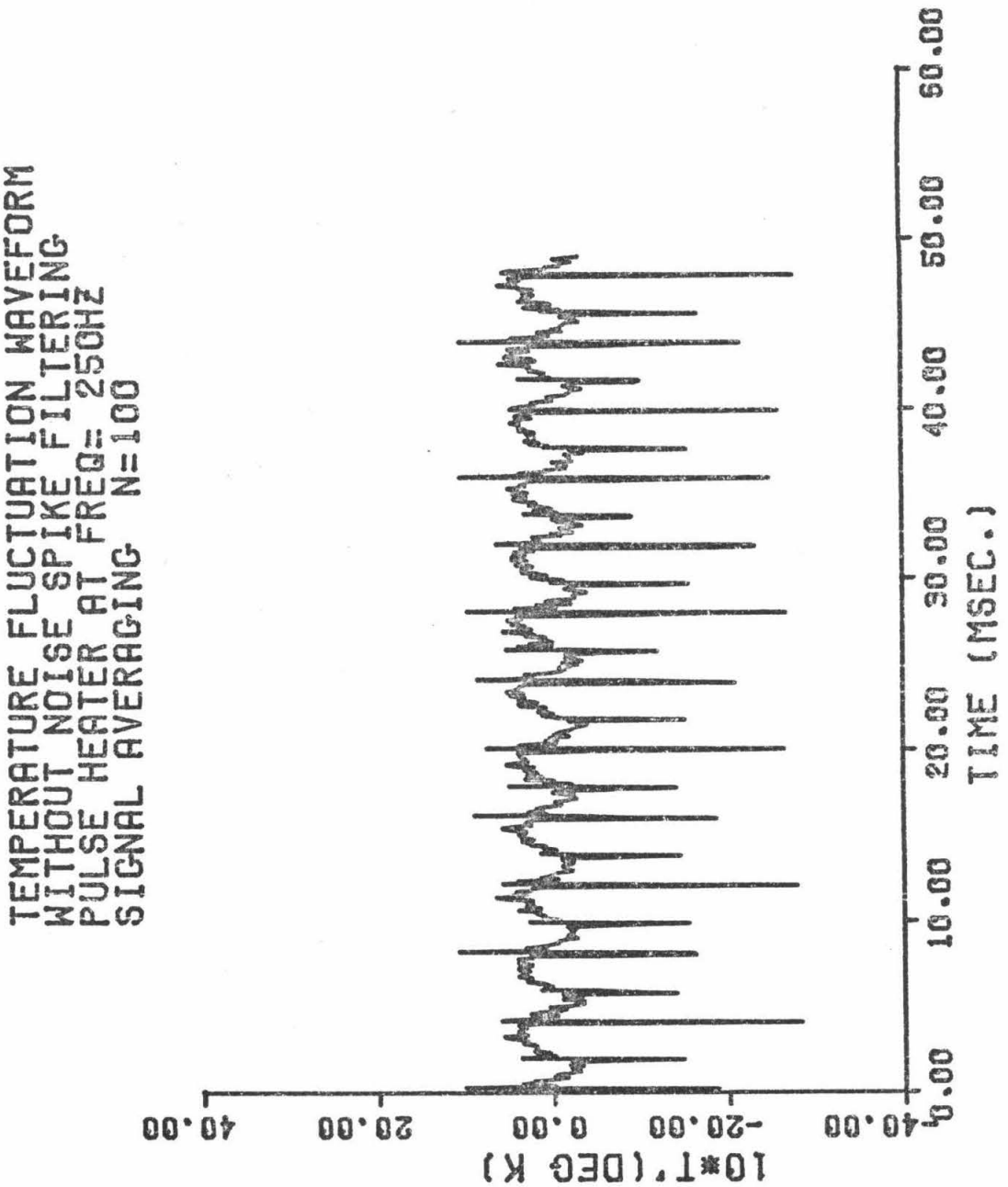

Fig. 5.48 Temperature Fluctuation Waveform
With Noise Spike Filtering

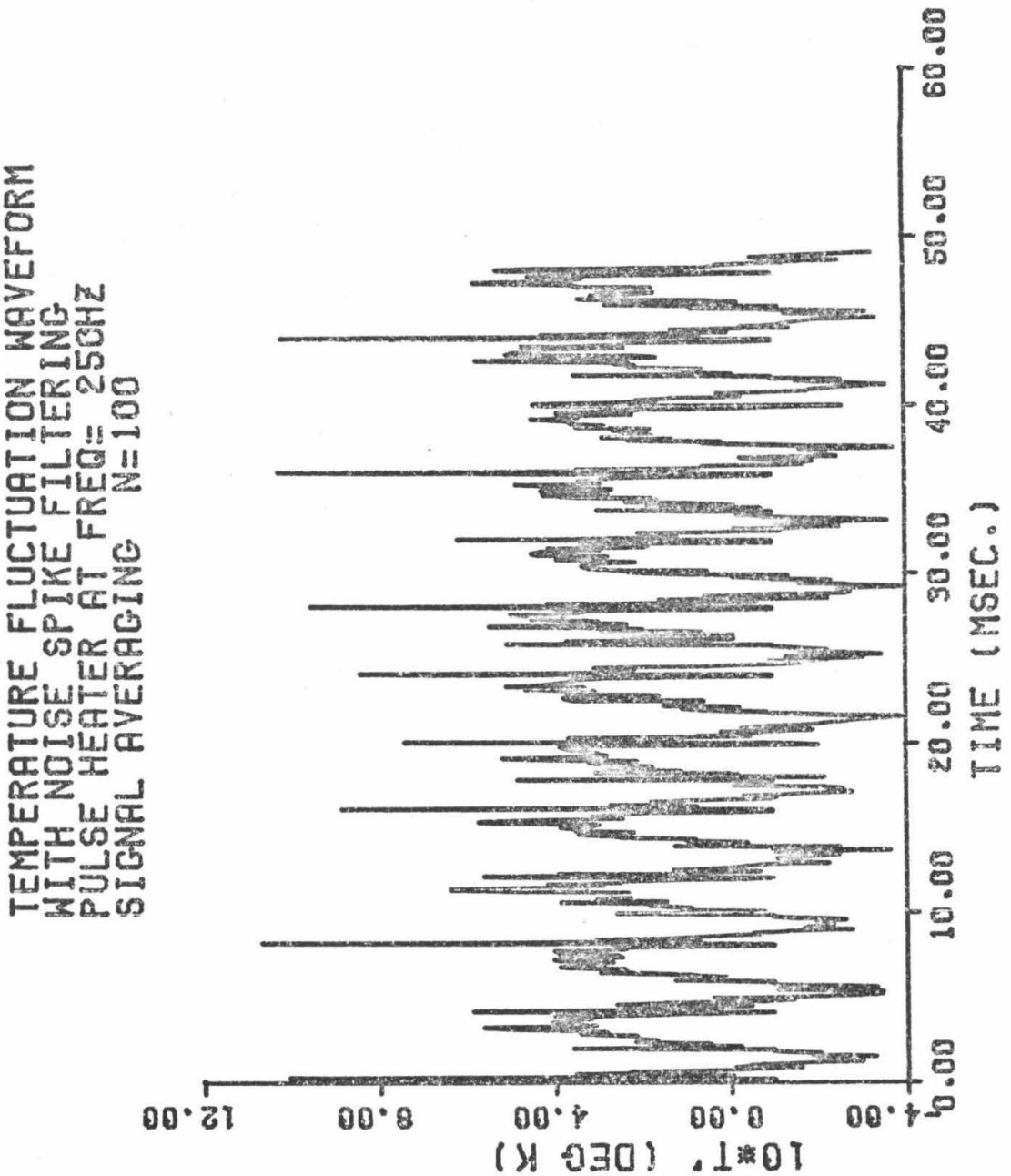

operations. This can be attributed to the fact that the probe amplifier had to amplify microvolts to volts, and hence at these high gains (approximately 50,000) some residual electrical noise is inevitable. However, when the Fourier coefficients of the waveform are evaluated using equations (4.33), the sums in the equations are taken over a large number of cycles resulting in further increase of signal-noise ratio.

5.5.3 Nozzle sound field produced by the pulse heater. The measurements of the sound field produced by operation of the pulse heater and comparison of the data with the theory of Chapter II are presented in figs. 5.49 - 5.56. Four sets of experiments were made at heater frequencies of 250 Hz, 300 Hz, 400 Hz, and 500 Hz, corresponding to values of β of .96, 1.16, 1.54, 1.93, respectively. For each frequency there are two graphs; the first shows measured values of the magnitude of $p'/\bar{p}$ at the six transducer positions plus the theoretical curve. The second graph of the set shows the measured values of the phase of $p'/\bar{p}$ and the theoretical values of the phase. The theoretical curves for $p'/\bar{p}$ were generated using the following procedure.

Since the heater by its geometry obviously produces a plane pressure disturbance when heating up the gas passing through it, the constant of integration in the theoretical solution was evaluated using the magnitude and phase of the downstream-running pressure wave. The method of calculating the downstream-running pressure wave has been described in Sections 2.5 and 5.4. From the measurement of the temperature fluctuation and pressure fluctuation at the entrance of the nozzle, the dimensionless entropy fluctuation Z_3 was evaluated

using equation (2.52):

$$Z_3 = \frac{\tilde{s}}{C_p} = \frac{\tilde{T}}{T} - \frac{\gamma - 1}{\gamma} \frac{\tilde{p}}{p} \quad . \tag{2.52}$$

Z_3 was then used to generate the theoretical solution for the $p'/\overline{p}$ distribution produced by the entropy fluctuation Z_3 . Then the theoretical solution for the $p'/\overline{p}$ distribution produced by the downstream-running wave was calculated. These two $p'/\overline{p}$ solutions were then added to give the complete solution corresponding to the sound field produced by the "bleedless" operation of the pulse heater.

The theoretical and experimental results show excellent agreement at 250 Hz down to reasonably good agreement at 500 Hz. At 500 Hz, the pressure signals due to the heater are comparable to the noise even after 100 signal-averaging operations (recall fig. 5.26), so less agreement is to be expected.

For frequencies of 250 Hz, 300 Hz, and 500 Hz (β = .96, 1.16, 1.93, respectively), the magnitude plots all show an increase of p'/p with distance along the nozzle. For the case of a pure pressure disturbance, recall that $p'/\overline{p}$ was essentially constant through the nozzle. Thus, the entropy fluctuation can be seen to be a noise source. At 400 Hz, that portion of the $p'/\overline{p}$ magnitude curve for the nozzle region exhibits an almost flat behavior. This implies that the sound field due to the entropy fluctuation and the sound field due to the downstream-running pressure wave have a phase relationship so as to cancel each other. Because of this anomalous behavior, it was decided to do the downstream wave cancellation for heater operation at 400 Hz.

Thus, this set of four experiments has verified the theory of

Fig. 5.49 Theoretical Solution and Experimental Data for the Amplitude of the Sound Field at 250 HZ Produced by Operation of the Pulse Heater. Theoretical Solution is calculated with the measured values of entropy fluctuation and downstream running pressure wave in the entrance section.

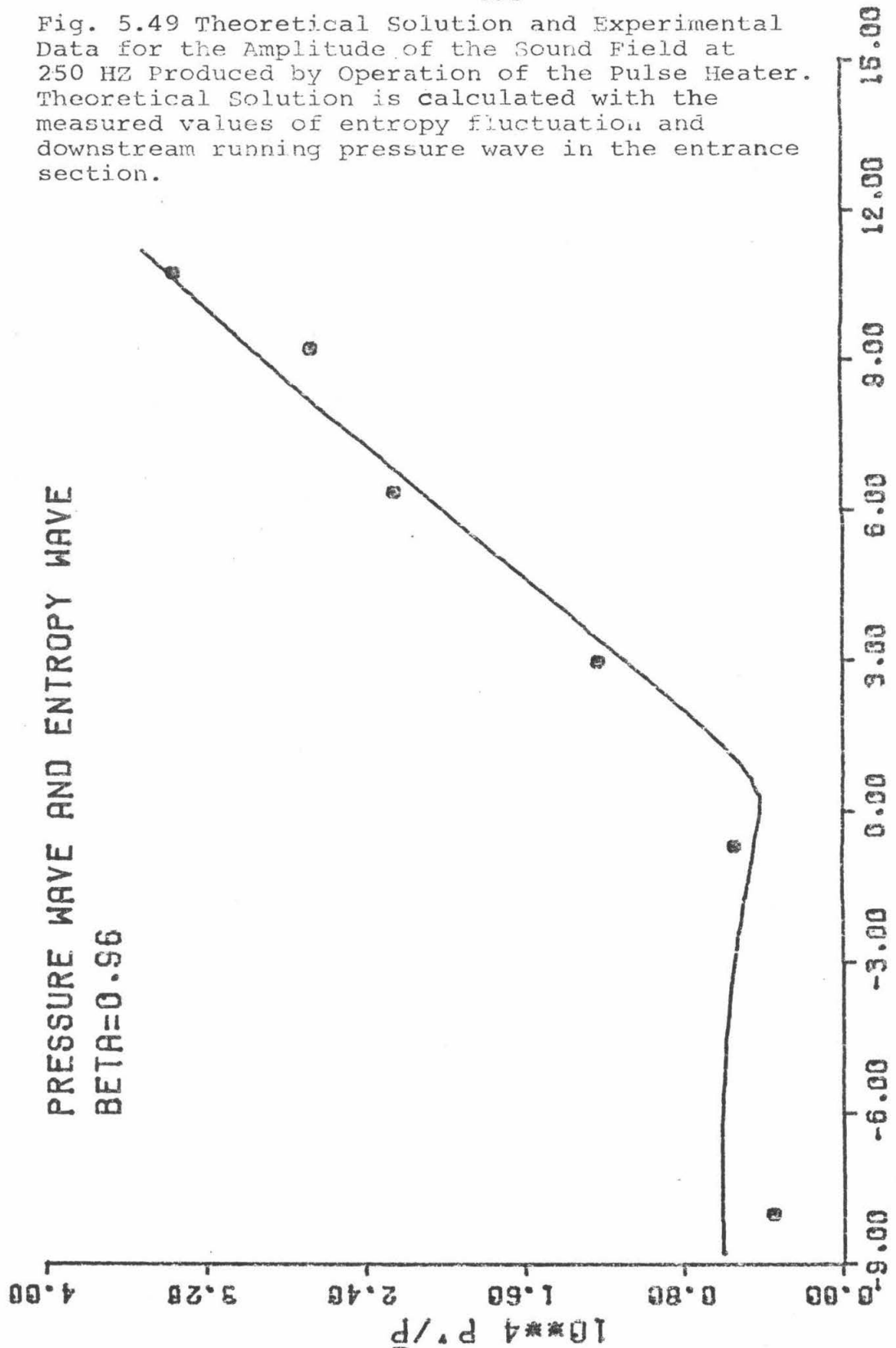

Fig. 5.50 Theoretical Solution and Experimental Data for the Phase of the Sound Field at 250 HZ Produced by Operation of the Pulse Heater. Theoretical solution is calculated with the measured values of entropy fluctuation and downstream running pressure wave in the entrance section.

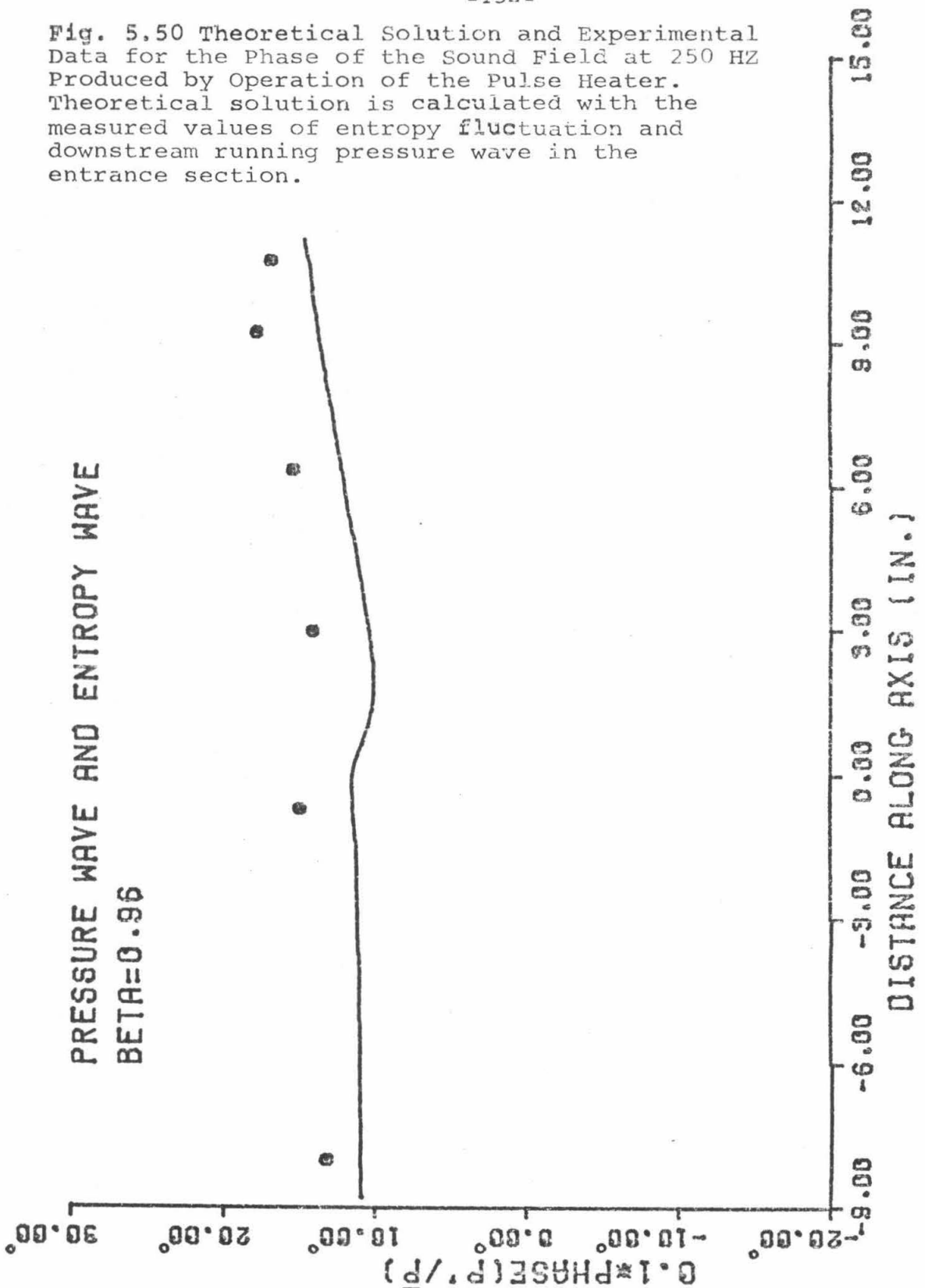

Fig. 5.51 Theoretical Solution and Experimental Data for the Amplitude of the Sound Field at 300 HZ Produced by Operation of the Pulse Heater. Theoretical solution is calculated with the measured values of entropy fluctuation and downstream running pressure wave in the entrance section.

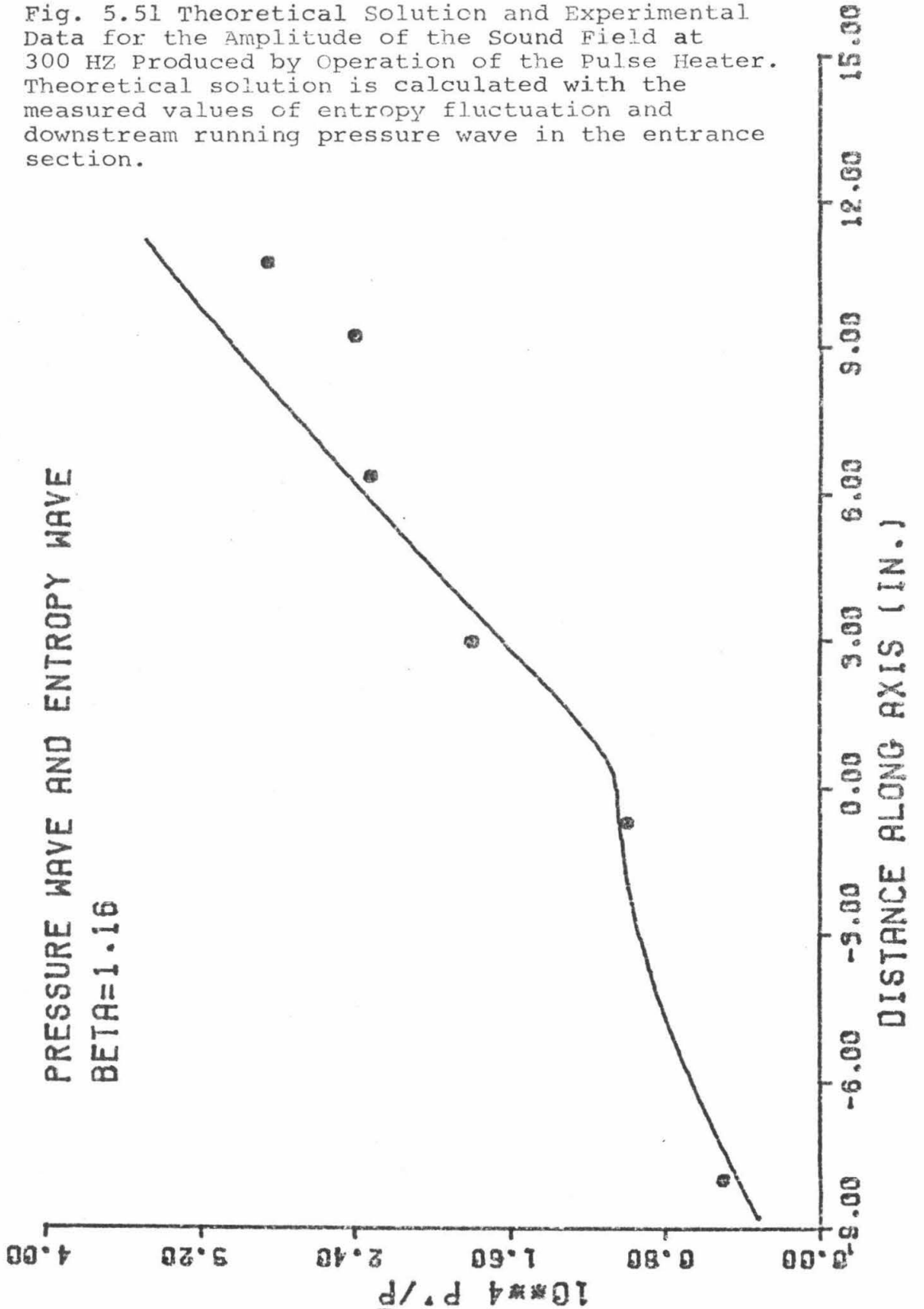

Fig. 5.52 Theoretical Solution and Experimental Data for the Phase of the Sound Field at 300 HZ Produced by Operation of the Pulse Heater. Theoretical solution is calculated with the measured values of entropy fluctuation and downstream running pressure wave in the entrance section.

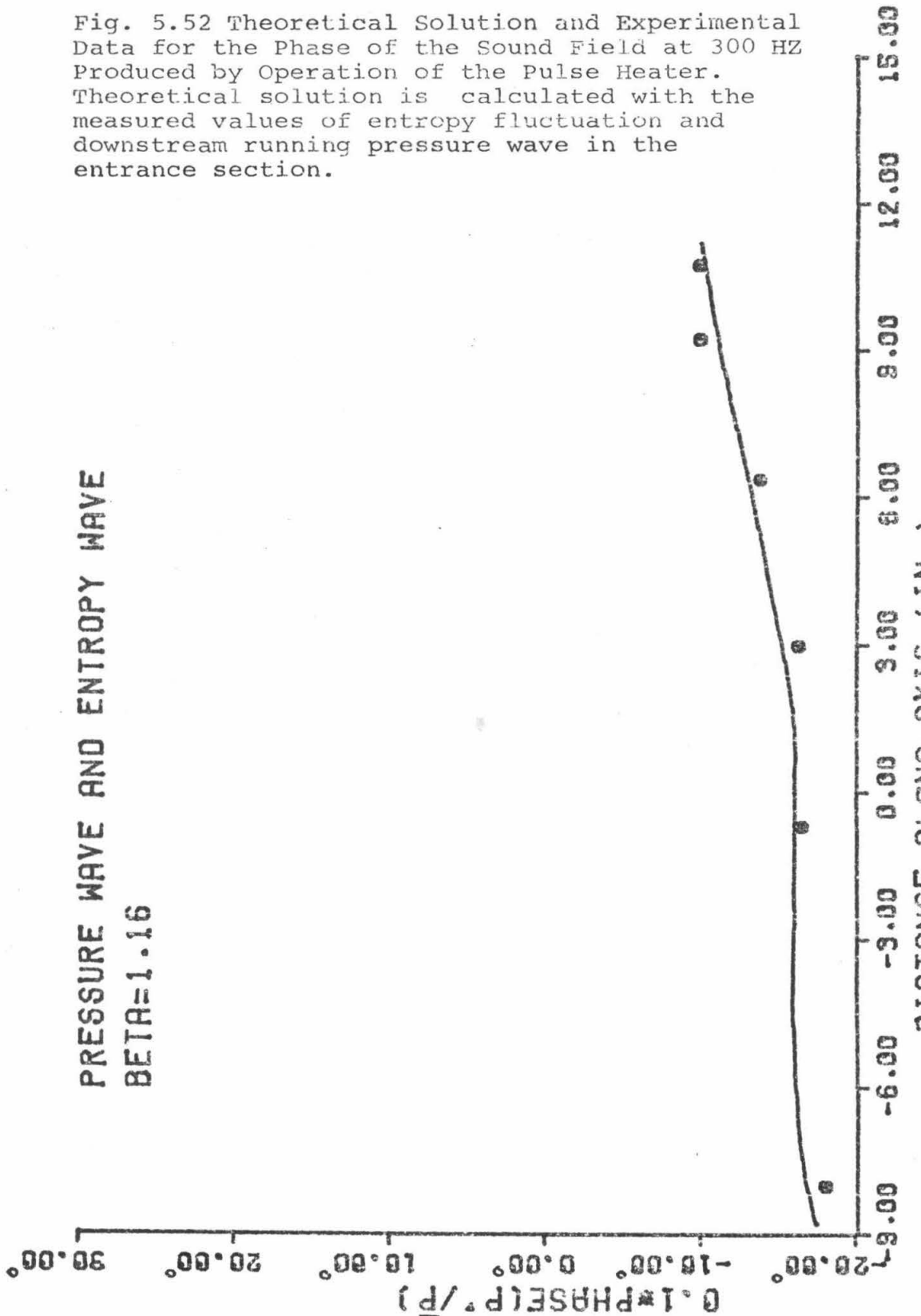

Fig. 5.53 Theoretical Solution and Experimental Data for the Amplitude of the Sound Field at 400 HZ Produced by Operation of the Pulse Heater. Theoretical solution is calculated with the measured values of entropy fluctuation and downstream running pressure wave in the entrance section.

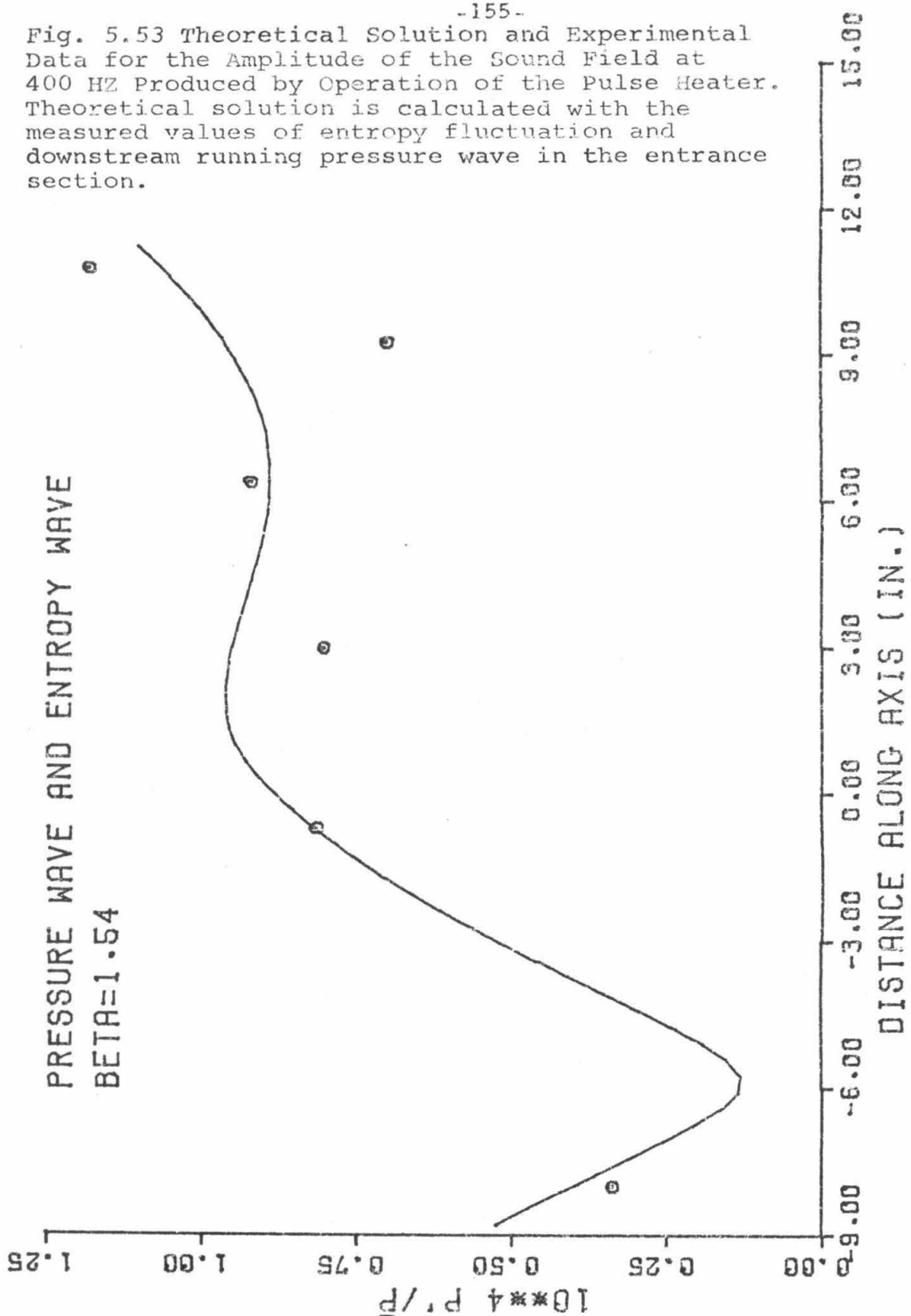

Fig. 5.54 Theoretical Solution and Experimental Data for the Phase of the Sound Field at 400 HZ Produced by Operation of the Pulse Heater. Theoretical solution is calculated with the measured values of entropy fluctuation and downstream running pressure wave in the entrance section.

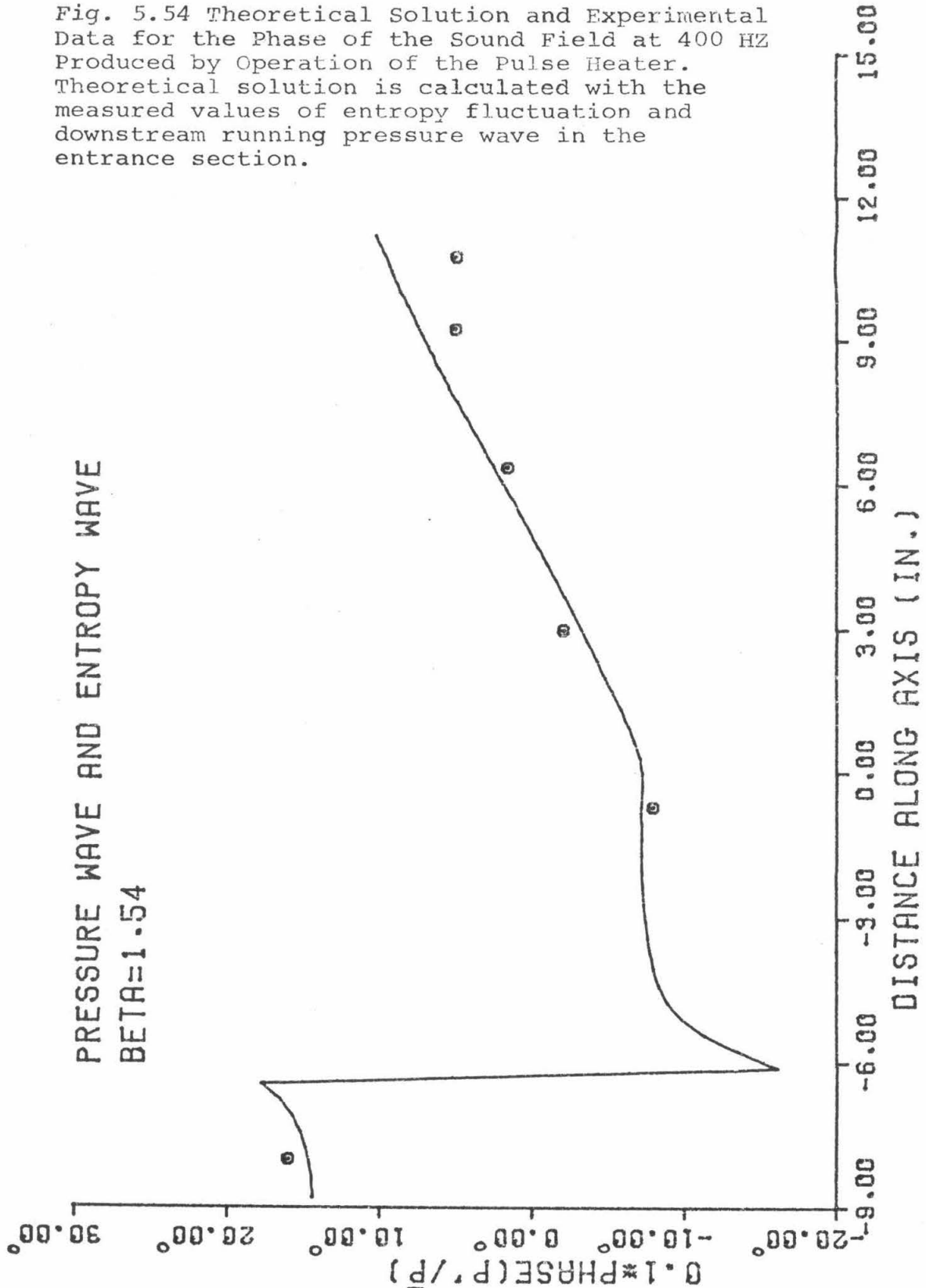

Fig. 5.55 Theoretical Solution and Experimental Data for the Amplitude of the Sound Field at 500 HZ Produced by Operation of the Pulse Heater. Theoretical solution is calculated with the measured values of entropy fluctuation and downstream running pressure wave in the entrance section.

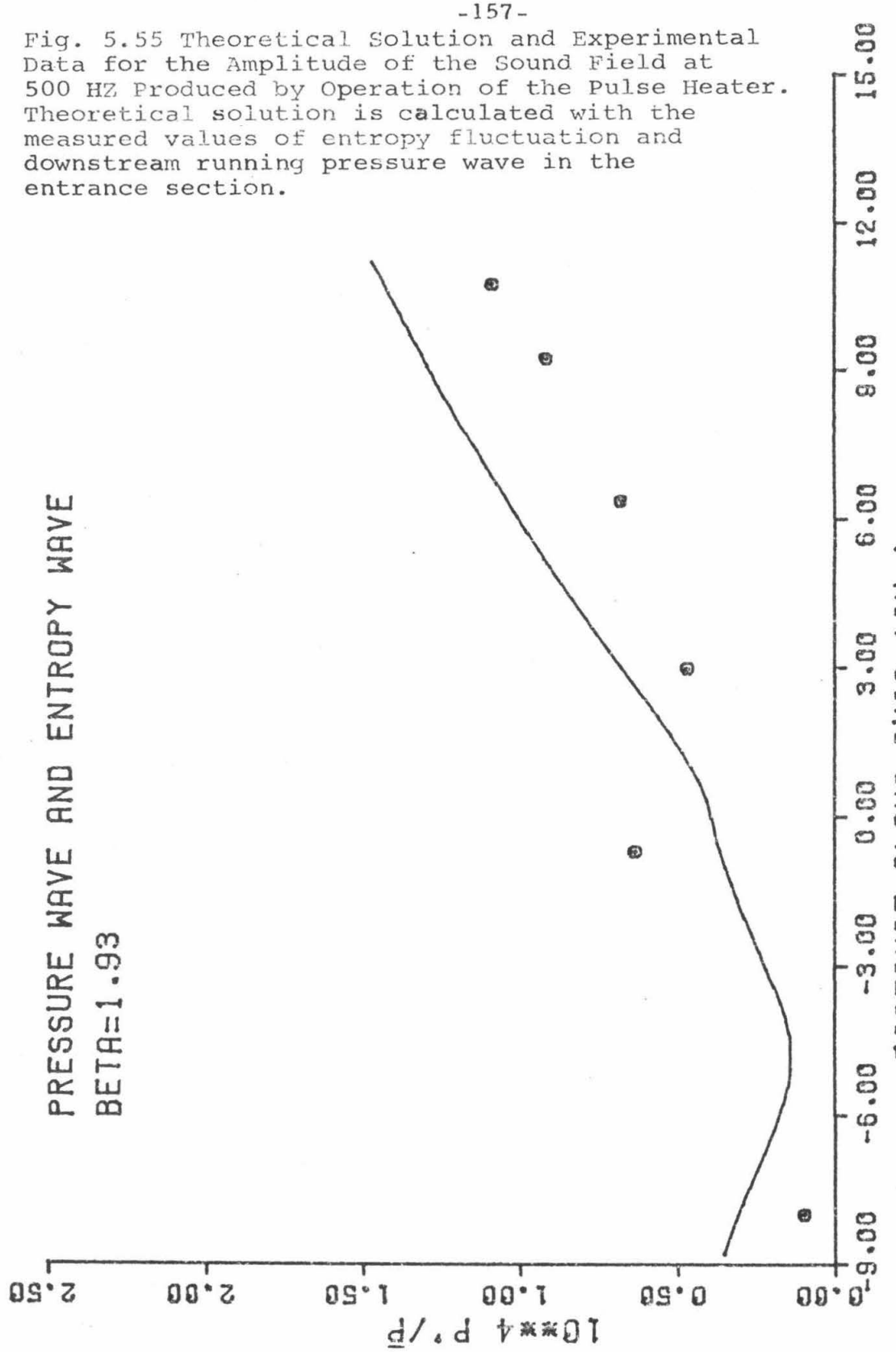

Fig. 5.56 Theoretical Solution and Experimental Data for the Phase of the Sound Field at 500 HZ Produced by Operation of the Pulse Heater. Theoretical Solution is calculated with the measured values of entropy fluctuation and downstream running pressure wave in the entrance section.

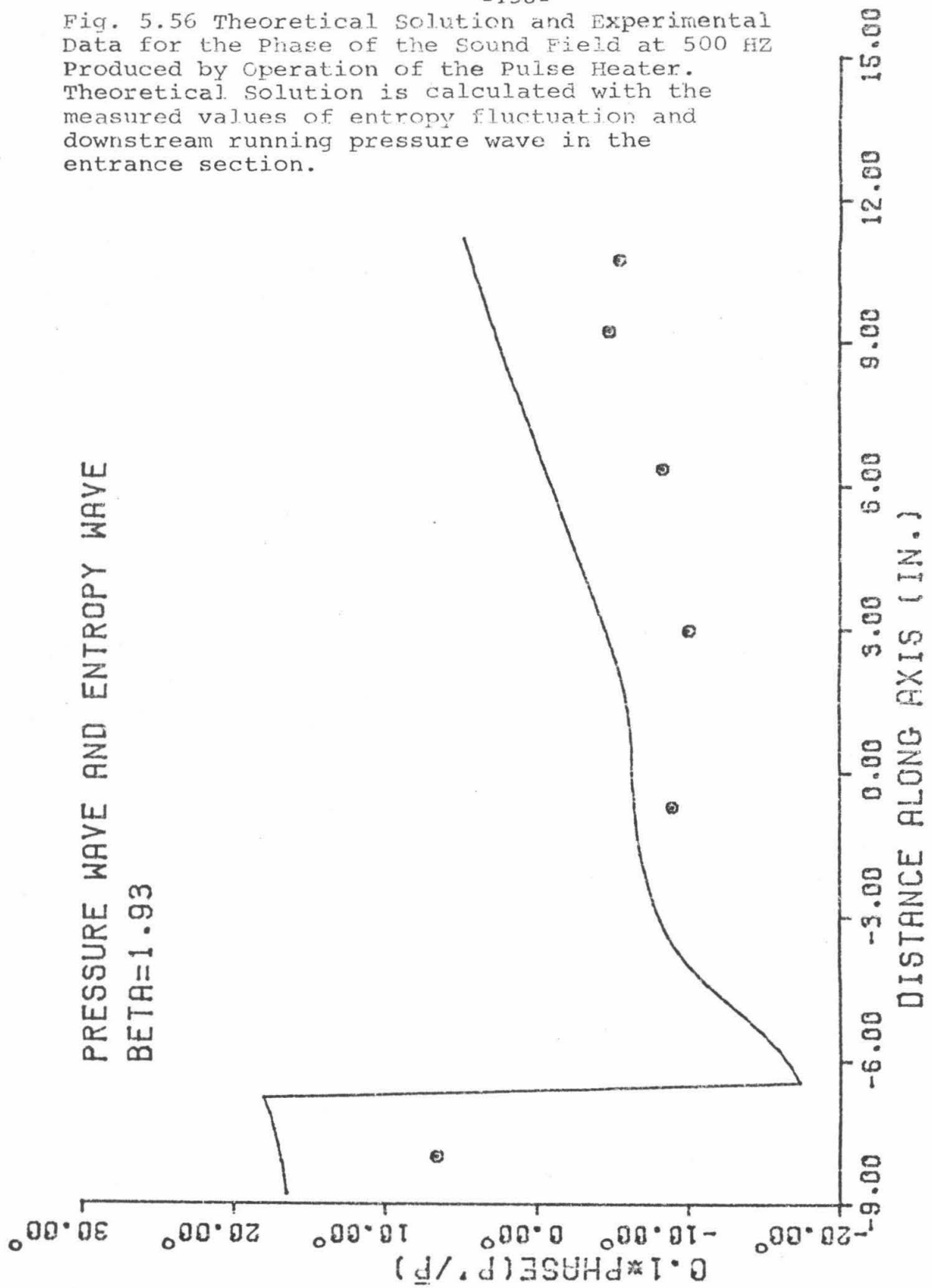

Chapter II on two points: (i) it correctly describes the production of noise by a one-dimensional entropy wave in an accelerating mean flow; (ii) it correctly describes the interaction between entropy disturbances and incident pressure disturbances.

5.6 Sound Field Produced by a Pure Entropy Wave

5.6.1 Scope. Although the experiments and analytical work described in the last section verified the fact that temperature and density uniformities (e.g. entropy waves) are a source of noise, it was still desired to show this experimentally for an actual pure entropy disturbance. As described previously, this disturbance would be achieved by running the heater and bleed valve system together so as to cancel the downstream-running pressure wave created during heating of the gas.

5.6.2 Cancellation of the downstream-running pressure wave. Because of the complex pattern of transverse modes created by the bleed valve flow within the heater boundaries, no predetermined method of cancellation was feasible. The processes were done strictly on a trial and error basis. Various orifice sizes and delay times between the time the valve was at its maximum open position and the time the pulse heater turned on were tried until the downstream-running pressure wave was minimized. As in the other experiments, the magnitude of the downstream-running wave was evaluated using equations (2.52) and the pressure fluctuation data at the transducer positions 2 and 3 (-8.0 in. and -0.5 in., respectively).

One guideline for the cancellation process, however, was evi-

dent. The short distance between the bleed valve slits and orifice caused a delay between maximum open valve position and maximum bleed flow through the slits. Therefore, the time delay was set so as to have the heater turned on after the valve shaft was at maximum open position.

At 400 Hz, it was found that the orifice size which made the pressure fluctuations from the bleed valve approximately the same size as the heater pressure fluctuations in the entrance section was 4/64 in. in diameter. This size orifice was selected to be the one used in the compensation process.

Several experiments were then conducted in which the delay between the times of maximum valve open position and switching on of the heater was varied. Table 5-3 shows the variation of the magnitude of the downstream-running wave with time delay.

Table 5-3. Cancellation of Downstream-Running Pressure Wave Produced by Heater Operating at Full Power and Frequency of 400 Hz by the Bleed System.

Forward running pressure wave from heater alone, $p^+/\bar{p} = 5.53 \times 10^{-5}$.

orifice diameter	time delay	magnitude of downstream-running wave p^+/p	
6/64 in.	-0.15 msec	7.02×10^{-5}	
5/64 in.	-0.15 msec	5.44×10^{-5}	
4/64 in.	-0.4 msec	3.04×10^{-5}	
4/64 in.	+0.35 msec	1.05×10^{-5}	* minimum
3/64 in.	-0.15 msec	3.51×10^{-5}	
3/64 in.	-0.4 msec	3.20×10^{-5}	

As can be seen from Table 5-3, with a 4/64-in. diameter orifice and a time delay of +0.35 msec from maximum open position, the downstream-running wave at 400 Hz is reduced by a factor of 5.5. At this magnitude the values of $p'/\overline{p}$ at transducer positions 2 and 3 were down at the residual noise level (after 100 signal-averaging operations) so further attempts at reduction would be meaningless.

The fact that the entrance section signal levels are the same values as the noise will make phase measurements meaningless in the entrance section since the phases measured will be the random values of the noise rather than those of the heater-induced signal. Hence, in this special case of this experiment, the phase of the pressure fluctuation at transducer position 7 (10.75 in. from nozzle entrance) will be used to initialize the theoretical curve for the phase of p'/p with the experimental data.

The results of the experiments to produce a pure entropy wave are shown in figs. 5.57 and 5.58. The theoretical curves shown are calculated for an entropy wave based on temperature fluctuation data at -0.9 in., a zero magnitude pressure fluctuation at -0.5 in., and a zero magnitude downstream-running pressure wave. This is the ideal situation of a pure entropy wave. Figure 5.57 illustrating the $p'/\overline{p}$ magnitude data indicates excellent agreement with theory and experiment. The phenomenon of noise production solely by temperature (entropy) nonuniformities has also been verified.

The phase plot on fig. 5.58 indicates reasonably good agreement except at -8.0 in. from the nozzle entrance. As explained above, this can be attributed to the fact that the signal level was

Fig. 5.57 Amplitude of the Sound Field at 400 HZ for a Pure Entropy Wave in the Entrance Section Theoretical solution is for a pure entropy wave with its magnitude and phase values based on experimental data. Data points obtained from synchronized operation of the bleed valve and pulse heater at a frequency of 400 HZ so as to cancel the downstream running pressure wave.

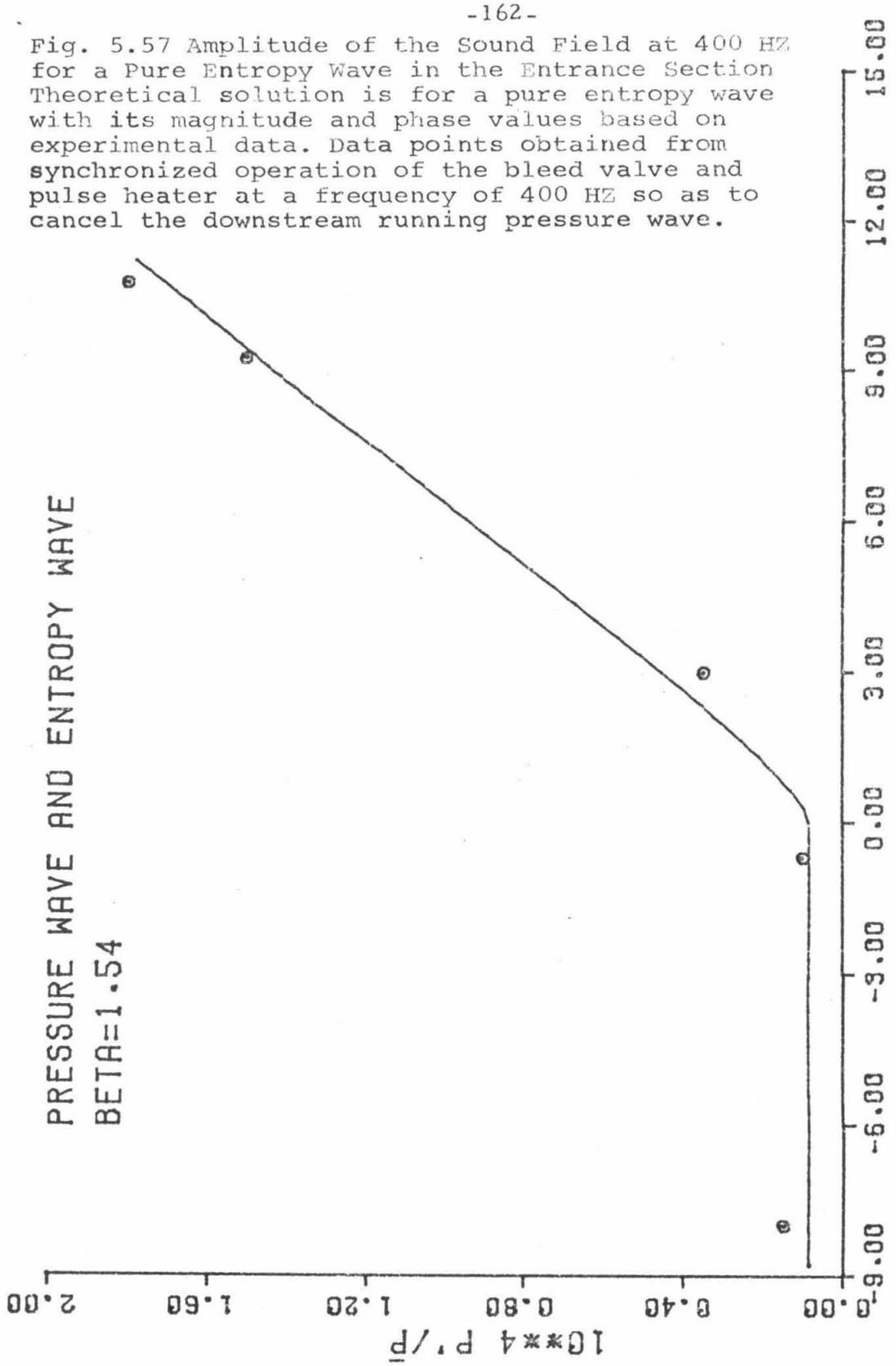

Fig. 5.58 Phase of the Sound Field at 400 HZ for a Pure Entropy Wave in the Entrance Section. Theoretical solution is for a pure entropy wave with its magnitude and phase values based on experimental data. Data points obtained from synchronized operation of the bleed valve and pulse heater so as to cancel the downstream running pressure wave.

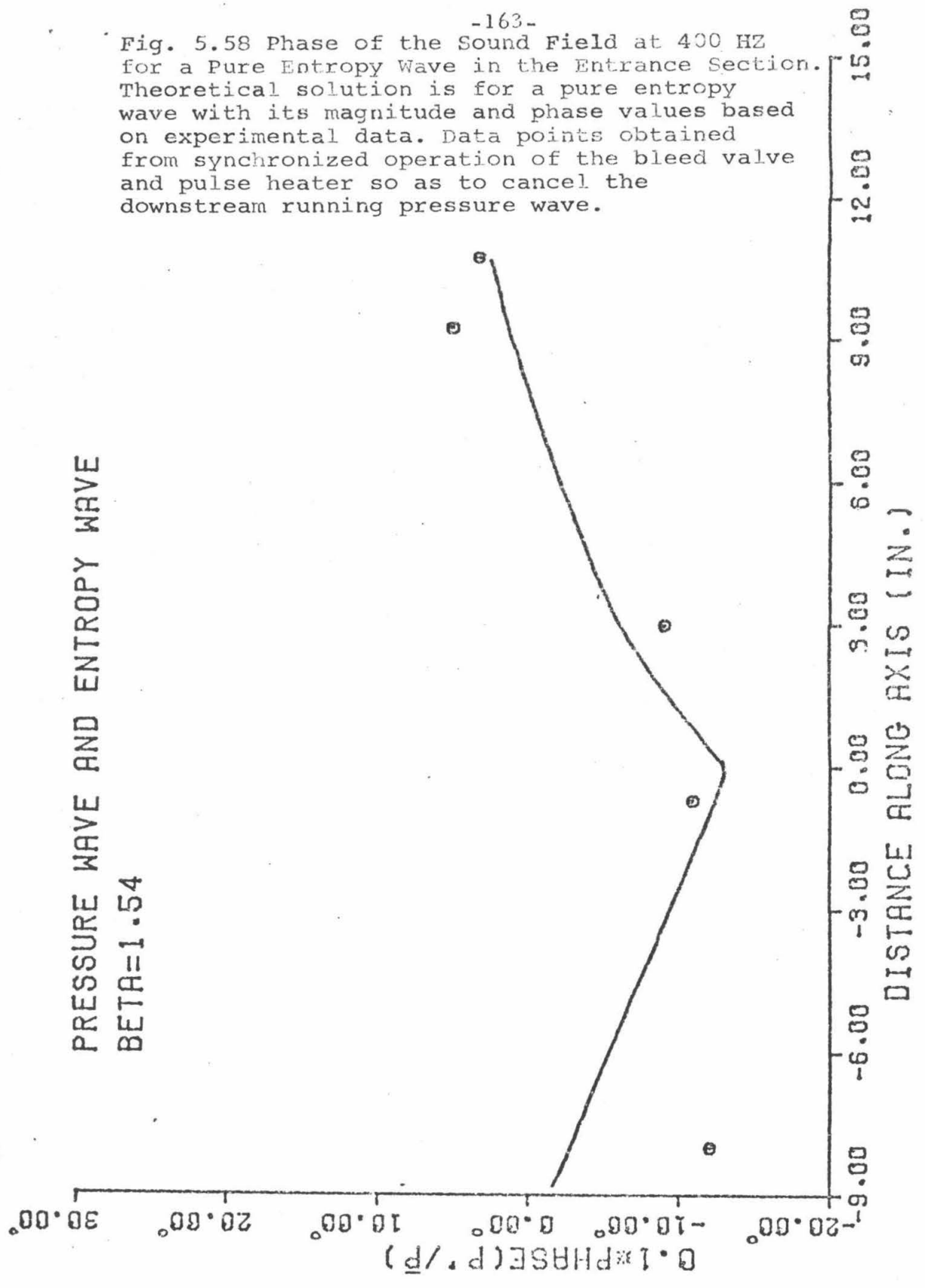

within the noise level and hence a random phase of the noise was measured.

VI. INVESTIGATION OF THE SOUND FIELD EXTERNAL TO THE NOZZLE

6.1 External Field Measurements

Having adequately described the sound field in the supersonic nozzle, the next logical step was to investigate the propagation of the sound at the nozzle exit into the external field consisting of a supersonic jet and a "bounded free space" environment simulated by the anechoic chamber described in Section 3.1. The experiments described herein consisted of measurements of the noise from the unperturbed supersonic jet and measurements of the noise field produced when only the bleed valve system was used to perturb the jet. Study of the external noise produced by an entropy wave in the nozzle will be described in later work, which will use a more efficient and sophisticated signal-averaging process. The results for the bleed valve sound field consist of (i) amplitude and phase of the pressure fluctuations along arcs 3 ft., 6 ft., and 9 ft. from the nozzle exit in both the horizontal and vertical planes passing through the center of the nozzle, and (ii) cross correlations between the pressure fluctuations at the nozzle exit and the pressure fluctuations in the external field.

6.2 Structure of the Supersonic Jet

Unlike the simple one-dimensional isentropic flow in the nozzle, the supersonic jet leaving the nozzle is so exceedingly complex as to make any theoretical analysis of sound propagation within its boundaries impossible. Hence, a comparison of the experimental results in this chapter with a corresponding theory cannot be pre-

sented here.

Although the study of the propagation of sound in a perturbed jet is a new endeavor, many experimental studies of unperturbed jet noise are available for comparison with measurements in this experiment. By comparing these contemporary studies with the work presented here, it will be shown that the jet under study and instrumentation have operated as expected.

After a review of supersonic jet characteristics, a comparison will be made of this thesis' results and past and current supersonic jet studies.

A supersonic jet can be divided into the following distinct regions: (1) supersonic potential core, (2) supersonic mixing layer, (3) transition region, (4) subsonic turbulent jet. An estimate of the size and location of each of these regions can be made from empirical formulas found by Nagamatsu and Sheer[15], which are:

length of potential core

$$L_c = \ell_c/D = 5.22\, M^{0.9} + 0.22 \qquad (6.1)$$

length of supersonic region

$$L_s = \ell_s/D = 5\, M^2 + 0.8 \qquad (6.2)$$

where D is the hydraulic diameter of the jet which, for the experiment, is 1.05 in. At an exit Mach number of 1.35, one has

$$\ell_c = 7.412 \text{ in.} \quad , \quad \ell_s = 10.41 \text{ in.}$$

Data on the width of the jet are usually specified in terms of its velocity half width, $\Delta_{\frac{1}{2}}$, which is the distance from the centerline at which the axial velocity is half its value at the corresponding point

on the centerline. For the supersonic mixing layer, an expression for the velocity half width is given from ref. 53 as

$$\Delta_{\frac{1}{2}} = \frac{C}{2}(1 + T_j/T_a)x \ , \qquad (6.3)$$

where

T_j/T_a = $\frac{\text{temperature in potential core}}{\text{ambient temperature}}$

C = empirical constant = 0.1 to 0.11

x = distance from nozzle exit.

For the experiment, the half width at the end of the potential core is calculated to be .642 in. In the subsonic turbulent region, far away from the core region, the half width is given by the relation

$$\Delta_{\frac{1}{2}} = \varepsilon x \qquad \text{for} \qquad x \gg D \ , \qquad (6.4)$$

where again ε = 0.1 to 0.11. Thus, 10 ft. away from the nozzle exit the half width is 10.8 in.

In the acoustic measurements described in this chapter, it was necessary to know where the jet boundary was located so the microphone could be placed outside of this boundary. Rather than using the half width, a more meaningful coordinate would be where the jet velocity was down to 5 per cent of its centerline value. Heskestad[54] measured velocity profiles in a plane air jet, and his results show that the axial velocity is down to 5 per cent of the local centerline value at about 2.5 half widths. Thus, for purposes of defining the subsonic jet boundary, the following relation is used:

$$\Delta_j = .25\,x \ . \qquad (6.5)$$

The validity of this approximation can be seen by considering the results of Albertson[55], who measured the boundary layer thickness of

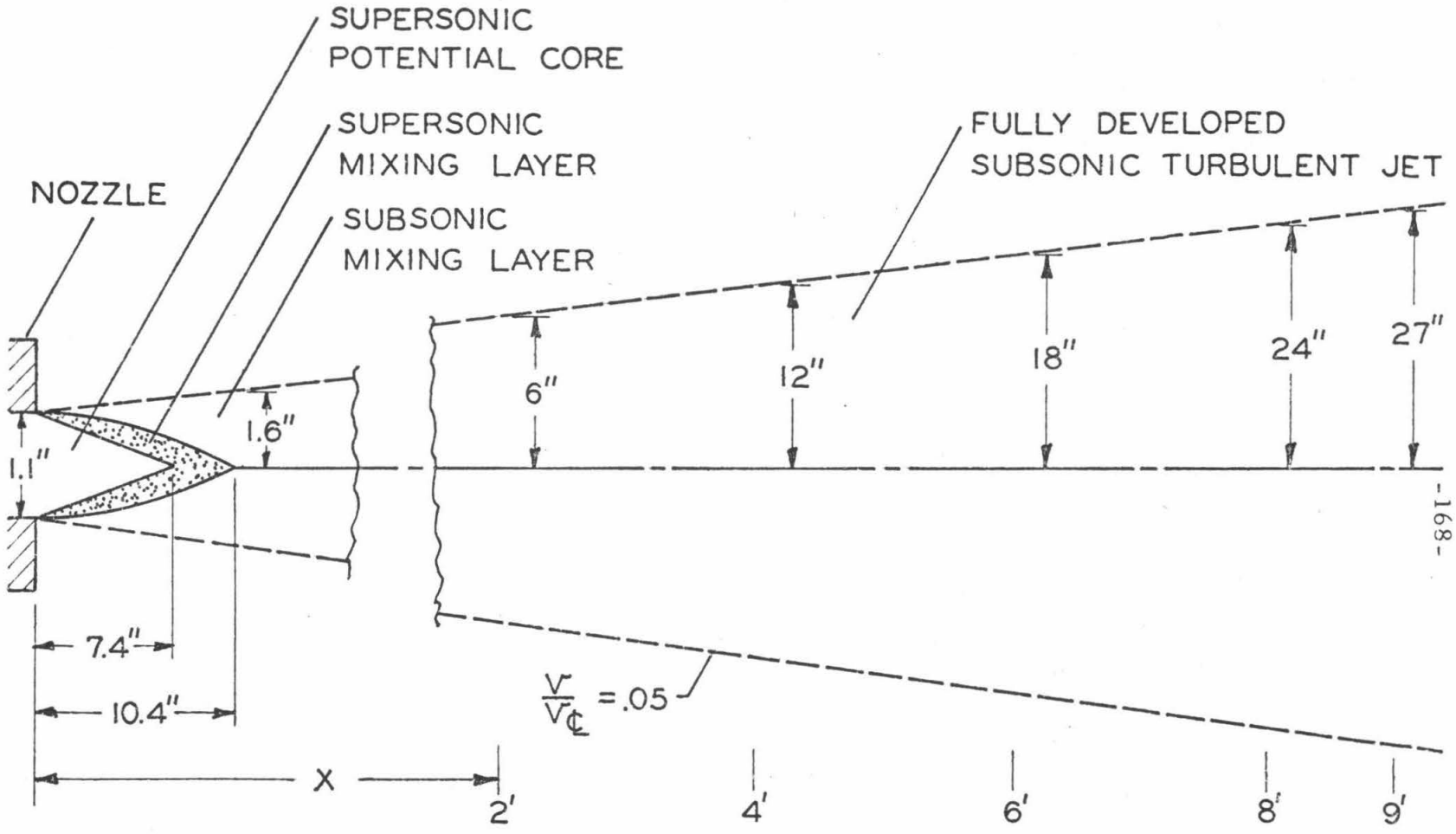

Fig. 6.1 Regions of Supersonic Jet

jet in water and found

$$\delta = .27\, x \quad . \tag{6.6}$$

The above equations and results are used to map out the jet boundaries shown in fig. 6.1. The microphone was placed outside this boundary to reduce the flow noise produced by the interaction of the microphone and the velocity field of the jet. Note that at the rear of the chamber, flow patterns are set up due to the jet impinging on the walls. It must be concluded that inevitably some of the sound measurements in the rear of the chamber originate from flow from the jet impinging on the head of the microphone.

6.3 Jet Noise Field

6.3.1 Directivity measurements. Measurements of the r.m.s. level of the jet noise were taken along 3 ft., 6 ft., and 9 ft. arcs centered at the nozzle exit and lying in horizontal and vertical planes passing through the center of the nozzle. The nozzle pressure was maintained to within 0.5 psi of atmospheric pressure or slightly higher to prevent the formation of strong shocks at the nozzle exit.

The r.m.s. values were computed from 1024 word records of digital data. The results are shown in figs. 6.2 and 6.3. Note in fig. 6.3 that there are two abnormally high noise levels on the 9 ft. arc. This can be attributed to the fact that these measurements were taken in the region of strong jet flow. Comparison of the angular dependence of the jet noise was made with reported measurements given in refs. 15 and 17. This comparison is shown in fig. 6.4.

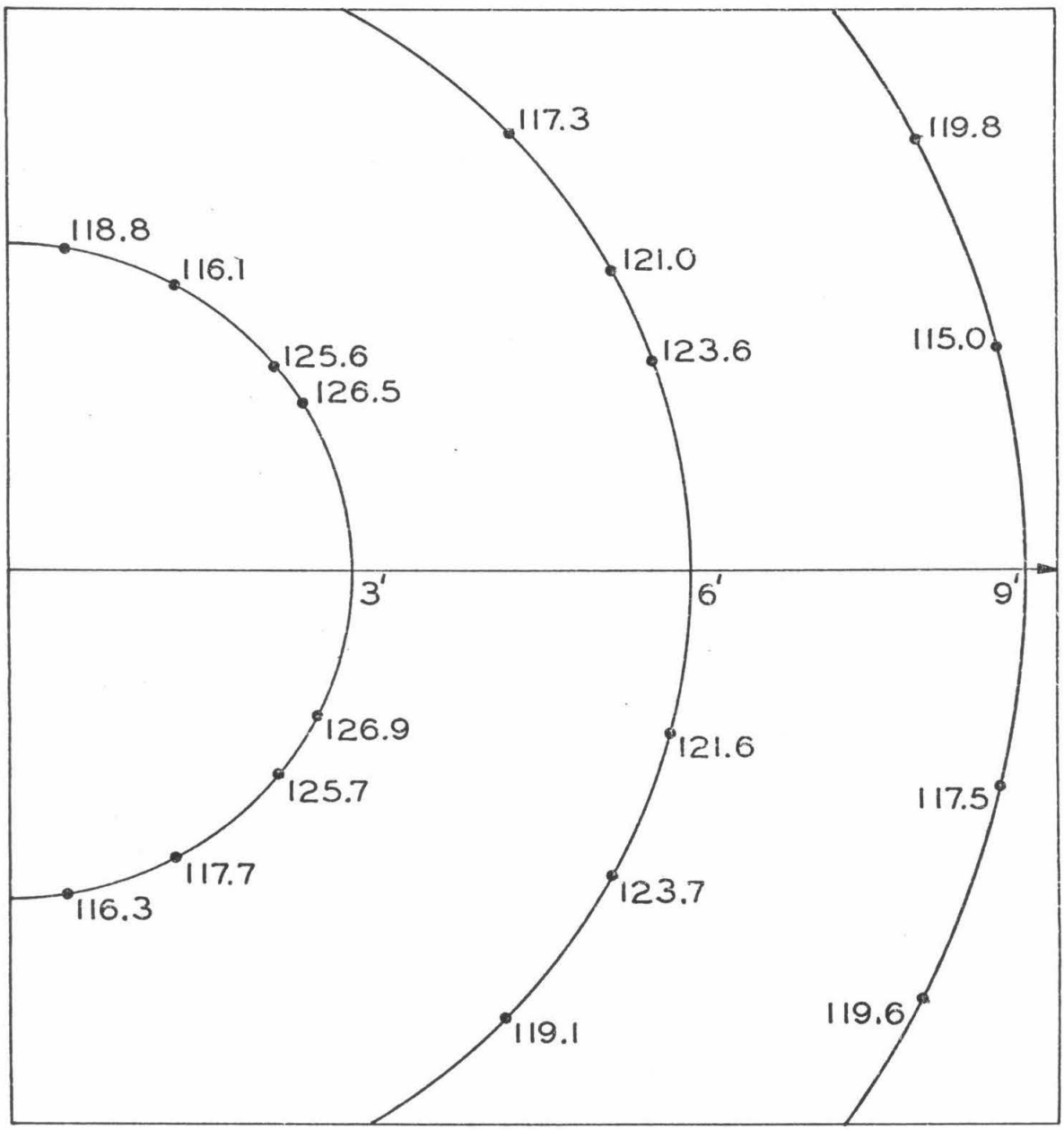

Fig. 6.2 The Jet Noise Field in the Horizontal Plane Passing Through the Jet Axis. R.M.S. values of the sound level are given in units of DBA.

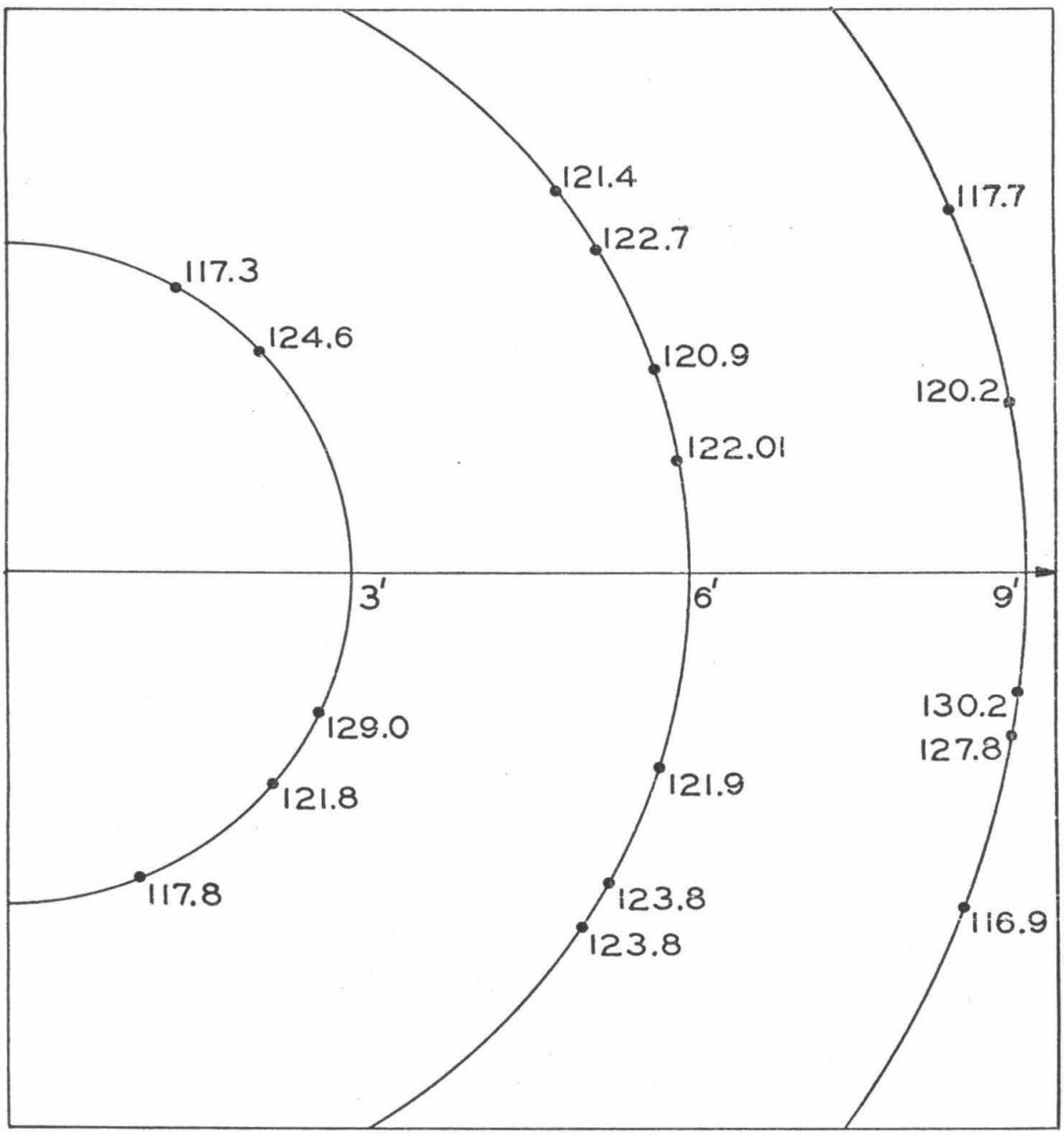

Fig. 6.3 The Jet Noise Field in the Vertical Plane Passing Through the Jet Axis. R.M.S. values of the sound level are given in units of DBA.

Nagamatsu[15] reported the angular dependence of a Mach 1.4, 2-in. circular jet at a 10 ft. radius from the nozzle (54 diameters away). These data are shown in the upper curve of fig. 6.4. Also shown are the data for this experiment for the 6 ft. arc in the horizontal plane. This arc is 70 hydraulic diameters away. The close agreement between the two curves indicates that far away from the nozzle exit, the rectangular nozzle appears essentially the same as an axisymmetric nozzle. The lower curve in fig. 6.4 shows the angular dependence for the measurements along the 3 ft. arc in fig. 6.2. The dependence is given in decibels relative to the noise level at $\pm 30^{o}$. Howes[17] gives similar data for an axisymmetric jet exiting from a convergent-divergent nozzle with a 3.1 design pressure ratio. This corresponds to an exit Mach number of 1.38. The curve shows that Howe's data and the data of this experiment fall on essentially the same curve. Thus, directivity measurements have been shown to agree with other reported results.

6.3.2 Jet noise spectra. The final phase of jet noise measurements consisted of determining the noise spectra. The Fast Fourier Transform with a rectangular window function was used on 1024-word digital data records to compute a spectrum between 0 and 5 KHz. The maximum frequency of 5 KHz is the Nyquist frequency for the selected sampling rate of 10 KHz. This sampling rate was based on computer capabilities to give a 10 Hz spectrum resolution. Two sets of typical spectra results are shown in figs. 6.5 through 6.8. Each set shows spectra amplitudes on a linear scale (psia) and a logarithmic scale (DBA). Both sets of plots show that

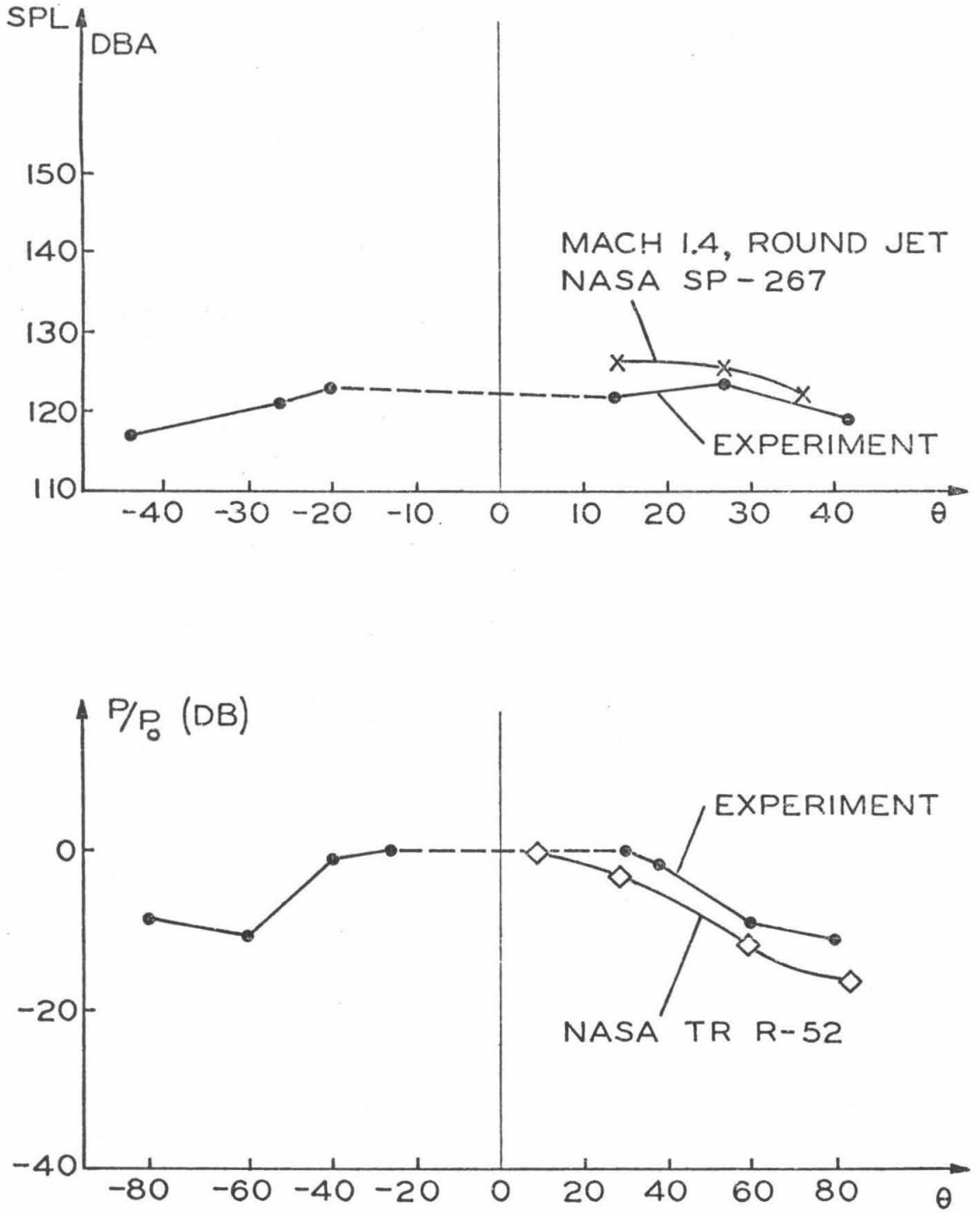

Fig. 6.4 Comparison of Jet Noise Data of This Experiment with That of Other Reported Supersonic Jet Noise Studies.

Fig. 6.5 Amplitude Spectrum on a Linear Scale of the Jet Noise at a Large Distance from the Jet Boundary.

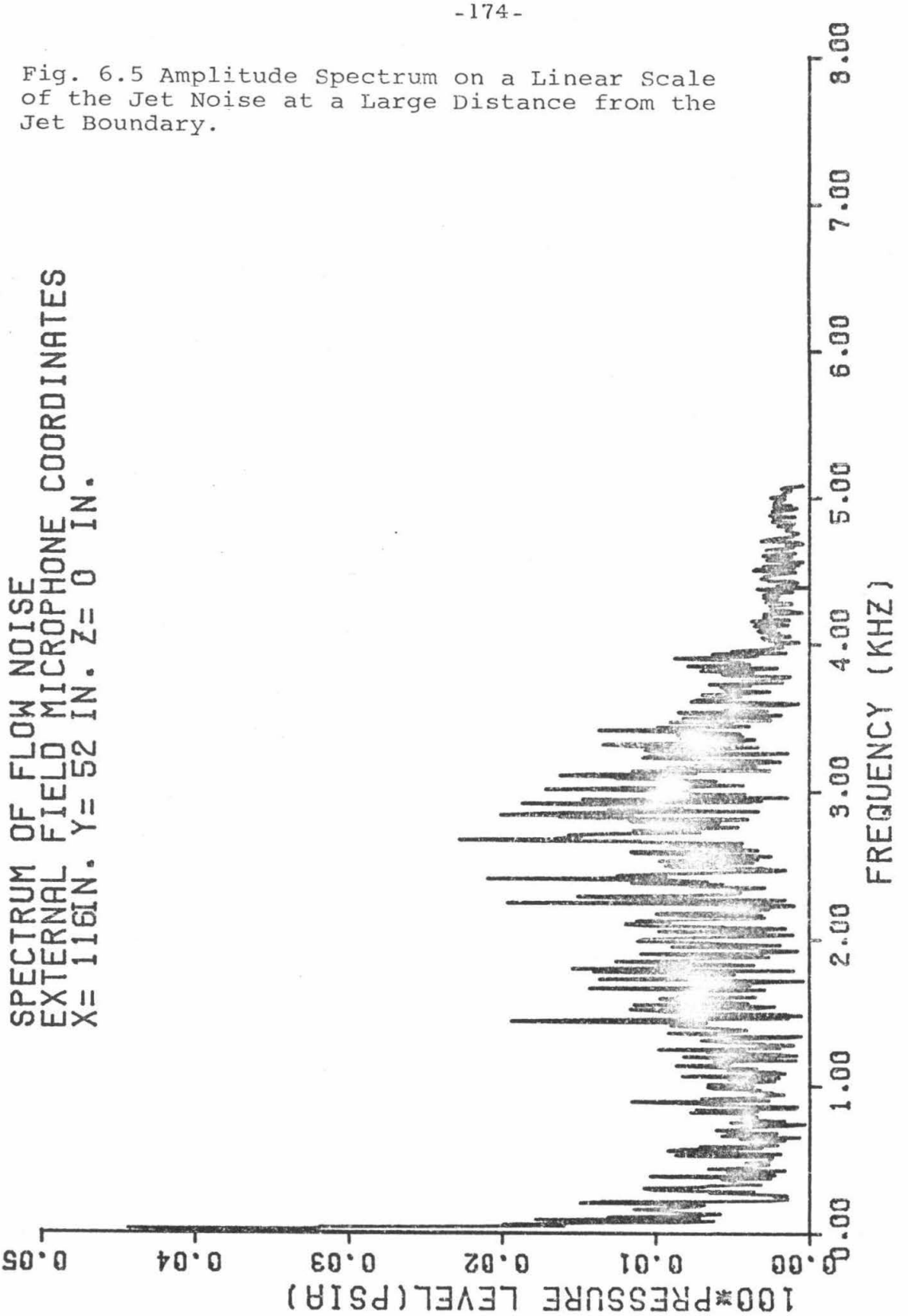

Fig. 6.6 Amplitude Spectrum on a Logarithmic Scale of the Jet Noise at a Large Distance from the Jet Boundary.

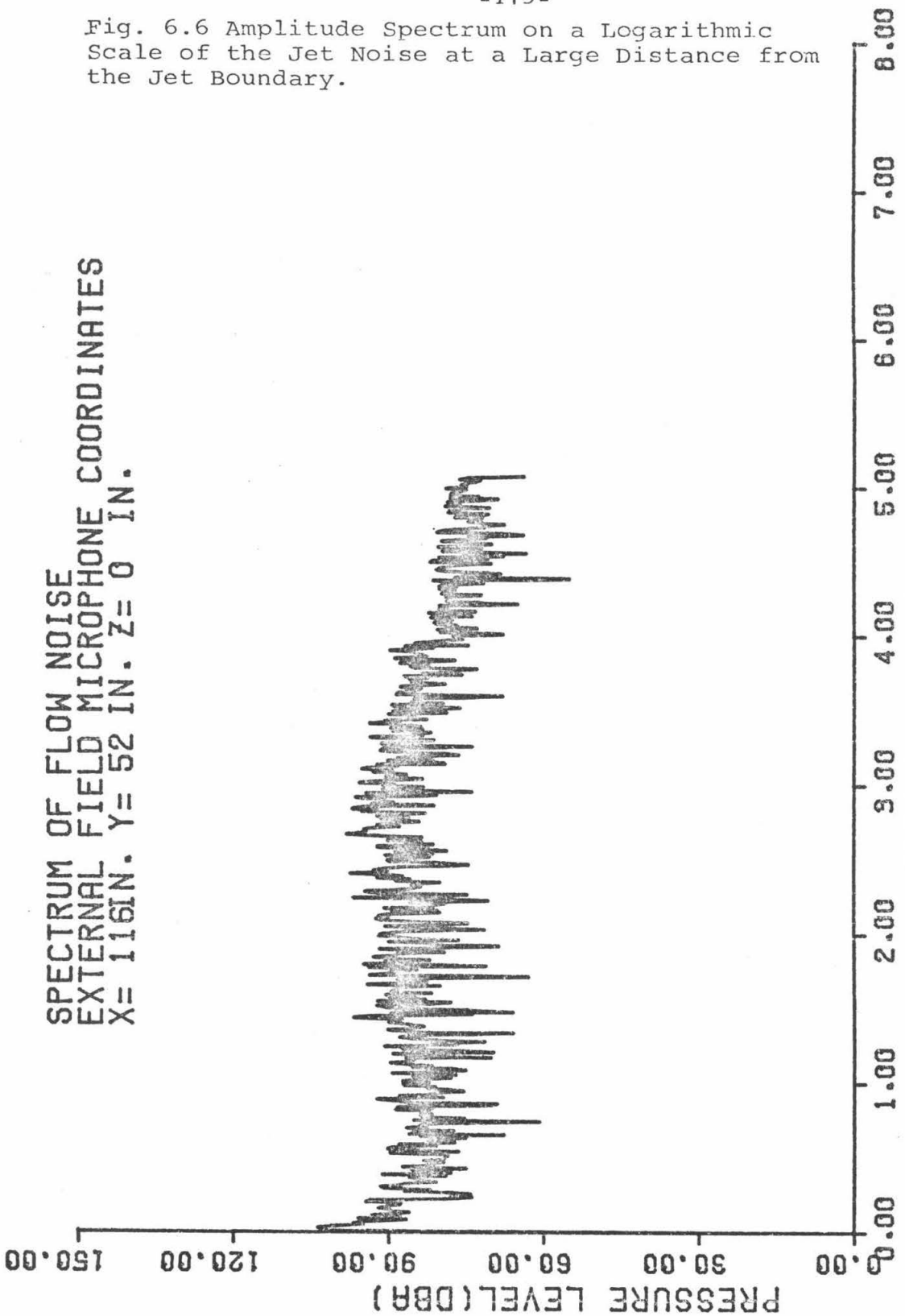

Fig. 6.7 Amplitude Spectrum on a Linear Scale of the Jet Noise at a Small Distance from the Jet Boundary

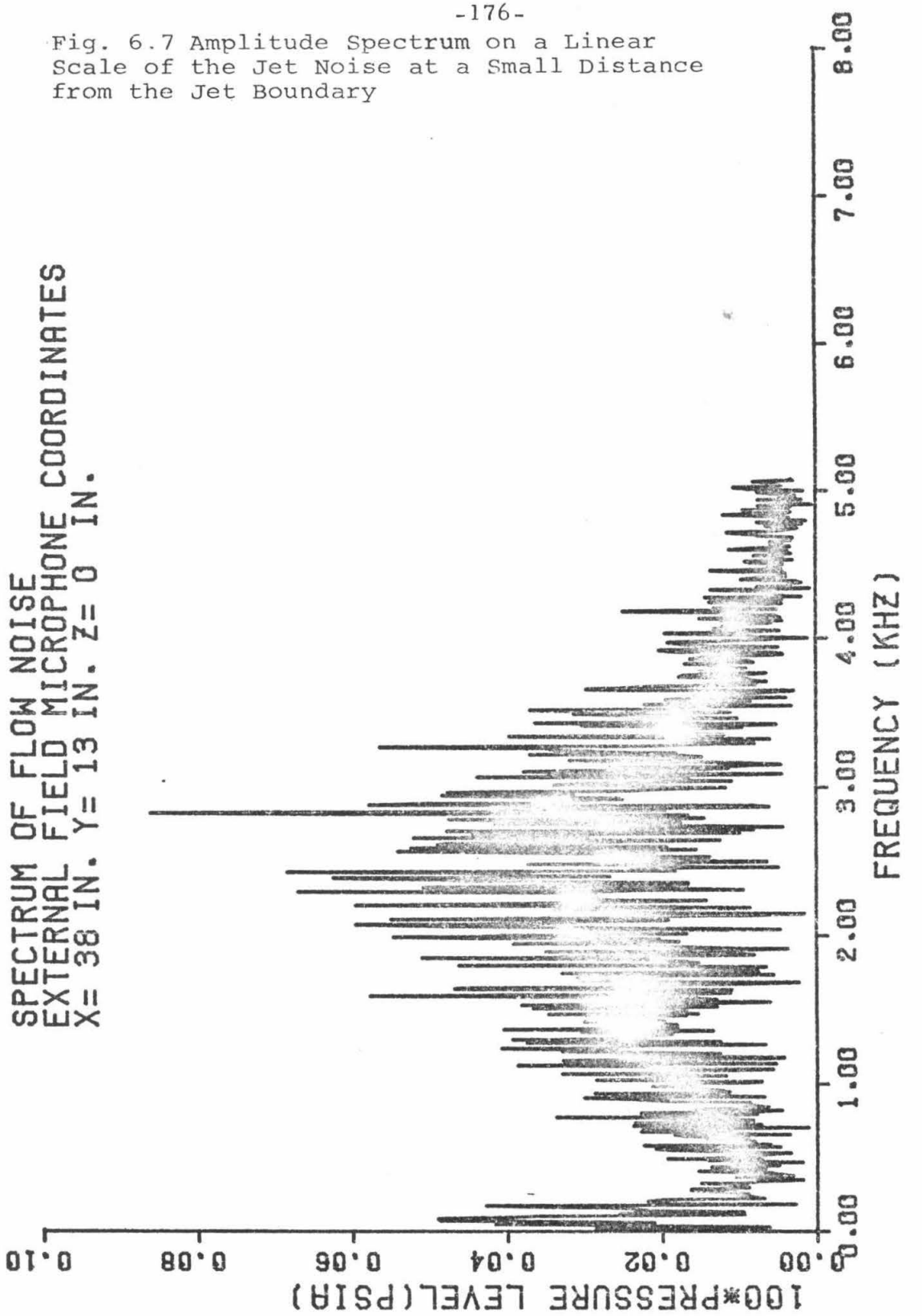

Fig. 6.8 Amplitude Spectrum on a Logarithmic Scale of the Jet Noise at a Small Distance from the Jet Boundary.

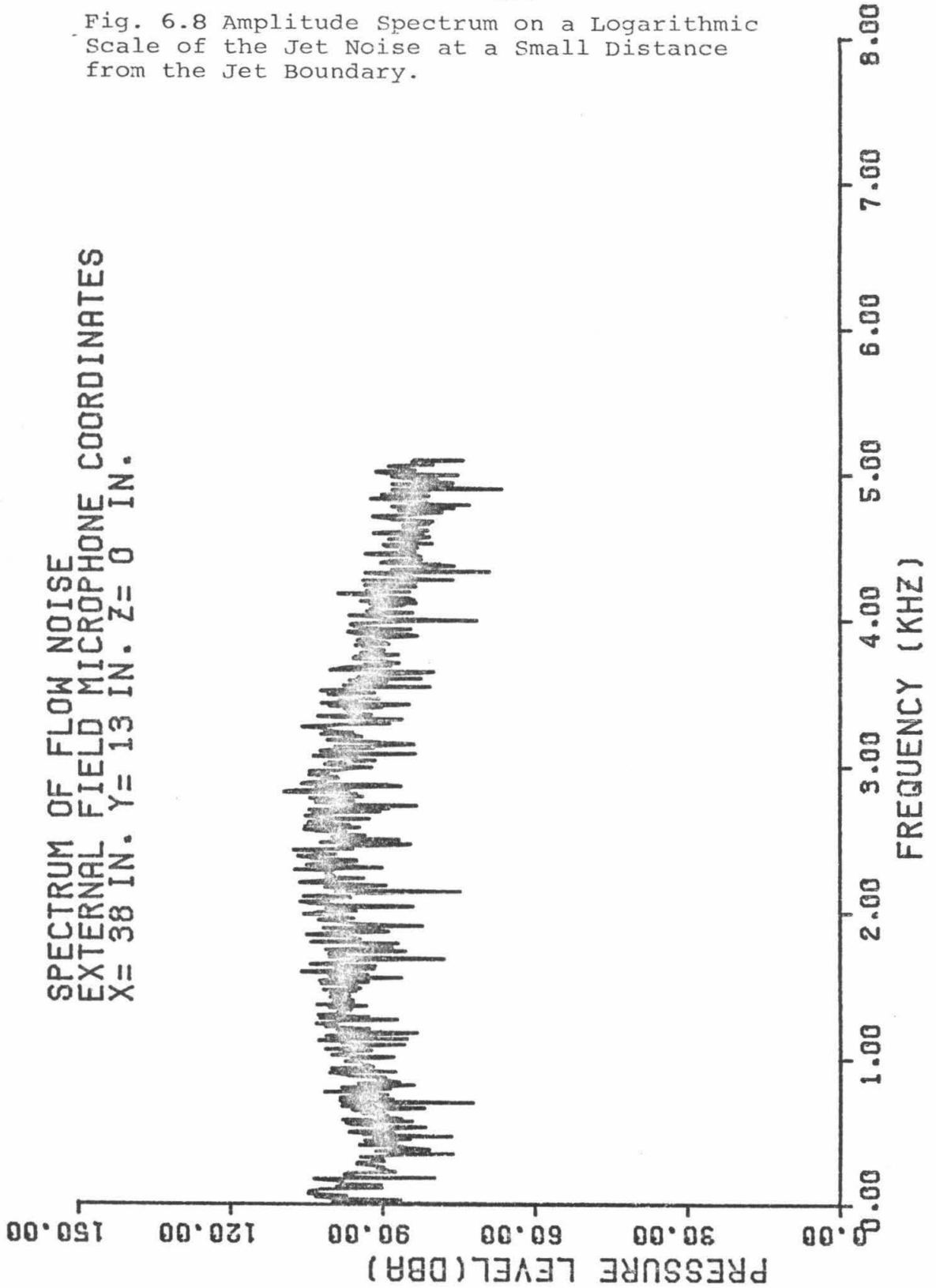

there is a peak in the spectrum between 2 KHz and 3 KHz. The drop in the spectral curves after 4 KHz is the result of the low-pass filter used to prevent aliasing errors (see Chapter IV). The above-mentioned peak has been observed by previous investigators: Westley and Woolley[14], in their investigation of choked jets, found that for ideal expansion or small degrees of underexpansion the noise spectrum was almost flat, with a broad peak between 2 KHz and 3 KHz. Howes[17] correlated spectral data for axisymmetric supersonic jets and found that the frequency corresponding to the spectral peak tended to follow the relation

$$0.1 \leq \frac{f_{max} D_e}{a^*} \leq 0.2 \quad , \tag{6.7}$$

where

f_{max} = peak spectral frequency

D_e = nozzle exit diameter

a^* = speed of sound at throat

Taking for the rectangular nozzle an hydraulic diameter of 1.0 in., from figs. 6.5 - 6.8 one finds for $f_{max} \sim 2.7$ KHz and $a^* = 1000$ ft/sec. that the Strouhal number $(f_{max} D_e)/a^* = .214$ slightly above Howe's limits.

Louis and Patel[16] investigated the noise spectra of a rectangular convergent-divergent nozzle with an exit Mach number of 2.74 and a stagnation temperature of 1350°R. The nozzle exit cross section was 0.5 in. x 3.3 in. Noise measurements in both the horizontal and vertical planes passing through the center of the nozzle cross section indicated a spectral peak at 3.0 KHz for the plane parallel to the 0.5-in. side and 2.5 KHz for the plane parallel to the 3-in. side. The

equivalent diameter of this section is 1.44 in., which is reasonably close to the 1.1-in. diameter of the nozzle in this experiment to justify comparison.

Hence, the jet noise measurements have been shown to be consistent with other reported data, thus indicating far-field measuring techniques and data processing are sound. The next step is then to measure the external sound field as modified by the perturbation produced within the nozzle.

6.4 External Sound Field Produced by a Pure Pressure Disturbance at the Nozzle Exit

6.4.1 Measurement procedure and data review. A pure pressure disturbance was produced in the nozzle by running the bleed valve system at 400 Hz with a 7/64-in. diameter orifice setting the magnitude of the bleed flow.

Transducer positions 3 and 7 (-0.5 in. and 10.75 in. respectively) were monitored during each run to check for repeatibility of the nozzle pressure disturbance. Microphone measurements were made in the horizontal and vertical planes passing through the center of the nozzle cross section.

The sound field due to the bleed valve flow was extracted from the background of jet noise using 81 signal-averaging operations. Digital records of the microphone output for no signal averaging and 81 signal-averaging operations are shown in figs. 6.9 and 6.10 respectively. For the figures shown, the microphone was placed 6 ft. from the nozzle exit in the horizontal plane of the jet. Note from

Fig. 6.9 Typical Microphone Pressure Fluctuation Waveform with no Signal Averaging.
The Bleed Valve is operating at a frequency of 400 Hz with a 7/64 in. diameter orifice.

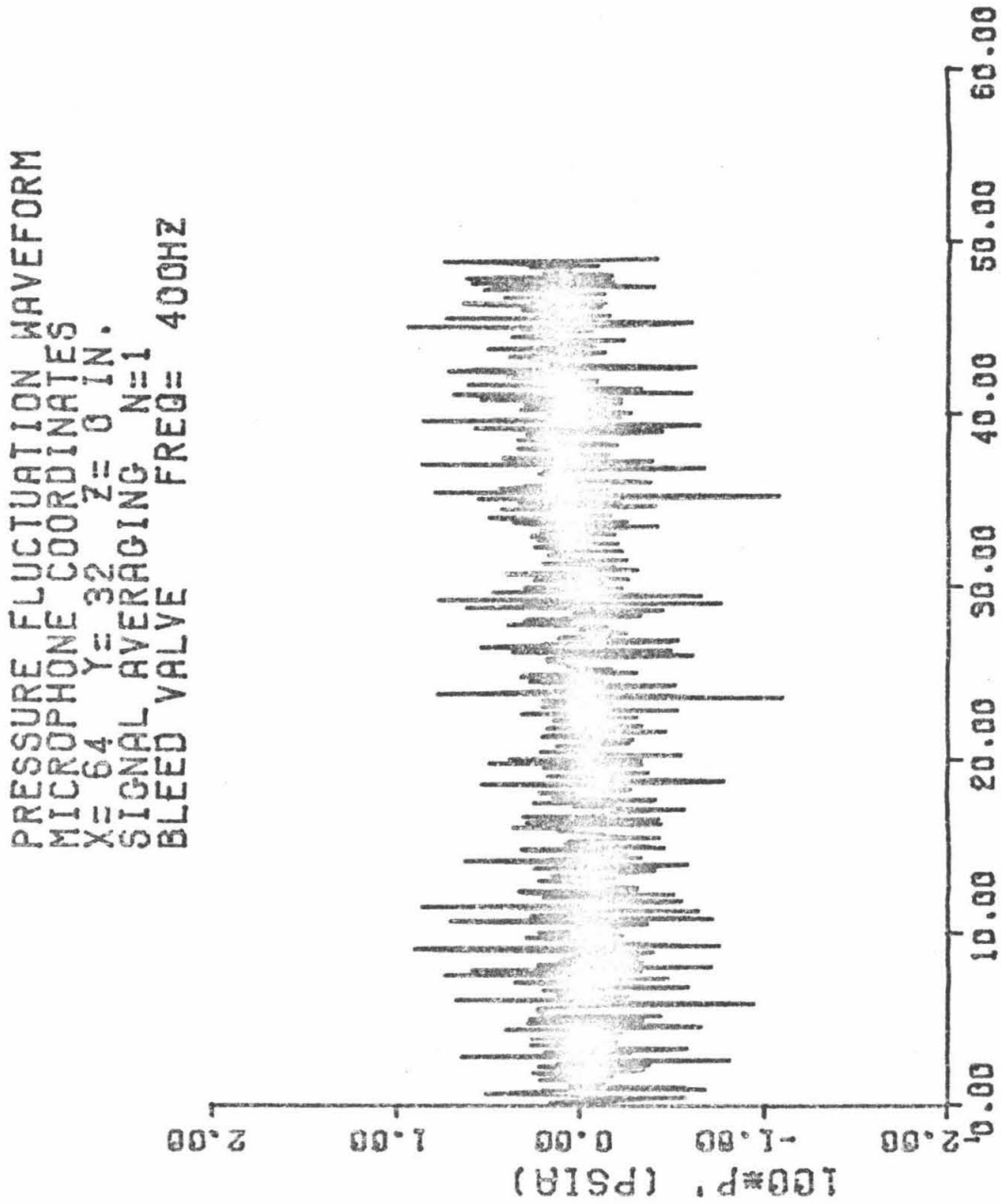

Fig. 6.10 Typical Microphone Pressure Fluctuation Waveform After 81 Signal Averaging Operations. The Bleed Valve is operating at a frequency of 400 Hz with a 7/64 in. diameter orifice.

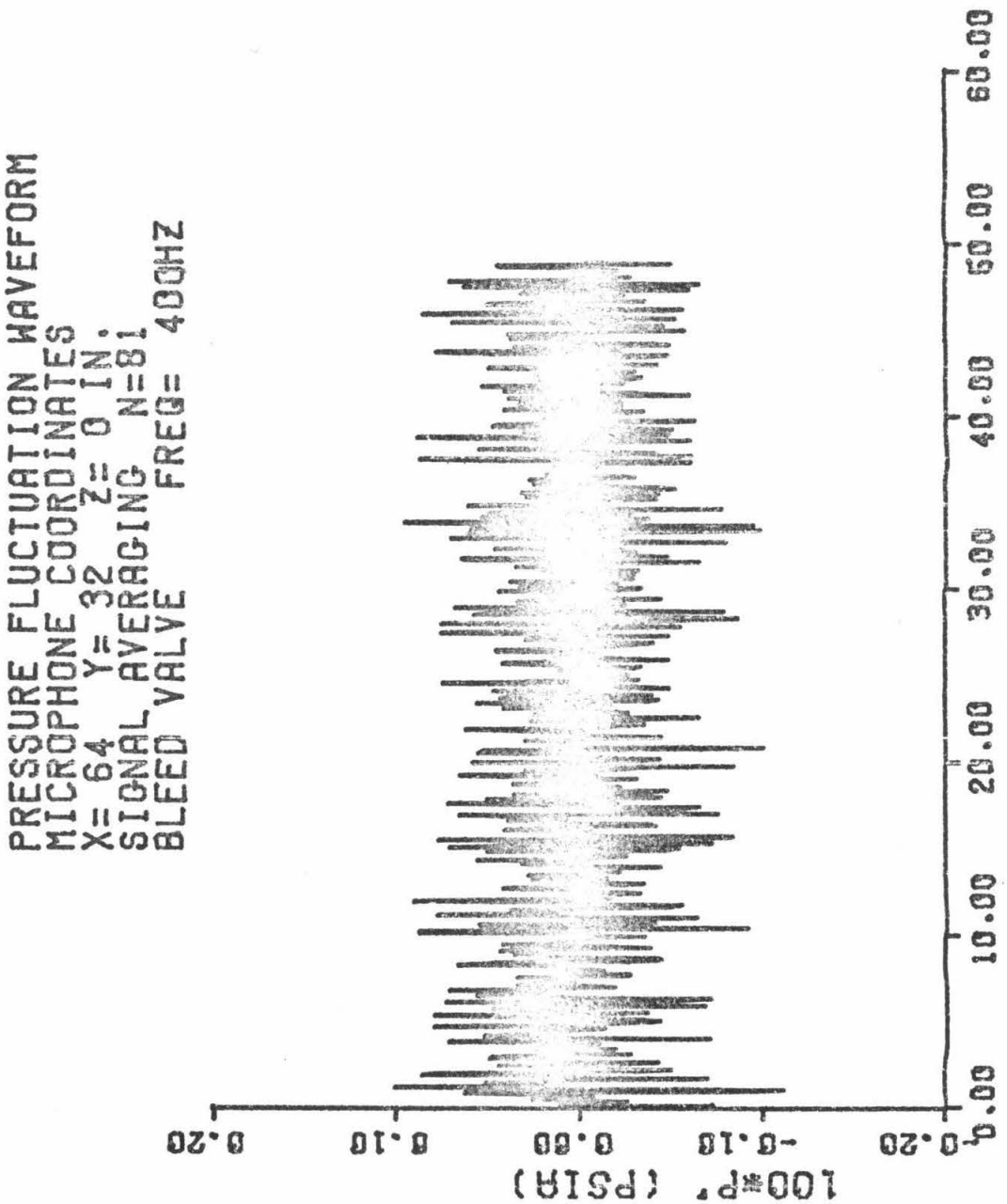

fig. 6.10 that even after 81 signal-averaging operations, the jet noise is still masking the waveform. Thus, in the external field, the jet noise is much larger with respect to the bleed flow sound than was the relative magnitude in the nozzle. However, spectral analysis allowed the detection of the bleed flow signal, as will be explained below.

In evaluating the spectrum of the signal-averaged waveform, the signal-to-noise ratio is further increased due to the fact that the spectral computations involve integrations over a large number of cycles of the waveform. To see this more clearly, consider the formula for the computation of the Fourier sine coefficient

$$b_k = \frac{2}{MT} \int_0^{MT} f(t) \sin \frac{k\pi t}{T} \, dt \quad , \tag{6.8}$$

where M is the number of cycles at the driving frequency (i.e., heater or valve frequency) in the waveform and T is the period corresponding to the driving frequency. The signal-averaged waveform f(t) is the sum of a periodic function $\hat{G}(t)$ and the residual random noise n'(t):

$$f(t) = \hat{G}(t) + n'(t) \quad . \tag{6.9}$$

The mean value of the random noise $\overline{n'(t)} = 0$.

When the integral (6.8) is evaluated, there will be the sum of terms $\sin \frac{k\pi t}{T} \, n'(t)$. Since a periodic function times a random function will be a random function with zero mean value, these numbers when added will cancel each other. Thus, the noise level in the result of the spectral calculation is lower than before.

The above argument also applies to calculations with the Fast

Fig. 6.11 Amplitude Spectrum of the Sound Emitted by the Unperturbed Jet Measured 6 ft. from the Nozzle Exit. The bleed Valve is shut down.

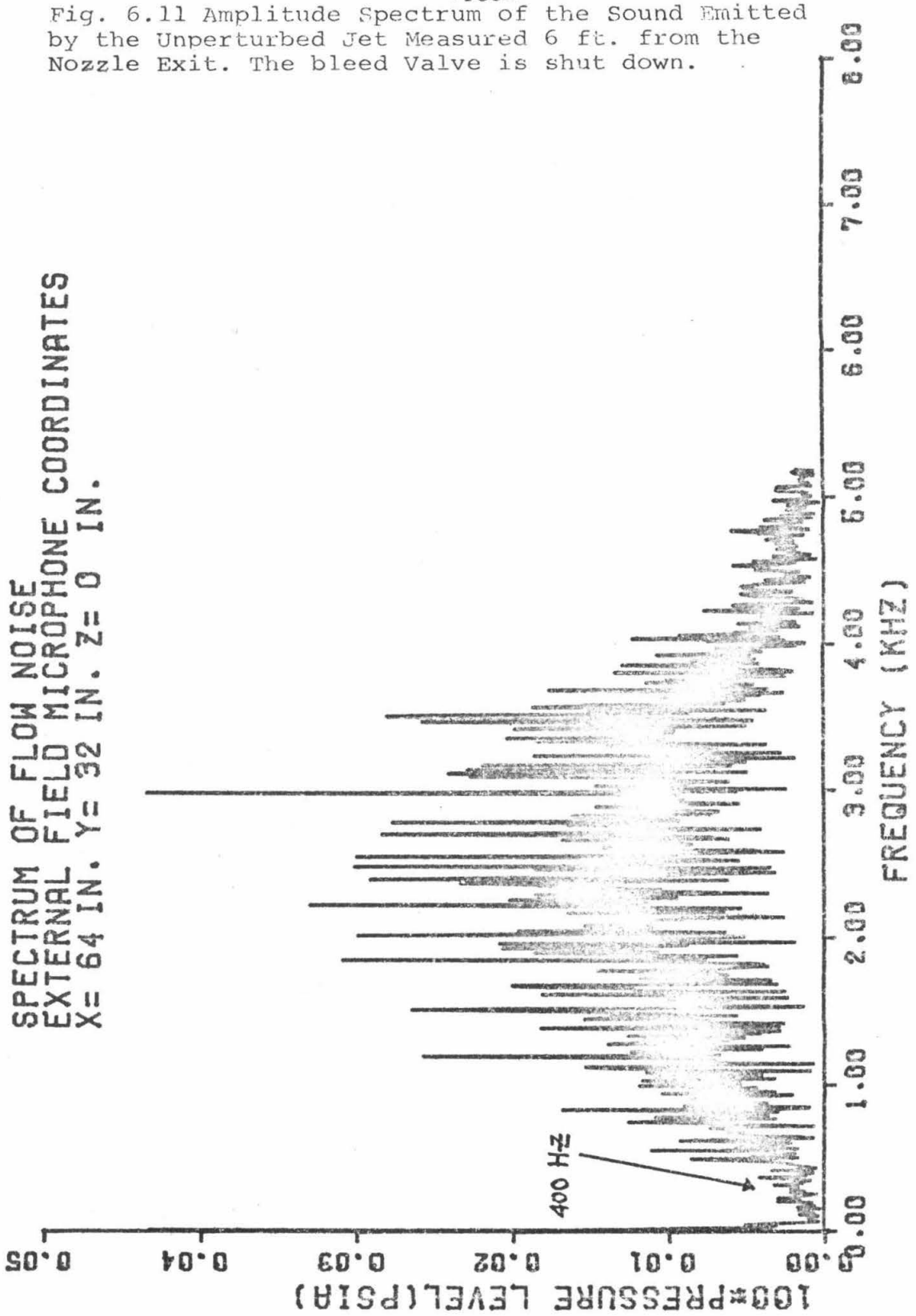

Fig. 6.12 Amplitude Spectrum of the Signal Averaged Pressure Fluctuation Waveform Recorded at 6 ft. from the Nozzle Exit with the Bleed Valve Operating at 400 Hz. Notice the spectrum is identical in shape to the spectrum of fig. 6.11 except for the pronounced spike at 400 Hz.

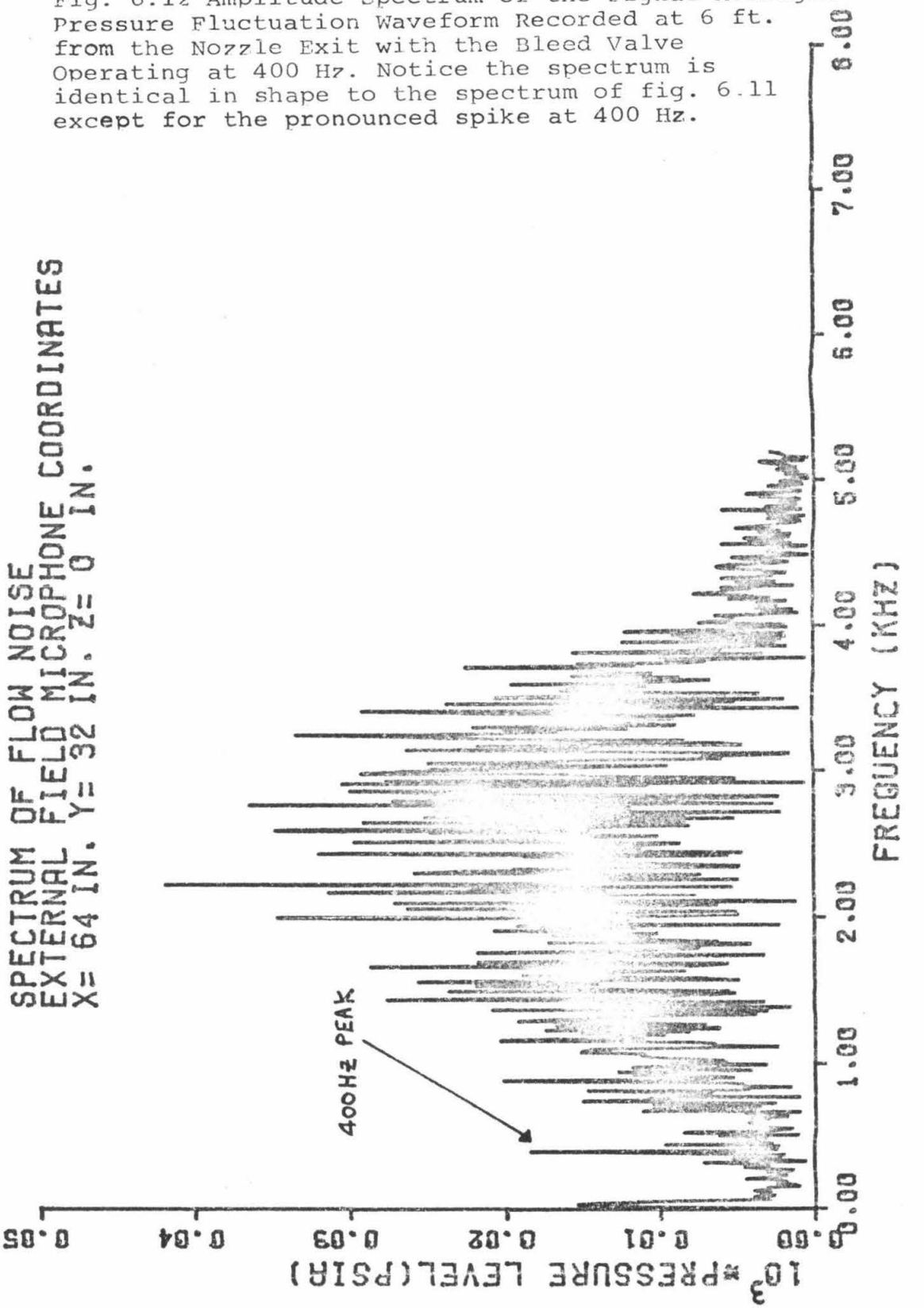

Fourier Transform (FFT) which calculates a spectrum $A(\omega)$ according to the relation

$$A(\omega) = \frac{1}{T_s} \int_0^{T_s} f(t) e^{-i\omega t} dt \quad . \tag{6.10}$$

To show that the combined effect of signal averaging and spectral computation results in detection of the bleed valve sound, figs. 6.11 and 6.12 are presented. Figure 6.11 shows a spectrum computed by the FFT for a 1024-word record of jet noise; no signal averaging was done. Note in the vicinity of 400 Hz that the spectrum is relatively low and flat. Figure 6.12 shows a spectrum computed from a waveform of bleed flow induced sound extracted by 81 signal-averaging operations. Note that the overall magnitude of spectral components is an order of magnitude lower, agreeing with the fact that the signal averaging reduces the noise level by a factor of 9 . However, in contrast to fig. 6.11 which has a low flat portion of the spectrum at 400 Hz, fig. 6.12 shows a pronounced peak at 400 Hz.

Since the digital record doesn't contain exactly an integral number of cycles at 400 Hz, the FFT calculated peak is lower than its true value. The reason for this error has been discussed in Chapter IV. Nevertheless, the detection of the bleed valve induced sound has been accomplished. The spectrum of fig. 6.12 also shows that the waveform of fig. 6.10 is still dominated by the remaining noise in the 2 KHz - 3 KHz frequency range.

More detailed plots showing the sharpness of the spectra for the bleed flow induced sound are shown in figs. 6.13 and 6.14. These spectra were calculated using the Fourier coefficients formulas in

Fig. 6.13 Portion of the Spectrum of a Signal Averaged Pressure Fluctuation Waveform Recorded Close to the Nozzle Exit. The Bleed Valve was being operated at a frequency of 400 Hz.

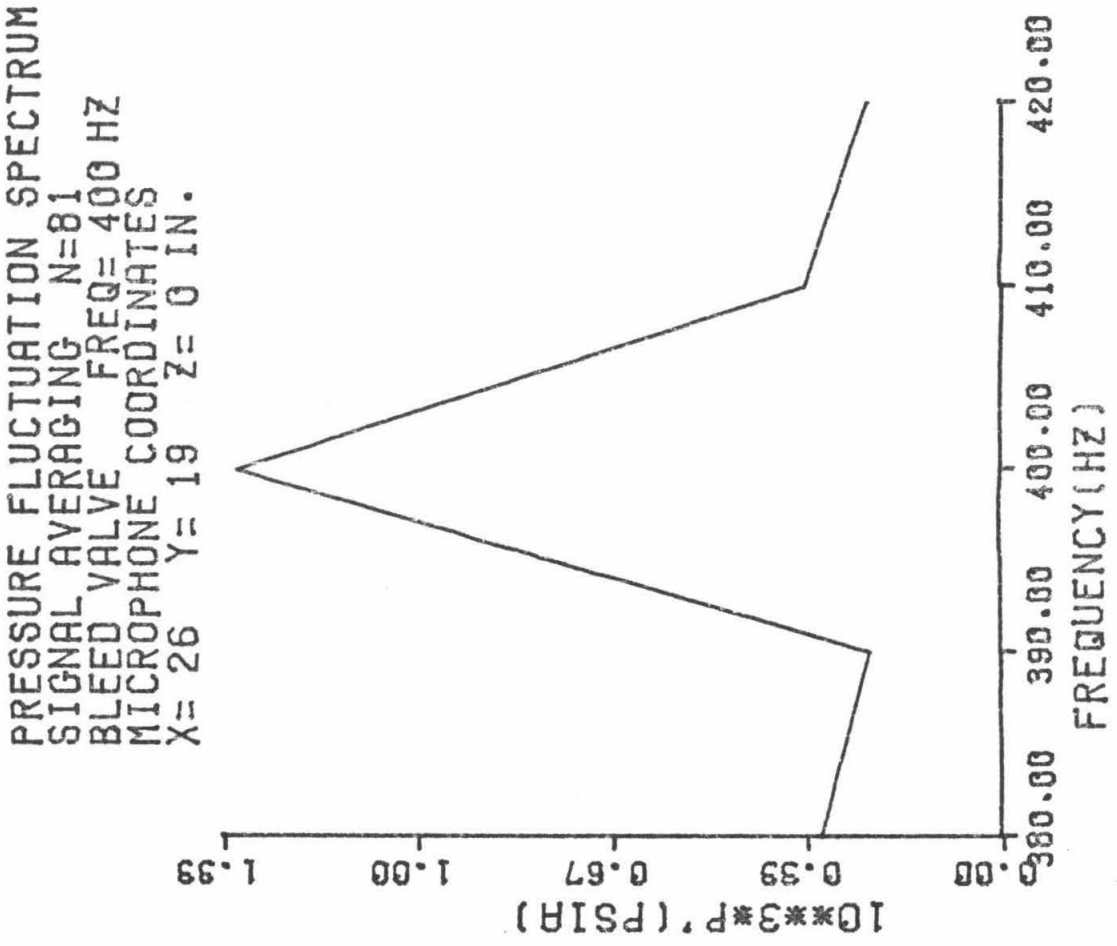

Fig. 6.14 Portion of the Spectrum of a Signal Averaged Pressure Fluctuation Waveform Recorded Far from the Nozzle Exit. The Bleed Valve was being operated at a frequency of 400 Hz.

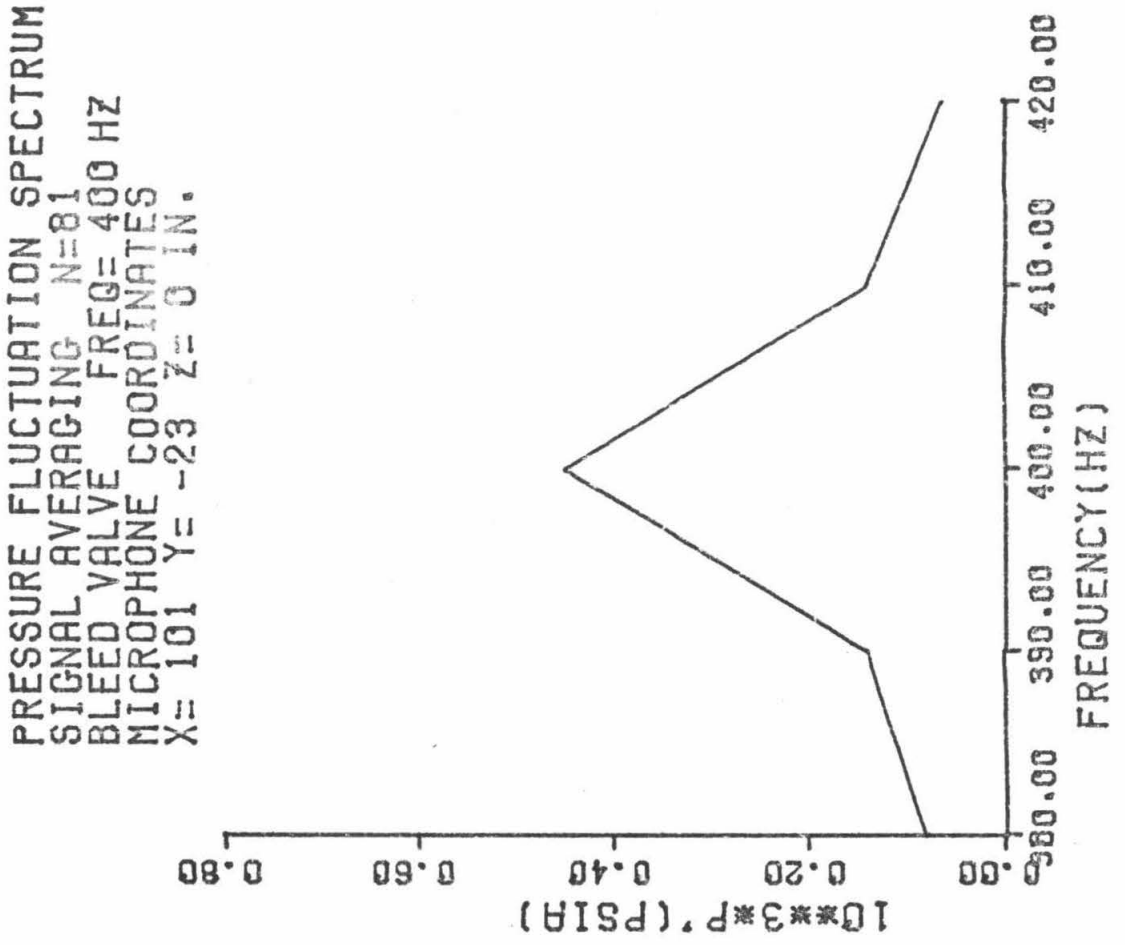

Chapter IV for frequencies of 380, 390, 410, and 420 Hz. All amplitudes except the one at 400 Hz indicate the spectral components of residual noise after signal averaging. The component of noise at 400 Hz is essentially the same value. The actual peak shown is the amplitude of the bleed valve sound. Thus, one can see that the signal-noise ratio obtained varies from 3:1 to 6:1.

These signal-noise ratios, though, indicate the need for the development of a more powerful signal-averaging scheme than now used. This development will require significant modification of the data acquisition system, which will be accomplished in the future but not as part of this work.

6.4.2 Sound field due to bleed flow within the nozzle. The 400 Hz component of the external sound field produced by operation of the bleed valve at 400 Hz is shown in figs. 6.15 through 6.18. Figures 6.15 and 6.16 show data for the horizontal plane of the jet, and figs. 6.17 and 6.18 show data for the vertical plane. Each set of figures shows the following noise field quantities: (a) the amplitude of the sound in units of DBA at various locations in each plane; (b) the phase of the 400 Hz component of the sound at a given point in the external field relative to the phase of the 400 Hz component of the bleed flow produced pressure fluctuation at the nozzle exit.

Upon first glance at the phase data in figs. 6.16 and 6.18 one will notice a wide scatter of values in some regions. In the author's opinion, the scatter can be attributed to the large amount of residual noise in the signal-averaged waveform. As can be seen in fig. 6.10, the 400 Hz waveform is embedded in a background of high-frequency

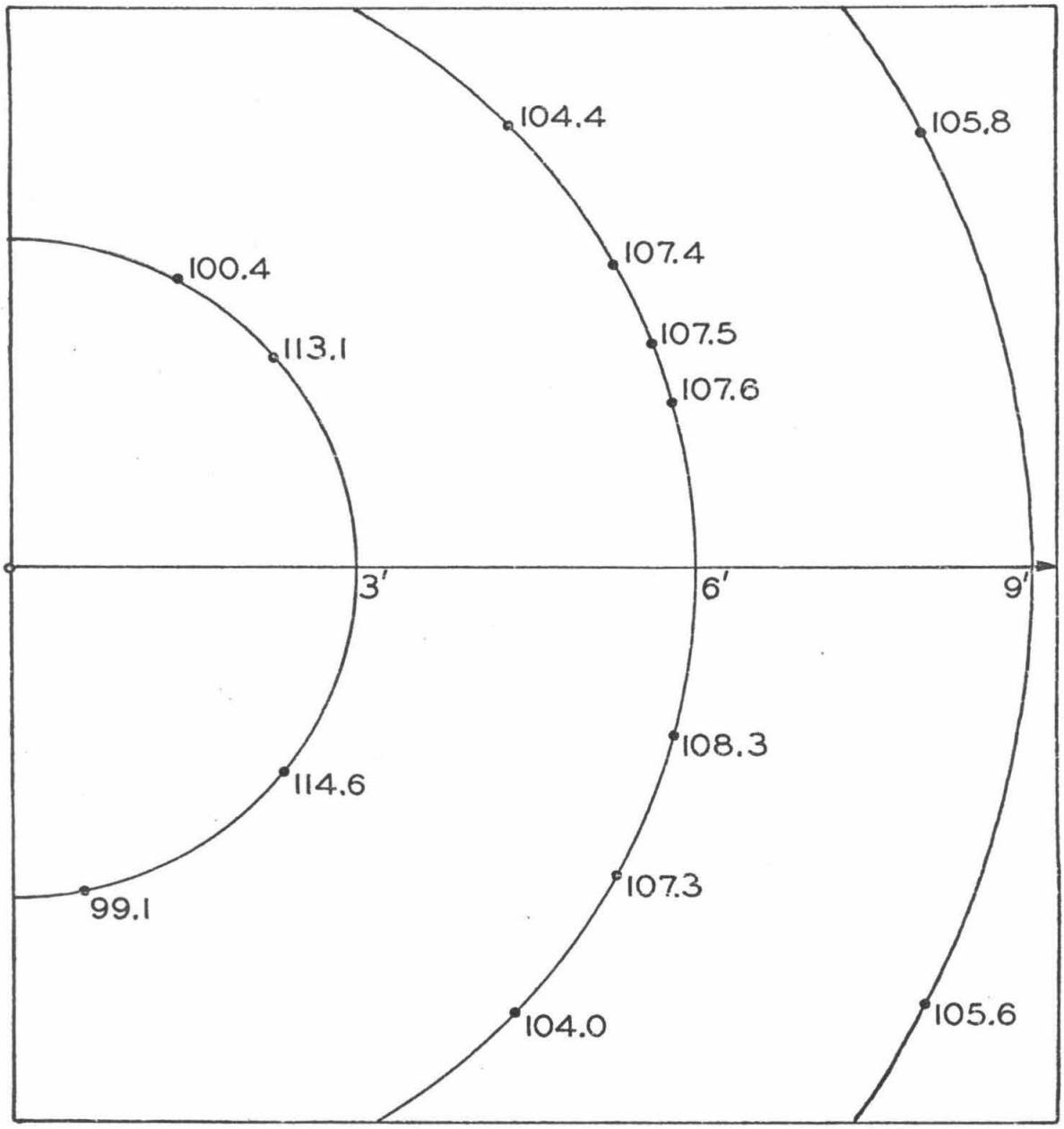

Fig. 6.15 Amplitude of the Bleed Valve Produced Sound Field in the Horizontal Plane of the Jet. Bleed Valve frequency is 400 Hz. Amplitude values are presented in units of DBA.

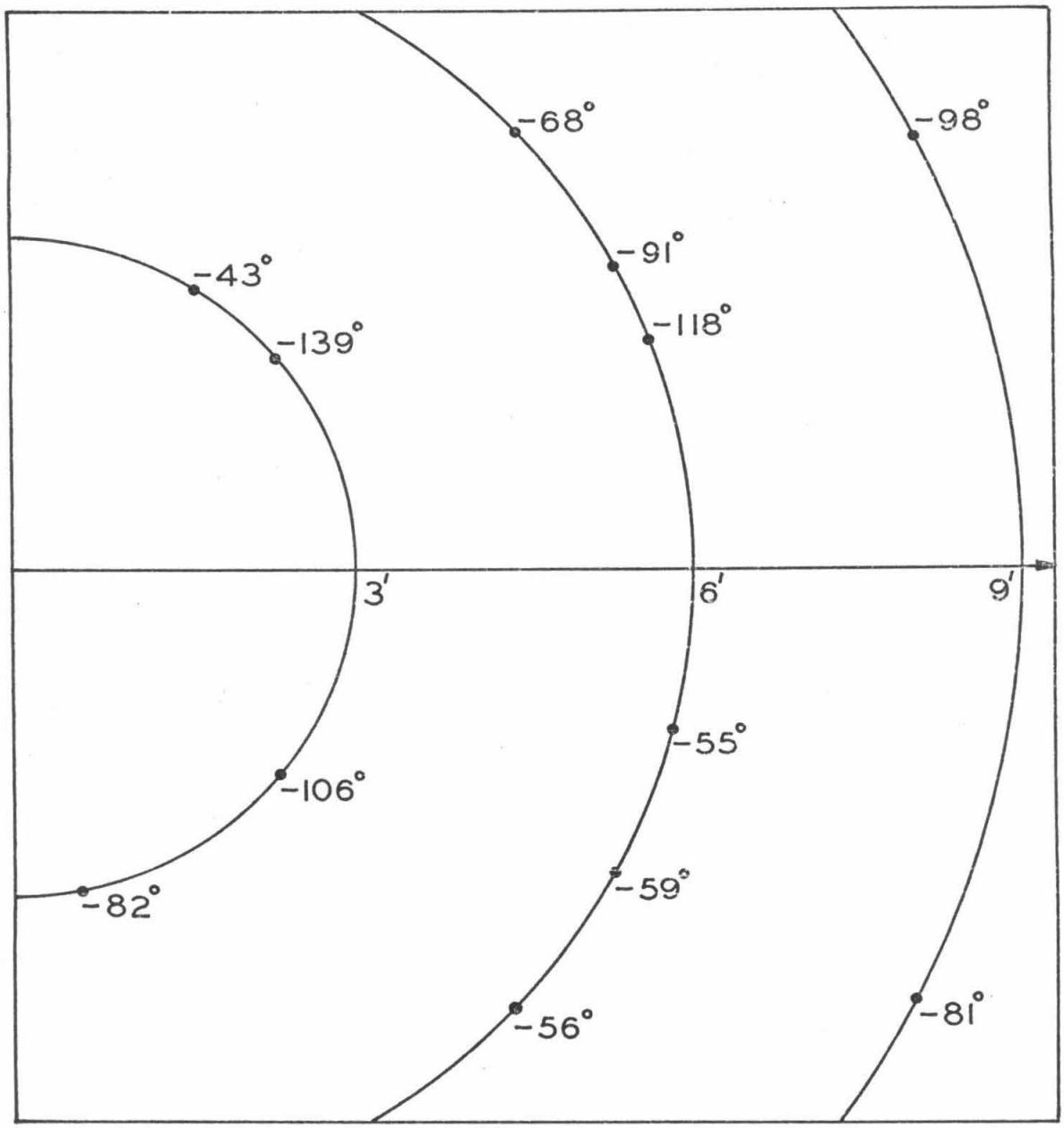

Fig. 6.16 Phase of the Bleed Valve Produced Sound Field in the Horizontal Plane of the Jet. All phases are with respect to the phase of the pressure fluctuation at the nozzle exit. Bleed Valve frequency is 400 Hz.

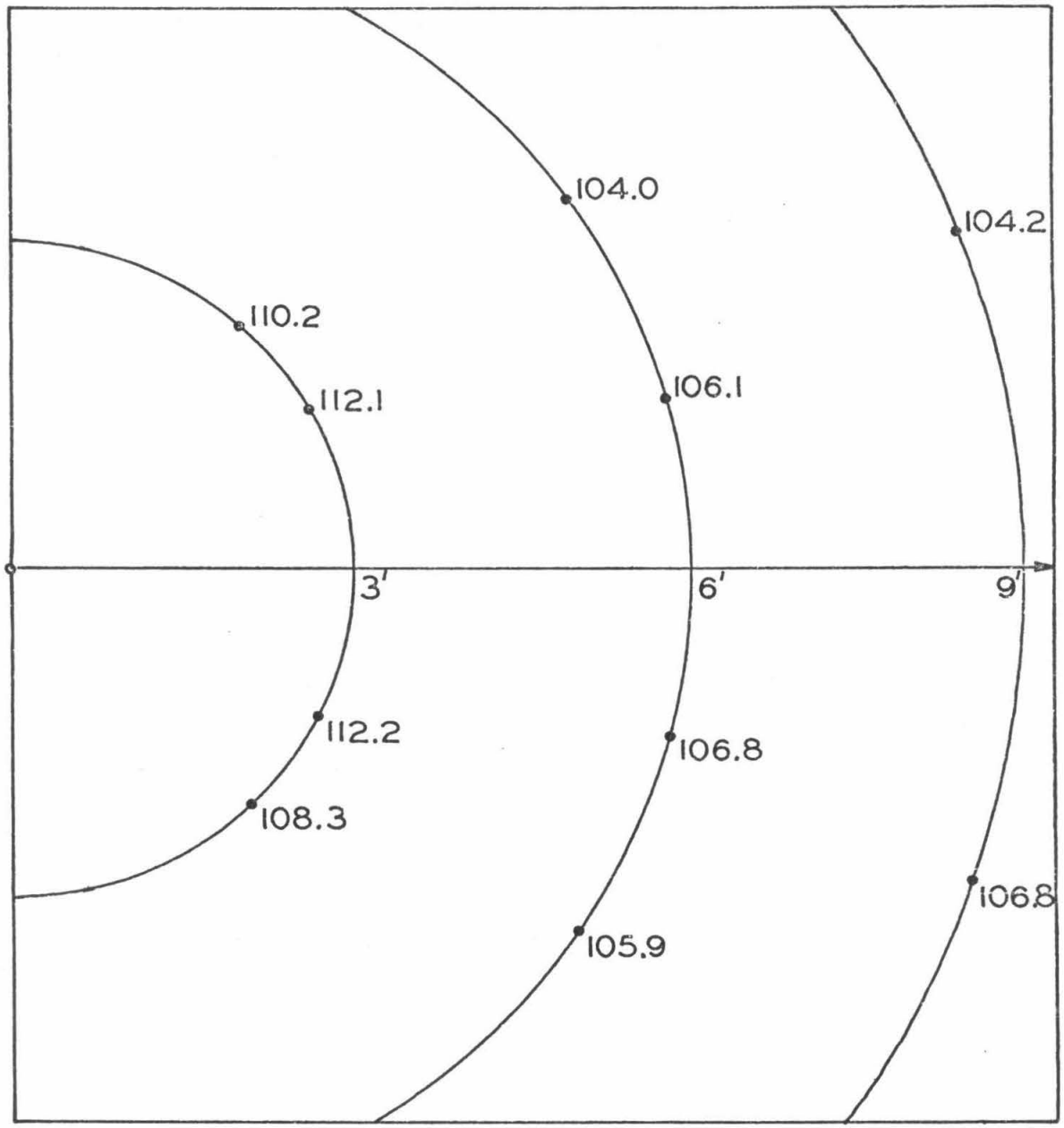

Fig. 6.17 Amplitude of the Bleed Valve Produced Sound Field in the Vertical Plane of the Jet. Bleed Valve frequency is 400 Hz. Amplitude values are presented in units of DBA.

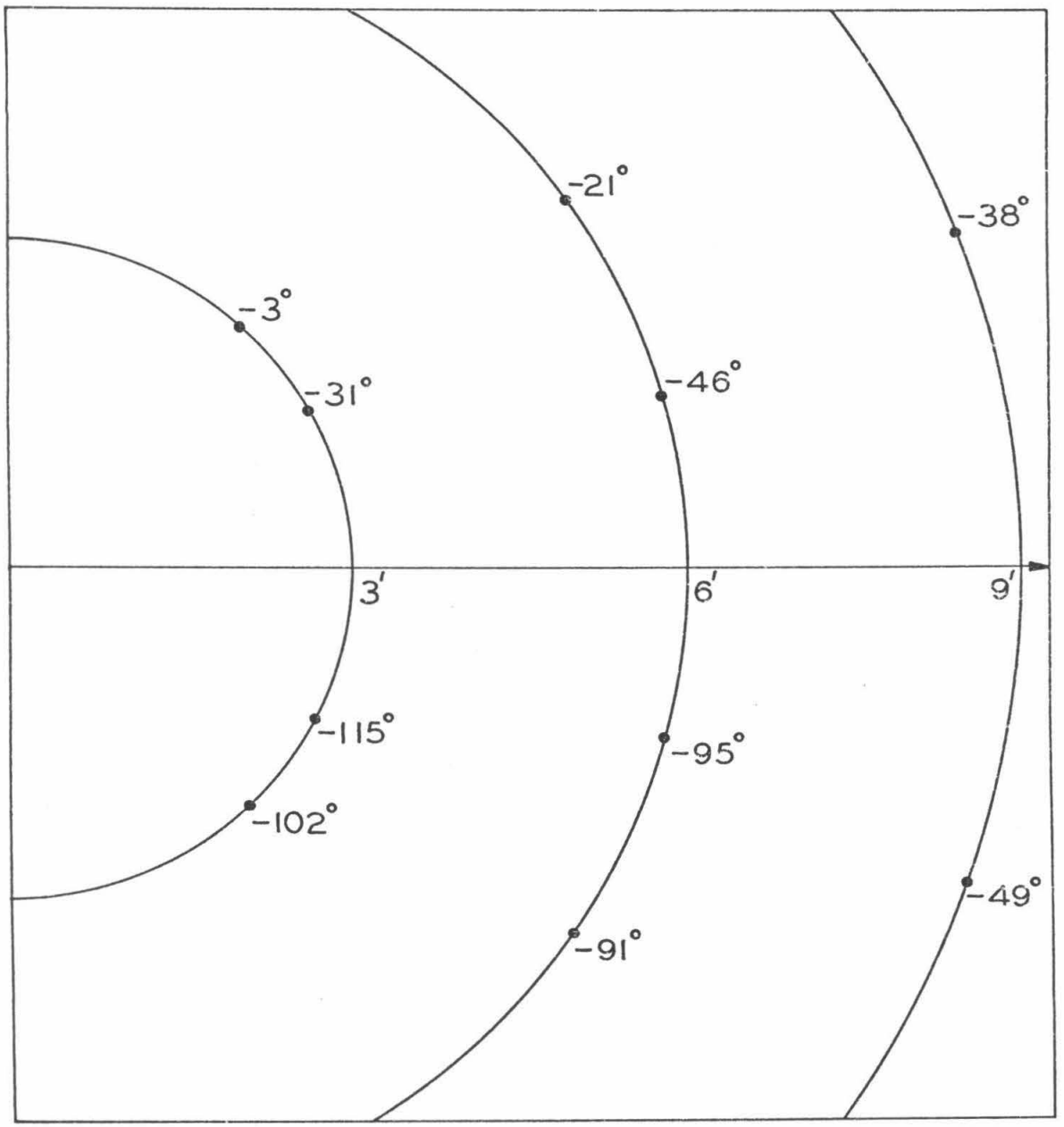

Fig. 6.18 Phase of the Bleed Valve Produced Sound Field in the Vertical Plane of the Jet. All phases are with respect to the phase of the pressure fluctuation at the nozzle exit. Bleed Valve frequency is 400 Hz.

noise. The noise will obscure the zero crossings of the 400 Hz signal. This will lead to numerical errors in the Fourier coefficient calculations. That is, the Fourier sine and cosine coefficients will be smaller or larger, depending on where the computations see the apparent zero crossings. The errors in each of the Fourier coefficients do not appear in the amplitude, since it is the sum of the squares of the two coefficients. The positive error in one coefficient cancels the negative error in the other when the sum of the squares is made. The result that is affected by a blurred zero crossing is the phase of the 400 Hz component. Different noise waveforms will lead to different obscured zero crossings and hence a scatter of phase values. Again, the need for a more powerful signal-averaging technique has been shown to be necessary.

Having discussed the limitations of the data, the next logical step is to extract some results which define the nature of the sound field.

(i) In both the horizontal and vertical planes of the jet, the magnitude of the sound field drops approximately 6 db from the 3 ft. to the 6 ft. arcs. This implies that the bleed flow noise is behaving in the far field like the sound emitted from a monopole source at the nozzle exit. Also note in fig. 6.15 that the sound level rapidly decreases along the 3 ft. arcs at angles approaching 90^{o} off the jet axis. This appears to indicate that the supersonic jet tends to constrain the sound field initially into a downstream expanding cone.

(ii) The data of figs. 6.15 and 6.17 show that in magnitude the sound field is the same in the horizontal and vertical planes of the jet

and is symmetric about the jet axis in both planes. Thus, the sound field produced by an almost square nozzle can be considered axisymmetric.

(iii) The phase data in fig. 6.16 show that most of the phase values along the 6 ft. and 9 ft. arcs are in close agreement for each arc. Assuming that the largely different values are due to noise, as explained before, it appears that the constant phase values along arcs indicate again that the sound field is monopole in nature. The phase data for the 9 ft. arc in the vertical plane (fig. 6.18) also indicate the monopole character. The large scatter at the 3 ft. and 6 ft. arcs allows no conclusions to be drawn.

6.5 Cross Correlation Measurements

6.5.1 Cross correlation processing. Cross correlation functions and cross correlation coefficients were calculated using the relationships outlined in sections 4.5.3 and 4.5.4. First, the cross correlation function was calculated for the pressure fluctuation at the nozzle exit and the sound at a given point in the external field. Plots of three typical correlation functions are shown in figs. 6.19, 6.20, and 6.21. Note the dimension for the vertical axes is $psia^2$.

The horizontal axis for the plot is $\Delta\tau$, the lag time between the occurrence of a certain phase of the pressure signal at the nozzle exit and the occurrence of another certain phase of the signal in the far field. All three plots show that the cross correlation function is periodic in $\Delta\tau$ with a period of 2.5 msec. This implies that the 400 Hz (2.5 msec period) bleed valve induced signals dominate the cross

Fig. 6.19 Cross Correlation Function of the Bleed Valve Produced Sound at the Nozzle Exit and a Point 6 ft. Away in the Vertical Plane of the Jet. Bleed Valve frequency is 400 Hz.

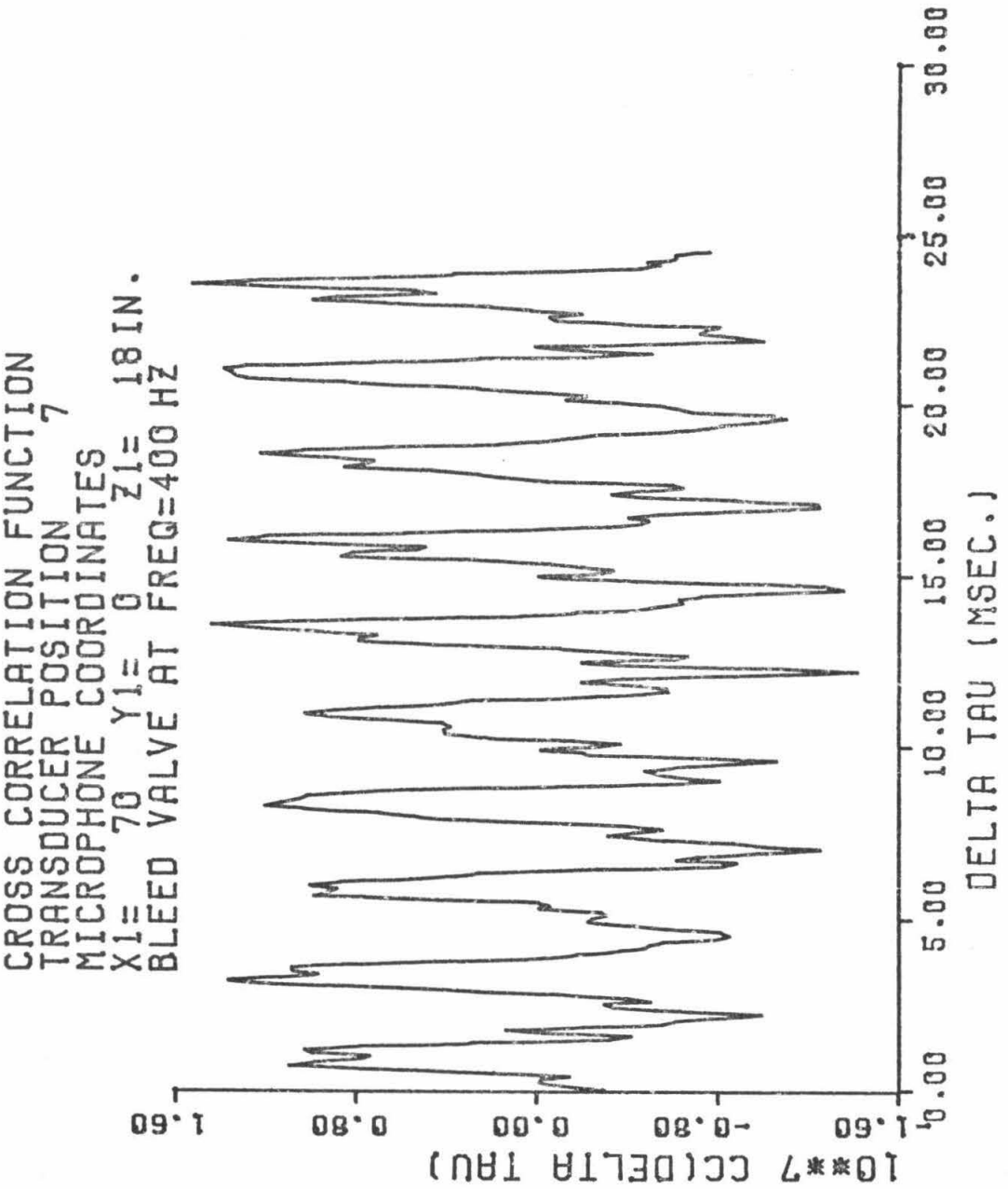

Fig. 6.20 Cross Correlation Function of the Bleed Valve Produced Sound at the Nozzle Exit and a Point 3 ft. Away in the Horizontal Plane of the Jet. Bleed Valve frequency is 400 Hz.

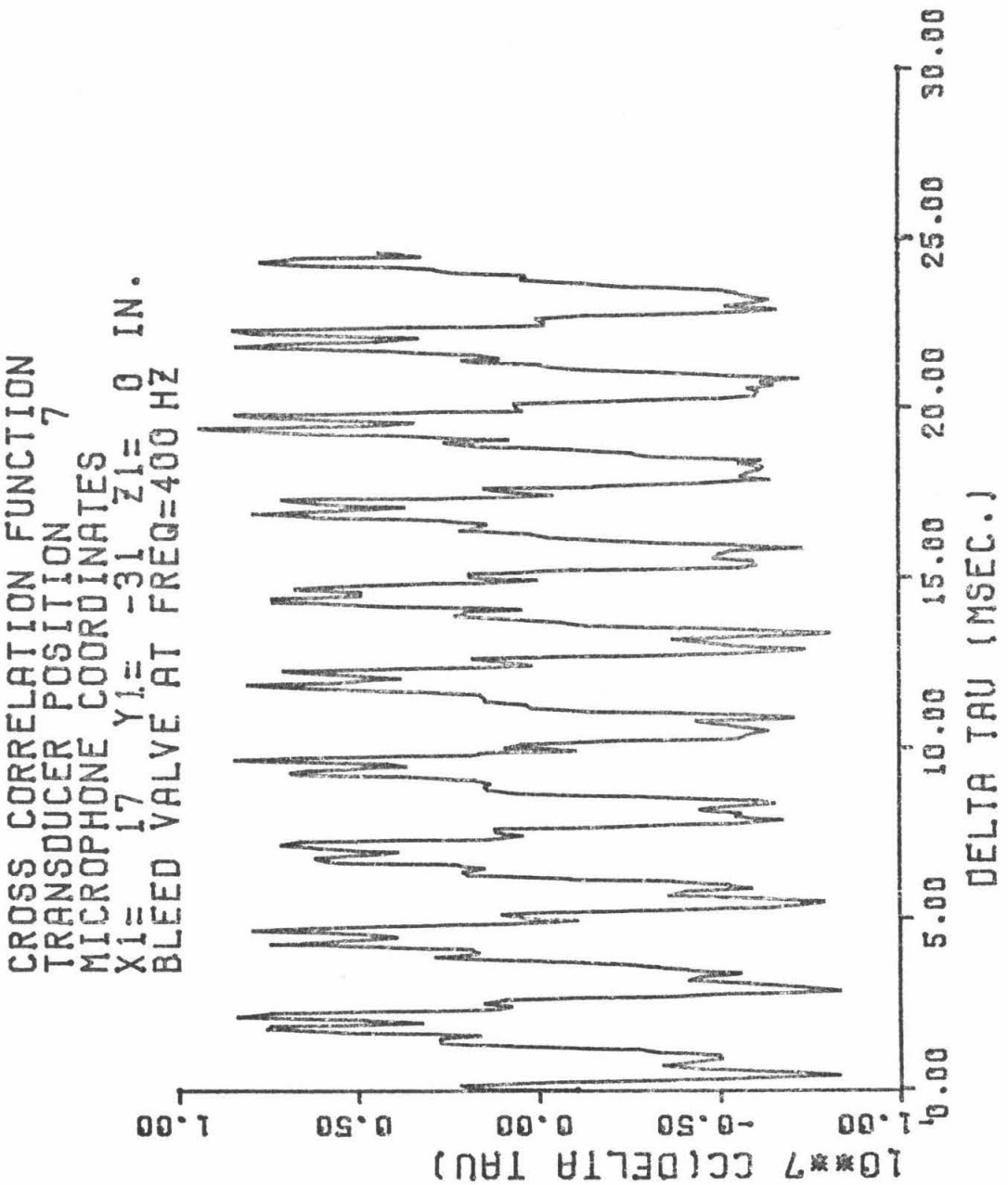

Fig. 6.21 Cross Correlation Function of the Bleed Valve Produced Sound at the Nozzle Exit and a Point 3 ft. Away in the Vertical Plane of the Jet. Bleed Valve frequency is 400 Hz.

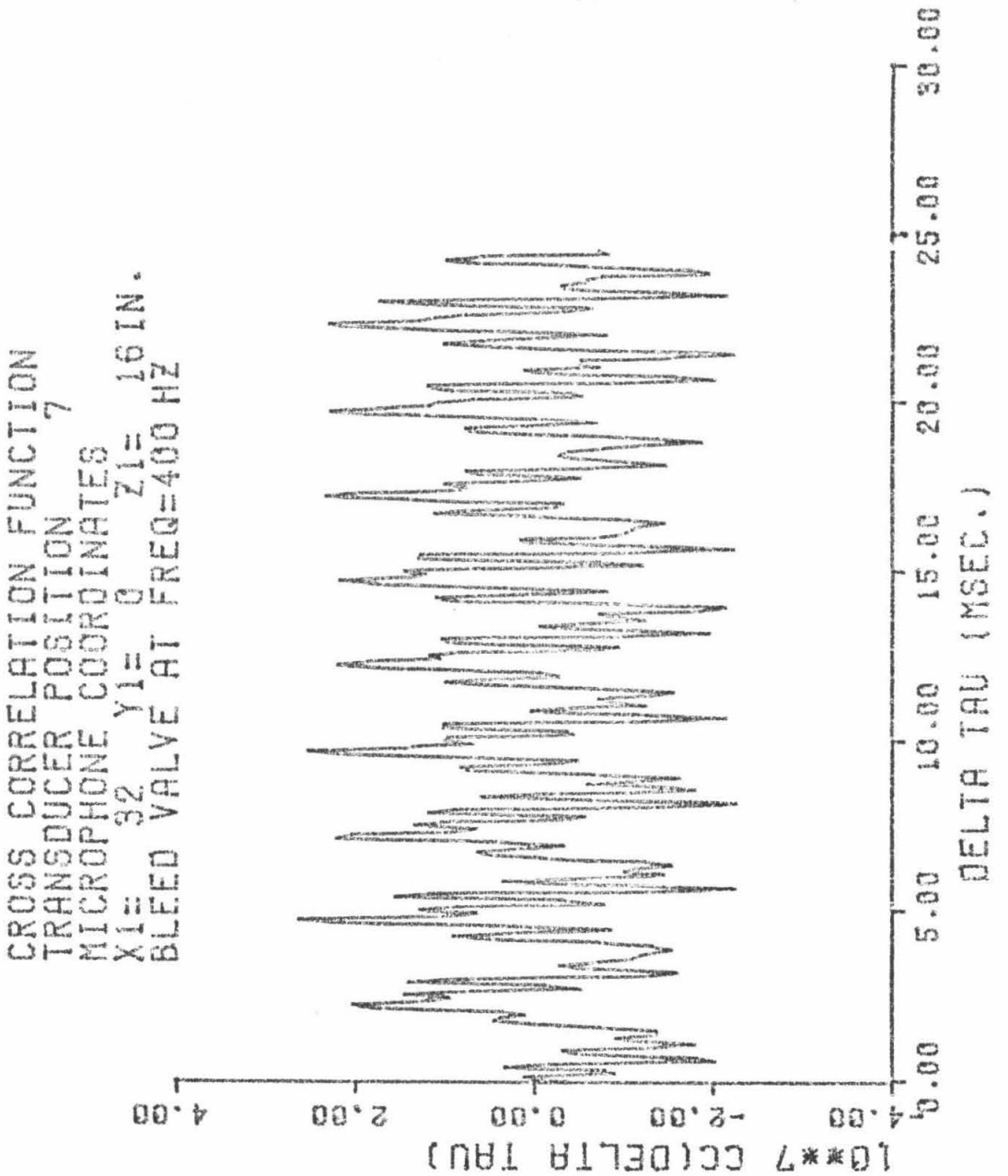

correlation. The bleed signals are strongly correlated, as they should be.

The amplitude of the 400 Hz component of the correlations was evaluated using the formulas (4.33) and (4.34) for coefficients of a discrete Fourier series. The cross correlation coefficient was then evaluated by dividing the amplitude of the 400 Hz component of the cross correlation function by the product of the r.m.s. amplitudes of the 400 Hz components of the pressure signals used to form the cross correlation function. The results are shown in figs. 6.22 and 6.23. The plots are maps of the horizontal and vertical planes of the jet with the values of the cross correlation coefficient shown at the corresponding locations. The results on both graphs show that the correlation at all points is approximately 6 per cent.

It is significant to compare this value to those obtained for the correlation between the turbulent pressure fluctuations within a jet and the far field noise of the jet. Siddon and Rackl[8] measured the cross correlation between the jet pressure fluctuation and the far field sound for a Mach .32, 1.5-in. diameter round jet and found a cross correlation coefficient of .02. Meecham and Hurdle[56] measured the cross correlation between the pressure fluctuations at various points in a jet engine exhaust and the far field sound and found values ranging from .004 to .155. The highest correlation coefficients occurred at the highest operating Mach number of .99.

The correlation coefficients for the bleed valve produced sound field are in general higher than those for the turbulence studies. This implies that the sound field produced by disturbances within the noz-

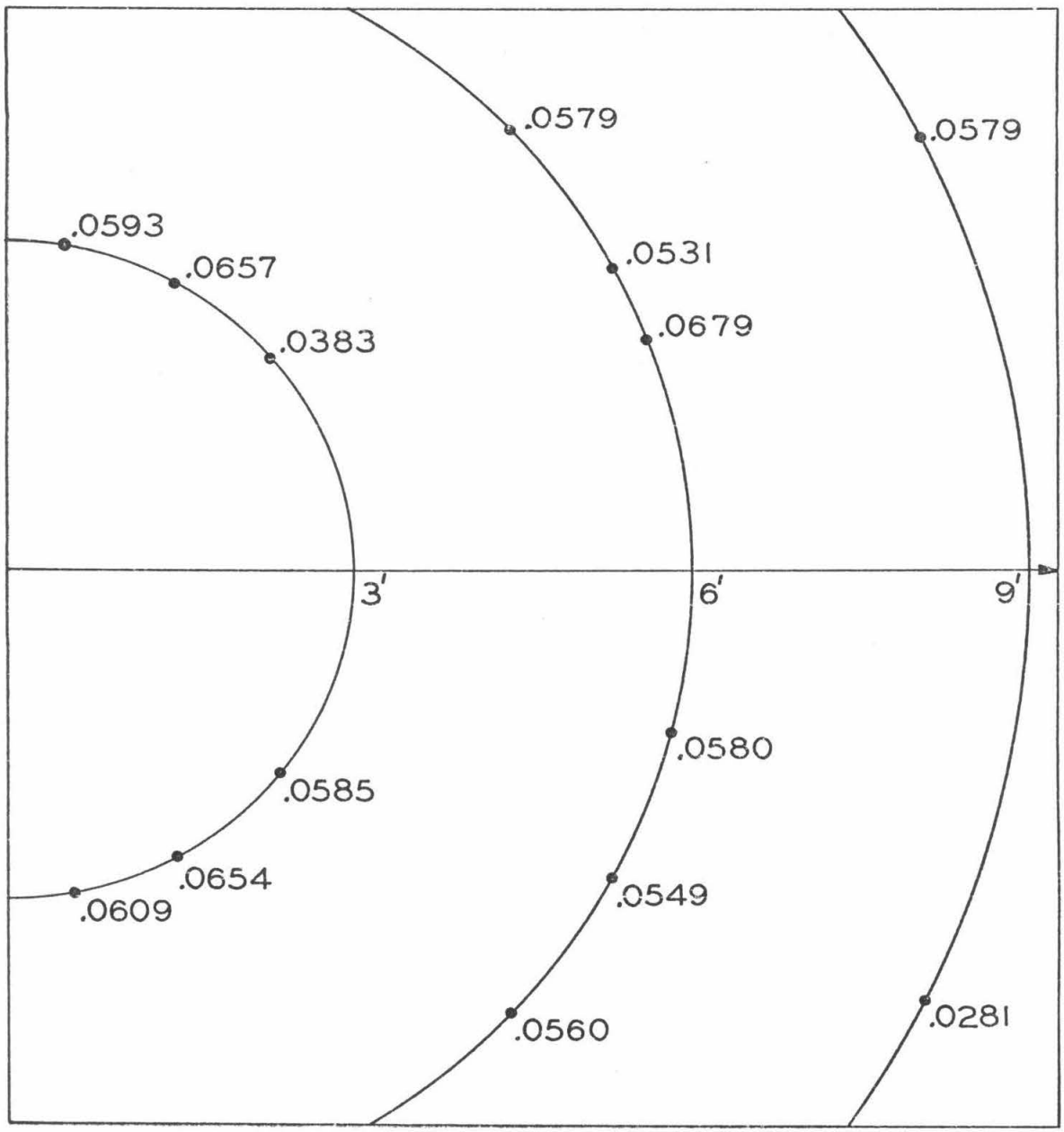

Fig. 6.22 Cross Correlation Coefficients of the Bleed Valve Produced Sound at the Nozzle Exit and at Various Points in the Horizontal Plane of the Jet.Bleed Valve frequency is 400 Hz.

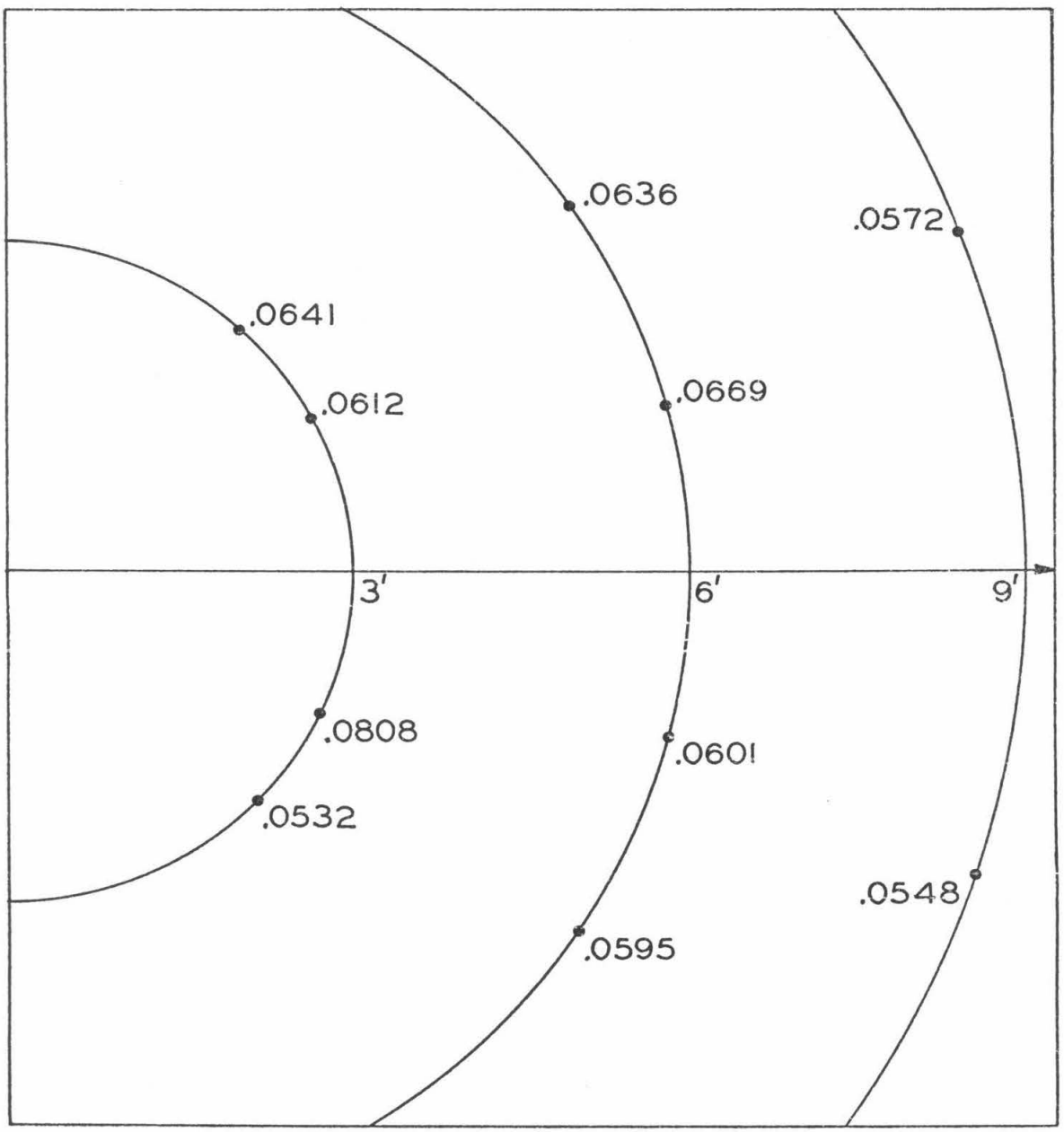

Fig. 6.23 Cross Correlation Coefficients of the Bleed Valve Produced Sound at the Nozzle Exit and at Various Points in the Vertical Plane of the Jet. Bleed Valve frequency is 400 Hz.

zle can be associated with a source close to the nozzle exit. This is different from the turbulence source where it is postulated that the noise arises from sources distributed along the jet.

VII. CONCLUSIONS

The production of noise by temperature nonuniformities in an accelerating flow has been studied. A novel noise source, whose existence was postulated through analysis, has now been unambiguously verified experimentally.

The experiments not only show the general aspects of the mechanism but provide for measurement of data which show the operation of the mechanism in great detail. This detail allows for the verification of a complex analytical model which considers noise production at each point in the flow.

The development of the experiment unveiled a technique for using a digital computer system as a signal-averaging device. This technique will continue to be used in investigating the noise source in cases of more complex forms of temperature disturbances. The results of the future experiments will give valuable data for complex flows where analysis may not be feasible.

This thesis began with an introduction which stated that the experiments described herein were one small step in the solution of the jet engine noise problem. It seems an ideal time to substantiate this statement.

Consider a real supersonic jet engine. At full power operation, its exhaust Mach number would be in the $M = 1$ to $M = 2$ range. Then the results of the experiments described herein can be used to estimate the noise produced by nonuniform burning in the combustion chamber. Typical turbine temperatures are in the neighborhood of $1500^{\circ}F$. It is reasonable to expect that nonuniform burning could

produce hot spots 50 - 100°F above the mean flow temperature. Then the ratio of the temperature fluctuation to the mean temperature varies from .033 to .066.

Now let us apply the result of fig. 5.57 to estimate the noise level due to this hot spot being convected into the engine exhaust nozzle. The dimensionless temperature fluctuation used to generate the plots in fig. 5.57 was $T'/\overline{T} = 4 \times 10^{-4}$. This produced a dimensionless pressure fluctuation at the exit of $p'/\overline{p} = 2 \times 10^{-4}$. Assuming ideal expansion at the engine nozzle exit, one has, assuming a linear theory and $\overline{p}$ = 1 atm at the exit,

$$\begin{aligned} p'_{engine} &= .243 \text{ to } .486 \text{ psia} \\ p'_{engine} &= 159 \text{ dba to } 165 \text{ dba} \end{aligned} \qquad (7.1)$$

This is quite significant considering 135 dba is the threshold of pain, and 30 db above the threshold is a factor of 33. Suppose the nozzle exit was 5 ft. in diameter and the sound level decreases from the nozzle inversely with the number of diameters away, so at 1 mile away (1,000 diameters) the sound level would be around 120 dba. This is as noisy as an automobile horn, not painful but irritating.

Thus, one must conclude that to decrease engine noise, one should strive toward more uniform mixing and burning processes in combustion chambers.

APPENDIX A. DETAILS OF ANECHOIC CHAMBER

A.1 Construction

This appendix supplements data on the anechoic chamber described in Section 3.2. Detailed descriptions on the construction of anechoic chambers of various sizes and cutoff frequencies are readily available in the literature (refs. 27-31). The critical point of construction is the design and fabrication of the wall wedges. Details of wedge design are given in ref. 27. Also to be considered is the size of the free field measurement area; the maximum free field measurement distance must be at a sufficient distance from the tip of the wedges.

A.1.1 Wedge Construction. The cutoff frequency of the chamber was selected to be 300 Hz. Reference 27 requires that wedges for this cutoff frequency have an 8-inch base and an 8-inch altitude. From this requirement, a basic wedge module was constructed as follows.

On a 2 ft. × 2 ft. base of 2 in. thick fiberglas, three triangular wedges of base 8 in., height 8 in., and depth 2 ft. would be mounted. The 4 ft.^{2} wedge modules were mounted adjacent to one another on the sides of the chamber with their long wedge axes perpendicular.

Wedge material was Owens-Corning 704 Fiberglas Insulation with a nominal density of 4.2 lb. m/ft^3. The fiberglas consisted of 2 in. × 4 in. × 48 in. rectangular slabs. The slabs were stacked four thick and the triangular wedges were cut from these 8 in. thick slabs. The triangular wedges were bonded using duct liner adhesive and nylon cord. For rigidity, three aluminum rods of 1/16 in. diameter

were inserted from the apex of each wedge to the base slab of the module.

A.1.2 Framework. The size of the chamber was selected to satisfy the far field criteria for the cutoff frequency of 300 Hz. These criteria are as follows (refs. 31 and 32).

1) The distance of measurement from the source, r, must be very much greater than the wavelength divided by 2π:

$$r >> \lambda/2\pi \ . \qquad (A.1)$$

In acoustics, 'very much greater' is taken to be a factor greater than 3.

2) Any measurement at a specific frequency should be taken no less than 1/4 wavelength away from the tips of the wedges.

The working volume of the chamber was chosen to be a 10 ft. cube. At 300 Hz the wavelength of sound is approximately 3 ft. Thus, the free field measurement volume is approximately an $8\frac{1}{2}$ ft. cube, and if the source is located at one wall, the ratio of $\lambda/2\pi$ to say r = 8 ft. is 16, well exceeding the requirement of criterion 1.

To construct the 10 ft. cube described above, a cubic framework of slotted steel angle iron was constructed, 11 ft. 4 in. on a side. Additional runs of angle iron were mounted on the framework 2 ft. apart. These runs provided the mounting frames for the wedge modules. The modules were held firmly to the framework by means of thin aluminum rods which ran through the slots in the runs and then pierced adjacent module bases.

Reference 1 specifies that for maximum sound absorption by the wedges, a 1 in. air gap should exist between the module bases and the solid wall bounding the chamber. To achieve this, 1 $in.^2$ x 11 ft. wooden runners were attached to the top and sides of the framework, and the framework floor was mounted on 1 in. thick hard rubber blocks. After the wedges were mounted in the slotted angle iron runs, the top and sides of the framework were covered with $\frac{1}{2}$ in. thick fiberboard, with the exception of the jet vent and door areas which will be described below.

A. 1. 3 Jet Exhaust Duct, Chamber Door, and Walkway Grating. A floor plan of the chamber is shown in Fig. A. 1. Each component of the chamber described in this section is shown in the figure.

To allow escape of the large amount of nitrogen discharged into the chamber by the supersonic nozzle, a 2 ft. square hole was cut in the rear of the chamber. Following this hole, an acoustically lined duct was constructed which conveyed the nitrogen to the nearest window. The duct area immediately behind the hole was covered with wedges identical to those used in the chamber. This guaranteed that the duct would not act as a resonance chamber. The remainder of the duct was lined with two inches of $\frac{1}{2}$ lb./ft^3 fiberglas sheet to minimize flow noise and reflections back into the chamber vent area.

The chamber door is basically a framework of slotted angle iron which holds three wedge modules. It is 6 ft. high, 2 ft. wide, and its base is 1 ft. above the floor framework of the chamber. Fastened to the rear of the framework is a wooden rectangular tray 78 in. high by 30 in. wide by 2 in. deep. The tray holds 2 in. thick slabs

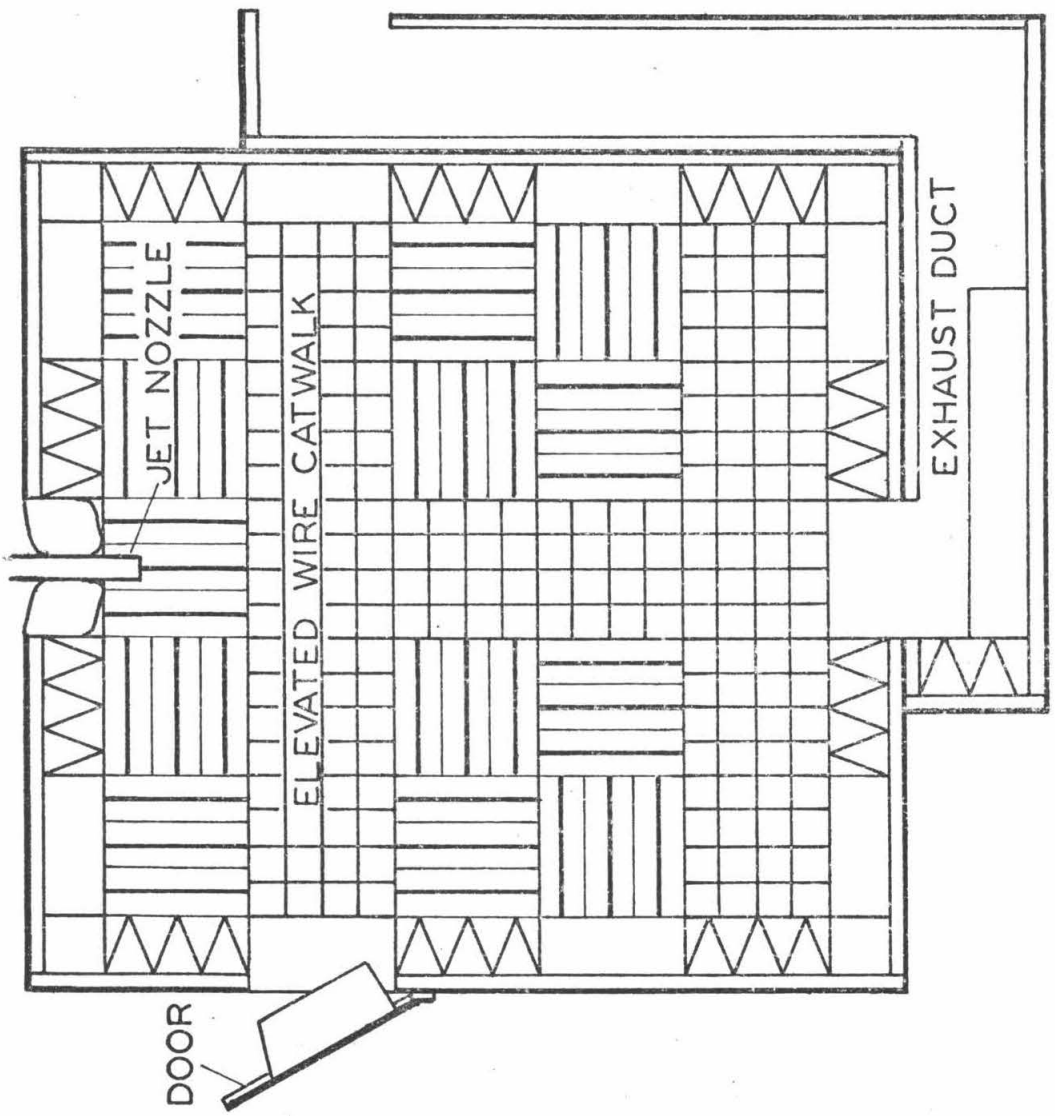

Fig. A.1 Anechoic Chamber Floor Plan

of Owens-Corning 704 Fiberglas which form a soundproof seal around the periphery of the door area when the door is closed and latched.

To allow rapid and easy access to all areas of the chamber as well as providing a base for microphone stands, an acoustically transparent floor was constructed using slotted angle iron and a steel wire grating having a 6 in. square grid with 0.1 in. diameter wire. The extent of the walkway is shown in Fig. A.1. The walkway is 5 in. above the tips of the floor wedges. The support sections of the walkway are constructed of slotted steel angle iron and covered with several layers of $\frac{1}{2}$ in. thick, $\frac{1}{2}$ lb./ft.^{3} fiberglas sheet to eliminate reflections. The wire grating is clamped onto the horizontal portions of the support framework by long aluminum slotted bars which can be bolted to the slotted angle iron.

A.2 Calibration

The standard test for checking the quality of anechoic chambers is to place a small speaker at one end of the chamber and then measuring the sound level at various distances from the speaker, in particular along a given radial from the speaker and along an arc a constant distance from the speaker. These data are then compared to what the sound level at these points would be had the chamber acted like free space, in which case the sound level would vary inversely with the distance.

Commercial manufacturers of anechoic chambers specify that above the cutoff frequency and at sufficient distance from the wedge tips, the deviation should be no more than 2 db (12.5 percent) from the inverse distance law. The calibration tests made on this chamber

indicate that the quality was superior to this criterion.

Measurements were made in the horizontal and vertical planes of the jet nozzle, since all measurements of the jet sound field would be taken in this plane. The jet nozzle was located midway both horizontally and vertically in the working volume of the chamber. Tests were made for the following frequencies: 200 Hz, 250 Hz, 300 Hz, 400 Hz, 1000 Hz, 3000 Hz. The sound source was a 6 in. diameter, 8 Ohm speaker driven by a McIntosh MI-75 amplifier and a Hewlett Packard Audio Oscillator. Sound levels were measured with a Bruel and Kjaer 4136 microphone with a 2618 preamplifier whose output was filtered about the selected frequency using a Bruel and Kjaer 1416 Octave Filter set and then indicated on a Bruel and Kjaer 2607 amplifier.

The test results have been discussed in section 3.2 and have demonstrated the chamber is superior to commercial standards for anechoic quality.

APPENDIX B. DETAILS OF NOZZLE DESIGN

B.1 Summary

This section presents details on the design and boundary layer analysis for the nozzle described in Section 3.3.3.

B.2 Uncorrected Nozzle Dimensions

As described in Chapter III the design Mach number distribution along the nozzle is:

$$M(x) = .164 + .108x + .036\, e^{-3x} \tag{B.1}$$

The exponential term guarantees a smooth transition at the entrance: $\left.\frac{dM}{dx}\right|_{x=0} = 0.$

Let A be the cross-sectional area at a station x, A_* the area at the throat, then for a one-dimensional inviscid isentropic flow with isentropic index γ, A_*/A and the Mach number, M, are related by

$$\frac{A_*}{A} = \left(\frac{\gamma+1}{2}\right)^{\frac{\gamma+1}{2(\gamma-1)}} M\left(1 + \frac{\gamma-1}{2}M^2\right)^{-\frac{\gamma+1}{2(\gamma-1)}} \tag{B.2}$$

With the fact that $\gamma = 1.4$ for Nitrogen, equations (B.1) and (B.2) can be combined to give

$$\frac{A_*(x)}{A(x)} = \frac{216}{125}\,(.164+.108x+.036e^{-3x})\left(1+\frac{(.164+.108x+.036e^{-3x})^2}{5}\right) \tag{B.3}$$

Let $h_o(x)$ be the distance between nozzle contours, then if the width of the nozzle is 1 in. and if the throat height is 1 in.,

$$h_o(x) = \frac{A(x)}{A^*(x)} \tag{B.4}$$

$h_o(x)$ is the uncorrected nozzle height defined in Section 3.3.3.

B.3 Equations of the Boundary Layer

The following variables are defined:

x = nozzle axial coordinate

y = vertical coordinate

$\delta(x)$ = boundary layer thickness

$\rho(x, y)$ = local density

$\rho_e(x)$ = freestream density

$\overline{U}(x)$ = freestream velocity distribution

τ = viscous shear stress

$u(x, y)$ = horizontal velocity component

$v(x, y)$ = vertical velocity component

The governing differential equations of the boundary layer are:

CONTINUITY:

$$\frac{\partial}{\partial x}(\rho u) + \frac{\partial}{\partial y}(\rho v) = 0 \qquad \text{(B.5)}$$

MOMENTUM:

$$\rho u \frac{\partial u}{\partial x} + \rho v \frac{\partial u}{\partial y} = \rho_e \overline{U} \frac{d\overline{U}}{dx} + \frac{\partial \tau}{\partial y} \qquad \text{(B.6)}$$

The equations are converted into a single ordinary differential equation in x by taking the integral of each from $y_o(x)$ to $\delta(x)$ with respect to y where $y_o(x)$ is the local nozzle contour surface. Making use of the fact that $u = v = 0$ at $y = y_o$ and $u = \overline{U}$ at $y = \delta$, the following equation is derived

$$\frac{1}{\overline{U}} \frac{d\overline{U}}{dx} \delta^* + \frac{d\theta}{dx} + \frac{\theta}{\rho_e \overline{U}^2} \frac{d}{dx}\left[\delta_e \overline{U}^2\right] = \tfrac{1}{2} C_f \qquad \text{(B.7)}$$

where θ is the boundary layer momentum thickness defined by:

$$\theta = \int_{y_o}^{\delta} \frac{\rho u}{\rho_e \bar{U}} \left(1 - \frac{u}{\bar{U}}\right) dy \tag{B.8}$$

δ^* is the boundary layer displacement thickness defined by:

$$\delta^* = \int_{y_o}^{\delta} \left(1 - \frac{\rho u}{\rho_e \bar{U}}\right) dy \tag{B.9}$$

and C_f is the wall shear stress coefficient defined by

$$C_f = \frac{\tau_w(x)}{\frac{1}{2} \rho_e \bar{U}^2} \tag{B.10}$$

$\tau_w(x)$ = wall shear stress.

Equation (B.7) will now be expressed completely in terms of θ, M, and H where H is the compressible shape factor

$$H = \frac{\delta^*}{\theta} \tag{B.11}$$

From the one-dimensional isentropic gas flow relations

$$\rho_e = \rho_o \left[1 + \frac{\gamma-1}{2}\right]^{-\frac{1}{\gamma-1}} \tag{B.12}$$

where ρ_o is the stagnation density

$$\bar{U} = Ma = M\sqrt{\gamma RT} \tag{B.13}$$

$a = \sqrt{\gamma RT}$ is the speed of sound.

$$T = T_o \left(1 + \frac{\gamma-1}{2} M^2\right)^{-1} \tag{B.14}$$

where T_o is the stagnation temperature. Combining (B.13) and (B.14)

yields

$$\bar{U}^2 = \gamma R T_o M^2 \Big/ \left(1 + \frac{\gamma-1}{2} M^2\right) \tag{B.15}$$

Differentiation of equation (B.15) yields

$$\bar{U} \frac{d\bar{U}}{dx} = \frac{\gamma R T_o M \, dM/dx}{(1 + \frac{\gamma-1}{2} M^2)^2} \tag{B.16}$$

and then (B.15) and (B.16) yield

$$\frac{1}{\bar{U}} \frac{d\bar{U}}{dx} = \frac{1}{(1 + \frac{\gamma-1}{2} M^2)} \frac{1}{M} \frac{dM}{dx} \tag{B.17}$$

The remaining term in equation (B.7) which must be converted into a function of Mach number is $\frac{1}{\rho_e} \frac{d\rho_e}{dx}$. Since

$$\frac{1}{\rho_e \bar{U}^2} \frac{d}{dx} (\rho_e \bar{U}^2) = \frac{2}{\bar{U}} \frac{d\bar{U}}{dx} + \frac{1}{\rho_e} \frac{d\rho_e}{dx} \tag{B.18}$$

differentiation of (B.12) yields

$$\frac{1}{\rho_e} \frac{d\rho_e}{dx} = \frac{-M dM/dx}{[1 + \frac{\gamma-1}{2} M^2]} \tag{B.19}$$

Combining (B.7), (B.11), (B.17) and (B.19) yields

$$\frac{d\theta}{dx} + \frac{1}{(1 + \frac{\gamma-1}{2} M^2)} \left[\frac{2+H-M^2}{M} \frac{dM}{dx}\right] \theta = \frac{C_f}{2} \tag{B.20}$$

The task now is to find H as a function of θ and select a form for C_f which represents the skin friction coefficient in a compressible boundary layer. The form of C_f to be used is taken from Ref. 36

$$C_f = .246 e^{-1.56 H_i} (Re_\theta)^{-.268} \left(\frac{T_e}{T_{ref}}\right)^{1.268} \tag{B.21}$$

where T_e is the freestream temperature, T_{ref} is a reference temperature to be defined below, and Re_θ is the Reynolds number based on θ.

$$Re_\theta = \frac{\overline{U}\,\theta}{\nu_{ref}} \qquad \nu_{ref} = \text{kinematic viscosity at temperature } T_{ref}$$

H_i is the corresponding incompressible boundary layer shape factor, the ratio of δ^*/θ for an incompressible boundary layer in a freestream flow $\overline{U}(x)$. It will be shown below that H, the compressible shape factor is a function of H_i, M, and θ.

Let δ_i^* and θ_i be the incompressible counterparts of δ^* and θ. δ_i^* and θ_i are computed with a new transverse boundary layer coordinate, y_i, based on Howarth's Transformation.[37] This transformation when applied to the compressible boundary layer equations reduces them to the standard form for a boundary layer in an incompressible flow. The new coordinate y_i is given by

$$y_i = \int_o^y \frac{\rho}{\rho_e}\, dy' \qquad dy_i = \frac{\rho}{\rho_e}\, dy \tag{B.22}$$

In terms of y_i the expressions for θ and δ^* (equations B.8 and B.9) become

$$\theta = \int_{y_o}^{\delta} \frac{\partial u}{\rho_e \overline{U}} \left(1 - \frac{u}{\overline{U}}\right) dy = \int_{y_o}^{\delta_i} \frac{u}{\overline{U}} \left(1 - \frac{u}{U}\right) dy_i = \theta_2 \tag{B.23}$$

$$\delta^* = \int_{y_o}^{\delta} \left(1 - \frac{\rho u}{\rho_e \overline{U}}\right) dy = \int_{y_o}^{\delta_i} \left(\frac{\rho_e}{\rho} - \frac{u}{\overline{U}}\right) dy_i \tag{B.24}$$

From the assumption of constant pressure across the boundary layer and the ideal gas law

$$\frac{\rho_e}{\rho} = \frac{T}{T_e} \tag{B.25}$$

For moderate Mach numbers and zero heat transfer at the nozzle surface, the stagnation temperature across the boundary layer can be considered constant, therefore

$$C_p T_e + \tfrac{1}{2} \bar{U}^2 = C_p T + \tfrac{1}{2} u^2 \tag{B.26}$$

$$\frac{T}{T_e} = 1 + \tfrac{1}{2} \frac{\bar{U}^2}{C_p T_e} \left(1 - \frac{u^2}{\bar{U}^2}\right) = 1 + \frac{\gamma-1}{2} M^2 \left(1 - \frac{u^2}{\bar{U}^2}\right) \tag{B.27}$$

Equations (B.25) and (B.27) combine to give

$$\frac{\rho_e}{\rho} - \frac{u}{\bar{U}} = 1 + \frac{\gamma-1}{2} M^2 \left(1 - \frac{u^2}{\bar{U}^2}\right) - \frac{u}{\bar{U}} \tag{B.28}$$

Adding and subtracting $\frac{\gamma-1}{2} M^2 \frac{u}{\bar{U}}$ on the r.h.s. of equation (B.28) yields

$$\frac{\rho_e}{\rho} - \frac{u}{\bar{U}} = \frac{\gamma-1}{2} M^2 \frac{u}{\bar{U}} \left(1 - \frac{u}{\bar{U}}\right) + \left(1 + \frac{\gamma-1}{2} M^2\right)\left(1 - \frac{u}{\bar{U}}\right) \tag{B.29}$$

so

$$\delta^* = \left(1 + \frac{\gamma-1}{2} M^2\right) \int_{y_o}^{\delta_i} \left(1 - \frac{u}{\bar{U}}\right) dy_i + \frac{\gamma-1}{2} M^2 \int_{y_o}^{\delta_i} \frac{u}{\bar{U}} \left(1 - \frac{u}{\bar{U}}\right) dy_i \tag{B.30}$$

Now $$\delta_i^* = \int_{y_o}^{\delta_i} \left(1 - \frac{u}{\bar{U}}\right) dy_i$$

$$\theta_i = \int_{y_o}^{\delta_i} \frac{u}{\bar{U}} \left(1 - \frac{u}{\bar{U}}\right) dy_i$$

so

$$\delta^* = \left(1 + \frac{\gamma-1}{2} M^2\right) \delta_i^* + \frac{\gamma-1}{2} M^2 \theta_i \tag{B.31}$$

From equation (B.23) $\theta_i = \theta$; and $H_i = \delta_i^*/\theta_i$ so

$$\delta^* = \left\{\left(1 + \frac{\gamma-1}{2} M^2\right) H_i + \frac{\gamma-1}{2} M^2\right\} \theta \tag{B.32}$$

δ^* is thus a function of H_i, M, and θ. It also follows from equation (B. 32) that the compressible shape factor H and the incompressible shape factor H_i are related by

$$H = (1 + \frac{\gamma-1}{2} M^2)H_i + \frac{\gamma-1}{2} M^2 \qquad \text{(B. 33)}$$

The remaining problem now is to find a suitable value for H_i, then equation (B. 20) can be integrated. Since the Karman-Polhausen integral method is being used, a form for the boundary layer velocity distribution must be assumed. A logarithmic law of the wall profile which takes into account the negative pressure gradient in the freestream flow is used

$$\frac{u}{u_\tau} = \frac{1}{K} \ell n \left(\frac{y u_\tau}{\nu}\right) + C + \frac{\tilde{\pi}(x)}{K} \left(1 - \cos\frac{\pi y}{\delta}\right) \qquad \text{(B. 34)}$$

u_τ is the shear velocity $u_\tau = \sqrt{\frac{\tau_w}{\rho_e}}$

$K = 0.4$, $C = 5.0$ and the last term on the r. h. s. takes into account the external flow. Values of $\tilde{\pi}$ are tabulated in ref. 38. To find H_i it is necessary to evaluate the integrals

$$\begin{aligned} \frac{\delta_i^*}{\delta_i} &= \frac{u_\tau}{\overline{U}} \int_0^1 \left(\frac{\overline{U}-u}{u_\tau}\right) d\left(\frac{y}{\delta_i}\right), \\ \frac{\delta_i^* - \theta_i}{\delta_i} &= \frac{u_\tau^2}{\overline{U}} \int_0^1 \left(\frac{\overline{U}-u}{u_\tau}\right)^2 d\left(\frac{y}{\delta_i}\right). \end{aligned} \qquad \text{(B. 35)}$$

Substituting (B. 34) into (B. 35) yields

$$\frac{\delta_i^*}{\delta_i} = \frac{u_\tau}{\overline{U}} \left(1 + \frac{\tilde{\pi}}{k}\right) \qquad \text{(B. 36)}$$

$$\frac{\delta_i^* - \theta_i}{\delta_i} = \frac{u_\tau^2}{\overline{U}^2} \cdot \frac{1}{k^2}\left[2 + 2\left(1 + \frac{1}{\pi}\mathrm{Si}(\pi)\right)\tilde{\pi} + \frac{3}{2}\tilde{\pi}^2\right] \qquad \text{(B. 37)}$$

where

$$\mathrm{Si}(\pi) = \int_0^\pi \frac{\sin\xi}{\xi}\, d\xi \ .$$

Let $f = u_\tau / \overline{U}$. Then

$$\frac{\theta_i}{\delta_i} = \frac{f(1+\tilde{\pi})}{k} - \frac{f^2}{k^2}\left[2 + 2\left[1 + \frac{1}{\pi}\mathrm{Si}(\pi)\right]\tilde{\pi} + \frac{3}{2}\tilde{\pi}^2\right] \qquad \text{(B. 38)}$$

$$H_i = \frac{\delta_i^*/\delta_i}{\theta_i/\delta_i}$$

$$H_i = 1 - \frac{2f}{k}\,\frac{\left[2 + 2\left(1 + \frac{1}{\pi}\mathrm{Si}(\pi)\right)\tilde{\pi} + \frac{3}{4}\tilde{\pi}^2\right]}{(1+\tilde{\pi})}^{1} \qquad \text{(B. 39)}$$

B. 3. 1 Numerical calculation of H_i . For incompressible flows with a pressure gradient

$$f = \frac{u_\tau}{\overline{U}} = \sqrt{\frac{C_f}{2}} \cong .05 \ ,$$

$$k = 0.4 \ ,$$

$$\mathrm{Si}(\pi) = .59 \ .$$

From ref. 38, a suitable value for $\tilde{\pi}$ when the flow has a negative pressure gradient is $\tilde{\pi} = .25$. This gives

$$H_i = 1.147 \ .$$

B. 4 Numerical Calculation of C_f

Recall equation (B. 21):

$$C_f = .246\, e^{-1.56H_i}(\mathrm{Re}_\theta)^{-.268}\left(\frac{T_e}{T_{ref}}\right)^{1.268} \ .$$

T_{ref} is defined by the equation

$$\frac{T_{ref}}{T_e} = \frac{1}{2}\left(\frac{T_w}{T_e} + 1\right) + 0.22\left(\frac{T_{aw}}{T_e} - 1\right) \tag{B.40}$$

where

T_w = wall temperature ,

T_{aw} = adiabatic wall temperature.

For this low Mach number flow,

$$T_w = T_{aw} = T_o \ , \tag{B.41}$$

so

$$\frac{T_{ref}}{T_e} = 0.72\,\frac{T_o}{T_e} + 0.38 \ .$$

Now

$$\frac{T_o}{T_e} = 1 + \frac{\gamma - 1}{2} M^2 = 1 + .2M^2 \ ,$$

so

$$\frac{T_{ref}}{T_e} = 1 + .144M^2 \ ,$$

$$\left(\frac{T_e}{T_{ref}}\right)^{1.268} = (1 + 0.144M^2)^{-1.268} \tag{B.42}$$

and

$$Re_\theta = \frac{\bar{U}\theta}{\nu_{ref}} = \frac{\sqrt{\gamma R T_o}}{\nu_{ref}}\,\frac{M\theta}{(1+.2M^2)^{\frac{1}{2}}} \ . \tag{B.43}$$

Let ν_o = kinematic viscosity at $T_o = 520^\circ R$ and $p_o = 44.1$ psia. Then

$$(Re_\theta)^{-.268} = 8.85\times10^{-4}\,\frac{(1+.2M^2)^{.134}}{M^{.268}}\left(\frac{\gamma_{ref}}{\gamma_o}\right)^{.268}(1+.144M^2)^{-1.268} \ . \tag{B.44}$$

Now assume the viscosity has the following temperature dependence:

$$\frac{\mu_{ref}}{\mu_o} = \left(\frac{T_{ref}}{T_o}\right)^{.75} ,$$

and $p_{ref} \sim p_e$; then one has

$$\frac{\nu_{ref}}{\nu_o} = \frac{\mu_{ref}}{\mu_e} \cdot \frac{\rho_e}{\rho_{ref}} \cdot \frac{\mu_e}{\mu_o} \cdot \frac{\rho_o}{\rho_e} .$$

Then

$$\frac{\nu_{ref}}{\nu_o} = \left(\frac{T_{ref}}{T_e}\right)^{0.75} \left(\frac{T_{ref}}{T_e}\right) \cdot \left(\frac{T_o}{T_o}\right)^{0.75} (1+.2M^2)^{2.5} . \qquad (B.45)$$

Now

$$\begin{aligned} (T_e/T_o)^{.75} &= (1+.2M^2)^{-.75} , \\ T_{ref}/T_e &= (1 + 0.144M^2) . \end{aligned} \qquad (B.46)$$

Equations (B.45) and (B.46) yield

$$\frac{\nu_{ref}}{\nu_o} = (1+0.144M^2)^{1.75} (1+.2M^2)^{1.75} . \qquad (B.47)$$

Thus, $C_f/2$ can now be expressed as a function of M and θ:

$$\frac{C_f}{2} = \frac{4.43\times10^{-4}(1 + .2M^2)^{.604}}{(1+.144M^2)^{.799} M^{.268}} \theta^{-.268} . \qquad (B.48)$$

Equations (B.20), (B.33), and (B.48) yield the desired differential equation for θ:

$$\frac{d\theta}{dx} = -\left[3.147 - \frac{0.2M^2}{1+.2M^2}\right] \frac{1}{M} \frac{dM}{dx} \theta + \frac{.000443(1+.2M^2)^{.604}}{(1+.144M^2)^{.799} M^{.268}} \theta^{-.268} . \qquad (B.49)$$

APPENDIX C. PERFORMANCE ANALYSIS OF THERMAL PULSE HEATER

C. 1 Model

As described in Section 4 of Chapter III, the performance of the heater is modeled by a set of cylindrical wires, each of which is considered to have a heat transfer independent of the other wires.

The differential equation governing the wire temperature is from Chapter III.

$$C_w \frac{dT_w}{dt} = I^2R_1 - h_c A_1 (T_w - T_\infty) \qquad (C.1)$$

where

C_w = heat capacity of wire

T_w = wire temperature

A_1 = wire surface area

I^2R_1 = electrical power dissipated

h_c = film heat transfer coefficient

T_∞ = gas temperature

Let

$$\Theta = \frac{T_w - T_\infty}{T_\infty}$$

$$F = F(t) = \frac{I^2R_1}{h_c A_1 T_\infty} \qquad (C.2)$$

$$\tau = \frac{t}{C_w/h_c A_1}$$

Then (C. 1) can be rewritten in the dimensionless form

$$\frac{d\Theta}{d\tau} + \Theta = F \quad . \qquad (C.3)$$

Let $F = F(\tau)$ be a rectangular waveform with dimensionless period a_H , duty cycle $\alpha_1 a_H$, and an amplitude of A_o . The

steady-state solution for Θ will be found for this form of F.

At steady state,

$$\Theta(\tau) = \Theta(\tau + a_H) \quad . \tag{C.4}$$

Let

$$\begin{aligned} F(\tau) &= A_o && 0 \le \tau \le \alpha_1 a_H \\ F(\tau) &= 0 && \alpha_1 a_H < \tau < a_H \end{aligned} \tag{C.5}$$

at steady state. Let the minimum value of Θ be Θ_o; then, solving

$$\frac{d\Theta}{d\tau} + \Theta = A_o \qquad 0 \le \tau \le \alpha_1 a_h$$

subject to $\Theta = \Theta_o$ at $\tau = 0$ yields

$$\Theta = A_o + (\Theta_o - A_o)e^{-\tau} \qquad 0 \le \tau \le \alpha_1 a_H \quad . \tag{C.6}$$

For $\alpha_1 a_H \le \tau < a_H$, equation (C.3) becomes

$$\frac{d\Theta}{d\tau} + \Theta = 0 \quad , \tag{C.7}$$

the solution of which can be written

$$\Theta = K_2 e^{-(\tau - \alpha_1 a_H)} \qquad \alpha_1 a_H < \tau \le a_H \quad . \tag{C.8}$$

For a periodic steady-state solution, one must have

$$\begin{aligned} &\Theta(\tau = 0) = \Theta(\tau = a_H) \quad , \\ &\Theta(\tau = \alpha_1 a_H) \text{ be continuous} \quad . \end{aligned} \tag{C.9}$$

Equations (C.6), (C.8), and (C.9) yield the following equation for Θ_o:

$$\Theta_o = \frac{A_o\left[e^{\alpha_1 a_H} - 1\right]}{e^{a_H} - 1} \quad . \tag{C.10}$$

The maximum value of Θ occurs at $\tau = \alpha_1 a_H$. Let Θ_1 denote this value; then from equations (C.8), (C.9), and (C.10),

$$\Theta_1 = \frac{A_o\left[e^{a_H} - e^{a_H(1-\alpha_1)}\right]}{e^{a_H} - 1} \quad . \tag{C. 11}$$

The amplitude of the fluctuating component of Θ is thus $\Theta_1 - \Theta_o = \Delta\Theta$.

$$\Delta\Theta = \frac{A_o\left[e^{a_H} - e^{a_H(1-\alpha_1)} - e^{\alpha_1 a_H} + 1\right]}{e^{a_H} - 1} \tag{C. 12}$$

For a fixed value of A_o and a_H, we want to find the value of α_1 that maximizes $\Delta\Theta$.

Setting $(d\Delta\Theta)/(d\alpha_1) = 0$ yields $\alpha_1 = 1/2$, and

$$\Delta\Theta_{max} = \frac{A_o\left[1 + e^{a_H} - 2e^{a_H/2}\right]}{e^{a_H} - 1} \quad . \tag{C. 13}$$

Let I_{max} be the on state wire current. Then for a square wave current waveform, the average temperature rise in the wire is given by

$$h_c A_1 (\overline{T}_w - T_\infty) = I_{max}^2 R_1/2 \quad . \tag{C. 14}$$

From equations (C. 2),

$$I_{max}^2 R_1/2 = \frac{h_c A_1 T_\infty A_o}{2} \quad . \tag{C. 15}$$

Combining (C. 14) and (C. 15) yields

$$\frac{\overline{T}_w - T_\infty}{T_\infty} = \frac{A_o}{2} \quad . \tag{C. 16}$$

Let $T_\infty \Delta\Theta_{max} = \widetilde{T}_w = T_{w_{max}} - T_{w_{min}}$. Then from (C. 13),

$$\frac{\widetilde{T}_w}{(\overline{T}_w - T_\infty)} = 2\left\{\frac{1 + e^{a_H} - 2e^{a_H/2}}{e^{a_H} - 1}\right\} \quad . \tag{C. 17}$$

The remaining task is to find an expression for the temperature fluctuation in the gas. Let $\dot{m}_o$ be the mass flow rate of the gas, and A_T the total area of the heater wires. Then the average rate of heat transfer from the wire to the gas is given by:

$$h_c A_T(\overline{T}_w - T_\infty) = \dot{m}_o C_p(\overline{T}_g - T_\infty) \quad . \tag{C.18}$$

Similarly, one can write

$$\begin{aligned} h_c A_T(T_{w_{max}} - T_\infty) &= \dot{m}_o C_p(T_{g_{max}} - T_\infty) \\ h_c A_T(T_{w_{min}} - T_\infty) &= \dot{m}_o C_p(T_{g_{min}} - T_\infty) \end{aligned} \tag{C.19}$$

Let

$$\begin{aligned} \widetilde{T}_g &= T_{g_{max}} - T_{g_{min}} \quad , \\ \beta_1 &= (\dot{m}_o C_p)/(h_c A_T) \quad . \end{aligned}$$

Then from equations (C.17) and (C.19), the ratio of the temperature fluctuation in the gas to the average temperature rise in the wire is:

$$\frac{\widetilde{T}_g}{\overline{T}_w - T_\infty} = \frac{2}{\beta_1}\left\{\frac{1 + e^{a_H} - 2e^{a_H/2}}{e^{a_H} - 1}\right\} \quad . \tag{C.20}$$

C.2 Effect of Finite Heater Length

This section derives in detail the reduction of gas temperature fluctuation amplitude caused by the finite length of the heater.

Let U be the speed of the gas, L the length of the heater. Then a small volume of gas, say, of length $\delta x \ll L$, is in the heater for a time

$$\Delta t_H = L/U \quad . \tag{C.21}$$

The fluctuating temperature component of the wire which consists of

rising and falling exponentials is represented for purposes of this analysis by a sawtooth wave. This approximation is valid if the fluctuating amplitude is much smaller than the average value. Then

$$\begin{aligned} \tilde{T} &= \tilde{T}_w \, t/\frac{T}{2} && 0 \le t \le T/2 \\ \tilde{T} &= 2\tilde{T}_w(1 - t/T) && T/2 \le t \le T \end{aligned} \tag{C.22}$$

For a temperature wave to be produced, one must have $\Delta t_H < T$. The average temperature fluctuation of the wire seen by the gas is

$$\tilde{T}_{avg} = \frac{1}{\Delta t_H} \int_{T/2 - \Delta t_H/2}^{T/2 + \Delta t_H/2} \tilde{T} \, dt \, . \tag{C.23}$$

Integrating gives the result

$$\frac{\tilde{T}_{avg}}{\tilde{T}_w} = \left(1 - \frac{\Delta t_H}{2T}\right) . \tag{C.24}$$

Thus, the effect of the finite travel time of the gas through the heater is to reduce the gas fluctuation amplitude by a factor of $(1 - (\Delta t_H/2T))$. For L = 2 in. and U = 200 ft/sec , no fluctuation is generated when T = .417 msec or a square wave frequency of 2.4 KHz is used to drive the heater.

APPENDIX D. DETAILS OF ELECTRONIC AND ELECTRICAL EQUIPMENT

This appendix describes in detail the electronic and electrical equipment which was first introduced in Sections 6 and 7 of Chapter III.

D. 1 Kilowatt Pulse Generator

Figure D. 1 illustrates the power supply and pulsing circuit for producing the 300-volt, 60-ampere rectangular wave for the pulse heater. Power is brought into the system through a 3-phase, Y-connected transformer where the voltage is stepped up from 208 V to 240 V r.m.s. This voltage is the input to a 3-phase, Y-connected autotransformer whose variable voltage output is rectified and then routed to a bank of electrolytic capacitors whose total capacitance is .52 farad. The large capacitance results in negligible 60 Hz ripple and eliminates spiking in the autotransformer. Switches for the power supply are heavy duty AC and DC remote-controlled contactors.

The pulsing of the heater is accomplished by a dual SCR (silicon-controlled rectifier) commutation circuit. The SCR's are General Electric type "C154D[40] high speed inverter SCR's." Depending on the train of gate pulses used, rectangular voltage waveforms of various frequencies and duty cycle can be produced across the heater resistance.

DC output voltage is adjusted by varying the AC output of the autotransformer. Monitoring instruments for the power supply include the following:

1) autotransformer input voltage (3 phases),

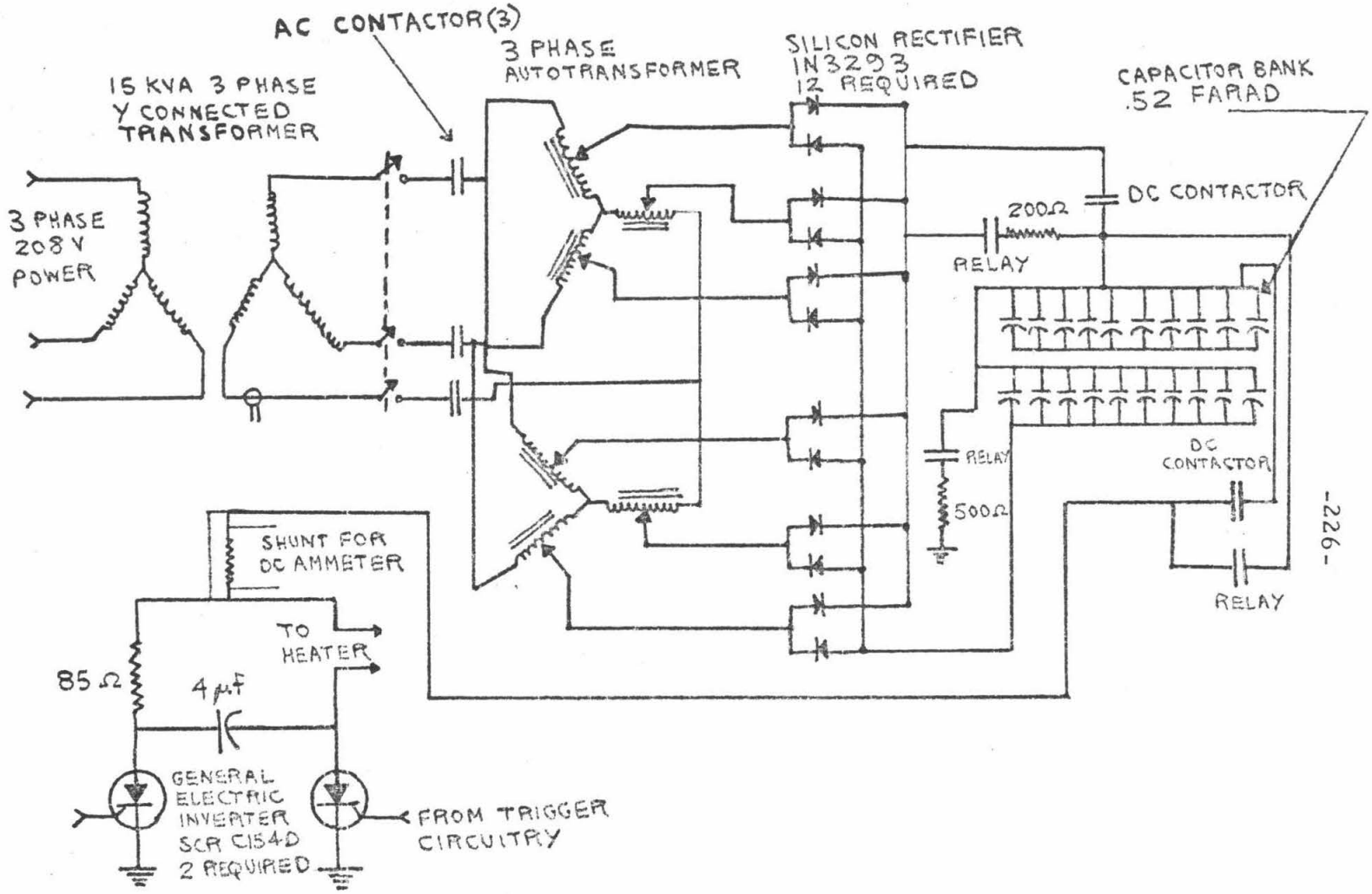

Fig. D.1 Power Supply and SCR Circuit for Thermal Pulse Heater

2) autotransformer input current (1 phase),

3) autotransformer output voltage (3 phases),

4) DC output voltage,

5) DC output current.

The capacitor bank can be charged directly from the rectified output of the autotransformer or through a 200 Ω power resistor. For discharging the capacitor bank, a 500 Ω power resistor can be switched in between the capacitor bank's positive terminal and ground.

D.2 SCR Control Circuitry

As described in Chapter III, the SCR's can be triggered by a self-running pulse generator or by the pulses produced by a phototransistor circuit in the bleed valve system.

Figure D.2 is a circuit diagram of the self-running pulse generator. The top of the diagram shows the 5 V power supply. The working part of the generator is five interconnected SN74121 monostable multivibrators[41] which produce pulse pairs with controlled intervals between the two pulses and with controlled repetition frequency as shown on Fig. D.2. Timing is controlled with five potentiometers, labeled #1 - #5 on fig. D.2. Pots #4 and #5 control the pulse pair frequency; pots #1 and #3 control the pulse widths; and pot #2 controls the time between pulses. The output pulses are amplified by the circuitry in fig. D.3 before being used to trigger the SCR's. The pulse amplifier circuitry is built in two modules, each module having its own electrical ground. The SCR trigger pulses are transmitted from the first module to the second through two TRIAD PL-31 pulse

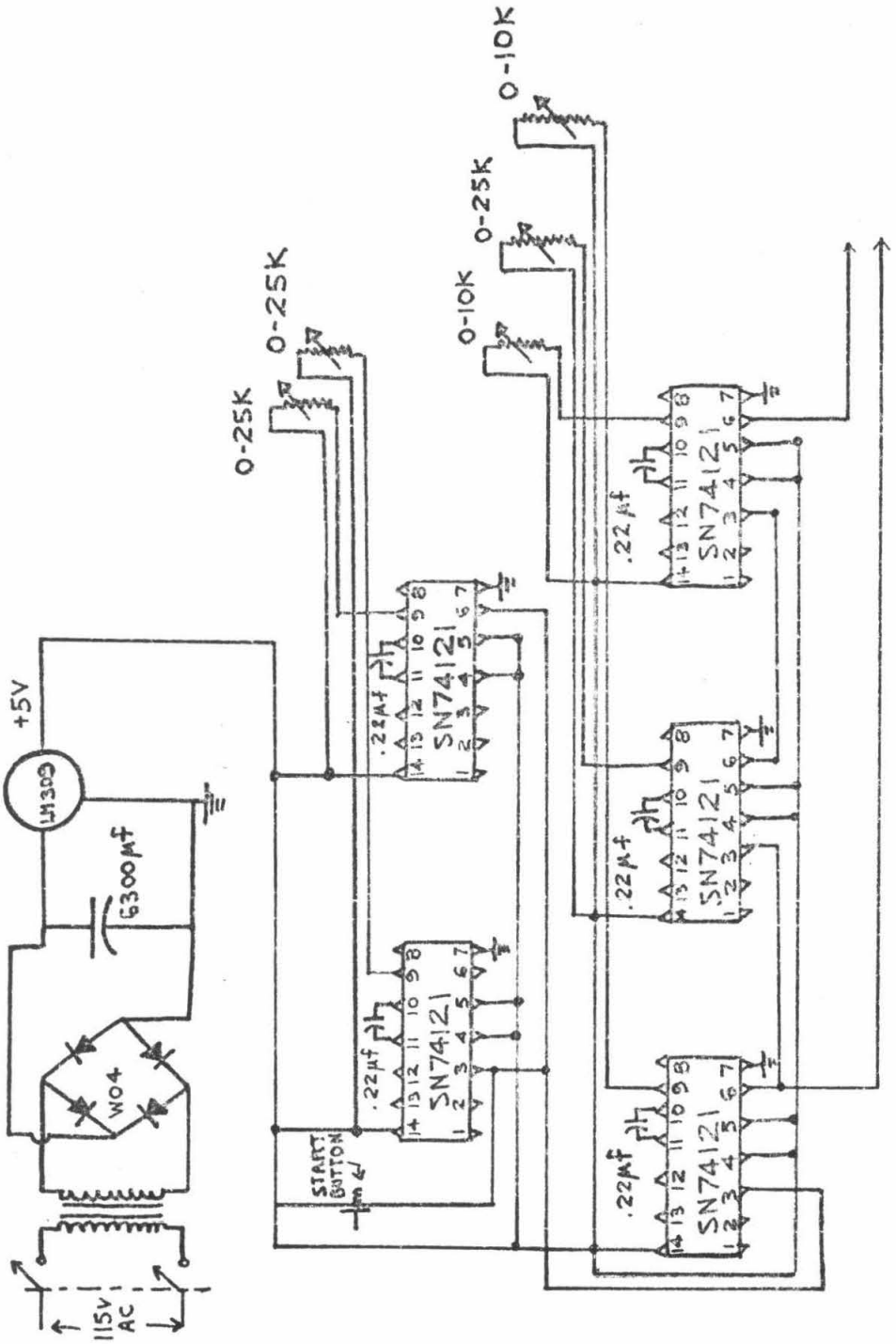

Fig. D.2 Self-Running Pulse Generator

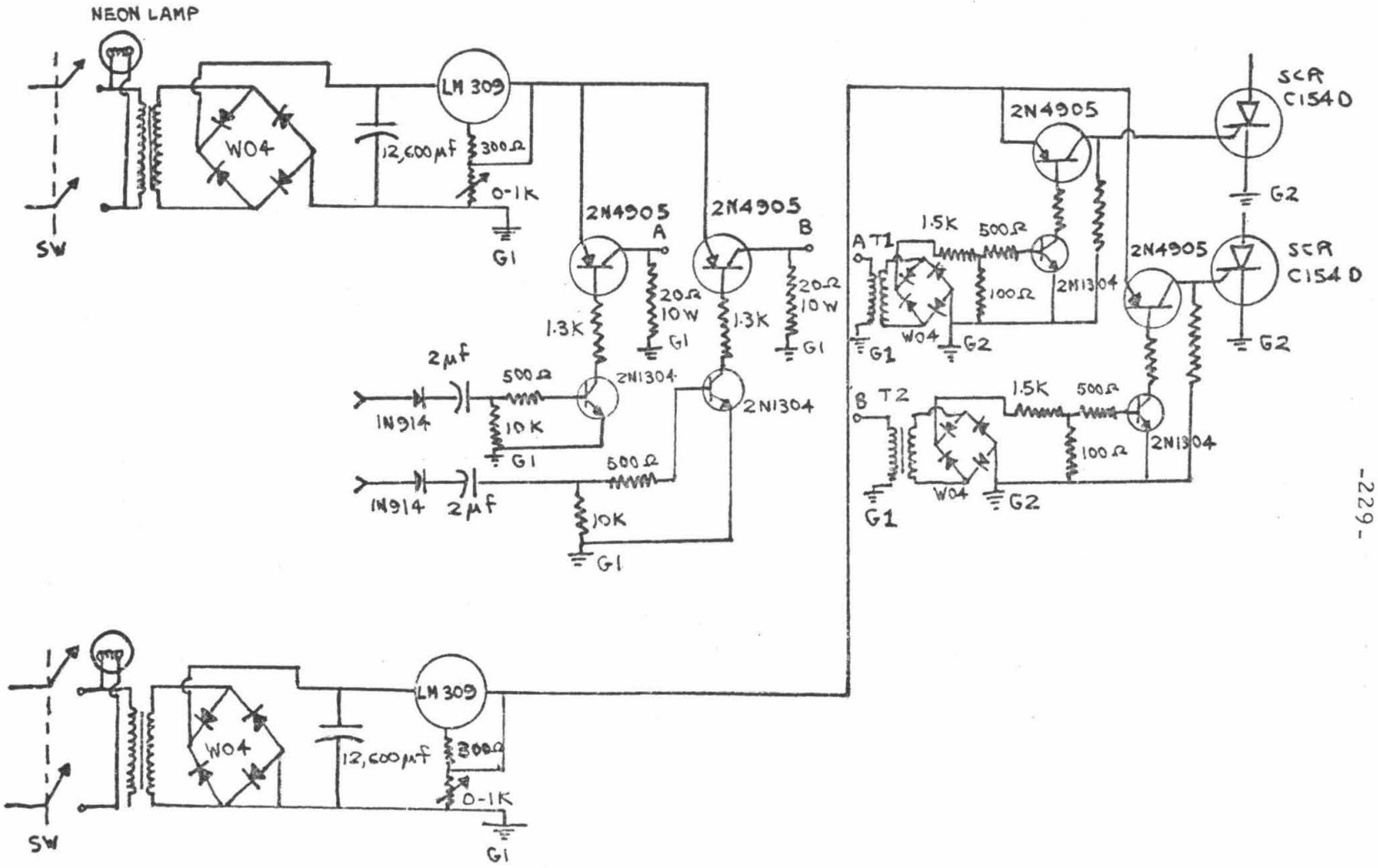

Fig. D.3 Pulse Amplifier and SCR Trigger Circuitry

transformers, as shown in fig. D. 3. The combination of the pulse transformer and diode bridge in the second module prevents the large negative voltage spikes caused by commutation of the SCR's from being transmitted back into the sensitive TTL control circuits of the self-running pulse generator. These negative spikes can cause extremely erratic operation of the self-running pulse generator and also the valve/heater synchronization circuitry to be described below.

D. 3 Heater/Valve Synchronization Circuitry

The bleed valve/heater synchronization circuitry is constructed in two modules, circuit diagrams of which are shown in fig. D. 4 (module I) and fig. D. 5 (module II). The top of each diagram shows the power supply circuitry: the circuitry of fig. D.4 uses a ±15 V DC power supply, while that of fig. D.5 uses a +15 V DC power supply.

Module I contains the phototransistor detector circuitry, with the exception of the FPT 120 phototransistor which is housed in the valve block assembly. The connections from the phototransistor to the other circuitry are made through 10-ft. long BNC cables. The output of the phototransistor is noise-spike filtered and sharpened by the SN-72741 [42] operational amplifier and 2N3704 NPN transistor. The output of the 2N3704 goes to a NE555 [42] precision timer integrated circuit. This NE555 is the basic element of the synchronization circuit: it provides a pre-selected time lag between a given valve shaft position and firing of the pulse heater. The output of the NE555 is transmitted to Module II, where the pulse waveform necessary for firing the SCR's is produced. The first and third NE555 timers in fig. D. 5

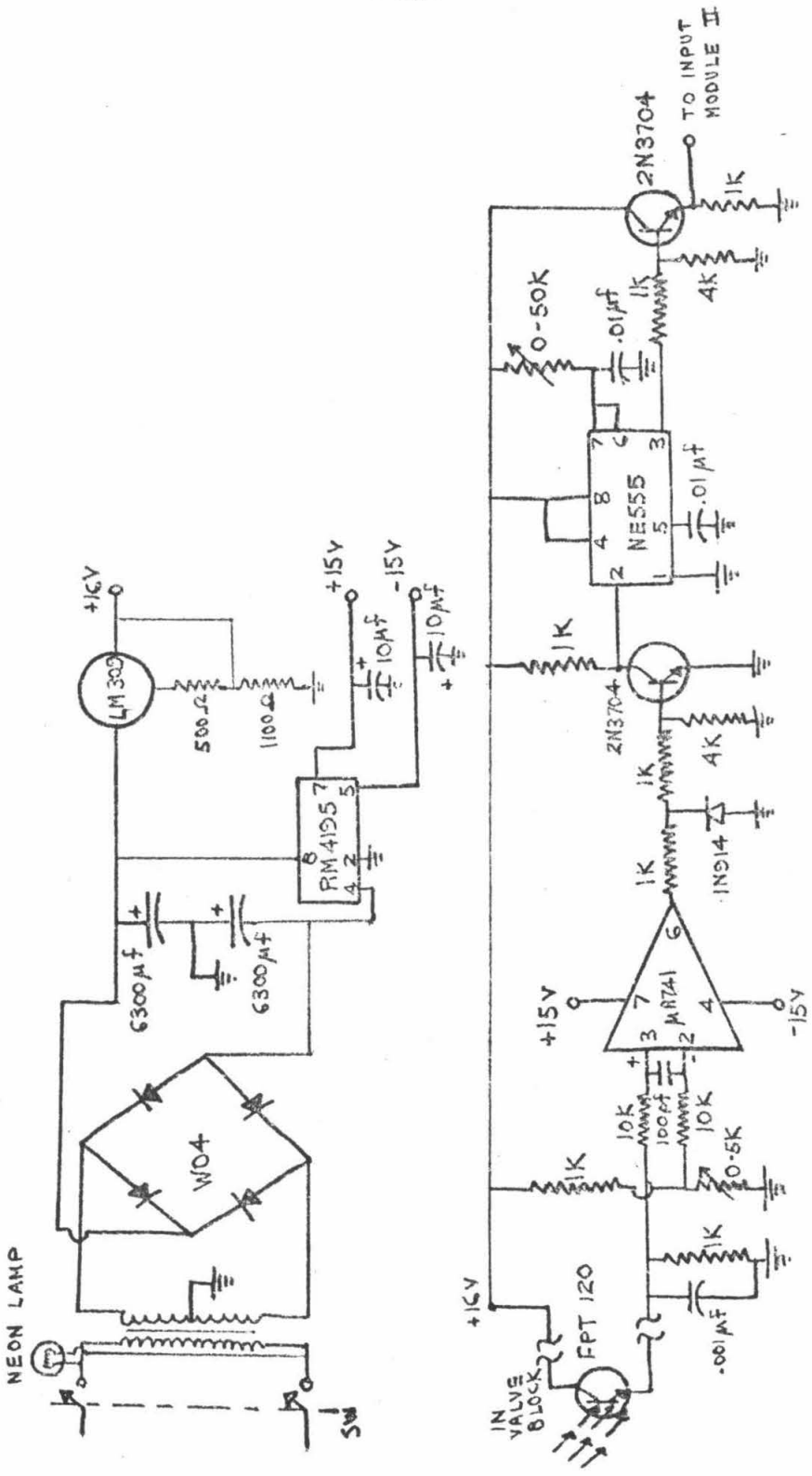

Fig. D.4 Bleed Valve/Heater Synchronization Circuitry

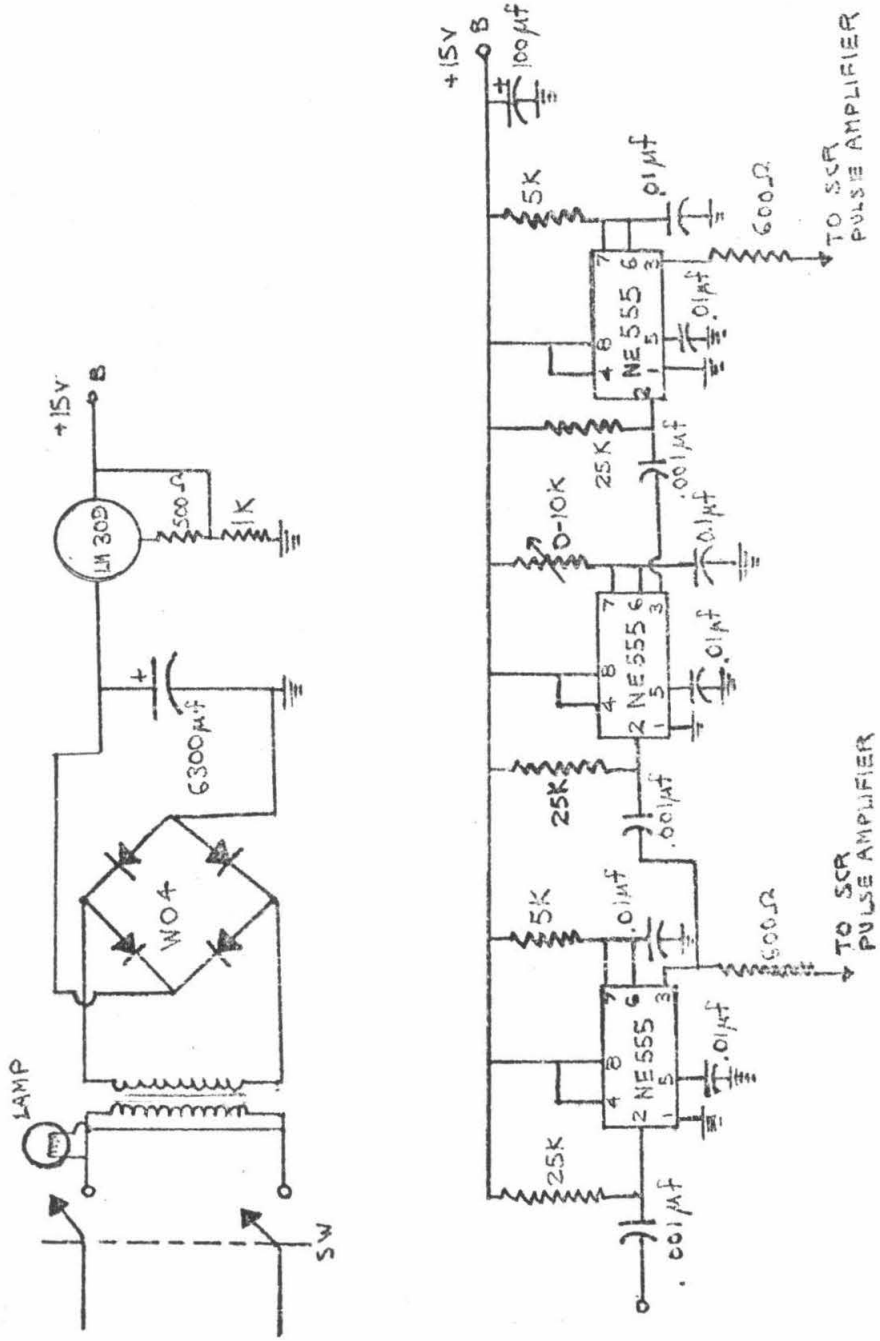

Fig. D.5 Bleed Valve/Heater Synchronization Circuitry

produces 10 μsec wide pulses which go to the pulse amplifier circuitry (fig. D. 3). The second NE555 produces a time delay between the two 10μsec pulses and hence is the controlling device for the duty cycle of the rectangular heater voltage waveform. For proper operation of this system, the time delay between pulses must be less than the period of the phototransistor signal.

D. 4 Signal-Averaging Control Device

As explained in Chapter III, the link between the heater/valve control circuitry and the data acquisition system is the signal-averaging control device. This subsection describes the electronic construction of the device, which consists of a power supply, one linear interface integrated circuit, and six TTL integrated circuits. A circuit diagram is given in fig. D. 6. The trigger pulse from the pulse amplifier circuitry (fig. D. 3) that goes to the gate of SCR 1 is used also as the input to the LM311H voltage comparator shown on the left of the circuit diagram.

The comparator reduces the pulse amplitude to +5 V and shapes it for compatibility with the TTL integrated circuitry. The "start sample" gate pulses and "sample" pulses for the A/D converter are produced by the three SN74121 monostable multivibrators shown in the diagram. The first two SN74121's (going from the left of the diagram) are coupled together to produce a continuous train of "start sample" pulses. The period of the waveform is set by a 0 - 50 KΩ potentiometer on the middle SN74121. This potentiometer thus controls the pause time of the A/D converter, the time between the end

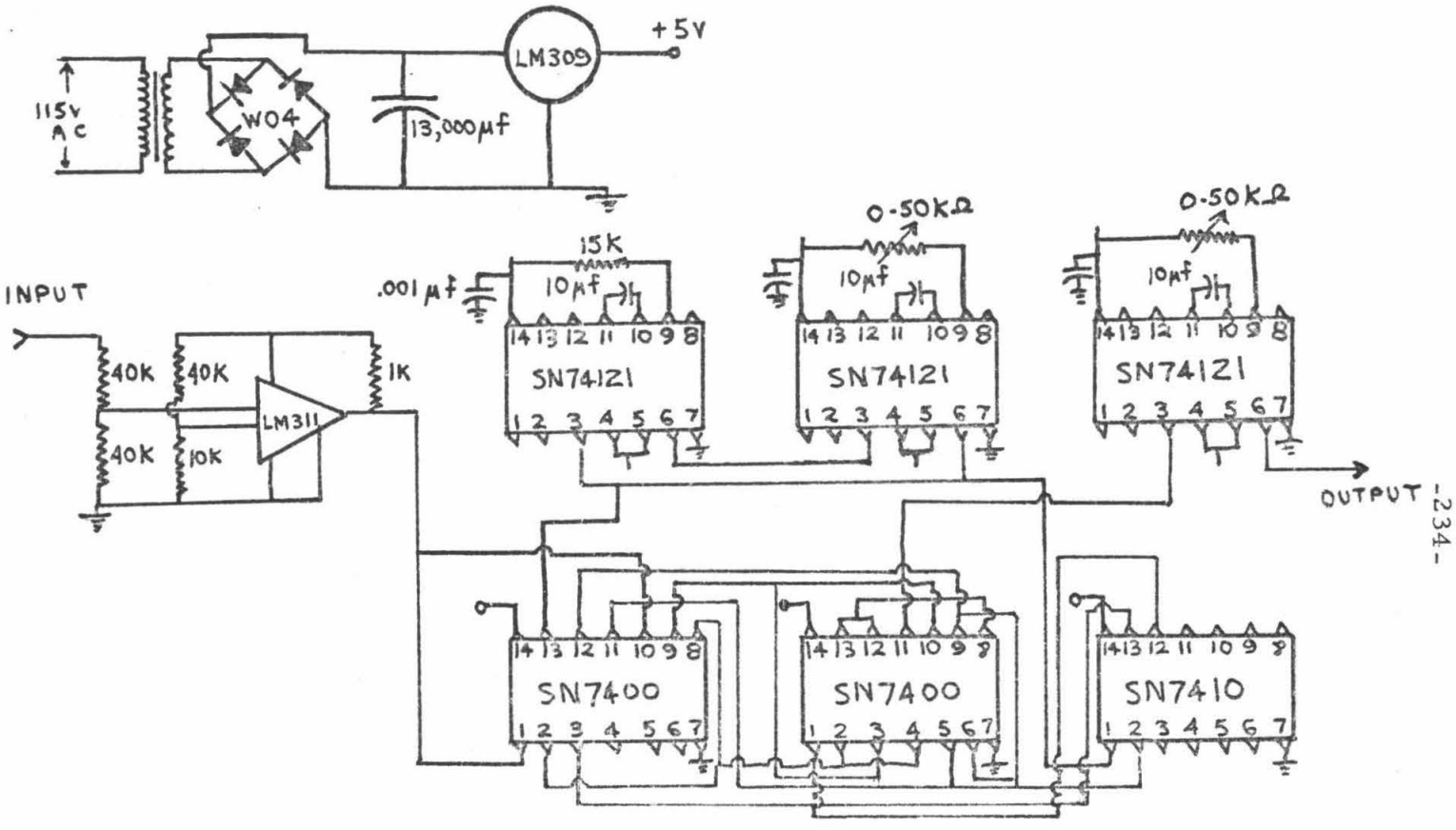

Fig. D.6 Signal Averaging Control Device Circuit Diagram

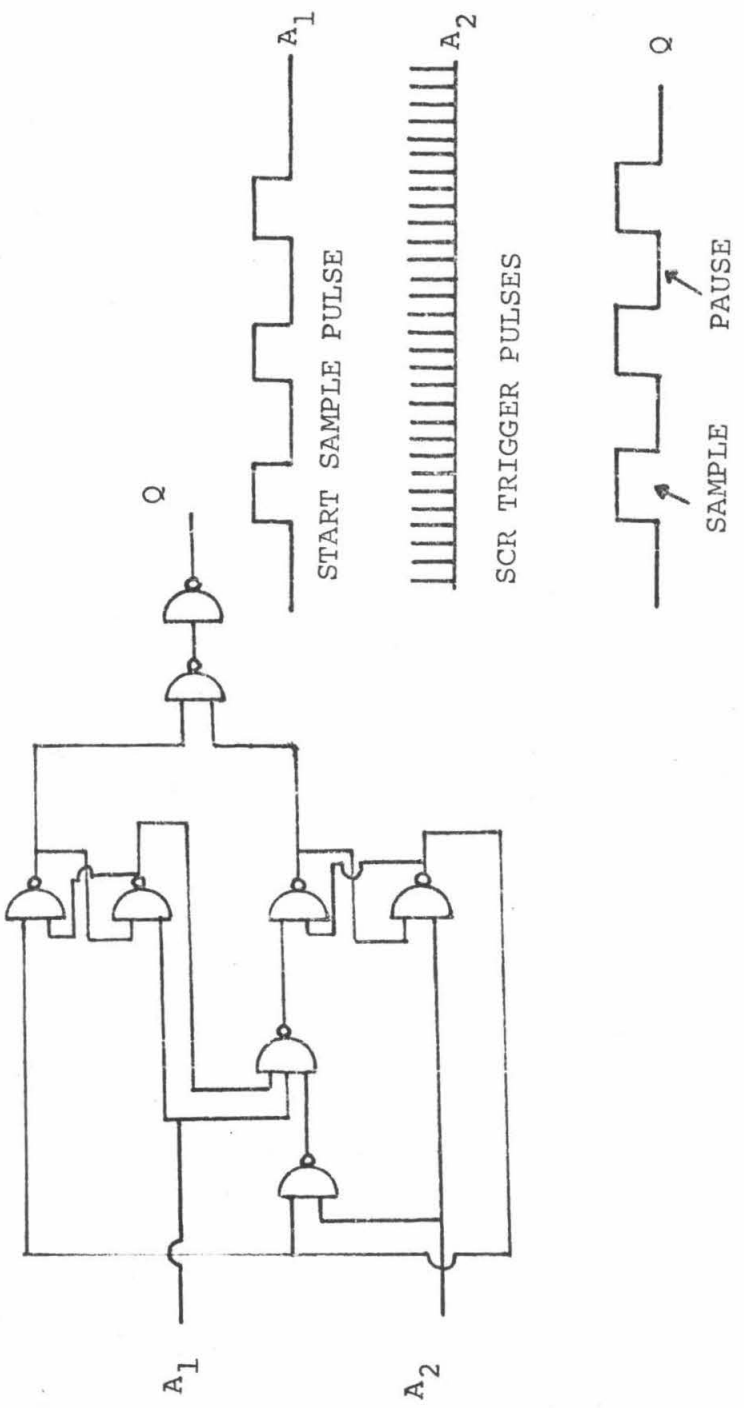

Fig. D.7 Signal Averaging Control Device Logic Diagram

and beginning of adjacent data samplings.

The output of the LM311H comparator and the output of the second SN74121 are the inputs to a logic circuit consisting of two SN7400 [41] 2-input NAND gates and a SN7410 [41] 3-input NAND gate. The logic functions are such that the sample pulse starts only when the first integral SCR control pulse occurs simultaneously with the gate after the latter has started. Once the sample pulse has started, it is independent of the SCR control and "start sample" gate pulses. After the sample pulse has dropped to zero, it will not go to a high level again until the first integral SCR control pulse occurs simultaneously with the gate pulse after the latter has started. A logic diagram is given in fig. D. 7.

The output of the signal-averaging device is connected to the BETA switch of the A/D converter with BNC cables and connections.

D. 5 Butterworth Low-Pass Filter

As described in Chapter III, it was necessary to use a low-pass filter to prevent aliasing errors in the processing of the digitally sampled signals. This requirement led to the contruction of a four-channel Butterworth 7-pole low-pass filter, a circuit diagram of which is shown in fig. D. 8. Shown in the upper part of the figure is a ± 15 volt, 2 ampere power supply for the four filter channels. The lower part of the diagram shows a typical filter channel. The channel consist of nine μA741 operational amplifiers interconnected with passive components so as to form a low-pass active filter with a corner frequency (attenuation of $1/\sqrt{2}$) at 4 K Hz and a rolloff of -50 db/oc-

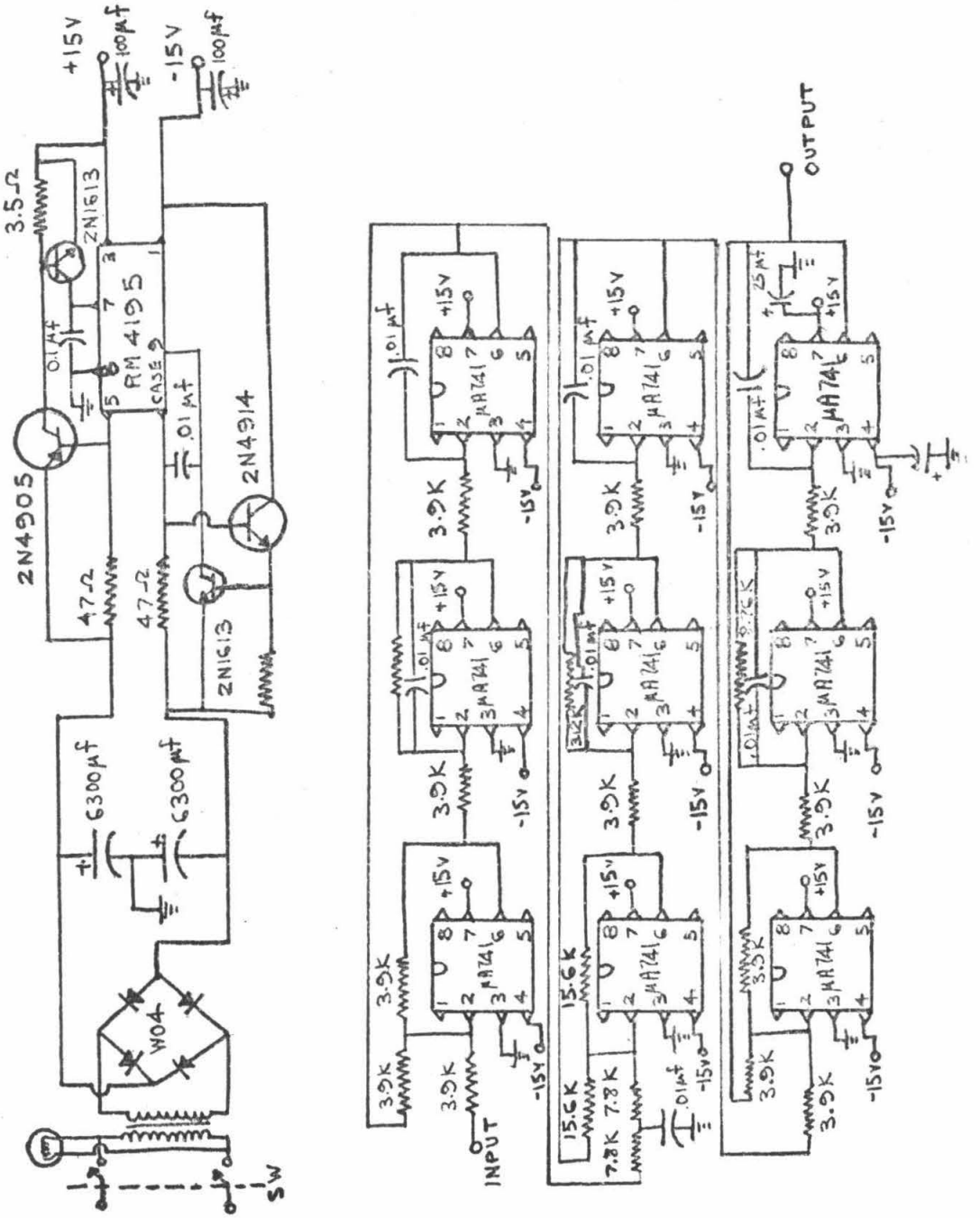

Fig. D.8 Butterworth 7 Pole Low Pass Active Filter Circuit Diagram

tave. The 25 μf capacitors on the ± 15 volt terminals of the operational amplifier in the lower right hand corner act as power-supply noise bypass capacitors and also tend to prevent oscillations during large voltage swings of the operational amplifiers in the channel.

The four filter channels were tested with a sine wave oscillator to see if the filters performed according to design. The tests showed all channels to have unity gain up to a frequency of 3800 Hz. As the oscillator frequency was increased above this value, the channel outputs dropped at -50 db/octave with respect to the constant amplitude input.

APPENDIX E. THREE-DIMENSIONAL SOUND PROPAGATION IN A RECTANGULAR DUCT WITH UNIFORM FLOW IN THE AXIAL DIRECTION

Consider an infinitely long rectangular duct in which there is a perfect gas moving with uniform velocity U in the axial direction. Let ϕ be the perturbation velocity potential for the flow; then in a frame of reference moving with the fluid, ϕ is determined by the wave equation

$$\frac{\partial^2 \phi}{\partial t'^2} = a^2 \frac{\partial^2 \phi}{\partial x_i'^2} \quad . \tag{E.1}$$

This equation must now be rewritten for a stationary frame of reference in which the fluid is moving with velocity U .

Let x_i , t be the space and time coordinates in the stationary frame; x_i' , t' be the space and time coordinates in the moving frame; then

$$\begin{aligned} x_i' &= x_i - U_i t' \\ t' &= t \end{aligned} \tag{E.2}$$

Now

$$\frac{\partial \phi}{\partial x_i'} = \frac{\partial \phi}{\partial x_i} \frac{\partial x_i}{dx_i'} + \frac{\partial \phi}{\partial t} \frac{\partial t}{\partial x_i'} = \frac{\partial \phi}{\partial x_i} \quad ; \tag{E.3}$$

$$\begin{aligned} \frac{\partial \phi}{\partial t'} &= \frac{\partial \phi}{\partial t} \frac{\partial t}{\partial t'} + \frac{\partial \phi}{\partial x_i} \frac{\partial x_i}{\partial t'} \quad , \\ \frac{\partial \phi}{\partial t'} &= \frac{\partial \phi}{\partial t} + U_i \frac{\partial \phi}{\partial x_i} \quad . \end{aligned} \tag{E.4}$$

Substituting (E. 3) and (E. 4) into (E. 1) and using the notation

$$U_i = U \delta_{i1}$$

$$x_1 = x$$

$$x_2 = y$$

$$x_3 = z$$

gives the following equation for ϕ in the stationary frame:

$$\frac{1}{a^2}\left[\frac{\partial^2\phi}{\partial t^2} + 2U\frac{\partial^2\phi}{\partial x \partial t}\right] = (1-M^2)\frac{\partial^2\phi}{\partial x^2} + \frac{\partial^2\phi}{\partial y^2} + \frac{\partial^2\phi}{\partial z^2} \quad , \tag{E.5}$$

where M is the Mach number, M = U/a. The boundary conditions to be described below will have a time dependence $e^{i\omega t}$; hence, the potential can be written

$$\phi = \hat{\phi}\, e^{i\omega t} \quad . \tag{E.6}$$

Substituting this last equation in (E.5) and then dropping the "^" superscript for convenience yields

$$\frac{1}{a^2}\left[-\omega^2\phi + 2i\omega U\frac{\partial\phi}{\partial x}\right] = (1-M^2)\frac{\partial^2\phi}{\partial x^2} + \frac{\partial^2\phi}{\partial y^2} + \frac{\partial^2\phi}{\partial z^2} \quad . \tag{E.7}$$

The boundary conditions for ϕ are given below: figure E.1 illustrates the situation.

on surfaces

$$-\infty < x < \infty$$

$$0 \le y \le d \qquad w = \frac{\partial\phi}{\partial z} = 0 \quad ; \tag{E.8}$$

$$z = \pm b$$

on surfaces

$$-\infty < x < \infty$$

$$-b \le z \le b \qquad v = \frac{\partial\phi}{\partial y} = 0 \quad ; \tag{E.9}$$

$$y = d$$

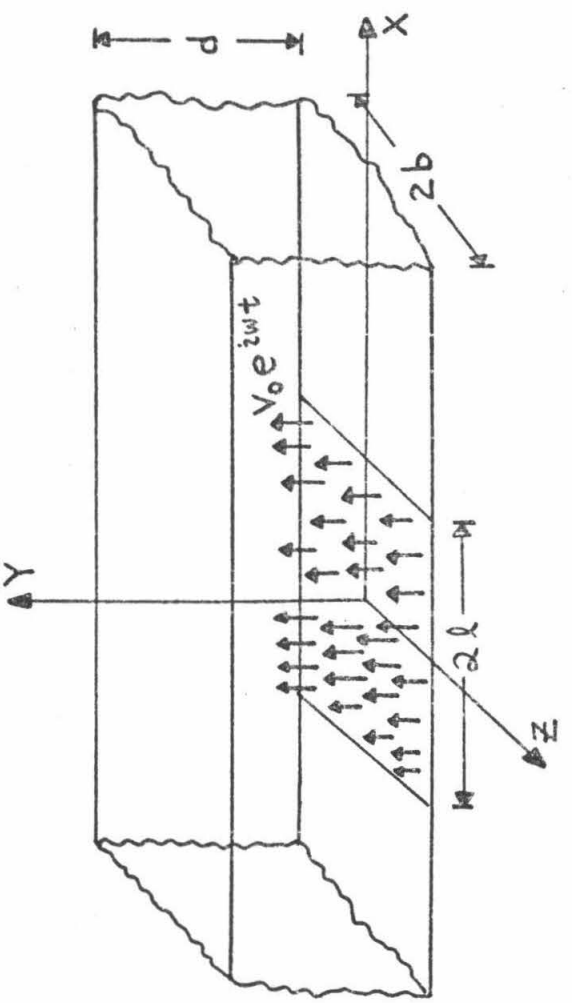

Fig. E.1 Infinitely Long Rectangular Duct with Periodic Bleed Flow on a Segment of One Wall.

on surfaces

$$-\infty < x < -\ell$$

$$\ell < x < \infty \qquad v = \frac{\partial \phi}{\partial y} = 0 \; ; \qquad \text{(E. 10a)}$$

$$y = 0$$

$$-b \leq z \leq b$$

on surfaces

$$-\ell \leq x \leq \ell$$

$$y = 0 \qquad \frac{\partial \phi}{\partial y} = v_o \; . \qquad \text{(E. 10b)}$$

$$-b \leq z \leq b$$

The last boundary condition for $y = 0$ operated on by a Fourier transform with respect to x:

$$\int_{-\infty}^{\infty} \frac{\partial \phi}{\partial y}_{y=0} e^{-ikx} \, dx \; . \qquad \text{(E. 11)}$$

Let $\frac{\partial \phi k}{\partial y}$ be the Fourier transform for wave number k . Then (E. 10) and (E. 11) yield

$$\frac{\partial \phi_k}{\partial y}_{y=0} = \frac{2v_o}{k} \sin k\ell \; ,$$

and (E. 9) and (E. 11) yield:

$$\frac{\partial \phi_k}{\partial y}_{y=d} = 0 \; . \qquad \text{(E. 12)}$$

Since the boundary conditions in z are homogeneous, the $\partial^2 \phi / \partial z^2$ term in equation (E. 7) can be set equal to zero. With this simplification, the next step is to take the Fourier transform of (E. 7) with respect to x . A transformed potential $\tilde{\phi}$ is defined by

$$\tilde{\phi}(k, y) = \int_{-\infty}^{\infty} \phi(x, y) \, e^{-ikx} \, dx \; . \qquad \text{(E. 13)}$$

From equation (E. 13) it follows that

$$-ik\tilde{\phi} = \int_{-\infty}^{\infty} \frac{\partial \phi}{\partial x} e^{-ikx}\, dx \quad ,$$

$$-k^2\tilde{\phi} = \int_{-\infty}^{\infty} \frac{\partial^2 \phi}{\partial x^2} e^{-ikx}\, dx \quad .$$

With the notation of $\tilde{\phi}_{yy} = \partial^2\tilde{\phi}/\partial y^2$, the transformed version of equation (E. 7) is:

$$\tilde{\phi}_{yy} - (1-M^2)\left[k^2 - \frac{2\omega kU}{a^2(1-M^2)} - \frac{\omega^2}{a^2(1-M^2)} \right]\tilde{\phi} = 0 \quad . \qquad \text{(E. 14)}$$

Let

$$\sigma^2 = (1-M^2)\left[k^2 - \frac{2\omega kU - \omega^2}{a^2(1-M^2)} \right] ;$$

then the solution of (E. 14) can be written

$$\tilde{\phi}_k = A'\cosh \sigma y + B'\sinh \sigma y \quad . \qquad \text{(E. 15)}$$

The boundary condition $\partial\tilde{\phi}/\partial y = 0$ at $y = d$ eliminates one constant of integration from (E. 15), putting $\tilde{\phi}$ in the form

$$\tilde{\phi}_k = A \cosh \sigma (d-y) \quad . \qquad \text{(E. 16)}$$

Using equation (E. 16), A is evaluated

$$\left.\frac{\partial \tilde{\phi}_k}{\partial y}\right|_{y=0} = -\sigma A \sinh \sigma d = \frac{2v_o}{k} \sin k\ell \quad ,$$

$$A = -\frac{2v_o}{k} \frac{\sin k\ell}{\sinh \sigma d} \quad . \qquad \text{(E. 17)}$$

(E. 16) and (E. 17) give the complete expression for $\tilde{\phi}_k$:

$$\tilde{\phi}_k = -\frac{2v_o \sin k\ell}{\sigma k \sinh \sigma d} \cosh \sigma (d-y). \qquad \text{(E.18)}$$

The potential function $\tilde{\phi}(x, y)$ is found by inversion of (E. 18) by the integral

$$\tilde{\phi}(x, y) = \frac{1}{2\pi} \int_{-\infty}^{\infty} \tilde{\phi}(k, y) e^{ikx} \, dk \quad ,$$

which in this case is

$$\tilde{\phi}(x, y) = -\frac{v_o}{\pi} \int_{-\infty}^{\infty} \frac{\sin k\ell \cosh \sigma (d-y) e^{ikx}}{\sigma k \sinh \sigma d} \, dk \quad . \qquad \text{(E. 19)}$$

The integral will be evaluated by considering it to be a segment of a contour integral in the complex plane for which k is the real part of a complex variable.

Let $k = \Re e(z)$; then on the real axis, (E. 19) is equivalent to

$$\tilde{\phi}(x, y) = -\frac{v_o}{\pi} \int_{-\infty}^{\infty} \frac{\sin z\ell \cosh \sigma (d-y)}{\sigma z \sinh \sigma d} \, e^{izx} \, dz \quad . \qquad \text{(E. 20)}$$

The right hand side of (E. 20) is considered to be part of a contour integral taken along a contour consisting of the real axis and a semicircle of infinite radius in the upper or lower half plane. Choice of the upper or lower half plane depends on the size of the integrand as $|z| \to \infty$. This choice will be discussed below.

The contour integral will be evaluated by the residue theorem; hence, it is necessary to know the zeroes of $\sigma z \sinh \sigma d$. One zero is at $z = 0$. The corresponding residue gives no contribution since $\sin z\ell = 0$ at $z = 0$.

Next consider the zeroes of σ . Since

$$\sigma^2 = (1-M^2)\left\{\left[z + \frac{\omega}{a(1-M)}\right]\left[z - \frac{\omega}{a(1+M)}\right]\right\} , \qquad \text{(E. 21)}$$

$\sigma^2 = 0$ for

$$z_{\pm} = \frac{\omega[M \pm 1]}{a(1-M^2)} \quad . \qquad \text{(E. 22)}$$

Thus, we have two poles on the real axis; the remaining poles occur

for $\sinh \sigma d = 0$. This condition yields an infinite number of imaginary values of σ :

$$\sigma = in\pi/d \qquad n = 1, 2, \ldots \tag{E.23}$$

These values of σ will be taken to correspond to poles denoted by z_n.

Now consider the problem of which contour to choose. Let $z = re^{i\theta}$. As $r \to \infty$, $\sigma \to z$; then the integrand of (E. 19) for large z is given by:

$$\frac{\sin z\ell \cosh z(d-y)\, e^{izx}}{z^2 \sin zd} \quad . \tag{E.24}$$

Now

$$\sin z\ell = \sin(r\ell \cos\theta)\cosh(r\ell \cos\theta) - i\cos(r\ell \cos\theta)\sin(r\ell \sin\theta) \times$$

$$e^{-r \sin\theta x}\, e^{ir \cos\theta x} \quad .$$

Since $d-y \leq d$, as $|z| \to \infty$,

$$\frac{\cosh z(d-y)}{\sinh zd} \leq 1 \quad ,$$

so for the integrand in equation (E. 24) to go to zero as $|z| \to \infty$ we must have

$$\begin{aligned} &\lim_{R\to\infty} e^{-r \sin\theta x} \cosh(r\ell \sin\theta) \to 0 \\ &\lim_{R\to\infty} e^{-r \sin\theta x} \sinh r\ell(\sin\theta) \to 0 \end{aligned} \tag{E.25}$$

The above will hold for $x > \ell$, $0 \leq \theta \leq \pi$, so a solution can be found downstream of the bleed valve slits. Since the behavior of the transverse modes is desired only in this region, the convergence problem need not be considered further. Thus, the semicircular contour is to be taken in the upper half plane with two small contours around the zeroes of σ as shown in fig. E. 2.

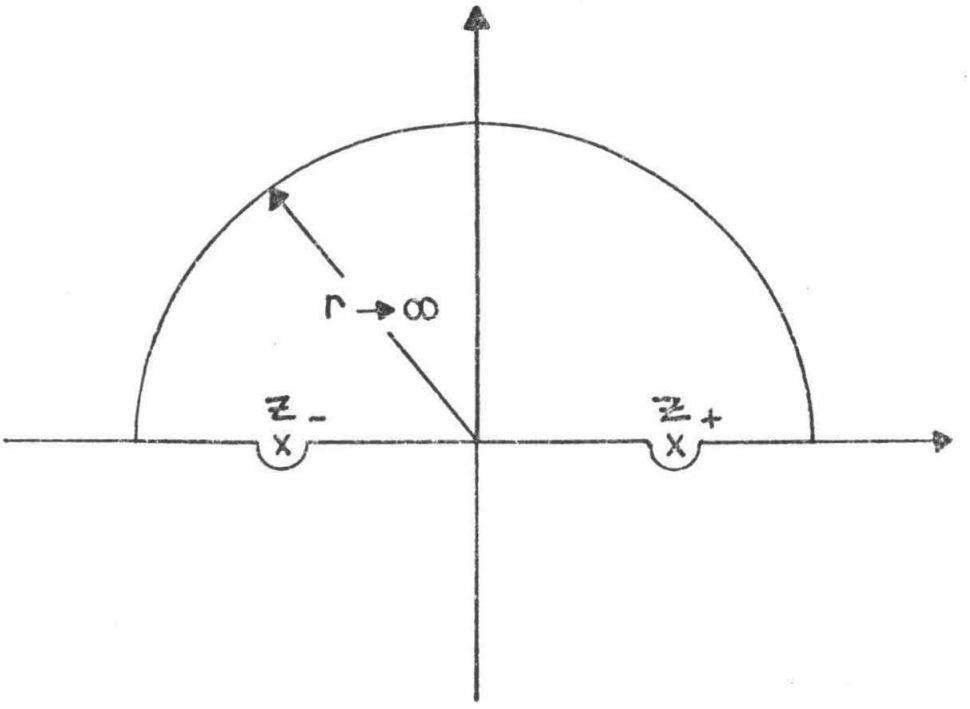

Fig. E.2 Integration Contour for Inversion of Fourier Transform.

Consider first the residues at z_+ and z_-. Let

$$f(z) = \frac{\sin z\ell \cosh \sigma (d-y) e^{izx}}{\sigma z \sinh \sigma d} \quad . \tag{E.26}$$

As $\sigma \to 0$,

$$\cosh \sigma (d-y) \to 1$$

$$\sinh \sigma d \to \sigma d \ ,$$

so near z_-,

$$f(z) = \frac{\sin z_- \ell\, e^{iz_-x}}{(1-M^2)(z-z_-)(z_- - z_+)z_- d}$$

and near z_+,

$$f(z) = \frac{\sin z_+ \ell\, e^{iz_+x}}{(1-M^2)(z-z_+)(z_+ - z_-)\, z_+ d} \quad .$$

Then $\pi i \times$ sum of the residues at these two poles is

$$\pi i \sum_{m=1}^{2} \mathrm{Res}(z_m) = \frac{\pi i a^2}{2\omega^2 d} \left\{ (1+M) \frac{\sin \omega\ell}{a(1+M)} e^{\frac{i\omega x}{a(1+M)}} - (1-M) \frac{\sin \omega\ell}{a(1-M)} e^{-\frac{i\omega x}{a(1-M)}} \right\} \tag{E.27}$$

Examining the exponentials on the right hand side of (E.26), it is immediately obvious that these residues give the steady state or plane wave part of the solution. The first exponential represents the downstream-running pressure wave with wave number

$$k_+ = \frac{\omega}{a(1+M)} \ ;$$

and the second exponential, the upstream-running pressure wave with wave number

$$k_- = -\frac{\omega}{a(1-M)} \quad .$$

Now consider the residues at z_n, where z_n are the zeroes of $\sinh \sigma d$. To put $f(z)$ in a form for evaluating the residues, expand $\sinh \sigma d$ in a Taylor series about z_n where $\sigma d = n\pi i$:

$$\sinh \sigma d = \sinh n\pi i + \cosh n\pi i \frac{d\sigma}{dz}(z-z_n) + \ldots$$

From equation (E.21) one finds

$$\frac{d\sigma}{dz}_{z_n} = \frac{(1-M^2)}{n\pi}\sqrt{\frac{n^2\pi^2}{(1-M^2)d^2} - \frac{\omega^2}{a^2(1-M^2)^2}} \quad . \qquad \text{(E.28)}$$

Also,

$$\sinh n\pi i = \sin n\pi = 0 ,$$

$$\cosh n\pi i = \cos n\pi = (-1)^n .$$

Then, near z_n, $f(z)$ is given by

$$f(z) = \frac{\sin z_n \ell \cos n\pi(d-y)/d \; e^{iz_n x}}{z_n(-1)^n(1-M^2)\sqrt{\frac{n^2\pi^2}{(1-M^2)d^2} - \frac{\omega^2}{a^2(1-M^2)^2}}\;(z-z_n)} . \qquad \text{(E.29)}$$

z_n can be evaluated from equation (E.21) by setting $\sigma^2 = n\pi i/d$; the result is

$$z_n = \frac{-M\omega}{a(1-M^2)} \pm \sqrt{\frac{\omega^2}{a^2(1-M^2)^2} - \frac{n^2\pi^2}{(1-M^2)d^2}} \quad . \qquad \text{(E.30)}$$

z will be complex when

$$\frac{\omega^2}{a^2(1-M^2)^2} - \frac{\pi^2}{(1-M^2)d^2} < 0 .$$

In terms of the wavelength λ this condition is

$$\lambda^2 > \frac{4d^2}{1-M^2} .$$

For the experiment, d = 1 in., M = 0.2, so we must have

$$\lambda > 2.04 \text{ in.}$$

In the experiment, the minimum wavelength is 24 inches, so the condition is satisfied. Thus,

$$z_n = \frac{-M\omega}{a(1-M^2)} + i\sqrt{\frac{n^2\pi^2}{(1-M^2)d^2} - \frac{\omega^2}{a^2(1-M^2)^2}} \quad . \qquad \text{(E. 31)}$$

Since only the values of z_n in the upper half plane are needed for the evaluation of the contour integral, the $\pm$ sign in (E. 30) has been reduced to only a + sign in (E. 31).

Using equations (E. 29) and (E. 31) to evaluate the residues of $f(z)$ at $z = z_n$, one observes that the result is a complex term which has a y-variation given by $\cos n\pi(d-y)/d$ and axial attenuation terms given by

$$\exp\left[- \sqrt{\frac{n^2\pi^2}{(1-M^2)d^2} - \frac{\omega^2}{a^2(1-M^2)^2}} \; (x-\ell) \right] ,$$

$$\exp\left[- \sqrt{\frac{n^2\pi^2}{(1-M^2)d^2} - \frac{\omega^2}{a^2(1-M^2)^2}} \; (x+\ell) \right] . \qquad \text{(E. 32)}$$

The cosine dependence in the y-direction immediately identifies the terms as the transverse modes. The relations (E. 32) are the desired results: the rate at which these transverse modes decay with distance along the duct. If these attenuation rates are large, then the assumption of an infinitely long duct to model the entrance section of the blowdown tunnel is justified. Calculated values for the attenuation coefficients are given in Chapter V.

REFERENCES

1. Ribner, H.S. "Jets and Noise," Canadian Aeronautics and Space Journal (October 1968), pp. 282-298.

2. Taylor, J.W.R. Jane's All the World's Aircraft, 1973-1974, Netherwood, Dalton & Co., Ltd., Great Britain (1974).

3. Lighthill, M.J. "On Sound Generated Aerodynamically," Proc. Roy. Soc., A211 (1952), pp. 564-587.

4. Proudman, I. "The Generation of Noise by Isotropic Turbulence," Proc. Roy. Soc., A214 (1952), pp. 119-132.

5. Ribner, H.S. "Aerodynamic Sound from Fluid Dilatations," UTIA Report No. 86, University of Toronto, Institute for Aerospace Studies (July 1962).

6. Chu, W.T. "Turbulence Measurements Relevant to Jet Noise," UTIAS Report No. 119, University of Toronto, Institute for Aerospace Studies (November 1966).

7. Lee, H.K., and Ribner, H.S. "Direct Correlation of Noise and Flow of a Jet," AIAA Paper No. 72-640, American Institute of Aeronautics and Astronautics, New York (1972).

8. Siddon, T.E. and Rackl, R. "Cross Correlation Analysis of Flow Noise with Fluid Dilatation as Source Fluctuation," Paper H-12, 82nd Meeting of the Acoustical Society of America, Denver, Colorado (19-22 October 1971).

9. Powell, A. "On the Mechanism of Choked Jet Noise," Proc. Phys. Soc. London, 66B (1953), pp. 1039-1056.

10. Powell, A. "The Noise of Choked Jets," Jour. Acous. Soc. Am., 25, no. 3 (1953), pp. 385-389.

11. Powell, A. "On the Noise Emanating from a Two-Dimensional Jet Above the Critical Pressure," Aero. Quart., 4, part 2 (1953), pp. 103-122.

12. Ribner, H.S. "Convection of a Pattern of Vorticity Through a Shock Wave," NACA Report 1164 (1954).

13. Ribner, H.S. "Shock-Turbulence Interaction and the Generation of Noise," NACA Report 1233 (1955).

14. Westley, R. and Woolley, J.H. "An Investigation of the Near Noise Fields of a Choked Axi-symmetric Air Jet," Proceedings of AFOSR-UTIAS Symposium on Aerodynamic Noise, Toronto (20-21 May 1968).

15. Nagamatsu, H. T., Sheer, R. E., and Horvay, G. "Supersonic Jet Noise Theory and Experiments," NASA SP-207 (1969), p. 17.

16. Louis, J. F., Letty, R. M. and Patel, J. R. "A Systematic Study of Supersonic Jet Noise," Gas Turbine Laboratory Report No. 106, Massachusetts Institute of Technology (December 1971).

17. Howes, W. L. "Similarity of Far Noise Fields of Jets," NASA Technical Report R-52 (1959).

18. Sears, W. R. "Fan Noise Research," NASA SP-207 (1969), pp. 189-305.

19. Crocco, L. "Supercritical Gaseous Discharge with High Frequency Oscillations," L'Aerotechnica, 33, part 1 (1953), p. 46.

20. Tsien, H. S. "The Transfer Function of Rocket Nozzles," Jour. Am. Rocket Soc., 22, no. 3 (1952), p. 139.

21. Candel, S. M. "Analytical Studies of Some Acoustic Problems of Jet Engines," Ph. D. Thesis, California Institute of Technology, Pasadena, California (1972).

22. Chang, C. T. "Interaction of a Plane Shock and Oblique Plane Disturbances with Special Reference to Entropy Waves," Jour. Aero. Sci., 24 (1957), pp. 675-682.

23. Cuadra, E. "Acoustic Wave Generation by Entropy Discontinuities Flowing Past an Area Change," Jour. Acous. Soc. Am., 42 (1967), pp. 725-732.

24. Belleval, J. F. and Perulli, M. "Representation de la Turbulence d'un Jet Chaud a Partir de Son Emission Infrarouge," ONERA T. P. No. 1277 (1973).

25. "Equations, Tables and Charts for Compressible Flow," NACA Report 1135 (1953).

26. Morse, P. M. and Ingard, K. U. Theoretical Acoustics, McGraw-Hill, New York (1968), pp. 698-701.

27. Beranek, L. L. and Sleeper, H. P. "The Design and Construction of Anechoic Sound Chambers," Jour. Acous. Soc. Am., 18 (1946), p. 140.

28. Ingerslev, F., Pedersen, O. J., and Møller, P. K. "New Rooms for Acoustic Measurements at the Danish Technical University," Acustica, 19 (1967/1968), p. 185.

29. Rivin, A. N. "An Anechoic Chamber for Acoustical Measurements," Soviet Physics-Acoustics, 7 (1962), p. 258.

30. Koidan, W., Hruska, G. R. and Pickett, M. A. "Wedge Design for National Bureau of Standards Anechoic Chamber," Jour. Acous. Soc. Am., 52 (1972), p. 1071.

31. "Anechoic Chambers Engineering Data," Eckel Industries, Cambridge, Massachusetts (undated).

32. Beranek, L. L. Acoustics, McGraw-Hill, New York (1958).

33. Pope, A. and Goin, K. High Speed Wind Tunnel Testing, John Wiley and Sons, New York (1965).

34. Loehrke, R. and Nagib, H. "Experiments on Management of Free Stream Turbulence," AGARD Report No. 598 (September 1972).

35. Persh, J. and Lee, R. "A Method for Calculating Turbulent Boundary Layer Development in Supersonic and Hypersonic Nozzles Including the Effects of Heat Transfer," NAVORD Report 4200 (June 1956).

36. Reshotko, E. and Tucker, M. "Approximate Calculation of the Compressible Turbulent Boundary Layer with Heat Transfer and Arbitrary Pressure Gradient," NACA TN4154 (December 1957).

37. Schlichting, E. Boundary Layer Theory, Fourth Edition. McGraw-Hill, New York (1951), Chapter 12.

38. Computation of Turbulent Boundary Layers, 1968 AFOSR-IFP Stanford Conference, Volume II (August 1968).

39. SCR Manual, Fifth Edition. General Electric Company, Syracuse, New York (1972).

40. Semiconductor Data Handbook, Second Edition. General Electric Company, Syracuse, New York (1972).

41. The TTL Data Book, First Edition. Texas Instruments, Inc., Dallas, Texas (1973).

42. Digital, Linear, MOS Data Book, Signetics Corp., Sunnyvale, California (1974).

43. A Pocket Guide to the 2100 Computer, Hewlett Packard Corp. Palo Alto, California (undated).

44. Davenport, W. B. and Root, W. L. An Introduction to the Theory of Random Signals and Noise, McGraw-Hill, New York (1958).

45. Panter, P. F. Modulation, Noise, and Spectral Analysis, McGraw-Hill, New York (1965).

46. Churchill, R. V. Complex Variables and Applications, Second Edition, McGraw-Hill, New York (1960).

47. Gold, B. and Rader, C. M. Digital Processing of Signals, McGraw-Hill, New York (1969).

48. Cooley, J. W. and Tukey, J. W. "An Algorithm for the Machine Calculation of Complex Fourier Series," Math. of Comput., 19 (April 1965), pp. 297-301.

49. General Fast Fourier Transform (FTN), Hewlett-Packard Program Documentation No. 22189B. Hewlett-Packard Corp., Palo Alto, California (1971).

50. Churchill, R. V. Fourier Series and Boundary Value Problems, Second Edition. McGraw-Hill, New York (1963).

51. Blackman, R. B. and Tukey, J. W. The Measurement of Power Spectra, Dover, New York (1958).

52. Phillips, R. S., Nichols, N. B., and James, H. B. Theory of Servomechanisms, McGraw-Hill, New York (1947).

53. Abramovich, G. N. The Theory of Turbulent Jets, M. I. T. Press, Cambridge, Mass. (1963).

54. Heskestad, G. "Hot Wire Measurements in a Plane Turbulent Jet," Trans. ASME, J. Appl. Mech., 32E (1966), pp. 721-734.

55. Albertson, M. L., Dai, Y. B., Jensen, R. A. and Rouse, H. "Diffusion of Submerged Jets," Proc. Am. Soc. Civil Engrs., 74 (1948), p. 1751.

56. Hurdle, P. M. and Meecham, W. C. "Correlation Investigation of the Noise Generating Region of a Jet Engine by Means of the Simple Source Fluid Dilatation Model," Proceedings, Interagency Symposium on University Research in Transportation Noise, Stanford University (March 1973), pp. 64-85.